

p - ISSN 1811-1165

e - ISSN 2413-2179

VOLUME 17, No.1(33), 2020

EURASIAN
PHYSICAL
TECHNICAL

JOURNAL

KARAGANDA STATE UNIVERSITY NAMED AFTER E.A. BUKETOV

KARAGANDA, THE REPUBLIC OF KAZAKHSTAN

EURASIAN PHYSICAL TECHNICAL JOURNAL

p - ISSN 1811-1165
e - ISSN 2413-2179

Volume 17, No. 1(33), 2020

1st issue – March, 2004

Journal Founder:

**KARAGANDA STATE UNIVERSITY
NAMED AFTER E.A. BUKETOV**

**Е.А.БӨКЕТОВ АТЫНДАҒЫ ҚАРАҒАНДЫ
МЕМЛЕКЕТТІК УНИВЕРСИТЕТІ**

**КАРАГАНДИНСКИЙ
ГОСУДАРСТВЕННЫЙ УНИВЕРСИТЕТ
ИМ. Е.А.БУКЕТОВА**

Contact information:

Editorial board of EPhTJ (Build. 2, room 216)
Karaganda State University
named after E.A. Buketov
Universitetskaya Str.28, Karaganda,
Kazakhstan, 100028
Subscription index: 75240
Tel: +7(7212)77-04-03
Fax: +7(7212)77-03-84
E-mail: ephjt@mail.ru

Signed to print on **23.06.2020**.
Format 60x84 1/8. Offset paper.
Volume **24.13 p.sh.** Circulation 300 copies.
Agreed price. Order No. 78.

Басуға **23.06.2020**ж. қол қойылды.
Пішімі 60×84 1/8. Офсеттік қағазы.
Көлемі **24.13 ес.-б.т.** Таралымы 300 дана.
Бағасы келісім бойынша. Тапсырыс № 78.

Подписано к печати **23.06.2020**.
Формат 60 × 84 1/8. Офсетная бумага.
Объем **24.13 печ.л.** Тираж 300 экз.
Цена договорная. Заказ № 78.

Printed in the Publishing House
of the KarSU named after academician
E.A. Buketov

академик Е.А. Бөкетов атындағы ҚарМУ
баспасының баспаханасында басылып шықты

Отпечатано в Издательстве
КарГУ имени академика Е.А. Букетова

Chief EDITOR

Sakipova S.E., E.A. Buketov Karaganda State University,
Karaganda, Kazakhstan

EDITORIAL BOARD

Aringazin A.K., Institute for Basic Research, L.N. Gumilyov
Eurasian National University, Nur-Sultan, Kazakhstan

Dueck J., Erlangen-Nuernberg University, Erlangen, Germany

Dzhumanov S., National University of Uzbekistan named after
M. Ulugbek, Tashkent, Uzbekistan

Ibrayev N.Kh., Institute of Molecular Nanophotonics,
E.A.Buketov Karaganda State University, Kazakhstan

Jakovics A., Faculty of Physics and Mathematics, University
of Latvia, Riga, Latvia

Kidibaev M.M., Issyk-kul State University named after
K.Tynystanov, Karakol, Kyrgyzstan

Kucherenko M.G., Director of the Centre of Laser and
Information Biophysics, Orenburg State University, Orenburg,
Russia

Kumekov S.E., K. Satbaev Kazakh State National Technical
University, Almaty, Kazakhstan

Kuritnyk I.P., Department of Electronics and Automation, High
school in Oswiecim, Poland

Miau J.J., Department of Aeronautics and Astronautics,
National Cheng Kung University, Tainan, Taiwan

Pedrini C., University Claude Bernard Lyon I, France

Potapov A.A., V.A. Kotelnikov Institute of Radio Engineering
and Electronics of RAS, Moscow, Russia

Pribaturin N.A., Institute of Thermal Physics, SB RAS,
Novosibirsk, Russia

Saulebekov A.O. Kazakhstan Branch of Lomonosov Moscow
State University, Nur-Sultan, Kazakhstan

Senyut V.T., Joint Institute of Mechanical Engineering of
National Academy of Sciences of Belarus, Minsk, Belarus

Shrager E.R., National Research Tomsk State University,
Tomsk, Russia

Stoev M., South-West University «Neofit Rilski», Blagoevgrad,
Bulgaria

Trubitsyn A.A., Ryazan State Radio Engineering University,
Ryazan, Russia

Zhanabaev Z.Zh., Al-Farabi Kazakh National State University,
Almaty, Kazakhstan

TECHNICAL EDITORS

Kambarova Zh.T., Akhmerova K.E., E.A.Buketov Karaganda
State University, Karaganda, Kazakhstan

CONTENTS

PREFACE	4
MATERIALS SCIENCE	
Nikolaev E.V., Astafyev A.L., Nikolaeva S.A., Lysenko E.N., Zeinidenov A.K. INVESTIGATION OF ELECTRICAL PROPERTIES HOMOGENEITY OF Li-Ti-Zn FERRITE CERAMICS.....	5
Eremin E.N., Yurov V.M., Guchenko S.A. WEAR RESISTANCE AND TRIBOLOGICAL PROPERTIES OF HIGH ENTROPY COATINGS CrNiTiZrCu.....	13
Senyut V.T. STUDY OF SYNERGISTIC EFFECT OF MECHANICAL ACTIVATION AND HIGH PRESSURE AND HIGH TEMPERATURE SINTERING ON THE STRUCTURE OF THE MATERIAL BASED ON BORON NITRIDE.....	19
Surzhikov A.P., Lysenko E.N., Malyshev A.V., Petrova A., Ghyngazov S.A., Aimukhanov A.K. PHASE TRANSFORMATIONS IN FERRITES DURING RADIATION-THERMAL SINTERING.....	26
Ospanali A.T., Kenzhegulov A.K., Zhumadilov B.E., Suyundykova G.S., Medyanova B.S., Partizan G., Aliev B.A. OBTAINING OF CARBON NANOFIBERS BASED ON POLYACRYLONITRILE BY THE METHOD OF ELECTROSPINNING.....	35
Nazarov K.M., Kichanov S.E., El Abd A., Taman M., Kozlenko D.P. STUDY OF WATER INFILTRATION INTO CEMENT-BASED MORTARS USING REAL-TIME THERMAL NEUTRON RADIOGRAPHY.....	39
Kadyrzhanov K.K., Tinishbaeva K., Uglov V.V. INVESTIGATION OF THE EFFECT OF EXPOSURE TO HEAVY XE ²²⁺ IONS ON THE MECHANICAL PROPERTIES OF CARBIDE CERAMICS.....	46
Dikhanbayev K.K., Bondarev A.I., Ikramova S.B., Shabdan E. ELECTRICAL PROPERTIES OF SILICON NANOWIRES UNDER AMMONIA ADSORPTION CONDITIONS.....	54
Rakhadilov B.K., Buitkenov D.B., Wieleba W., Kylyshkanov M.K., Yerbolatuly D. IMPACT OF THE DETONATION GAS SPRAYING MODE ON THE PHASE COMPOSITION AND ADHESIONAL STRENGTH OF Ti-Si-C COATINGS.....	59
Sharipov M.Z., Hayitov D.E., Raupova I.B., Sadikova M.I. INFLUENCE OF HEXAGONAL SYMMETRY STRESSES ON DOMAIN STRUCTURE AND MAGNETIZATION PROCESS OF FeBO ₃ SINGLE CRYSTAL.....	65
Karipbayev Zh., Alpysova G., Mussakhanov D., Lisitsyn V., Kukenova A., Tulegenova A. TIME-RESOLVED LUMINESCENCE EXCITED WITH N ₂ LASER OF YAG:CE CERAMICS FORMED BY ELECTRON BEAM ASSISTED SYNTHESIS.....	73
ENERGY. THERMOPHYSICS. HYDRODYNAMICS	
Obukhov S.G., Plotnikov I.A., Masolov V.G. DYNAMIC WIND SPEED MODEL FOR SOLVING WIND POWER PROBLEMS.....	77
Toleuov G.K., Isataev M.S., Seydulla Zh.K., Zulfukharova E.M., Masina M.N. CALCULATION OF THE END PLATES FRICTION RESISTANCE EFFECT ON THE FLAT JET DYNAMICS.....	85
Sharifov D.M., Sakipov K.E., Merzadinova G.T., Kaliyeva Zh.E., Userbaev M.T. STUDY OF SOME FEATURES OF THE LASER OPTICAL-ACOUSTIC METHOD FOR TECHNICAL DIAGNOSTICS OF HEAT AND POWER ENGINEERING OBJECTS.....	91

Nizhegorodov A.I., Gavrilin A.N., Moyzes B.B., Kuvshinov K.A. STUDY OF DYNAMIC PROCESSES IN BULK MATERIAL DURING ITS BAKING.....	98
Sakipova S.E., Tanasheva N.K., Minkov L.L. MODELING AERODYNAMICS OF A WIND TURBINE WITH CYLINDRICAL BLADES IN A TURBULENT AIR FLOW.....	106
Karabekova D.Zh., Khassenov A.K., Kissabekova P.A., Satybaldin A.Zh., Tungushbekova M.K. VARIATION OF SPATIALLY HETEROGENEOUS RADIATION BY COORDINATE- SENSITIVE RECEIVER.....	113
ENGINEERING. TECHNIQUE, DEVICES, PHYSICAL METHODS OF EXPERIMENT	
Baldytchev M.T., Laptev I.V., Chebotar I.V., Gaychuk Y.N., Pivkin I.G., Timoshenko A.V., Galtseva O.V. EVALUATION OF THE POTENTIAL ACCURACY OF THE PULSED RADIO SIGNALS SOURCE COORDINATE DETERMINATION BY THE POSITIONING SYSTEM USING A SINGLE UAV-SENSOR.....	119
Makeeva O.V., Oleshko V.S., Fedorov A.V., Yurov V.M. DEVELOPMENT OF A DEVICE FOR DETERMINING WORK ELECTRON OUTPUT.....	127
Temiraliev A., Tompakova N., Fedosimova A., Dmitriyeva E., Lebedev I., Grushevskaya E., Mukashev B., Serikkanov A. BIRTH AND FUSION IN A SOL-GEL PROCESS WITH LOW DIFFUSION.....	132
ENGINEERING. MODELING OF THE NONLINEAR PHYSICAL AND TECHNICAL PROCESSES	
Plotnikova I.V., Redko L.A., Baus S.S., Starý O., Kassymov S.S., Baltabekov A.S. CALCULATION OF STRUCTURAL PARAMETERS AND DESIGN OF A PROTECTIVE SHIELD FOR AN X-RAY SYSTEM.....	138
Kazhikenova S.Sh., Belomestny D., Shaltakov S.N., Shaihova G.S. FINITE DIFFERENCE METHOD IMPLEMENTATION FOR NUMERICAL INTEGRATION HYDRODYNAMIC EQUATIONS MELTS.....	145
Aitkhozhayeva Ye.Zh., Tynymbayev S., Adilbekkyzy S., Skabylov A., Ibraimov M. DESIGN AND RESEARCH OF THE BEHAVIORAL MODEL FOR THE MODULAR REDUCTION DEVICE.....	151
Baktybekov K.S., Aimbetov A., Rakhimzhanov B.K., Murat A. MODELING OF FLOOD INUNDATION FOR ZHABAY RIVER BASIN IN CENTRAL KAZAKHSTAN REGION.....	157
PHYSICS AND ASTRONOMY	
Saulebekov A.O., Venos D., Kambarova Zh.T. THE HIGH RESOLUTION ELECTROSTATIC ENERGY ANALYZER FOR SPACE RESEARCH.....	163
Shaikhova G.N., Kutum B.B. TRAVELING WAVE SOLUTIONS OF TWO-DIMENSIONAL NONLINEAR SCHRÖDINGER EQUATION VIA SINE-COSINE METHOD.....	169
SUMMARIES	175
INFORMATION ABOUT AUTHORS	187
GUIDELINES FOR AUTHORS	191

Dear Authors and Readers!
Honourable colleagues!

Since the beginning of 2020, the whole world has been faced with trials and difficulties due to outbreaks of coronavirus. Everything was literally broken, transport communications and production processes stopped, educational institutions and research centers were forced to go online, etc. Undoubtedly, during this period medical doctors and nurses who heroically worked with an increasing number of infected people overcome the greatest difficulties. Without diminishing the invaluable contribution of all workers, I would like to note that many scientists and young researchers in the field of technical physics problems, among whom are our authors, have managed not only to continue their work, but also to obtain quite interesting results, some of which are for your attention.

You can see original scientific articles by researchers from different countries devoted to solving urgent problems of modern physics, materials science and engineering. There are the research results of phase transformation features, various properties, the strength of solids and coatings under the external influence under high pressure or high temperature, during radial thermal sintering, etc. In this issue results of research problems of traditional and green energy, combustion and melting processes, and other are proposed to discuss. The results of the possibilities widespread use of computer calculation and 3D modeling are presented. For example, to optimize laser-acoustic methods for heat diagnostics at energy facilities, to improve methods for determining the dynamic speeds and aerodynamic parameters of wind generators, to assess the accuracy of pulsed radio signals, etc.

As you know in accordance with the CSAB decision from May 8, 2019 Eurasian phys. tech. j. had been included in the Scopus database on four research areas: Energy; Engineering; Materials Science; Physics and Astronomy. The number and geography of interested readers have expanded, and works by authors with a high Hirsch index have appeared.

Recently another good information has become known. On June 10, as a result of updating the SCOPUS database the Eurasian Physical Technical Journal received a citation index of 0.2 (with the highest percentile of 16% in the Energy). So, now Eurasian Physical Technical Journal has a non-zero impact factor in SCOPUS database.

This remarkable and important result was achieved thanks to You - our authors, to the joint work of editorial board members from 11 countries, as well as due to comprehensive support of the university leadership of the quality preparation articles to publication by the programmer, technical editors, library specialists, etc.

Eurasian Physical Technical Journal offers to publish scientific articles for those who are interested in discussing and verification new scientific results at the international level.

I hope and am even sure that the rating (citation index) of the Eurasian Physical Technical Journal will continue to grow thanks to you.

Take care of yourself and your loved ones!

We hope to see you in good health among the authors of our future issues.

Respectfully,
Chief Editor, Saule E. Sakipova
Kazakhstan, June, 2020

DOI 10.31489/2020No1/5-12

UDC 538.956

INVESTIGATION OF ELECTRICAL PROPERTIES HOMOGENEITY OF Li-Ti-Zn FERRITE CERAMICS

Nikolaev E.V.¹, Astafyev A.L.¹, Nikolaeva S.A.¹, Lysenko E.N.¹, Zeinidenov A.K.²

¹National Research Tomsk Polytechnic University, Tomsk, Russia, nikolaev0712@gmail.com

²E.A. Buketov Karaganda State University, Karaganda, Kazakhstan

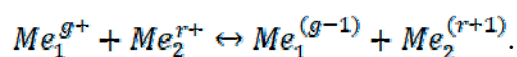
In this article the distribution of electrical conductivity homogeneity of lithium ferrite ceramics was studied. Investigations of the conductivity were performed on samples of lithium substituted ferrite with addition of zirconium dioxide (0%; 0.2%; 0.3%; 0.5 weight %). Experimental samples were sintered at 1010 °C for 2 hours by using the standard ceramic technology. Temperature dependences of electrical conductivity were obtained by the two-probe method (spreading resistance analysis). According to spreading resistance analysis, it was found that the distribution of electrical conductivity in the surface layers varies depending on the chemical composition and this distribution has inhomogeneous character. Also, the activation energy and measurement error were calculated.

Keywords: lithium ferrites, ceramics, electrical conductivity, zirconium dioxide.

Introduction

Ferrite ceramics have a wide range of applications and are used in the most modern electronic computing and radio devices [1, 2]. One of those materials are lithium ferrites, which are widely used in technique that is used both at radio frequencies and at ultrahigh frequencies (microwave range), as well as like cathodes of lithium batteries [3, 4]. The high demand for these materials is due to the low cost of this class of ferrites and excellent ferromagnetic properties. For example, high values of the Curie temperature and saturation magnetization [5], beside low values of dielectric losses [6]. These properties are important for creating ferrite devices with magnetic memory [7].

Spinel of lithium ferrite contains reducible iron ions and lithium ions therefore it is expected that this material has both electronic and ionic conductivity [8]. Experimental data show the electrical conductivity of ferrites increases significantly when ions with different valences are located in equivalent crystallographic positions. The electrical conductivity of ferrites is explained by the Verwey mechanism [9], which means that electrons hop from ion to ion. In this case, the valence of the ions changes in accordance with the expression:



In case when ferrite has the same ions in equivalent crystallographic lattice sites, which has differ by one, then both ions exchange their valences. The corresponding valence states migrate along the crystal, and if it has a sufficiently high concentration of ions with different valences so it leads to high conductivity.

From the Verwey mechanism of electrical conductivity discussed above, it follows that the conductivity of ferrites is more dependent on the content of multivalent ions in them. Such ions in ferrites are often iron ions, as well as ions of zinc, manganese, titanium, and some others [10].

The ceramic method is a classic method of manufacturing lithium ferros spinels, which includes a synthesis stage with the formation of a single-phase product and a further sintering stage at high temperatures [11-13]. However, during high-temperature annealing, the capabilities of this method are limited by the low thermal stability of some reagents [14] (evaporation of lithium and zinc oxide) of the initial mixture and their incomplete ferritization. For this reason, it is observed

probability of increasing of adverse phase inclusions and decreasing of the chemical and product structural homogeneity. These facts lead to a deterioration in its structural, electrical and magnetic properties, which increases the yield of defective products [15, 16].

Conventional methods for solving these problems are using of additional technological methods, including operations of multiple grinding, briquetting and subsequent firing of reaction mixtures. At the same time, such approaches are extremely laborious, energy consuming, and difficult to implement due to the multiple increase in intermediate operations. In addition, the appearance probability of impurities (contaminants) in the reaction mixture is increased.

Effective methods to reduce sintering temperature include such methods as adding oxides with a low melting point, ball mill grinding [17–20], sol-gel [21], and other technologies [22–24]. It was shown in [25, 26] that heating reagents with intense electron beams is an effective method of intensifying solid-state reactions [27], leading to a decrease in the synthesis temperature and an increase in the homogeneity of ferrites [28].

Despite the availability of ferrite production around the world, there are still problems associated with the need to improve the quality of products. In the same time, the development and improvement of electronic technology is accompanied by an ever-increasing tightening of requirements for magnetic materials. Today, there is an urgent necessity for highly specialized magnetic materials with a certain combination of electro-physical and magnetic properties. Alloying lithium and lithium substituted ferrites with different additives allow achieving the necessary characteristics or improving existing electrical, magnetic and mechanic characteristics. It allows get almost any properties inherent in more expensive materials.

Several types of added additives can be distinguished: ones of those form a liquid phase during sintering, thereby affecting the ferrite microstructure, others are located at the grain boundaries as the second phase, which has a very high resistivity. In addition, some additives can be integrated into the ferrite lattice and replace ions at tetrahedral or octahedral levels.

Recently, zirconium dioxide has become an effective additive allowing one to influence the properties and structural state of a wide class of materials [29-31]. Previous scientific results show the additive affects the structure of ferrites, which makes it possible to control other structurally sensitive properties, such as electrical conductivity [32], magnetic permeability [33], thermal conductivity [34], and the shape of the hysteresis loop.

Therefore, there is every reason to suppose that the introduction of zirconia additives can be used in the manufacture of lithium ferrites. This can effect on the formation of structural and electromagnetic characteristics and will allow obtain improved properties compared with prototypes. Thus, the homogeneity of the distribution of electrical conductivity in the surface layers of multi-component lithium ferrite (with the chemical composition $\text{Li}_{0.65}\text{Fe}_{1.6}\text{Ti}_{0.5}\text{Zn}_{0.2}\text{Mn}_{0.05}\text{O}_4$) was studied. The effect of the introduction of zirconia additives on the electrical properties of this ferrite is considered.

1. Experimental part

The measurements were carried out on samples of Li-Ti-Zn ferrite with a low contain of ZrO_2 additive. The initial reagents were chemically pure powders of zinc oxide (ZnO), manganese oxide (MnO), zirconium dioxide (ZrO_2), titanium dioxide (TiO_2) and iron oxide (Fe_2O_3), as well as lithium carbonate (Li_2CO_3) [32, 33]. All initial reagents were pre-dried in a laboratory furnace at a temperature of 200°C for 240 minutes.

In accordance with the chemical equation ($\text{Li}_{0.65}\text{Fe}_{1.6}\text{Ti}_{0.5}\text{Zn}_{0.2}\text{Mn}_{0.05}\text{O}_4$), the initial reagents were weighed on Shimadzu AUW-D digital analytical balances. Then powders were mixed in an agate mortar with tenfold rubbing through a metal sieve with a mesh size of $100\ \mu\text{m}$. It was done to achieve the most uniform distribution of the initial reagents. The mixture of initial powders was divided into four equal parts, after that the zirconia (ZrO_2) was added in different weight ratios to each part. The weight content of ZrO_2 additive was 0; 0.2; 0.3; 0.5 wt. %.

Each part of the mixture was mechanically activated in EMAX (Retsch) high-speed ball mill to increase the homogeneity of the distribution of zirconium dioxide in the mixture and its reactivity [34-35]. Mechanical activation was carried out in steel grinding vials and balls with a diameter of 2 mm. The weights of the mixture and balls were in the ratio 1:10. The mechanical activation was performed at 2000 rpm for 30 minutes.

Mechanically activated powders were pressed by single-sided cold pressing in a hydraulic hand press PGr-10. The pressing pressure was 200 MPa. The pressing time was 3 minutes. After pressing, the samples had a cylindrical shape with a diameter of 15 mm.

The studied samples were sintered at 1010° C for 120 minutes in a laboratory resistance furnace in an air atmosphere. The X-ray diffraction analysis was carried out by using ARL X'TRA (Switzerland) diffractometer with a semiconductor Si (Li) Peltier detector and Cu K α radiation. XRD patterns were measured in the range $2\theta = (10-70)^\circ$ with scanning rate of $0.02^\circ \cdot \text{sec}^{-1}$ and were processed by the full profile analysis using the Powder Cell 2.5 software, where the pseudo-Voigt profile function was used. Phases were identified by the PDF-4+ powder database of the International Center for Diffraction Data (ICDD). The electrical characteristics of the samples were measured by the two-probe method [36].

It is possible to record the current change during the heating of sample with using this method. The studying sample is located on a substrate, which is gradually heated to a temperature of 540 K with using a spiral heater. Two probes are fixed on the surface of the sample, one of which is supplied with a voltage of 5V, and the measured current is detected from the other probe with a voltmeter. This method is characterized by a high locality of measurements, since the spreading resistance is determined mainly by the contact area. The volume of the region where the resistivity is determined is approximately 10^{-10} cm^3 . According to the data, which obtained from measurements by the two-probe method, it is possible to calculate the volume resistivity by the equation:

$$\rho = \frac{U \cdot r_0 \pi}{I}, \quad (1)$$

where U is the applied voltage, I is the current, r_0 is the diameter of the contact.

The diameter of the contact is approximately $\sim 10 \mu\text{m}$ and corresponds to the spatial resolution of the method. For Li-Ti-Zn ferrite samples, temperature dependences of the current on temperature were obtained. Each sample was heated from room temperature to 540°K. To determine the accuracy of the study, the surface current of each sample was measured at four points. According to the temperature dependences of the current, experimental curves were calculated in the coordinates $\ln(I) = f(1/(k \cdot T))$ to determine the activation energy. The activation energy is defined as the tangent of the angle of inclination to the approximation curve [37].

2. Results and discussions

Figure 1 shows X-ray diffraction patterns of Li-Zn-Ti ferrite with a 2% content of ZrO $_2$ and the initial powder of ZrO $_2$. Diffraction patterns show all the high-intensity reflections which belongs to zirconium dioxide, coincide with the Li-Zn-Ti ferrite reflections. Only one reflection located at $2\theta \approx 51^\circ$ does not coincide. By the presence of reflections at these angles, it is possible to detect zirconium dioxide in the composition of ferrite, however, the small weight content of ZrO $_2$ in the mixture, as well as the presence of overlapping reflections, does not allow to detecting its content in the studied samples.

Figure 2 shows the diffraction patterns of the initial powder components Fe $_2$ O $_3$ (JCPDS No. 40-142), Li $_2$ CO $_3$ (JCPDS No. 66-941) and TiO $_2$ (JCPDS No. 82-656) phases.

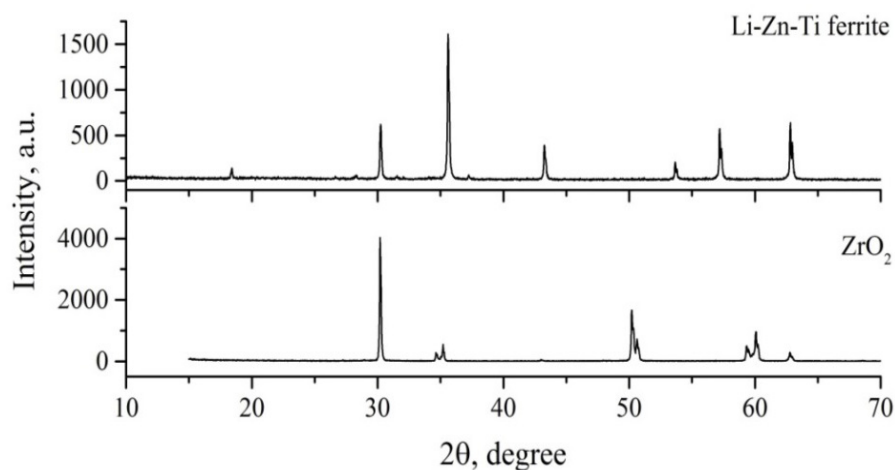


Fig.1. X-ray diffraction patterns of Li-Zn-Ti ferrite and ZrO_2 powder

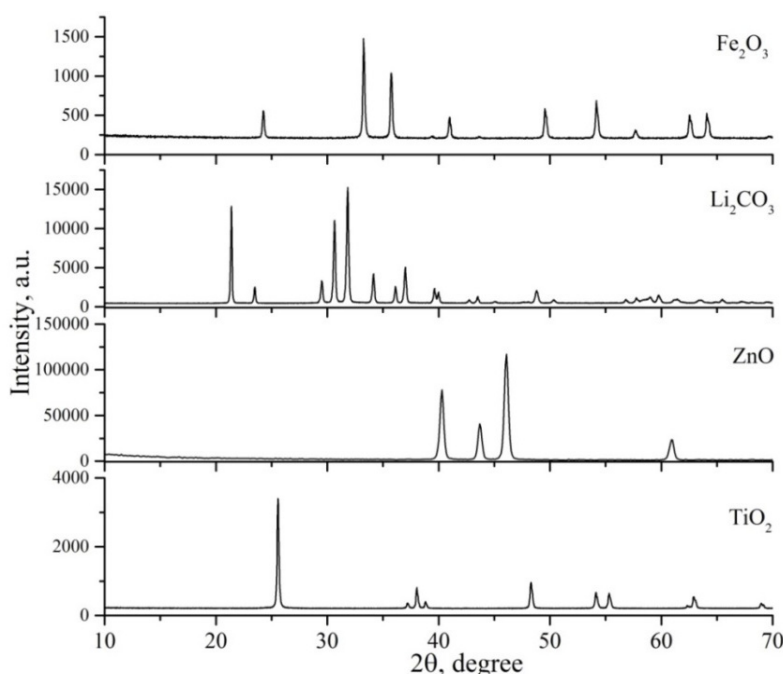


Fig.2. X-ray diffraction pattern of initial powders

Analysis X-ray diffraction patterns shows absences of reflections which can be belong to initial powder and all observed reflection belongs to spinel phase. It shows that the selected technological modes of sintering, pressing, as well as the time and energy of mechanical activation allow us to obtain the spinel phase, which corresponds to final composition of Li-Zn-Ti ferrite without impurities. For all Li-Ti-Zn ferrite samples, current measurements were carried out during the heating of the sample. Values of the current were taken on the surface of the sample at four randomly selected points.

Figure 3 shows the temperature dependences of the bulk conductivity current for a sample without zirconia, which measured at four points on the surface. The temperature curves of the bulk conductivity current are characterized by a linear dependence in logarithmic coordinates $\ln(I)=f(1/kT)$. With increasing temperature, an increase in electrical conductivity is observed, which is characteristic of lithium ferrites.

Figures 4, 5 and 6 show curves for samples with additive of zirconium dioxide (0.2, 0.3 and 0.5wt %). In these graphs, the curves are located as close as possible to each other, which indicate a small experimental error and may indicate a uniform distribution of electrical conductivity over the surface of the sample.

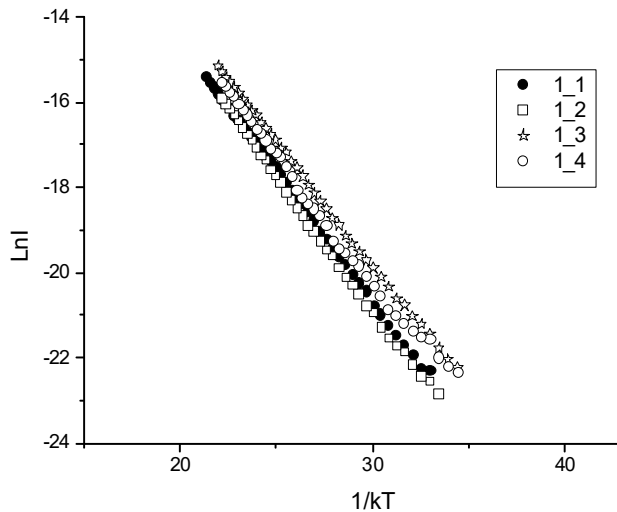


Fig.3. The temperature dependence of conductivity current for samples without ZrO_2

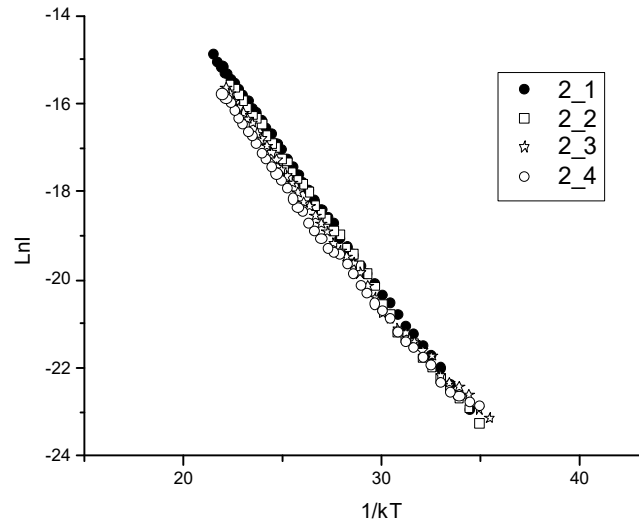


Fig.4. The temperature dependence of conductivity current for Li-Ti-Zn ferrite with 0.2 wt% ZrO_2

The linear form of dependence without kinks in Figures 3–6 indicates that in the temperature range 300–540 °K there is only one conduction mechanism with certain activation energy. This type of temperature dependence is due to a change in electron mobility in Li-Ti-Zn ferrite, during the heating of the sample. In this case, the Verwey mechanism of conductivity is best suited to describe the mechanism of electrical conductivity.

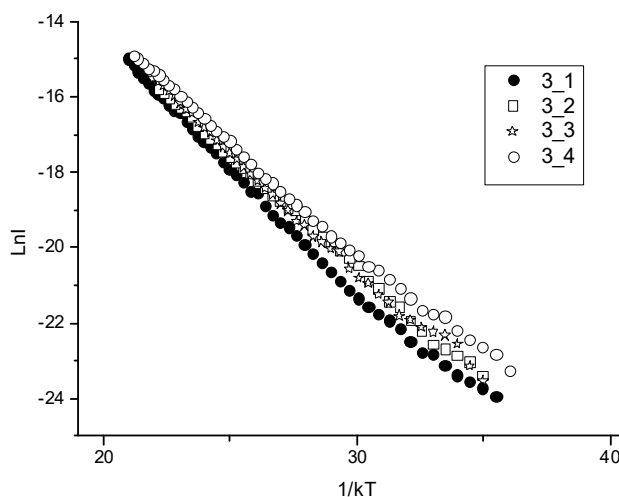


Fig.5. The temperature dependence of conductivity current for Li-Ti-Zn ferrite with 0.3 wt% ZrO_2

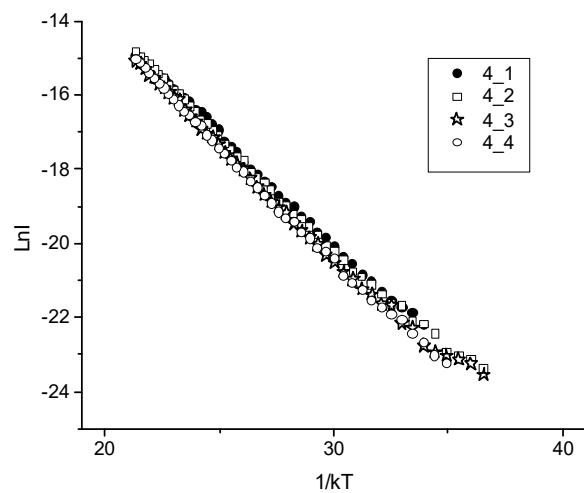


Fig.6. The temperature dependence of conductivity current for Li-Ti-Zn ferrite with 0.5 wt% ZrO_2

This mechanism explains the electrical conductivity of ferrites by the process of electron hopping from ion to ion, so the electrical conductivity will depend on the content of multivalent ions in the ferrite. For Li-Ti-Zn ferrite samples, the electrical conductivity will be determined by electron hopping between the multivalent iron ions Fe^{2+} and Fe^{3+} .

In Figures 3-6, the electrical conductivity of ferrite samples increases during the heating process. The similar character of the dependences $\ln(I) = f(1/kT)$ for samples with and without zirconium dioxide indicates that additive of zirconium dioxide does not significantly effect on the mechanism of electric conductivity in lithium ferrites. A slight change of the electrical characteristics may be due to the effect of zirconium dioxide on the microstructural properties of Li-Ti-Zn ferrite. As it is known, microstructural properties can effect on the electrical characteristics. So, for example, a decrease of grain size and an increase of porosity can affect on the electrical resistance of ferrites.

The experimental temperature curves were used to calculate the activation energy (E_a). The activation energy can be calculated if obtained experimental points fit in a straight line. In this work, the activation energy was calculated for all samples; the average value of the activation energy based on four measurements is presented in Table 1 (column 2). Also, for each measurement, the volume resistivity was calculated according to equation 1, the average value of the resistivity can be seen in table 1 (column 4). From the data of Table 1 it can be seen that the samples have a high volume resistivity. The activation energy and resistivity data, which obtained from the surface of samples with different ZrO_2 additive contents, have an insignificant difference, which indicates that small additions of zirconium dioxide up to 0.5% do not significantly affect the electric conductivity in Li-Ti-Zn ferrite.

Table 1. Electrophysical parameters of Li-Ti-Zn ferrite

Additive of ZrO_2 , %	E_a , eV	ρ , GO m·cm
0	0.597 ± 0.03059	1.45 ± 0.175
0.2	0.594 ± 0.02803	1.34 ± 0.109
0.3	0.604 ± 0.03086	1.58 ± 0.206
0.5	0.593 ± 0.02775	1.27 ± 0.115

According to Table 1, we can conclude that the electrical resistivity is evenly distributed over the surface of the sample; the deviation from the average value of the activation energy for each sample based on four measurements is not more than 7%. So the largest variation of the measurement is the sample without the addition of zirconium dioxide. For this sample, the actual error of the activation energy value exists in the probability interval with a standard deviation of ± 0.03059 eV at an arbitrary temperature of the sample in the temperature range 300-540 °K.

Conclusion

In the presented work, samples of Li-Ti-Zn ferrite with the addition of zirconium dioxide were made by the standard ceramic technology (Conventional method). X-ray phase analysis showed the presence of a spinel phase which corresponds to phase of final Li-Ti-Zn ferrite. This fact indicates a complete ferritization process.

In this article, small additives of zirconium dioxide up to 0.5 wt% were considered, it was found that such a low content of the additive does not has significantly affect on the electrically transfer process in Li-Ti-Zn ferrite. The samples under study possess semiconductor properties; an increase in the conductivity is observed with an increase in the temperature of the samples.

For the studied lithium ferrite, the conduction mechanism in the temperature range 300–540 °K is determined by electron hopping between the multivalent ions Fe^{2+} and Fe^{3+} . It was found that the deviation from the average value of the activation energy for each sample based on four measurements is not more than 7%.

Acknowledgements

This research was supported by the Russian Science Foundation (Grant no.19-72-10078).

REFERENCES

- 1 Sharif M., Jacob J., Javed M., Manzoor A., Mahmood K., Khan M.A. Impact of Co and Mn substitution on structural and dielectric properties of lithium soft ferrites. *Physics B: Condensed Matter*. 2019, Vol. 567, pp. 45 – 50.
- 2 Mazen S.A., Abu-Elsaad N.I. Structural, magnetic and electrical properties of the lithium ferrite obtained by ball milling and heat treatment. *Applied Nanoscience*. 2015, Vol. 5, pp. 105 – 114.
- 3 Yurov V.M., Baltabekov A.S., Laurinas V.C., et al. Dimensional effects and surface energy of ferro-electric crystals. *Eurasian phys. tech. j.* 2019, Vol.16, No.1(31), pp.18–23.
- 4 Dun C., Xi G., Zhang Y., Zhao T., Liu Y., Heng X., Yao L. Structural, magnetic and magneto-structural properties of $\text{Co}_{1-x}\text{Li}_x\text{Fe}_2\text{O}_4$ synthesized by cathode materials of spent Li-ion batteries. *Ceramic International*. 2018, Vol. 44, pp. 20984 – 20991.
- 5 Rathod V., Anupama A.V., Jali V.M., Hiremath V.A., Sahoo B. Combustion synthesis, structure and magnetic properties of Li-Zn ferrite ceramic powders. *Ceramic International*. 2017, Vol.43, pp. 14431–14440. DOI: 10.1016/j.ceramint.2017.07.213.
- 6 Gan G., Zhang D., Zhang Q., Wang G., Huang X., Yang Y., et al. Influence of microstructure on magnetic and dielectric performance of Bi_2O_3 -doped Mg-Cd ferrites for high frequency antennas. *Ceramic International*. 2019, Vol. 45, pp. 12035 – 12040.
- 7 Rashad M.M., Fayed M.G., Sami T.M., El-Shereafy E.E. Structural, microstructure and magnetic properties of superparamagnetic $\text{Mn}_x\text{Mg}_{1-x}\text{Fe}_2\text{O}_4$ powders synthesized by sol-gel auto-combustion method. *Journal of Materials Science: Materials in Electronics*. 2015, Vol. 26, pp. 1259 – 1267.
- 8 Sekulic D.L., Lazarevic Z.Z., Sataric M.V., Jovalekic C.D., Romcevic N.Z. Temperature complex impedance, electrical conductivity and dielectric studies of MF_{e204} (M=Mn, Ni, Zn) ferrites prepared by sintering of mechano-chemical synthesized nanopowders. *Journal of Materials Science: Materials in Electronics*. 2015, Vol. 26, pp. 1291 - 1303.
- 9 Şaşmaz Kuru T., Şentürk E., Eyüpoğlu V. Overlapping large polaron conductivity mechanism and dielectric properties of $\text{Al}_{0.2}\text{Cd}_{0.8}\text{Fe}_2\text{O}_4$ ferrite nanocomposite. *Journal of Superconductivity and Novel Magnetism*. 2017, Vol. 30, pp. 647 – 655.
- 10 Yang Y., Zhang H., Li J., Xu F., Gan G., Wen D. Effects of $\text{Bi}_2\text{O}_3\text{-Nb}_2\text{O}_5$ additives on microstructure and magnetic properties of low-temperature-fired NiCuZn ferrite ceramics. *Ceramic International*. 2018, Vol. 44, pp. 10545 – 10550. <https://doi.org/10.1016/j.ceramint.2018.03.076>.
- 11 Durgadsimi S.U., Chougule S.S., Kharabe R.G., Mathad S.N., Rendale M.K. Solid-state synthesis and structural features of $\text{Li}_{0.5}\text{Ni}_{0.75-x}\text{Fe}_2\text{O}_4$ ferrites. *International Journal of Self-Propagating High-temperature Synthesis*. 2019, Vol. 28, pp. 71 – 73.
- 12 Devi H.S., M. Maisnam M. Studies on the structural and piezoelectric properties of ZnO added on $\text{Na}_{0.47}\text{K}_{0.47}\text{Li}_{0.006}\text{NbO}_3$ ceramics prepared by ceramic method using high energy ball mill. *Journal of Materials Science: Materials in Electronics*. 2019, Vol. 30, pp. 11458 – 11463.
- 13 Anjum S., Seher A., Mustafa Z. Effect of La^{3+} ions substituted M-type barium hexa-ferrite on magnetic, optical and dielectric properties. *Applied Physics A*. 2019, Vol. 125 p. 664
- 14 Ridgley D.H., Lessoff H., Childress J.V. Effects of Lithium and Oxygen Losses on Magnetic and Crystallographic Properties of Spinel Lithium Ferrite. *Journal of the American Ceramic Society*. 1971, Vol.53, pp. 304 – 311.
- 15 Beregi E., Sterk E., Pal E., Farkas-Jahnke M. Crystal defects in flux grown lithium ferrite, LiFe_5O_8 single crystal. *Hungarian Academy of Sciences*. 1979, Vol. 47 pp. 263 – 273. DOI: 10.1007/BF03156535.
- 16 Vakhitov R.M., Shapayeva T.B., Solonetski R.V., Yumaguzin A.R. Structure of magnetic formations on the defects of ferrite-garnet films. *Doklady Physical Chemistry*. 2016, Vol. 470 pp. 165 – 167.
- 17 Kalinkin A.M., Usoltsev A.V., Kalinkina E.V., Nevedomskii V.N., Zalkind O.F. Solis-phase synthesis of nanocrystalline lanthanum zirconate using mechanical activation. *Russian Journal of General Chemistry*. 2017, Vol.87, pp. 2258 - 2264. <https://doi.org/10.1134/S1070363217100024>.
- 18 Surzhikov A.P., Pritulov A.M., Lysenko E.N., Sokolovskiy A.N., Vlasov V.A. Vasendina E.A. Calorimetric investigation of radiation-thermal synthesized lithium penta-ferrite. *Journal of Thermal Analysis and Calorimetry*. 2012 Vol. 101, No.1, pp. 11-13. DOI: 10.1007/s10973-010-0788-7
- 19 Anjum S., Nisa M., Sabah A., et al. Comprehensive analysis of structure and temperature, frequency and concentration-dependent dielectric properties of lithium-substituted cobalt ferrites ($\text{Li}_x\text{Co}_{1-x}\text{Fe}_2\text{O}_4$). *Applied Physics A*. 2017, Vol. 123, pp. 1 – 8. <https://doi.org/10.1007/s00339-017-1169-x>.

- 20 Mahmoudi M., Kavanlouei M., Maleki-Ghaleh H. Effect of composition on structural and magnetic properties of nanocrystalline ferrite $\text{Li}_{0.5}\text{Sm}_x\text{Fe}_{2.5-x}\text{O}_4$. *Powder Metallurgy and Metal Ceramics*. 2015, Vol.54, pp. 31 – 39. DOI: 10.1007/s11106-015-9676-9.
- 21 Berezhnaya M.V., Mittova I.Y., Perov N.S., Al'myasheva O.V., Nguyen A.T., Mittova V.O., Bessalova V.V., Viryutina E.V. Production of zinc-doped yttrium ferrite nanopowders by the sol-gel method. *Russian Journal of Inorganic Chemistry*. 2018, Vol. 63, pp. 742 – 746.
- 22 Kumar A., Yadav N., Rana D.S., Kumar P., Arora M., Pant R.P. Structural and magnetic studies of the nickel doped CoFe_2O_4 ferrite nanoparticles synthesized by the chemical co-precipitation method. *Journal of Magnetism and Magnetic Materials*. 2015, Vol. 394, pp. 379 – 384.
- 23 Merzadinova G.T., Sakipov K.E., Sharifov D.M., Mirzo A., Bekeshev A.Z. Laser photoacoustics method for determination of the coefficients of thermal conductivity and thermal diffusivity of materials. *Eurasian phys. tech. j.* 2019, Vol.16, No.1(31), pp. 94 – 98.
- 24 Rathod V., Anupama V.A., Kumar R., Jali V.M., B. Sahoo B. Correlated vibrations of the tetrahedral and octahedral complexes and splitting of the absorption bands in FTIR spectra of Li-Zn ferrites. *Vibrational Spectroscopy*. 2017, Vol. 92, pp. 267 – 272. DOI: 10.1016/j.vibspec.2017.08.008.
- 25 Boldyrev V.V., Voronin A.P., Gribkov O.S., et al. Radiation-thermal synthesis. Current achievement and outlook. *Solid State Ionics*.1989, Vol .36 pp. 1 – 6. [https://doi.org/10.1016/0167-2738\(89\)90051-9](https://doi.org/10.1016/0167-2738(89)90051-9).
- 26 Auslender V.L., Bochkarev I.G., Boldyrev V.V., et al. Electron beam induced diffusion controlled reaction in solids. *Solid State Ionics*.1997, Vol.103, pp. 489 – 493. DOI: 10.1016/S0167-2738(97)84073-8.
- 27 Surzhikov A.P., Pritulov A.M., Lysenko E.N., Sokolovskii A.N., Vlasov V.A., Vasendina E.A. Influence of solid-phase ferritization method on phase composition of lithium-zinc ferrites with various concentration of zinc. *Journal of Thermal Analysis and Calorimetry*, 2012, Vol. 109, pp. 63-67.
- 28 Surzhikov A.P., Lysenko E.N., Malyshev A.V., Vlasov V.A., Suslyayev V.I., Zhuravlev V.A., Korovin E.Y., Dotsenko O.A. Study of the radio-wave absorbing properties of a lithium-zinc ferrite based composite. *Russian Physics Journal*. 2014. Vol.57, No.5, pp. 621 – 626.
- 29 Surzhikov A.P., Lysenko E.N., Malyshev A.V., Pritulov A.M., Kazakovskaya O.G. Influence of mechanical activation of initial reagents on synthesis of lithium ferrite. *Russian Physics Journal*. 2012, Vol.55, pp. 672 – 677. <https://doi.org/10.1007/s11182-012-9865-7>.
- 30 Surzhikov A.P., Malyshev A.V., Lysenko E.N., Vlasov V.A., Sokolovskiy A.N. Structural, electromagnetic, and dielectric properties of lithium-zinc ferrite ceramics sintered by pulsed electron beam heating. *Ceramics International*. 2017, Vol. 43, No. 13, pp. 9778-9782.
- 31 Surzhikov A.P., Frangulyan T.S., Ghyngazov S.A. A thermoanalysis of phase transformations and linear shrinkage kinetics of ceramics made from ultrafine plasmochemical $\text{ZrO}_2(\text{Y})\text{-Al}_2\text{O}_3$ powders. *Journal of Thermal Analysis and Calorimetry*. 2014, Vol. 115, No. 2, pp. 1439-1445
- 32 Long X., Liu Y., Yao G., Du J., Zhang X., Cheng J., Hua J. Microstructure and mechanical properties of NiFe_2O_4 ceramics reinforced with ZrO_2 particles with different sintering temperatures. *Journal of Alloys and Compounds*. 2013, Vol. 551, pp. 444 – 450.
- 33 Bejbl, J., Bemš, J., Králík, T., et al. New approach to brown coal pricing using internal rate of return methodology. 2014, *Applied Energy*, Vol. 133, pp. 289 – 297.
- 34 Lysenko E.N., Ghyngazov S.A., Surzhikov A.P., Nikolaeva S.A., Vlasov V.A. The influence of ZrO_2 additive on sintering and microstructure of lithium and lithium titanium-zinc ferrites. *Ceramic International*. 2019, Vol.45, pp. 2736–2741.
- 35 Luchnikov P.A., Vetrova V.V., Zubkov N.P., Surzhikova, O.A. Chernova, N.I. Deformable Polymer Dielectric Films in Phase Light Modulators. *IOP Conference Series: Materials Science and Engineering*. 2017, Vol. 189.
- 36 Bemš, J., Starý, O., Macaš, M., Žegklitz, J., Pošík, P. Innovative default prediction approach // *Expert Systems with Applications*, 2015, Vol. 42, No 17-18, pp. 6277 – 6285.
- 37 Lysenko, E.N., Surzhikov A.P., Vlasov V.A., Nikolaev E.V., Malyshev A.V., Bryazgin, A.A., Korobeynikov, Mikhailenko, M.A. Synthesis of substituted lithium ferrites under the pulsed and continuous electron beam heating . *Nuclear Instruments and Methods in Physics Research, Section B: Beam Interactions with Materials and Atoms*.-2017.-Vol.392.-pp.1-7.

DOI 10.31489/2020No1/13-18

UDC 669.018.44

WEAR RESISTANCE AND TRIBOLOGICAL PROPERTIES OF HIGH ENTROPY COATINGS CrNiTiZrCu

Eremin E.N.¹, Yurov V.M.², Guchenko S.A.²¹Omsk State Technical University, Omsk, Russia, weld_techn@mail.ru²E.A. Buketov Karaganda State University, Karaganda, Kazakhstan, exciton@list.ru

A highly entropic alloy was first synthesized in the work by mechanical alloying followed by heat treatment in vacuum under certain conditions. The microhardness of the CrNiTiZrCu coating is not inferior and in most cases exceeds the hardness of highly entropic equiatomic alloys. The wear resistance of the CrNiTiZrCu coating is $3 \cdot 10^{-4}$ g/min, which also meets the special steels for wear resistance. High entropy coating has a low coefficient of friction (0.04) at the level of friction of layered crystals, which distinguishes them from high-entropy alloys (about 0.4-0.6) by an order of magnitude. They turn out to be anti-friction, which in all probability leads to energy savings. The coating is already used in the manufacture of turbine blades made of steel 20X13 at a turbo-mechanical plant in Karaganda.

Keywords: highly entropic coatings, target, equiatomic proportions, microhardness, wear resistance.

Introduction

Just over 15 years have passed since the discovery of high-entropy alloys (2004) [1]. The first review was performed as a complete material science cycle “production - structure - properties” for a new class of vacuum-plasma coatings - nitrides of multi-element high entropy metal alloys in [2].

A current state analysis was made for the production of such coatings, their morphology, elemental and phase compositions, structure, substructure, stress state and functional properties depending on the main formation parameters: substrate temperature during deposition, magnitude of the bias potential supplied to the substrate, and the composition of the gas atmosphere. Then many articles appeared on the synthesis and study of various high-entropy alloys [3-9].

The latest review on HEAs was made in [10]. An analysis of more than 200 obtained high entropy alloys (HEA) allowed to establish the relationship between the electron concentration, phase composition, lattice parameter and the properties of solid solutions based on BCC, FCC lattice. The basic conditions for the appearance of high-entropy chemical compounds — the Laves phase, σ - and μ -phases, are revealed. For the formation of a 100% high-entropy σ -phase, a necessary condition is that all the elements that make up the high-entropy alloys must form the σ -phase in two-component alloys in a different combination, and the electronic concentration of the alloy should be in the range of 6.7–7.3 electron/atom.

For the formation of a 100% high-entropy phase of Laves the following conditions are required: the total negative enthalpy of alloy mixing at the level of -7 kJ / mol and below; pairs with an atomic difference of more than 12%; the presence in the alloy of two elements with a mixing enthalpy of less than -30 kJ/mol, the average electron concentration should be in the range of 6-7 electron/atom.

It is shown that the ratio of the lattice parameters of solid-state HEA, determined in the experiment, to the lattice parameter of the most refractory metal of the HEA determine the magnitude of the elastic modulus. An analysis of the literature data showed that we synthesized the high-entropy alloys for the first time by us due to know-how. This effect is the basis of the Application for the Patent of the Republic of Kazakhstan filed in early 2020. The continuation of the results presented in this article has already been published by us in [11, 12]. We hope that this article will be an incentive for ongoing research.

1. Target preparation and coating

To prepare the CrNiTiZrCu target, micropowders of the corresponding metals were taken and mixed in equiatomic proportions. Then, the prepared powder mixture was placed in a grinding bowl of a planetary ball mill made of tungsten carbide and grinding bodies (balls with a diameter of 5-10 mm) also made of tungsten carbide, the mass of which was equal to 10 masses of the powder mixture, were added. After the glass was filled with Galosha gasoline, the lid was tightly closed and the planetary ball mill was turned on (rotation speed was 500 rpm, operation time 5 hours), Fig. 1a and b. The resulting homogenized composition was then dried in a vacuum and pressed with a mold into a flat disk with a diameter of 100 mm and a thickness of 5 mm. Next, the disk was placed in a vacuum thermo-furnace and sintered in it for 3 hours. Thus, the fabricated CrNiTiZrCu target (Fig. 1c) was used for further magnetron coating deposition at the NVN 6 facility.

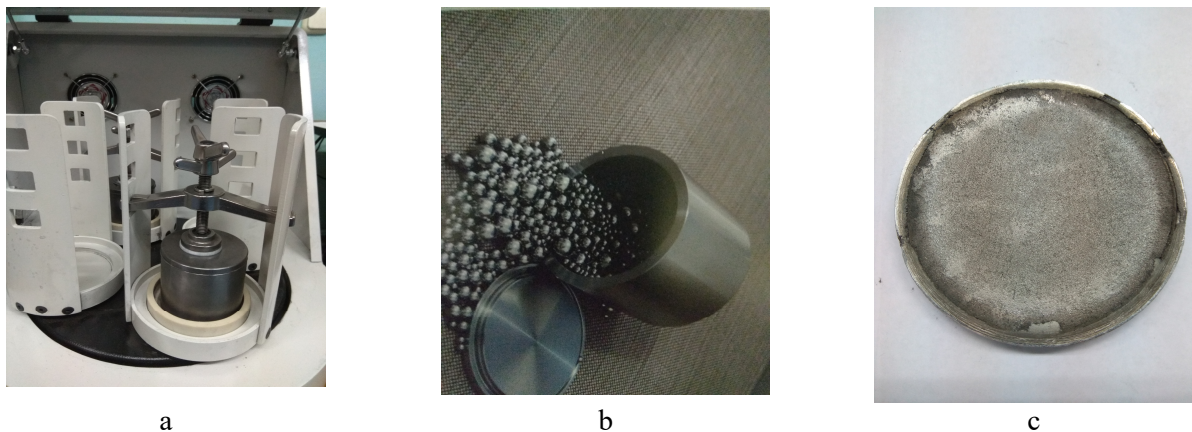


Fig.1. Magnetron target synthesis: a - planetary ball mill; b - micropowders of metals; c - finished target

Coating was carried out on prepared substrates made of AISI-201 steel (hexagons with a side length of 22 mm and a thickness of 5 mm.). The vacuum chamber was pumped out to a pressure of 0.003 Pa, then the PINK was turned on, and Ar was puffed up to a pressure of 1 Pa, a negative bias potential of 1000 V was applied to the substrate for 10 min. the surface of the substrate was cleaned and heated. After that, the argon pressure was lowered to 0.1 Pa and the magnetron was switched on. The bias on the substrate decreased to 150 V, the magnetron current was kept constant at 3 A. The substrate was located in the chamber at a distance of 15 cm, the spraying time was 1 hour.

2. Electron Microscopic Examination (EME)

Electron microscopy was carried out using a TESCAN MIRA 3 scanning electron microscope. The studies were carried out at an accelerating voltage of 20 kV and a working distance of about 15 mm. Dependencies are shown in Fig. 2.

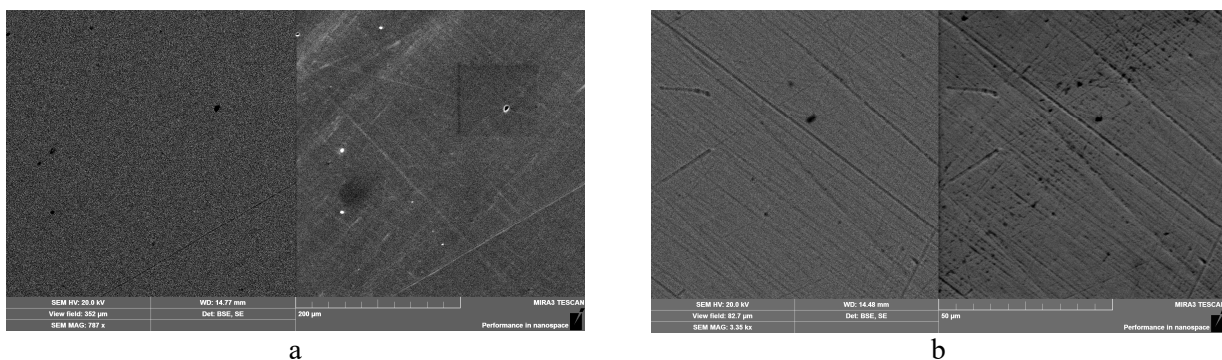


Fig.2. EME of the CrNiTiZrCu coating in argon: a) 500 μm; b) 50 μm

To measure the XPS, the test sample in the form of a disk with a diameter of 8 mm and a height of 3 mm is inserted into the recess of the holder of the microscope sample (Fig. 3).

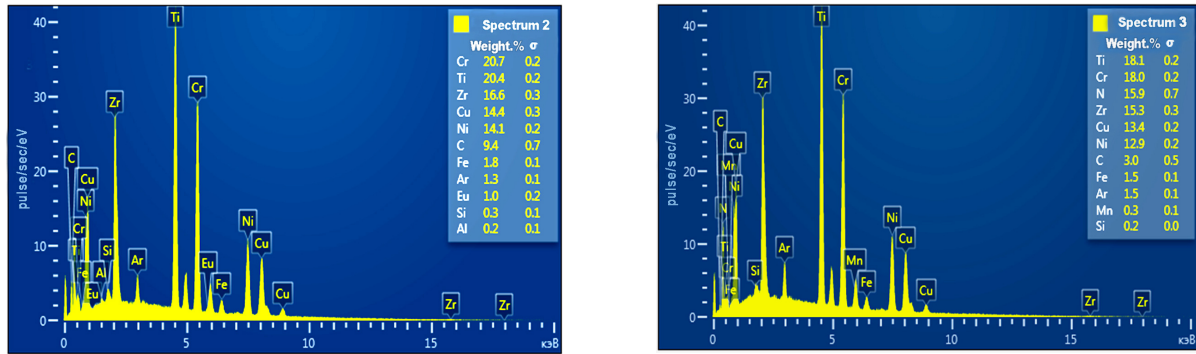


Fig.3. XPS CrNiTiZrCu in argon at 2 points

Fig.3 gives the chemical composition of CrNiTiZrCu, at.%, in equiatomic proportions (Table 1).

Table 1 - Quantitative chemical composition of CrNiTiZrCu, at. %

Element	Cr	Ni	Ti	Zr	Cu
Nominal	20	20	20	20	20
in Argon	23.2	21.2	19.9	17.1	6.8
in Nitrogen	22.8	20.8	19.7	16.9	7.0

With an increase in grinding time, the interdiffusion of the components increases and their solubility in the solid state increases until supersaturation is reached, beyond which there is no further increase in solubility (Fig. 4).

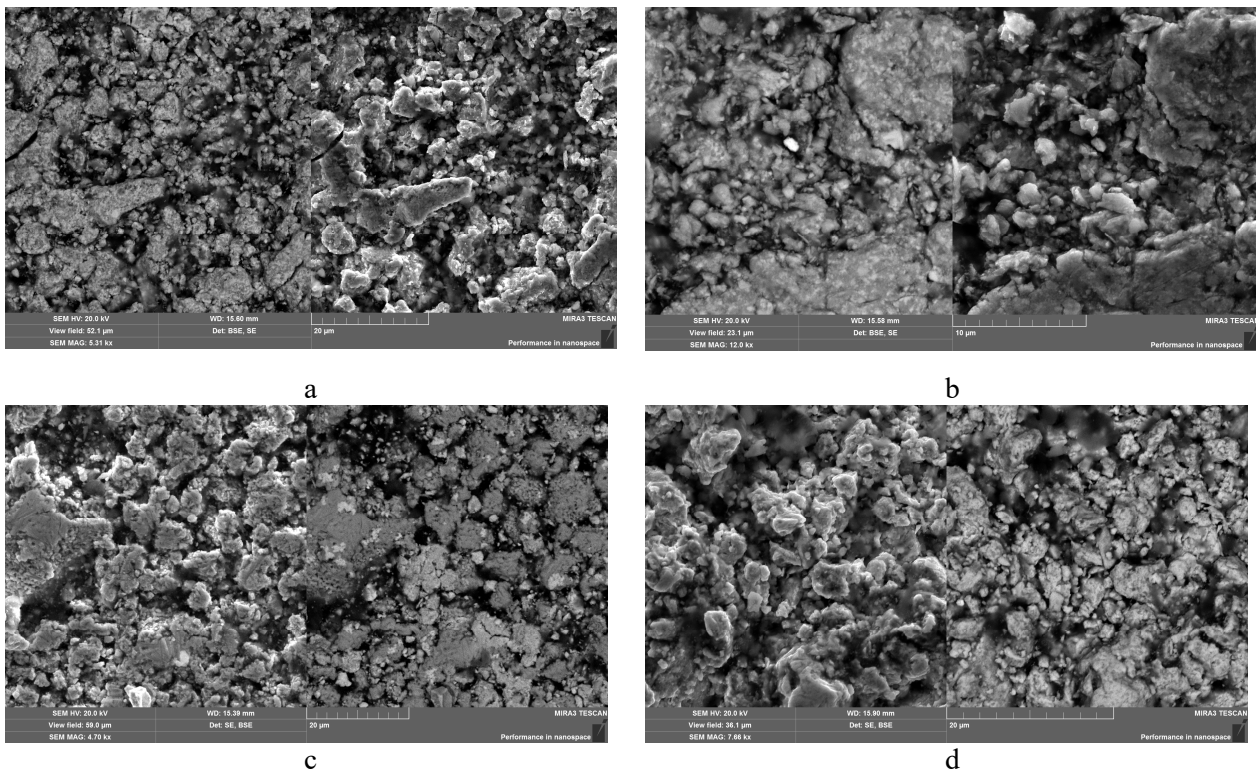


Fig.4. Microstructure of Cr-Ni-Ti-Zr components from CrNiTiZrCu alloy at a resolution: a) 20 μm ; b) 10 μm ; c) 20 μm ; d) 20 μm .

For traditional alloys in the Cr-Ni-Ti-Zr-Cu system, the formation of many intermetallic compounds, for example, such as Ni_3Ti , Ni_3Cu , Cr_2Ti , is characteristic. Whereas in the obtained multicomponent CrNiTiZrCu alloy they are not formed, and it completely consists of a simple bcc solid solution, and the total number of phases is much lower than the maximum equilibrium amount allowed by the Gibbs phase rule. The predominant formation of simple solid solutions over intermetallic compounds in multicomponent equiatomic alloys is mainly provided by the influence of high entropy of mixing. According to thermodynamics, it is preferable to form phases with a low Gibbs free energy. If the enthalpy is constant, phases with a higher entropy will have lower Gibbs free energy. This effect of entropy is significantly increased for wind farms. CrNiTiZrCu alloy contains five components and its mixing entropy is $> 1.61R$, which is high for metal alloys, since the melting entropy of traditional alloys is $1R$. As a result, the Gibbs free energy of the solid solution is lower than the Gibbs energy of the intermetallic compounds; therefore, a solid solution is predominantly formed. Moreover, the melting entropy of the individual elements present in the alloy (Table 1) is lower compared to the mixing entropy of the five-component system, which is 13.38 J/K mol , which causes the formation of a simple crystalline structure of a solid solution.

3. Microhardness of coatings

We used the HVS-1000A microhardness tester. The results of measurements of coatings CrNiTiZrCu are given in table. 2.

Table 2 - Microhardness of CrNiTiZrCu Coating in Argon and Nitrogen

Microhardness	1	2	3	4	5	6	7	8	The average
HV, in argon	839	909	864	842	967	753	821	902	886
HV, in nitrogen	897	899	899	863	879	887	966	962	888

The microhardness (HV) of the CrNiTiZrCu coating in the medium of argon and nitrogen did not change. This means that nitrogen does not form part of the coating. Compare the data Table 2 with the data on highly entropic alloys (Table 3).

Table 3 - Microhardness of high-entropy alloys [2]

Alloys	Initial hardness cast alloys, HV	Alloy hardness after annealing, HV
CuTiVFeNiZr	590	600
AlTiVFeNiZr	800	790
MoTiVFeNiZr	740	760
CuTiVFeNiZrCo	630	620
AlTiVFeNiZrCo	790	800
MoTiVFeNiZrCo	790	790
CuTiVFeNiZrCoCr	680	680
AlTiVFeNiZrCoCr	780	
MoTiVFeNiZrCoCr	850	890
Stainless steel	410	362
The microhardness of our coating CrNiTiZrCu	888	888

It turned out that these cast materials, along with characteristics typical of metal alloys, had unique and unusual properties inherent, for example, to cermets: high hardness and resistance to softening at high temperatures, dispersion hardening, positive temperature hardening coefficient,

and high level of strength characteristics at elevated temperatures, attractive wear resistance, corrosion resistance and a number of other properties. It is worth paying attention to the fact that, even at high temperatures, the alloys did not lose their sufficiently high mechanical properties, which significantly exceeded the properties of traditional widely used alloys and mainly consisted of simple bcc and fcc phases. After annealing, the alloys retained high hardness, corrosion resistance, oxidation resistance, and a number of other properties. Comparative data on the values of hardness (HV) of high-entropy equiatomic and traditional alloys (using typical high-strength stainless steels and alloys of nickel, cobalt, or titanium) in the initial state and after annealing are given in table. 3. The microhardness of our CrNiTiZrCu coating is not inferior to highly entropy equiatomic alloys.

4. Wear resistance of coatings

To solve these problems, an effective method of testing for microabrasive wear is applied by applying a rotating steel ball to a flat sample with the addition of an emulsion containing abrasive particles. At the point of contact, a spherical crater is formed - a calotte, therefore the device for providing this type of test was called a calotester (Fig. 5).



Fig.5. A device developed by us for testing materials and coatings for microabrasive wear

The results of studies of coatings are shown in table 4.

Table 4 - Wear resistance of CrNiTiZrCu coatings

Sample wear (weight in grams) 30 min each						
Before	15.14852	15.14857	15.14859	15.14856	The average	15.148566
After	15.14745	15.14763	15.14759	15.14759	Difference	0.000986

Tab.4 shows the wear resistance of the coating CrNiTiZrCu $\sim 3 \cdot 10^{-4}$ g/min, which corresponds to wear-resistant coatings. The mass was measured on a torsion balance with an accuracy of 0.0001 g.

5. Tribological features of CrNiTiZrCu coatings

CrNiTiZrCu was sprayed on a stationary sample for an hour with a reference voltage of 150 and 250 volts for an hour in a constant power mode of 1.5 kW. Sample No. 25 in nitrogen and sample No. 39 in argon. The friction coefficients were measured on the setup we developed [13].

Table 5 - Friction Coefficients for Copper and Aluminum

coating	on copper		on aluminum	
	friction coefficient	error	friction coefficient	error
CrNiTiZrCu in argon	0.041	0.006	0.066	0.002
CrNiTiZrCu in nitrogen	0.057	0.001	0.077	0.004

High-entropy CrNiTiZrCu coatings turn out to be anti-friction, which in all probability leads to energy savings.

Conclusion

Synthesis of a high-entropy alloy by mechanical alloying is more economically advantageous than remelting in a vacuum cast samples. We continue to study the CrNiTiZrCu coating on the details of machines and mechanisms, but the preliminary results look encouraging.

Acknowledgements

This work was supported by the Ministry of Education and Science of the Republic of Kazakhstan. Grants No. 0118PK000063 and No. Φ .0781.

REFERENCES

- 1 Yeh J.W., Chen Y.L., Lin S.J. High-entropy alloys – a new era of exploitation. *Materials Science Forum*, 2007, Vol. 560, pp. 1 – 9.
- 2 Azarenkov N.A., Sobol O.V., Beresnev V.M., Pogrebnyak A.D., et al. Vacuum-plasma coatings based on multi-element nitrides. *Metallofiz. Noveishie Tekhnol.* 2013, Vol. 35, No. 8, pp. 1061 – 1084.
- 3 Firstov S.A., Gorban V.F., Krapivka N.A., Pechkovsky E.P. A new class of materials - highly entropic alloys and coatings. *Vestnik TSU*, 2013, Vol. 18, No. 4, pp. 1938 – 1940. [in Russian]
- 4 Firstov S.A., Gorban V.F., Andreev A.O., Krapivka N.A. Superhard coatings of highly entropic alloys. *Science and Innovation*, 2013, Vol. 9, No. 5, pp. 32 - 39.
- 5 Pogrebnyak A.D., Bagdasaryan A., Yakushchenko I.I., et al. The structure and properties of highly entropic alloys and nitride coatings based on them. *Uspekhi Khimii*, 2014, Vol. 83, No. 11, pp. 1027-1061.
- 6 Maksimchuk I.N., Tkachenko V.G., Vovchok A.S., et al. The decay kinetics and thermal stabilization of the cast alloy system Mg-Al-Ca-Mn-Ti. *Metallofiz. Noveishie Tekhnol.* 2014, Vol. 36, No. 1, pp. 1 – 15.
- 7 Firstov S.A., Gorban V.F., Krapivka N.A., Pechkovsky E.P., Karpets M.V. The relationship between the ratio of the σ phase and the fcc phase with the electron concentration of cast two-phase high-entropy alloys. *Composites and Nanostructures*, 2015, Vol. 7, No. 2, pp. 72 – 84.
- 8 Shaginyan L.R., Gorban V.F., Krapivka N.A., et al. Properties of coatings of the high-entropy Al-Cr-Fe-Co-Ni-Cu-V alloy obtained by magnetron sputtering. *Superhard Materials*, 2016, No. 1, pp. 33 – 44.
- 9 Firstov S.A., Gorban V.F., Krapivka N.A., et al. The effect of plastic deformation on the phase composition and properties of high-entropy alloys. Interuniversity collection "Scientific notes, Lutsk, 2016, No. 54, pp. 326 – 338. [in Russian]
- 10 Gorban V.F., Krapivka N.A., Firstov S.A. High entropy alloys - electron concentration - phase composition - lattice parameter – properties. *Physics of Metals and Metallurgy*, 2017, Vol. 118, No. 10, pp. 1017-1029.
- 11 Yurov V.M., Guchenko S.A., Makhanov K.M. Structural Properties of the High-Entropy Coating TiNiZrCuCr. *Modern High-Tech Technologies*, 2020, No. 4, pp. 78 – 83.
- 12 Yurov V.M., Guchenko S.A., Makhanov K.M. Atomic force microscopy of highly entropic coatings. *International Journal of Applied and Basic Research*, 2020, No. 4, pp. 62 – 67.
- 13 Kubich V.I., Cherneta O.G., Yurov V.M. Potential difference of metal machine parts methodology for determining the parameters of adhesional properties of materials on the SMC-2 friction machine. *Eurasian Physical Technical Journal*, 2019, Vol.16, No. 2(32), pp. 78 – 82.

DOI 10.31489/2020No1/19-25

UDC 621.762:538

STUDY OF SYNERGISTIC EFFECT OF MECHANICAL ACTIVATION AND HIGH PRESSURE AND HIGH TEMPERATURE SINTERING ON THE STRUCTURE OF THE MATERIAL BASED ON BORON NITRIDE

Senyut V.T.

Joint Institute of Mechanical Engineering of NAS of Belarus, Minsk, Belarus, vsenyut@tut.by

The paper considers the results of the research of the material based on boron nitride after mechanical activation and high pressure and high temperature sintering of hexagonal boron nitride. It is shown, that the structure and phase composition of the resulting material strongly depend on the technological route and the material synthesis conditions. The subsequent chemical purification of the BN powder after mechanical activation leads to a decrease in the content of the hexagonal boron nitride phase. High pressure in the sintering process promotes the formation of material based on cubic boron nitride with a crystallite size of about 50 nm. The additional modifying of boron nitride by aluminum in combination with the second mechanical activation decreases the sintering pressure from 7.7 to 5.5 GPa. At the same time, it leads to the cubic boron nitride grain growth due to the recrystallization process.

Keywords: nanocrystalline boron nitride, mechanical activation, chemical purification, modifying, high pressure and temperature, sintering.

Introduction

Synthesis of nanostructured ceramics based on dense modifications of boron nitride (BN) (wurtzite and cubic BN) is an important material science task, since the transition to the nanometer range of grain size for such materials implies an increase in their hardness and wear resistance and improves the performance of tools based on them [1]. Developed methods for producing of nanostructured super hard materials (SHM) based on cubic BN (cBN) by sintering of cBN nanopowders or by phase transformation of graphite-like (hexagonal) BN (hBN) or wurtzite BN (wBN) into cBN require an application of pressures over 8 GPa. That significantly limits the synthesis process of nanostructured STM based on cBN in practice [2].

It is known that preliminary mechanical activation (MA) of graphite-like BN leads to a decrease in the temperature of cBN synthesis under conditions of high pressures and temperatures in comparison to the inactivated hBN [3]. On the other hand, the use of mechanically activated hBN powders is accompanied by an increase in the dispersion of the synthesized cBN phase due to an increase in the number of crystallization centers in BN during MA [4]. The aim of this work is to study of the synergistic effect of MA and high pressure and high temperature (HPHT) sintering of hBN on the structure of composite material on its base.

1. Starting materials and research methods

The hBN powder with the particle sizes within 5-100 μm is used as the initial material. Mechanical activation of the hBN powders is carried out in the planetary ball mill PBM AGO-2 (Novic, Russia) in an argon atmosphere at a drum rotation speed of 1000 rpm for 10 min. Steel balls of 5 mm diameter were used to achieve the ball-to-powder ratio of 20:1. Before the HPHT treatment, the BN powders after MA are purified from hBN by etching in a NaOH melt at 340°C, with adding 10% aqueous HCl solution, and subsequent washing in distilled water and drying. The HPHT treatment of powder mixtures after MA is carried out in a HPA of the "anvil with a hollow" type in the pressure range of 2.5-7.7 GPa and in the temperature range of 1000-2000 °C.

The study of the powder after MA is carried out with a high-resolution scanning electron microscope (SEM) Mira equipped with an electron backscatter diffraction (EBSD) detector (Tescan Co, Czech Republic). The morphology of the surface fracture of the obtained samples is studied with the atomic force microscope (AFM) NT-206 (MicroTestMachines Co, Belarus) in contact mode. Crystallographic studies of the samples are carried out with the EBSD method. X-ray powder researches are performed with a Bruker D8 ADVANCE diffractometer (Germany) in Cu-K α radiation. The study of specific surface is carried out with the BET method using analyzer SA 3100 (Beckman Coulter, USA). The Vickers microhardness of the samples is measured using a Buehler Micromet-II microhardness testing machine (Switzerland) at a load of 200 g.

2. Experimental part. Discussion of the results

2.1. Mechanical activation of the hBN powder

It is shown in [5] that during processing of hBN powder in the attritor the BN substructure transforms from crystalline to nanocrystalline and amorphous occurs. During MA of hBN for 4 hours, the BN powder with sizes of 30–300 nm is synthesized, however the long MA duration results in the contamination of the BN powder [6]. Mechanical activation of the hBN powders in PBM leads to a partial decomposition of hBN and a decrease in boron and nitrogen content in it, and with increasing processing time the B₂O₃ content increases due to the oxidation of released boron. MA of the hBN powders in PBM promotes the formation of round-shaped agglomerates with a size in the range of 0.5–2 μ m, consisting mainly of separate particles with a size in the range from 50 to 200 nm (Fig. 1). According to X-ray analysis data, the main phase of the powder after MA in PBM is hBN [7].

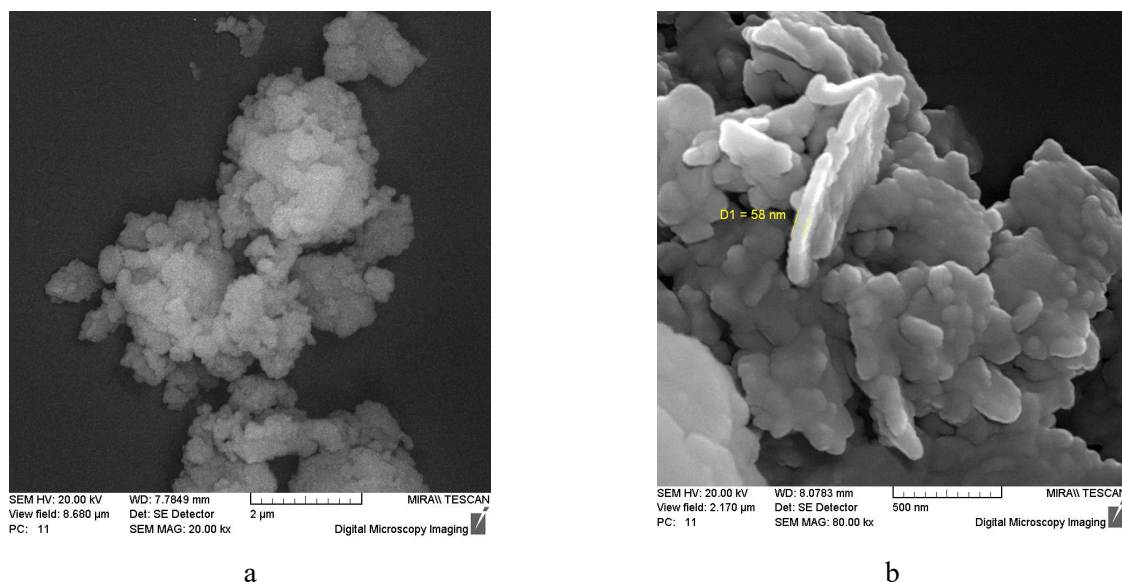


Fig.1. SEM images of the hBN powder after MA in the PBM: x 20 000(a); x 80 000 (b)

X-ray diffraction analysis of the hBN powder after MA in PBM for 10 min shows the formation of high-pressure phases wBN and cBN (Fig. 2). A further increase in the MA duration does not lead to an increase in the intensity of reflexes of cBN. On the contrary, an increase in the intensity and MA time leads to the reverse process of the hBN formation [6, 8]. The subsequent chemical purification of the mechanically activated BN powders results in a decrease in the mass of powders to 5-20 wt. %.

Chemical purification allows to affect different phases of BN selectively: the hexagonal phase is less resistant to the aggressive action of NaOH and HCl under high temperature, therefore it is more strongly etched compared to cBN, and it is manifested in a sharp decrease in the intensity of

the (002) hBN reflex on the X-ray pattern. At the same time, after chemical purification the intensity of the (111) cBN reflex practically does not decrease as compared to the powder before chemical purification. The specific surface of the powder after chemical purification increases up to values of 100-120 m²/g [9].

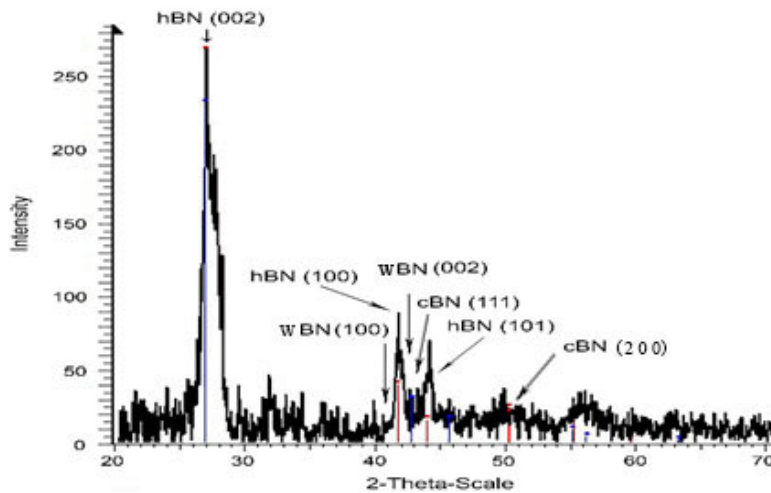


Fig. 2. X-ray diffraction patterns of the hBN powder after MA

2.2. HPHT sintering at the pressure of 2.5 GPa of the BN powder after MA and chemical purification

Sintering of the BN powder after MA at the pressures of 2.5 GPa in the temperature range of 1000-1300°C leads to the formation of compact material based on plate polyhedral crystallites of BN with a size of ~ 0.1-0.5 μm (Fig. 3 a).

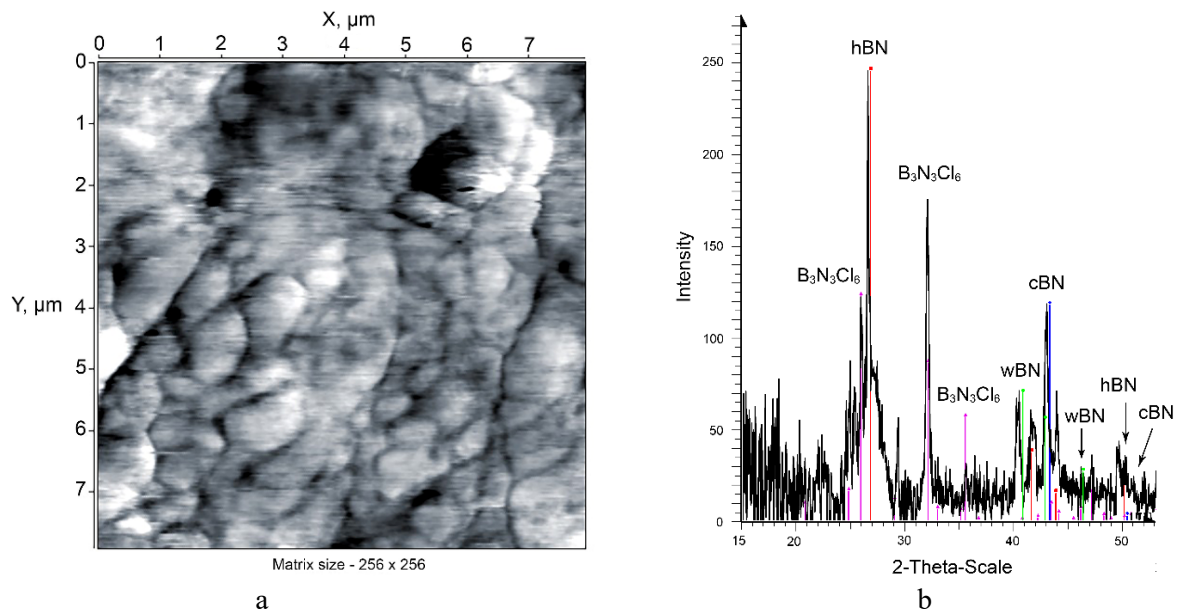


Fig. 3. Structure of the compact material based on boron nitride after MA, chemical purification and sintering under pressure of 2.5 GPa and temperature of 1300°C: AFM image of the surface (a); X-ray diffraction pattern (b)

X-ray analysis of the material after the HPHT treatment shows the presence of the hBN, wBN and cBN phases, as well as the compound B₃N₃Cl₆ which is formed in the material as a result of interaction between BN phases and HCl (Fig. 3 b). An assessment of crystallite sizes (coherent

scattering regions, CSR) of the formed phases shows that CSR is 50 nm for the hBN and cBN phase, and 40 nm for $B_3N_3Cl_6$ phase.

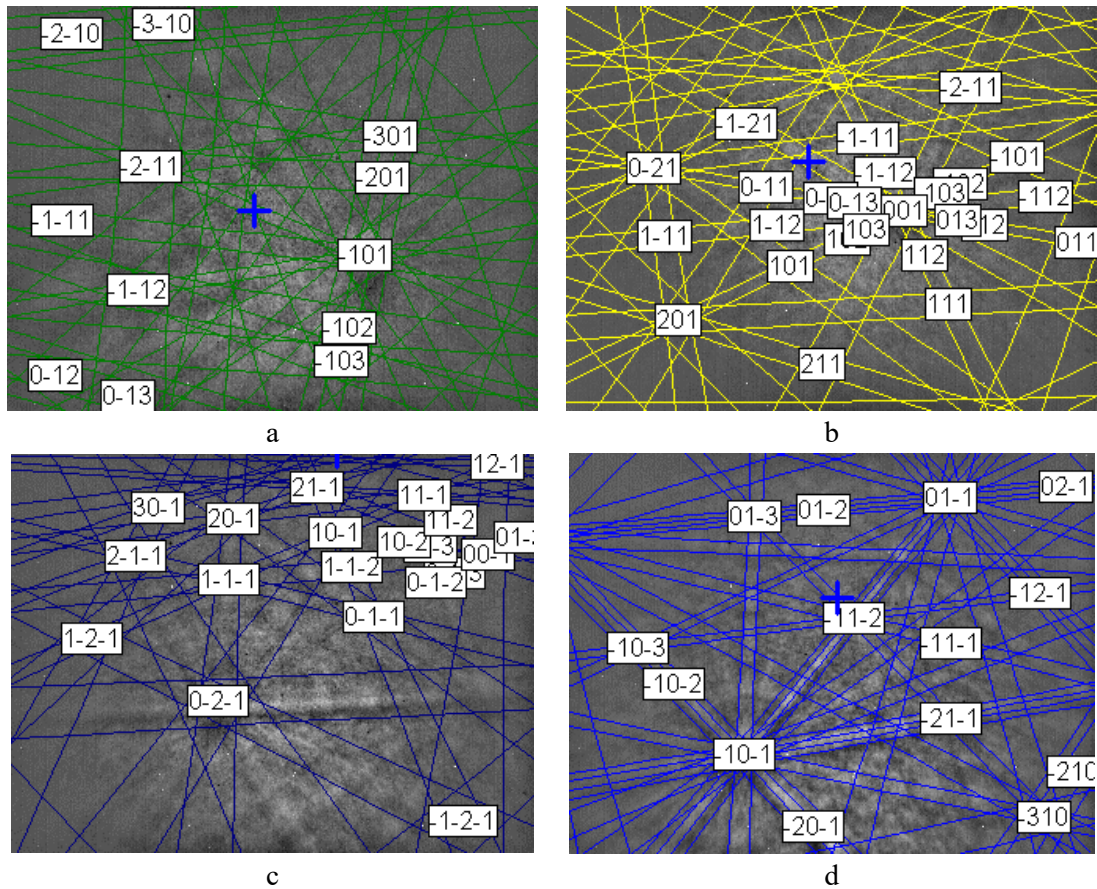


Fig.4. Crystallographic studies of the sintered samples based on hBN after MA, chemical purification and sintering at 2.5 GPa: orthorhombic BN phase (a); hexagonal BN phases (b, c); tetragonal BN phase (d)

Table 1. The parameters of the crystal structure of synthesized BN phases.

a			b			c			d		
Space group: 69			Space group: 164			Space group: 186			Space group: 134		
Laue group: 3.0mm			Laue group: 7.3m			Laue group: 9.6/mmm			Laue group: 5.4/mmm		
Ortorhombic syngony			Hexagonal syngony			Hexagonal syngony			Tetragonal syngony		
Unit cell length, Å			Unit cell length, Å			Unit cell length, Å			Unit cell length, Å		
a	b	c	a	b	c	a	b	c	a	b	c
2.50	4.34	3.35	2.51	2.51	6.69	2.52	2.52	6.70	8.63	8.63	5.13
Unit cell angles, grad			Unit cell angles, grad			Unit cell angles, grad			Unit cell angles, grad		
90°	90°	90°	90°	90°	120°	90°	90°	120°	90°	90°	90°
Composition, atom %			Composition, atom %			Composition, atom %			Composition, atom %		
B 50	N 50		B 50	N 50		B 50	N 50		B 96.5	N 3.5	

The analysis of the sintered material by the EBSD method shows, that along with the BN phases indicated above, there are the BN phases of the orthorhombic, hexagonal and tetragonal syngonias (Fig. 4, table 1). An increase in the temperature of the HPHT treatment above 1500°C at pressure of 2.5 GPa leads to the formation of the hBN phase. The Vickers microhardness of the obtained material is 7–10 GPa.

2.3. HPHT sintering of the BN powder after mechanical activation at the pressure of 7.7 GPa

According to X-ray analysis data, increasing the sintering pressure of mechanically activated BN powders up to 7.7 GPa and temperature up to 2000°C allows forming the material mainly based on the cBN phase. According to the AFM data, the obtained composite material has a grain microstructure with the grains of predominantly equilibrium shape and 0.4-0.6 μm in size (Fig. 5 a). Larger grains more than 1 μm, formed as a result of the high-temperature recrystallization (Fig. 5b) are also found.

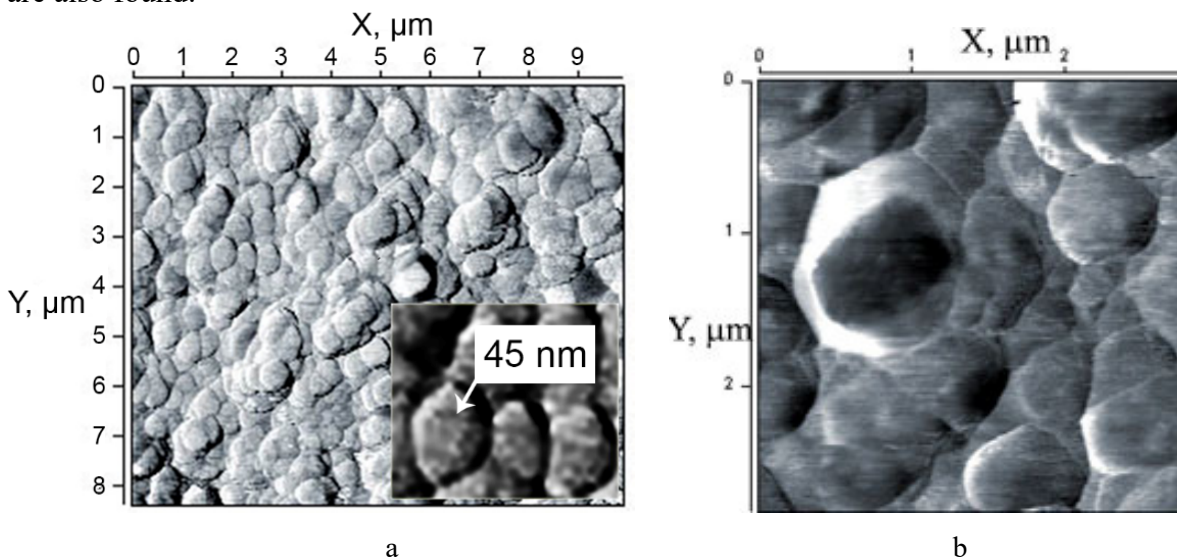


Fig.5. The structure of the cBN-based nanostructured material obtained from hBN after MA and HPHT at the pressure of 7.7 GPa: a general view [9] (a); recrystallized cBN grains (b)

2.4. HPHT sintering of the mechanically activated Al-modified BN powder

The use of additives activating the sintering of the cBN powder is of practical interest, because it leads to a decrease in the parameters (first of all, pressure) of the material sintering as compared to the sintering process without additives, and it is especially important in the case of the submicron- and nanopowders of cBN. Aluminum is often used as an activating additive for sintering the cBN powders under HPHT [10]. In addition, Al has catalytic properties and stimulates the phase transformation of hBN to cBN.

It is known [11] that the synthesis of cBN powders depends on the kinetics of dissolution of hBN in metal melts, i.e. on the degree of activity of its crystallite latter. For example, in [12] it is shown that electron beam processing of hBN+5% Al powder accelerates the phase transition of hBN into cBN and provides maximum values of compressive strength, microhardness and density of the cBN compacts. The activation of hBN+Al system is also possible with the "pumping" of mechanical energy into them. To improve the interaction between the hBN and Al during both MA and HPHT processes, it is suggested [13] to modify with Al mechanically activated hBN powder by the chemical-thermal method, and to apply the second MA again after modifying.

The chemical-thermal modifying of BN powder by Al after MA is high temperature processing at 900°C in a deoxidizing atmosphere in the presence of aluminum-containing compounds, was carried out at 900°C during 2 hours. After MA the chemical purification of BN powder was also

performed as described earlier. After the chemical purification, modifying and re-activation in the PBM the BN powder is dense aggregates based on round and polyhedral particles with a size of 50-100 nm (Fig. 6). The specific surface area of the powder measured by the BET method is $103.2 \text{ m}^2/\text{g}$, that is within the range for the chemically purified BN powder after one-time MA [7, 9].

HPHT sintering of the mechanically activated Al-modified BN powder was performed at the pressure of 5.5 GPa and temperatures of 1650-2000 °C. As a result, it has been found that a material on the basis of polyhedral cBN grains larger than $1 \mu\text{m}$ are formed. In the material it can also be observed the cBN grains up to $5 \mu\text{m}$ in size, which are formed as a result of collective recrystallization. The structure of the material is characterized by the presence of nanopores, there are separate micropores with a size of 1-3 μm (Fig. 7). Some of cBN particles after recrystallization represent discs with the diameter of 3-5 μm and the thickness up to $1 \mu\text{m}$.

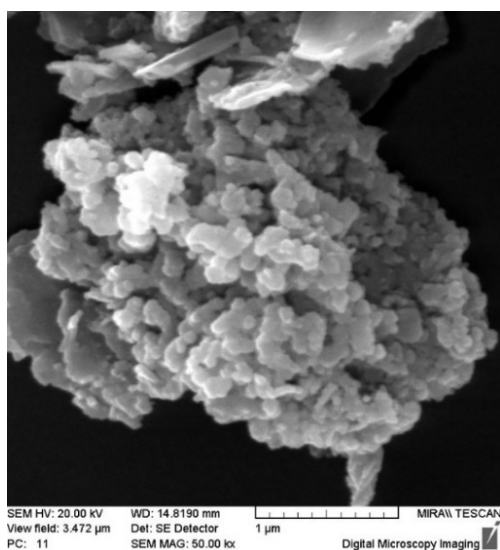


Fig. 6. SEM image of the morphology of the BN powder after MA, chemical-thermal modifying by Al and repeated MA in the PBM

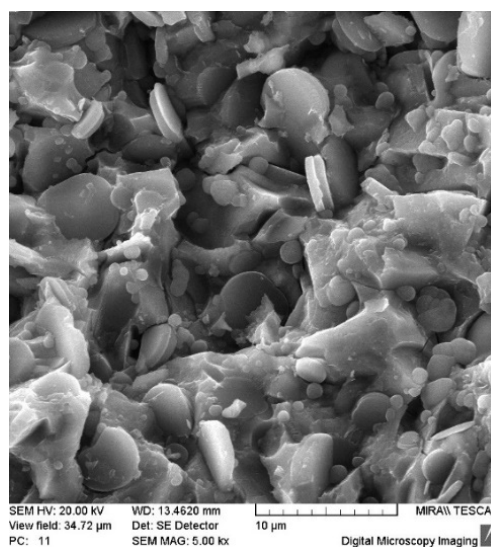


Fig. 7. Fracture of the polycrystalline material on the basis of cBN sintered at the pressure of 5.5 GPa and the temperature of 2000 °C

Along with cBN, in accordance with X-ray diffraction analysis in the sintered material there are the hBN phase, aluminum oxides Al_2O_3 , AlO, aluminum oxynitride $\text{Al}_9\text{O}_3\text{N}_7$, aluminum boride AlB_2 , and boron oxide B_2O_3 as well. The formation of oxides during the sintering can be explained by the oxygen adsorbed on the BN surface in the form of oxygen-containing compounds after chemical purification and washing the powder in water, as well as the diffusion of container material CaCO_3 from the container into the sintering region. The Vickers microhardness of the material sintered at the pressure of 5.5 GPa and the temperature of 2000 °C is 20 GPa. It can be concluded that both modifying by Al and the repeated MA activates cBN formation and its sintering, but at the same time there is the cBN recrystallization. In order to eliminate the cBN grain growth and preserve the nanostructured cBN it is necessary to increase the pressure while reducing the sintering temperature.

Conclusion

The synergistic effects of MA, chemical purification, chemical-thermal modifying by Al and HPHT sintering on the structure and phase composition of BN-based material were studied. The BN powder after chemical purification, modifying by Al and re-activation represent the dense aggregates based on nanoparticles with a size of 50-100 nm. The specific surface of the BN powder in this case is equal to $103.2 \text{ m}^2/\text{g}$.

In the material obtained at the pressure of 2.5 GPa and at the temperature range of 1000-1300°C there are the BN phases of orthorhombic and tetragonal crystallographic systems along with the hBN, wBN and cBN phases. Increasing the pressure of the HPHT sintering of the mechanically activated BN powders up to 7.7 GPa and the temperature up to 2000 °C allows to obtain the material mainly on the basis of the cBN phase with cBN crystallite size of about 50 nm. The chemical-thermal modifying by Al in combination with repeated MA makes it possible to activate HPHT sintering of BN powders at lower pressure of 5.5 GPa. In this case the size of the cBN grains increases up to 5 µm due to recrystallization of cBN.

Acknowledgements

The work is supported by the State Program of Scientific Research “Physical Materials Science, New Materials and Technologies” (“Nanomaterials and nanotechnology”), task 2.71.1

REFERENCES

- 1 Novikov N.V., Klimenko S.A. *Tools made of superhard materials*. Moscow, Mashinostroyeniye Publ., 2014, 608 p. [in Russian]
- 2 Vityaz P.A., Gritsuk V.D., Senyut V.T. *Synthesis and applications of superhard materials*. Minsk, Belorussian Science, 2005, 359 p. [in Russian]
- 3 Horiuchi S., Huang J.Y., He L.L., Mao J. F., Taniguchi T. Facilitated synthesis of cubic boron nitride by a mechanochemical effect. *Phil. mag. A*. 1998, Vol. 78, No. 5, pp.1065–1072.
- 4 Sokolov A.N., Shulzhenko A.A., Tkach V.N., Budyak A.A. Investigation of the effect of mechanical activation of hexagonal boron nitride on the phase transformation into cubic modification. *Rock-cutting and metal-working tools – equipment, technology for its manufacture and use*. Kiev: V. Bakul Institute for Superhard Materials, 2005, Issue 8. pp. 149-154. [in Russian]
- 5 Vityaz P.A., Senyut V.T., Gameza L.M., Stefanovich A.A., Mosunov E.I., Kovaleva S.A. Investigation of attritor and thermobaric treatment on the structure and properties of a material based on boron nitride. *Proceedings of the III Int. Workshop «Nanostructured Materials –2004: Belarus – Russia»*. Minsk, Belarus, 2004, pp. 154-155.[in Russian]
- 6 Senyut V.T., Kovaleva S.A., Mosunov E.I., Stefanovich A.A. Structural and phase transformations in boron nitride during attritor treatment. *Chemistry for sustainable development*, 2009, Vol. 17, No. 6, pp.647–652.
- 7 Vityaz P.A., Senyut V.T. Synthesis and application of nanostructuralsuperhard materials of tool appointment. *Proceedings of the National Academy of Sciences of Belarus. Physical-technical series*, 2015, No. 3, pp. 60-76. [in Russian]
- 8 Batsanov S.S., Gavrilkin S.M., Bezduganov S.V., Romanov P.N. Reversible phase transformation in boron nitride upon pulsed mechanical action. *Inorganic materials*, 2008, Vol.44, No.11, pp.1332–1334.
- 9 Senyut V.T., Kovaleva S.A., Gamzeleva T.V., Grigorieva T.F. Investigation of the structural features of boron nitride after mechanical activation in attritor and planetary mill followed by agglomeration at high pressure and temperature. *Chemistry for sustainable development*, 2016, Vol. 24, No. 2, pp.169–175. doi.org/10.15372/KhUR20160208.
- 10 Bezhenar N.P., Konoval S.M., Garbuz T.A., Bozhko S.A., Belyavina N.N. Solid solutions in cBN-Al and cBN-Al-TiB₂ systems obtained at high pressures and temperatures. *High Pressure Physics and Technology*, 2011, Vol.21, No 1, pp.38-45. http://nbuv.gov.ua/UJRN/PhTVD_2011_21_1_6.
- 11 Golubev A. S., Kurdyumov A. V., Pilyankevich A. N. *Boron nitride: structure, properties, production*. Kiev, Naukovadumka Publ., 1987, 200 p. [in Russian]
- 12 Vasilevsky I. N., Pobol I. L., Leusenko A. A. Study of the effect of electron beam heating on the kinetics of phase transformations and properties of boron nitride. *New materials and technologies*, Minsk, 1994, pp. 60–61. [in Russian]
- 13 Senyut V.T., Vityaz P.A., Kovaleva S.A., Mosunov E.I., Valkovich I.V., Gamzeleva T.V. Synthesis of polycrystalline cubic boron nitride from hexagonal boron nitride after mechanical activation and modification with aluminum. *Inorganic Materials: Applied Research*, 2016, Vol. 7, No.1, pp. 53–57.

DOI 10.31489/2020No1/26-34

UDC 538.9

PHASE TRANSFORMATIONS IN FERRITES DURING RADIATION-THERMAL SINTERING

Surzhikov A.P.¹, Lysenko E.N.¹, Malyshev A.V.¹, Petrova A.¹,
Ghyngazov S.A.¹, Aimukhanov A.K.²

¹National Research Tomsk Polytechnic University, Tomsk, Russia, malyshev@tpu.ru

²E.A. Buketov Karaganda State University, Karaganda, Kazakhstan

Electron microscopic studies of the phase composition, morphology, and defect structure of lithium-titanium ferrite powders and ceramic samples sintered under conditions of radiation-thermal and thermal effects were carried out. Radiation-thermal sintering of ferrite samples was carried out by irradiating the work pieces with a pulsed electron beam with energy of (1.5-2.0) MeV using the electron beam accelerator. The beam current in the pulse was (0.5-0.9) A, the irradiation pulse duration was 500 μs, the pulse repetition rate was (5-50) Hz, and the work piece heating rate was 1000 °C/min. The samples were irradiated in a box of lightweight fireclay with a bottom thickness of 15 mm. The microstructure studies were conducted by the methods of electron diffraction microscopy in the light using an electron microscope. It was shown that the most probable model of radiation intensification of the sintering process of ferrites can be the mechanism of radiation retardation of dislocations upon heating, which are formed during the decomposition of subgrain boundaries in grains of intermediate phases of ferrite.

Keywords: lithium-titanium ferrite, powder, sintering, electron beams, electron microscopy, morphology, phase composition, defectiveness.

Introduction

The most universal requirement for the microstructure of ferrites is the condition for the maximum density of the material and the equigranularity of its structure [1, 2]. For complying with these requirements, at economically reasonable firing times, several methods to increase the activity of sintering processes were developed. This is the two-stage introduction of the components, the pre-blending of ferrite with a ferrite powder of the same composition, the presence of a liquid phase, forced sintering, and the application of ultrasound to the sintering process [1, 3-9]. In recent years, the usage of the effects of ionizing radiation fluxes in the preparation and modification of materials was developed. Of the variety of ionizing radiation in radiation materials science, the most widely used are the flows of accelerated electrons. This is due, firstly, to the progress of accelerator technology, the creation of relatively small but powerful electron accelerators.

Secondly, electron beams have convenient geometric characteristics, wide opportunities to control the irradiation regime, do not create induced radioactivity, have a lower cost in comparison with other sources of ionizing radiation, and have a high efficiency of converting electricity to electron beam energy.

The first works on the implementation of solid-phase transformations in inorganic materials using high-temperature electron irradiation were studies on the synthesis of cement clinker [10, 11], hexagonal barium ferrite [12] and lithium ferrite [13], as well as sintering under such specific conditions of europium oxide [14], alumina-containing blends [15] and ferrite compacts [16-18]. Sintering was most fully studied under the conditions of combined exposure to high temperatures and intense electron flows [19]. The regularities of ferrite compacts compaction were established

[20]. In particular, multiple increases in the compaction rate of lithium-titanium ferrite compacts under such sintering conditions were shown [13, 21]. Microscopic methods have been used to study in detail the formation of a microstructure under conditions of such kind of processing [22].

In this case, the question remains open about the features of the formation of the magnetic characteristics of ferrites. Data on phase transformations in ferrites during radiation-thermal (RT) sintering are important and productive. For that purpose in this work was used electron microscopy to study the features of phase transformations of ferrite ceramics sintered under RT conditions. The inapplicability of the X-ray phase analysis method for lithium ferrites is due to the overlapping of the main phase lines LiFe_5O_8 , LiFeO_2 , Fe_3O_4 .

1. The object of the study and experimental technique

In this work powders of lithium-titanium ferrite synthesized from a mechanical mixture of oxides and carbonates containing: Li_2CO_3 – 11.2 wt.%; TiO_2 – 18.65 wt.%; ZnO – 7.6 wt.%; MnCO_3 – 2.74 wt.%; remain – Fe_2O_3 were used. After weighing the components according to the recipe, they are jointly ground and mixed in a vibratory mill for 1 h, after adding to the mixture of distilled water in the ratio (by weight) the mixture: water, equal to 1: 2. After the vibratory mill, the mixture is dried at 80 °C under normal atmospheric pressure for 24 hours and then wiped through a 0.7 sieve. Distilled water is introduced into the obtained powder in an amount of 10% by weight of the powder and briquetted. Briquettes are heated in thermal furnaces at a speed of 200 °C/h to 900 °C, maintained at this temperature for 6 hours, cooled to room temperature, after which they are crushed, ground and sieved through a 0.9 sieve.

After repeated grinding in a vibration mill for 45 minutes, Bi_2O_3 dissolved in concentrated nitric acid in suspension (0.22 wt.%) is added to the powder and mixing is carried out in a ball mill for 4 hours. Determination of the quality of the powder is carried out according to the method developed by our scientific group. For preparing a press powder, a 10% solution of polyvinyl alcohol in an amount of 12 wt.% of the charge, and the resulting mass is alternately wiped through a sieve of 0.7 and 0.45. Press-samples for studying sintering processes are made by cold unilateral pressing in the form of tablets (diameter 15 mm and thickness 2 mm). The pressing pressure is selected, as a rule, experimentally for each specific ferrite composition according to the established dependence of the bulk density ρ of the samples on the pressing pressure P .

Pressing pressure varied within (25–500) MPa. Sintering of the press-samples was carried out in a thermal furnace at 1100 °C for 30 min in an air atmosphere at a heating rate of 900 °C/min. Such a high speed is achieved by introducing press samples into a furnace heated to a predetermined temperature.

It has been established that at pressing pressures below 40 MPa, the press samples are characterized by low density, and at pressing pressures of more than 250 MPa, the samples have cracks and delaminations (the phenomenon of repressing). Thus, the most optimal pressing pressure, which provides an acceptable density of both raw and sintered samples, is in the range (110–200) MPa. The following pressing mode was used in the work: $P = 130$ MPa, the exposure time of the material under pressure 1 min; and two modes of sintering of press samples: radiation-thermal (RT) and thermal (T).

RT-sintering was carried out by irradiating the workpieces with a pulsed electron beam with energy of (1.5–2.0) MeV using the ILU-6 accelerator. The beam current in the pulse was (0.5–0.9) A, the irradiation pulse duration was 500 μs , the pulse repetition rate was (5–50) Hz, and the workpiece heating rate was 1000 °C/min. The samples were irradiated in a box of lightweight fireclay with a bottom thickness of 15 mm. On the irradiation side, the box was covered with a radiation-transparent tread of mass thickness 0.1 g cm^{-1} . The temperature was measured by a control sample placed close to the sintered blanks. Sintering in thermal furnaces (T-sintering) was carried out in a preheated chamber electric furnace, which provided a heating rate comparable to the rate of

radiation heating. The cell design and temperature control technique are similar to those used in RT-sintering. Both sintering modes were carried out in the air.

The studies were conducted by the methods of electron diffraction microscopy in the light using an electron microscope of the EM-125K brand at an accelerating voltage of 125 kV. The phase composition of the analyzed materials was determined by indicating microelectron diffraction patterns of objects. Due to the fact that the diameter of the microdiffraction analysis zone did not exceed 0.7 μm , the method is local and allows the phase analysis of individual grains and subgrains.

The morphology and defective structure of the material were studied by the bright field method obtained by direct passage of an electron beam through a thin sample, as well as by the dark field method, when the image of the material structure is formed in one of the diffracted electron beams.

3. Results and discussions

Indication of electron diffraction patterns (taking into account the chemical composition of the samples) showed that the studied material is a complex multiphase product. The phases based on LiFeO_2 (cubic lattice, $a = 4.1588 \text{ \AA}$), LiFe_5O_8 (cubic lattice, $a = 8.337 \text{ \AA}$), and FeTiO_3 (hexagonal lattice, $a = 5.075 \text{ \AA}$, $c = 14.06 \text{ \AA}$) are confidently identified. The relative phase content was determined by indicating microelectron diffraction patterns and counting the number of contacts of the planes of the above phases in microelectron diffraction patterns. Phase analysis showed that the phase ratio is determined by the heat treatment of the material (Table 1).

Thus, in the initial powder, the total content of the LiFeO_2 and FeTiO_3 phases is 1.41 times higher than the LiFe_5O_8 phases. After heat treatment of the compacted powder in an electron beam (RT-sintering regime), on the contrary, the content of the LiFe_5O_8 phase is 1.5 times higher than the content of the LiFeO_2 and FeTiO_3 phases. Thermal sintering in the furnace also increases the relative content of the LiFe_5O_8 phase, but despite the twice as long heating time, this increase is not so significant compared to the RT sintering regime.

Table 1. Relative content of the main phases in Li–Ti ferrite

Phase	Initial powder	Powder after heating at 1373 K, 2 h	Ceramic sample sintered in T-regime at 1373 K, 2 h	Ceramic sample sintered in RT-regime at 1373 K, 1 h
LiFe_5O_8	0.42	0.46	0.50	0.60
LiFeO_2	0.29	0.16	0.05	0.04
FeTiO_3	0.29	0.38	0.45	0.36
$\frac{\text{LiFeO}_2 + \text{FeTiO}_3}{\text{LiFe}_5\text{O}_8}$	1.41	1.18	1.0	0.67
$\frac{\text{LiFeO}_2}{\text{FeTiO}_3}$	1.0	0.43	0.1	0.1

Powder heating also leads to a change in the ratio of LiFeO_2 and FeTiO_3 phases towards a decrease in the relative fraction of LiFeO_2 . In the compacted state of the sample, this process proceeds more intensively and does not depend on the sintering method. Take into account the complex component composition of the mixture from which the powder was synthesized, it should be assumed that the identified phases are in fact solid solutions of Zn, Mn and Ti. This is evidenced, in particular, by our measurements of the Curie temperature of ferrite, which turned out to be 530 K, which corresponds to solid solutions of lithium ferrites [23]. Morphological analysis of the structure of ferrites was carried out on photographs with electron microscopic images of the structure. Two morphological varieties of grains were established: polycrystalline aggregates (Figure 1a, 1b) and single-crystal particles.

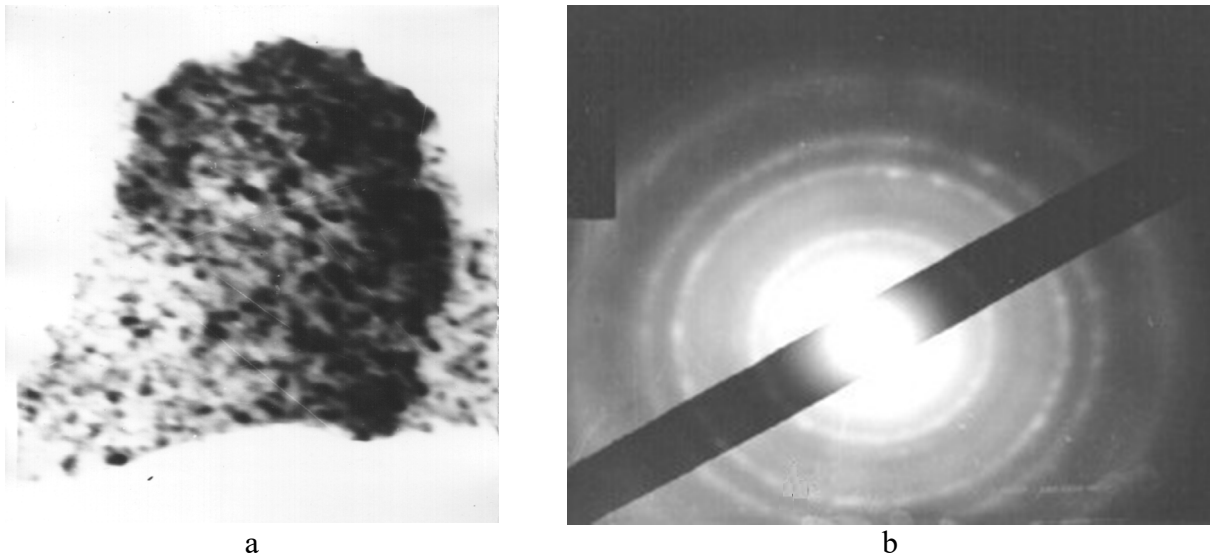


Fig.1. Polycrystalline aggregates of ferrite powder before sintering:
a – the structure image; b – the structure electron diffraction pattern

Both aggregates and particles have a very diverse shape with average grain size (0.5–0.8) μm . The sizes of the subgrains of polycrystalline aggregates are (0.02–0.07) μm . Most single-crystal particles have an almost perfect structure, however, in some cases, polygonal dislocation networks were observed inside the particles. Local phase analysis of individual grains revealed that before heating, the LiFeO_2 and FeTiO_3 phases are represented as polycrystalline aggregates, while it was found that the FeTiO_3 phase (Figure 2a) has a fine-grained structure compared to LiFeO_2 (Figure 2b). So, in the first case, the average size of subgrains is (0.02–0.04) μm , in the second – (0.04–0.07) μm . The LiFe_5O_8 phase is a single crystal particle. In some cases, under certain diffraction conditions, a domain structure can be observed inside such particles. Grains that are polyphase aggregates were rarely found (Figure 3). In this case, reflections from all the above phases are simultaneously present in the microdiffraction pattern.

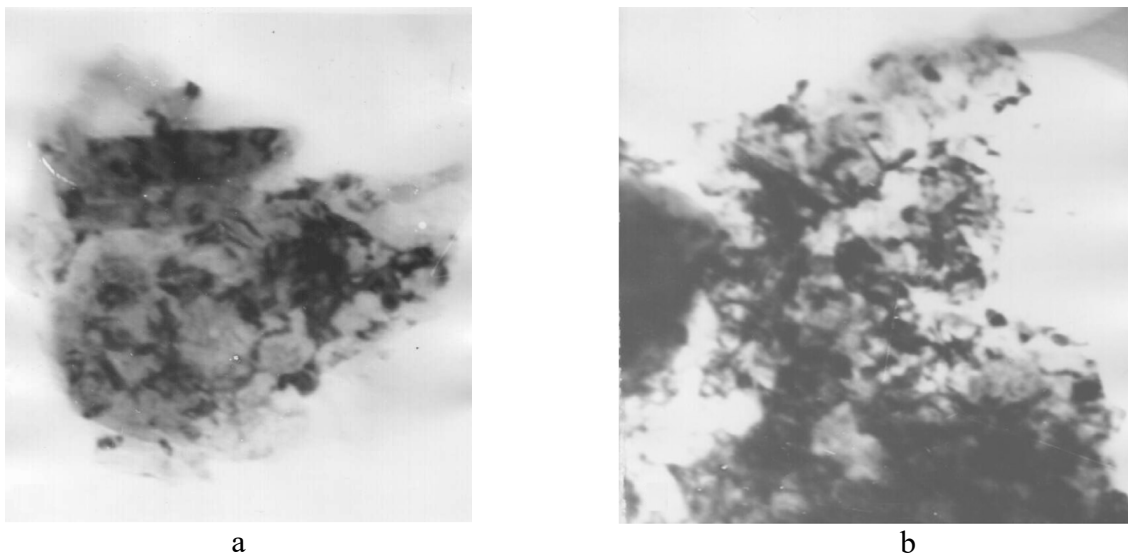


Fig. 2. Electron microscopic images of ferrite powder before sintering:
a – the phase FeTiO_3 ; b – the phase LiFeO_2

In some cases, under certain diffraction conditions, a domain structure can be observed inside such particles. Rarely found grains, which are polyphase aggregates (Figure 3). In this case, reflections from all the above phases are simultaneously present in the microdiffraction pattern. The morphological state of the LiFe_5O_8 phase has high thermal stability: under all processing conditions, it is observed only in the form of single-crystal particles. The morphology of the LiFeO_2 and FeTiO_3 phases depends on the processing method. So, in the case of a loose powder, the subgrain structure coarsens to an average grain size of $0.09 \mu\text{m}$. Thermal sintering of the pressed powder leads to an almost complete transition of polycrystalline aggregates (Figure 4) into single-crystal particles (Figure 5) (the ratio of the two types of structures is 9:1).

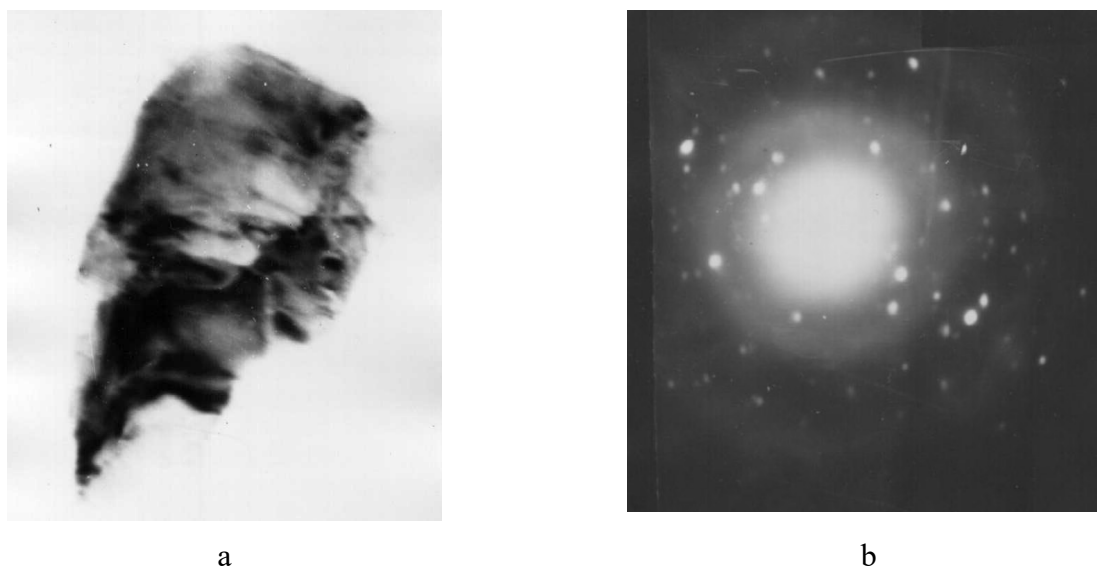


Fig.3. Polyphase aggregates of ferrite powder before sintering:
a – the structure electron microscopic image; b – the structure electron diffraction pattern

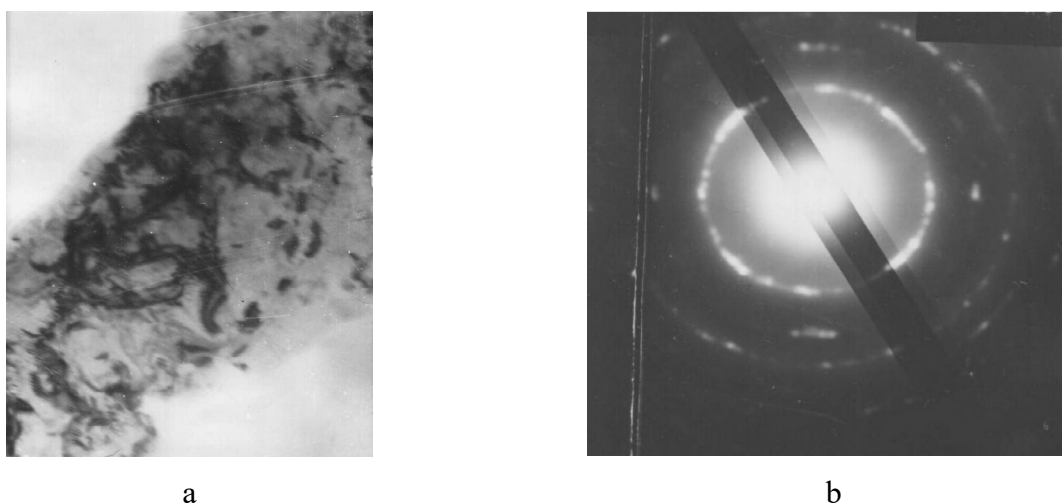


Fig.4. Polycrystalline compressed powder aggregates:
a – the structure electron microscopic image; b – the structure electron diffraction pattern

Sintering of the pressed powder by an electron beam eliminates polycrystalline aggregates with an ultrafine grain structure; only a coarse-grained structure is observed in ceramics. Grains formed in the process of destruction of the polycrystalline structure have a large block structure and a dislocation structure. In this case, in contrast to T-sintering, in grains after RT-sintering, a higher number of dislocations remain. A characteristic feature of ceramic materials (unlike powders) is the

presence of a large number of polyphase grains (Figure 6). Moreover, judging by the intensity of reflections in microdiffraction patterns, after thermal sintering, the phases LiFeO_2 and FeTiO_3 have advantages in such grains. After RT sintering, the total content of these phases is compared with the amount of LiFe_5O_8 phase.

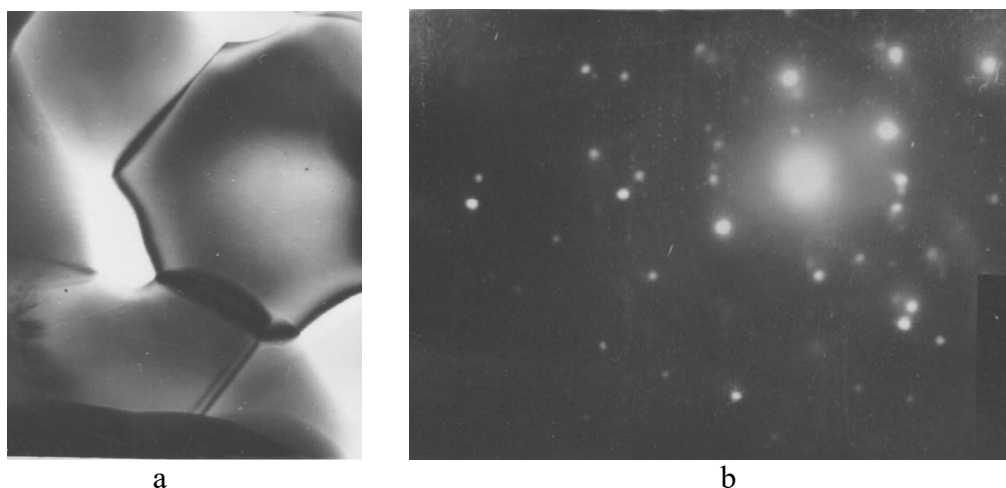


Fig.5. Single-crystal particles of ferrite ceramics after T-sintering for 3 hours at 1373 K: a – the structure electron microscopic image; b – the structure electron diffraction pattern

From the presented results, it follows that the initial powder used for sintering ceramic products is in a state of incomplete ferritization, since, along with the magnetic phase of LiFe_5O_8 , the intermediate phases of synthesis, LiFeO_2 and FeTiO_3 , are present in the powder. Such a structure of powders increases the sintering rate due to the high level of imperfection of the initial powder grains and is therefore widely used in ceramic technology [24-40].

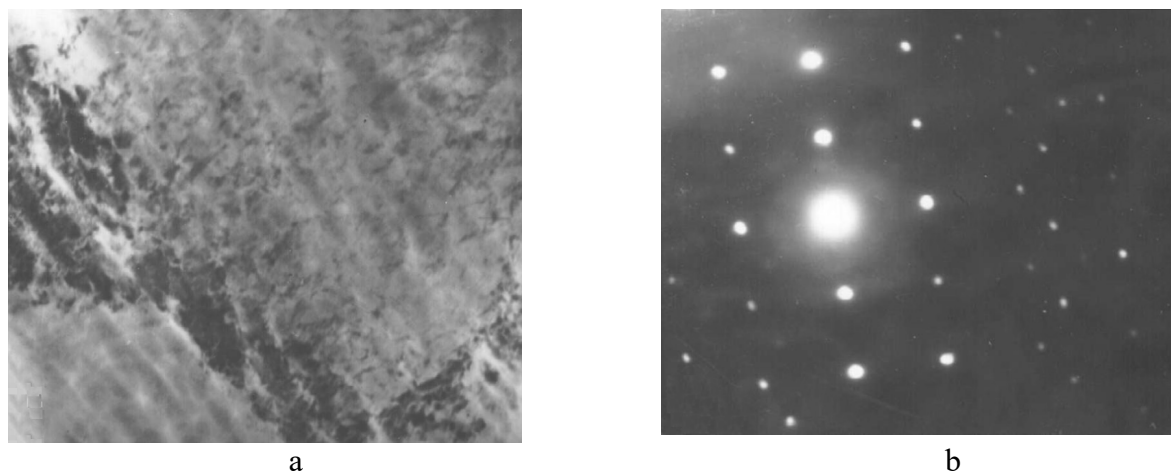


Fig.6. Polyphase grains of ferrite ceramics after RT-sintering for 3 hours at 1373 K: a – the structure electron microscopic image; b – the structure electron diffraction pattern

From this point of view, we are interested in the differences in the morphology of the main (LiFe_5O_8) and intermediate (LiFeO_2 , FeTiO_3) phases: the excessive defectiveness of the LiFeO_2 and FeTiO_3 phases in the form of subgrain boundaries is apparently a significant factor in the increased activity of the initial powder. The chemical interaction between LiFeO_2 and FeTiO_3 with the formation of a solid solution based on LiFe_5O_8 occurs more intensively on compressed samples and using RT exposure (Table 1). The consequence of this effect is an increase in the number of grains with a mixed phase composition.

Considering the nature of the RT effect, it is necessary to pay attention to the increased activity of the decay of subgrain boundaries in the intermediate phases under the conditions of electron irradiation. The consequence of this decay is the enrichment of the grain volume by dislocations, which, as is known, accelerates the diffusion processes of mass transfer. Higher content of dislocations in the irradiated material may be due to their radiation deceleration upon heating due to violation of the potential relief of the slip planes by point radiation defects. The same conclusion about the mechanism of RT activation of sintering of Li–Ti ferrites was made when analyzing the kinetic dependences of compaction of billets under similar irradiation conditions.

Conclusion

Based on the results of electron microscopy studies of the phase composition, morphology, and defective structure of Li–Ti ferrites, the following conclusions can be drawn:

- the studied material in the initial and sintered states is a multiphase mixture consisting of solid solutions based on compounds LiFeO_2 , FeTiO_3 и LiFe_5O_8 ;
- relative phase content is determined by the processing mode of the material;
- two morphological varieties of grains - polycrystalline aggregates with an ultrafine structure and single-crystal particles were revealed. By local diffraction analysis, it was found that the phases LiFeO_2 and FeTiO_3 have a polycrystalline structure; the LiFe_5O_8 phase is presented in the form of single-crystal particles;
- the thermal effect on the powder or the billet leads to the destruction of polycrystalline aggregates with the formation of large-block grains, inside which a dislocation structure is observed;
- sintering of the press blanks with an electron beam enhances the destruction of the nanograin structure, helps to preserve the dislocation substructure in the grains, and intensifies the processes of powder deferritization;

A probable model of the RT effect in Li–Ti ferrites can be the mechanism of radiation retardation of dislocations upon heating, which are formed during the decay of subgrain boundaries in grains of intermediate ferrite phases.

Acknowledgements

The research is funded by the Ministry of Education and Science of the Russian Federation as part of the “Science” Program (project No. FSWW-2020-0014). The results of the phase composition of ferrite samples were obtained within the RFBR grant (project No. 20-07-00662).

REFERENCES

- 1 Letyuk L.M., Andreev V.G., Gonchar A.V., Strygin A.A. Magnetic-field effect on the rheological properties of strontium ferrite suspensions. *Inorganic Materials*. 2006, Vol.42, pp. 423 – 426.
- 2 Zhuravlev G.I., Golubkov L.A., Strakhova T.A. Basic types of microstructure of ferrites and means of obtaining them. *Powder Metallurgy and Metal Ceramics*. 1990, Vol.29, pp. 478 – 480.
- 3 Jia L., Zhao Y., Xie F., Li Q., Li Y., Liu C., Zhang H. Composition, microstructures and ferrimagnetic properties of Bi-modified LiZnTiMn ferrites for LTCC application. *AIP Advances*. 2016, Vol.6, 056214.
- 4 Letyuk L.M. Recrystallization of ferrites and its effect on the processes of microstructure formation in ferrosinels. *Powder Metallurgy and Metal Ceramics*. 1980, Vol.19, No 5, pp. 359 – 364.
- 5 Zinovik M.A., Zinovik E.V. Ferrites with rectangular and square hysteresis loops. *Powder Metallurgy and Metal Ceramics*. 2005, Vol.44, pp. 66 – 74.
- 6 Andreev V.G., Letyuk, L.M., Maiorov V.R., Podgornaya S.V., Strygin, A.A. Binders in the manufacture of magnetic ceramics (ferrites). *Steel in Translation*. 2007, Vol.37, pp. 589 – 592.

- 7 Sudakar C., Naik R., Lawes G., Mantese J.V., Micheli A.L., Srinivasan G., Alpay S.P. Internal magnetostatic potentials of magnetization-graded ferromagnetic materials. *Applied Physics Letters*. 2007, Vol.90, 062502.
- 8 Teo M.L.S., Kong L.B., Li Z.W., Lin G.Q., Gan Y.B. Development of magneto-dielectric materials based on Li-ferrite ceramics I. Densification behavior and microstructure development. *Journal of Alloys and Compounds*. 2008, Vol.459, pp. 557–566.
- 9 Minin V.M. Effect of sintering conditions on the microstructure and electromagnetic properties of Li-Mg-Mn ferrite memory elements. *Powder Metallurgy and Metal Ceramics*. 1982, Vol.21, pp. 698 – 701.
- 10 Lysenko E.N., Surzhikov A.P., Vlasov V.A., Nikolaev E.V., Malyshev A.V., Bryazgin A.A., Korobeynikov M.V., Mikhailenko M.A. Synthesis of substituted lithium ferrites under the pulsed and continuous electron beam heating. *Nuclear Instruments and Methods in Physics Research, Section B: Beam Interactions with Materials and Atoms*. 2017, V. 392, pp. 1-7.
- 11 Sharma P., Uniyal P. Investigating thermal and kinetic parameters of lithium titanate formation by solid-state method. *Journal of Thermal Analysis and Calorimetry*. 2017, Vol.128, pp. 875 – 882.
- 12 Rakshit S.K., Parida S.C., Naik Y.P., Venugopal V. Thermodynamic studies on lithium ferrites. *Journal of Solid State Chemistry*. 2011, Vol.184, pp. 1186 – 1194.
- 13 Surzhikov A.P., Malyshev A.V., Lysenko E.N., Vlasov V.A., Sokolovskiy A.N. Structural, electromagnetic, and dielectric properties of lithium-zinc ferrite ceramics sintered by pulsed electron beam heating. *Ceramics International*. 2017, Vol. 43, No. 13, pp.9778-9782. DOI: .1016/j.ceramint.2017.04.155
- 14 El-Shobaky G.A., Ibrahim A.A. Solid-solid interactions between ferric oxide and lithium carbonate and the thermal stability of the lithium ferrites produced. *Thermochim. Acta*. 1987, Vol.118, pp. 151 – 158.
- 15 Salimov R.A., Cherepkov V.G., Golubenko J.I., Krainov G.S., Korabelnikov Yu.A., Kuznetsov S.A., Kuksanov N.K., Malinin A.B., Nemytov P.I. D.C. high power electron accelerators of ELV-series: status, development, applications. *Radiation Physics and Chemistry Journal*. 2000, Vol.57, pp. 661 – 665.
- 16 Cleland M.R., Parks L.A. Medium and high-energy electron beam radiation processing equipment for commercial applications. *Nuclear Instruments and Methods Journal*. 2003, Vol.208, pp. 74 – 89.
- 17 Mehnert R. Review of industrial applications of electron accelerators. *Nuclear Instruments and Methods Journal*. 1996, Vol.113, pp. 81 – 87.
- 18 Neronov V.A., Voronin A.P., Tatarintseva M.I., Melekhova T.E., Auslender V.L. Sintering under a high-power electron beam. *Journal of the Less Common Metals*. 1986, Vol.117, pp. 391 – 394.
- 19 Surzhikov A.P., Frangulyan T.S., Ghyngazov S.A. A thermoanalysis of phase transformations and linear shrinkage kinetics of ceramics made from ultrafine plasmochemical ZrO₂(Y)-Al₂O₃ powders. *Journal of Thermal Analysis and Calorimetry*. 2014, Vol. 115, No. 2, pp. 1439-1445 DOI: 10.1007/s10973-013-3455-y
- 20 Surzhikov A.P., Galtseva O.V., Vasendina E.A., Vlasov V.A., Nikolaev E.V. Processing line for industrial radiation-thermal synthesis of doped lithium ferrite powders. *Proceeding of the IOP Conference Series: Materials Science and Engineering*. 2016, Vol.110, No.1, 012002 DOI: 10.1088/1757-899X/110/1/012002.
- 21 Surzhikov A.P., Frangulyan T.S., Ghyngazov S.A., Lisenko E.N., Galtseva O.V. Physics of magnetic phenomena: Investigation of electroconductivity of lithium pentaferriite. *Russian Physics Journal*. 2006, Vol.49, No.5, pp. 506 – 510. DOI: 10.1007/s11182-006-0133-6
- 22 Lysenko, E.N., Surzhikov, A.P., Zhuravkov, S.P., Vlasov V.A., Pustovalov, A.V., Yavorovsky. The oxidation kinetics study of ultrafine iron powders by thermogravimetric analysis. *Journal of Thermal Analysis and Calorimetry*. 2014, Vol. 115, iss. 2, p. 1447-1452 DOI: 10.1007/s10973-013-3456-x
- 23 Surzhikov, A.P., Frangulyan, T.S., Ghyngazov, S.A. A dilatometric study of the effect of pressing on the kinetics of compression of ultrafine zirconium dioxide powders under thermal annealing. *Russian Physics Journal*. 2012. Vol.55, No.4, pp. 345 – 352 DOI: 10.1007/s11182-012-9818-1
- 24 Burlakova R.F., Edel'man I.S., Zabluda V.V. Magnetic linear and circular dichroism of lithium ferrite. *SOVIET PHYSICS SOLID STATE*. 1978, Vol.20, pp. 1672 – 1673.
- 25 Kong L.B., Teo M.L.S., Li Z.W., Lin G.Q., Gan Y.B. Development of magneto-dielectric materials based on Li-ferrite ceramics III. Complex relative permeability and magneto-dielectric properties. *Journal of Alloys and Compounds*. 2008, Vol.459, pp. 576–582.
- 26 Xu F., Zhang D., Wang G., Zhang H., Yang Y., Liao Y., Jin L., Rao Y., Li J., Xie F., Gan G. Influence of LZN nanoparticles on microstructure and magnetic properties of Bi-substituted LiZnTi low-sintering temperature ferrites. *Ceramics International*. 2019, Vol.45, pp. 1946–1949.

27 Cao X., Sun K., Sun C., Leng L. The study on microstructure and microwave-absorbing properties of lithium zinc ferrites doped with magnesium and copper. *Journal of Magnetism and Magnetic Materials*. 2009, Vol.321, pp. 2896–2901.

28 Verma V., Pandey V., Singh S., Aloysius R.P., Annapoorni S., Kotanala R.K. Comparative study of structural and magnetic properties of nano-crystalline $\text{Li}_{0.5}\text{Fe}_{2.5}\text{O}_4$ prepared by various methods. *Physica B*. 2009, Vol. 404, pp. 2309–2314.

29 Kumar P., Juneja J.K., Singh S., Raina K.K., Prakash C. Improved dielectric and magnetic properties in modified lithium-ferrites. *Ceramics International*. 2015, Vol. 41. pp. 3293–3297.

30 Widatallah H.M., Johnson C., Berry F.J. The influence of ball milling and subsequent calcination on the formation of LiFeO_2 . *Journal of Materials Science*. 2002, Vol.37, pp. 4621–4625.

31 Berbenni V., Marini A., Matteazzi P., Ricceri R., Welham N.J. Solid-state formation of lithium ferrites from mechanically activated $\text{Li}_2\text{CO}_3 - \text{Fe}_2\text{O}_3$ mixtures. *Journal of the European Ceramic Society*. 2003, Vol.23, pp. 527 – 536.

32 Parvin R., Momin A.A., Akther Hossain A.K.M. J. Improvement of microstructure, initial permeability, magnetization and dielectric properties of nanocrystalline $\text{Li}_x\text{Cu}_{0.1}\text{Co}_{0.1}\text{Zn}_{0.8-2x}\text{Fe}_{2+x}\text{O}_4$. *Journal of Magnetism and Magnetic Materials*. 2016, Vol. 401, pp. 760 – 769.

33 Widatallah H.M., Ren X.L., Al-Omari I.A. The influence of TiO_2 polymorph, mechanical milling and subsequent sintering on the formation of Ti-substituted spinel-related $\text{Li}_{0.5}\text{Fe}_{2.5}\text{O}_4$. *Journal of Materials Science*. 2006, Vol.41, pp. 6333 – 6338.

34 Yesbayev A.N., Yessenbayeva G.A., Ramazanov M.I. Investigation of the model for the essentially loaded heat equation. *Eurasian Physical Technical Journal*. 2019, Vol.16, No.1, pp. 113 – 120.

35 Zhumabekov A.Z., Seliverstova E.V., Ibrayev N.K. Investigation of photocatalytic activity of TiO_2 -GO nanocomposite. *Eurasian Physical Technical Journal*. 2019, Vol.16, No.1, pp. 42 – 46.

36 Liao Y., Wang Y., Chen Zh., Wang X., Lib J., Guo R., Liu Ch., Gan G., Wang G., Li Y., Zhang H. Microstructure and enhanced magnetic properties of low-temperature sintered LiZnTiMn ferrite ceramics with Bi_2O_3 - Al_2O_3 additive. *Ceramics International*. 2020. Vol.46, No.1, pp. 487 – 492.

37 Ahniyaz A., Fujiwara T., Song S-W., Yoshimura M. Low temperature preparation of β - LiFe_5O_8 fine particles by hydrothermal ball milling. *Solid State Ionics*. 2002, Vol.151, No.1–4, pp. 419 – 423.

38 An S.Y., Shim I-B., Kim C.S. Synthesis and magnetic properties of LiFe_5O_8 powders by a sol-gel process. *Journal of Magnetism and Magnetic Materials*. 2005, Vol.290, pp. 1551 – 1554.

39 Petrova A.B., Astafyev A.L., Ershov A.V. The study of initial permeability temperature dependences for LiTiZn ferrite ceramics. *IOP Conference Series: Materials Science and Engineering*. 2018, Vol. 81(289), pp.133575. DOI: 10.1088/1757-899X/289/1/012042.

40 Kavanlooe M., Hashemi B., Maleki-Ghaleh H., Kavanlooe J. Effect of annealing on phase evolution, microstructure, and magnetic properties of nanocrystalline ball-milled LiZnTi ferrite. *Journal of Electronic Materials*. 2012, Vol. 41, pp. 3082–3086.

41 Barba A., Clausell C., Feliu C., Monzo M. Sintering of $(\text{Cu}_{0.25}\text{Ni}_{0.25}\text{Zn}_{0.50})\text{Fe}_2\text{O}_4$ ferrite. *Journal of the American Ceramic Societ*. 2004, Vol.87, No.4, pp. 571 – 577.

DOI 10.31489/2020No1/35-38

UDC 538.975, 66.017

OBTAINING OF CARBON NANOFIBERS BASED ON POLYACRYLONITRILE BY THE METHOD OF ELECTROSPINNING

Ospanali A.T.^{1,2}, Kenzhegulov A.K.^{1,2}, Zhumadilov B.E.^{1,2}, Suyundykova G.S.^{1,2}, Medyanova B.S.^{1,2}, Partizan G.^{1,2}, Aliev B.A.²

¹Center of innovative technology at the Institute of Combustion Problems, Almaty, Kazakhstan

²al-Farabi Kazakh National University, Almaty, Kazakhstan, os_aziza@mail.ru

Since carbon nanofibers comprise a continuous reinforcing with high specific surface area, associated with the fact that they can be obtained at a low cost and in a large amount, they have shown to be advantageous compared to traditional carbon nanotubes. The main objective of this work is the processing of carbon nanofibers, using polyacrylonitrile (PAN) as a precursor, obtained by the electrospinning process via polymer solution, with subsequent use as a reinforcement in polymer composites. The paper reports the fabrication and characterization of PAN nanofibers by electrospinning and further development of the as-spun PAN nanofibers into carbon nanofibers. PAN nanofibers as a precursor of carbon nanofibers with diameters in the range of 100–500 nm were prepared by electrospinning of PAN/DMF solution. The aligned electrospun PAN nanofibers first stabilized in air at temperature 250°C for 1 hr. We also investigated several carbonization procedures by varying final carbonization temperatures in the range from 600–900°C in argon atmospheres and the carbon nanofibers were successfully obtained at 700°C and 1 hr. Morphologies of PAN, stabilized and carbonized nanofibers were investigated by scanning electron microscopy (SEM). The results obtained from SEM showed that the average diameter of the stabilized and carbonized PAN nanofibers was significantly reduced.

Keywords: electrospinning, nanofibers, polyacrylonitrile, dimethylformamide, scanning electron microscopy.

Introduction

Interest to nanofibers caused by the fact that the mechanical properties of materials such as tensile strength, tear strength, bending and compression, the elastic modulus increase with decreasing fiber diameter and reach a theoretical limit when reaching the nanoscale. This is due, on the one hand, to a decrease in the concentration of extended defects in the nanofiber, and on the other hand, to a change in the physical properties of the nanofiber material itself due to the contribution of the surface. This effect is valid for any nanomaterials, since the surface of any material is a special two-dimensional ordered state. In the case of polymer nanofibers, the dimensional effect can also be manifested in the volume properties as a result of additional interaction between the polymer molecules caused by their orientation, when the fiber diameter becomes comparable to the length of the molecule [1]. One of the methods for producing nanofibers is the formation of fibers from polymer solutions under the action of an electrostatic field. This method combines hardware simplicity, high performance and scalability of the process from the laboratory installation to the elements of the industrial conveyor [2-5].

The paper presents the results of investigations by scanning electron microscopy of nanofibers based on polyacrylonitrile (PAN) synthesized by the method of electrospinning.

1. Experiment details

The solution was prepared using PAN powder (Mw: 150000) and dimethylformamide. In order for the powder to be completely dissolved, the solutions were mixed together and thoroughly mixed

on a magnetic stirrer for 30 minutes at a temperature of 80°C. Figure 1 shows a diagram of the installation of electrospinning. The laboratory unit consists of a high-voltage source, a special syringe pump, a collector that can rotate and supply additional voltage for more efficient collection of fibers, a syringe holder and the syringe with a metal needle connected to a high-voltage source. A polymer solution is placed in the syringe, which is then pumped out at a controlled speed through the needle. When a high voltage is applied to the liquid needle, the liquid jet breaks off from the surface of the drop and collects on the collector in the form of fibers. A series of experiments was carried out in which the distance from the needle to the collector (20 cm) and the supplied voltage (16 kV) remained constant, the experiment duration was 3 hours, and the ratio of PAN and DMF concentrations varied from 6% to 10% in 2% increments.

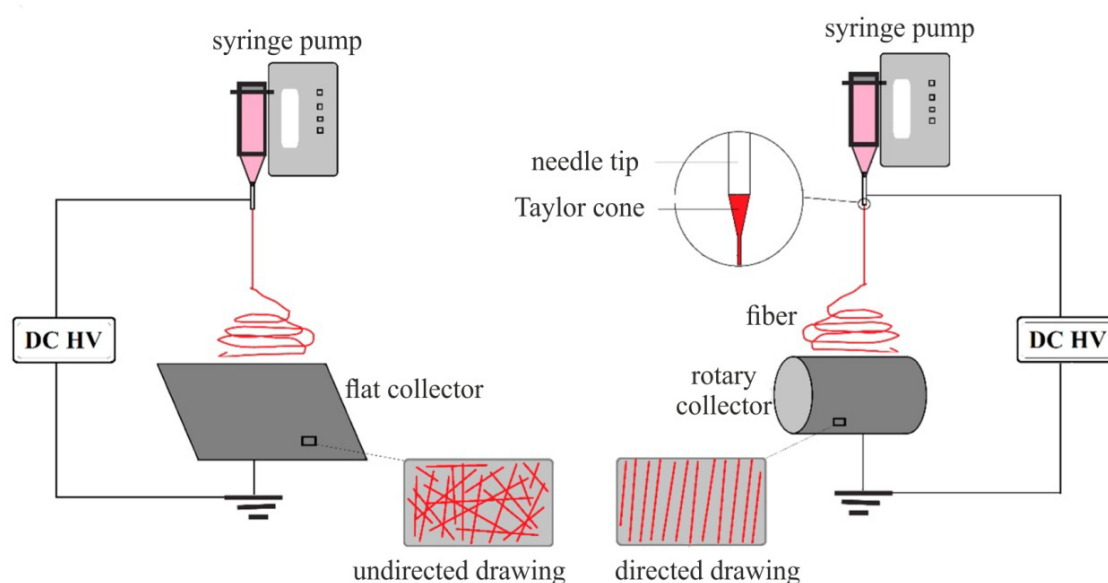


Fig.1. General scheme of the installation for the synthesis of nanofibers

In the second stage of the experiment, the synthesized fibers were dried in air before they were stabilized. Portions of samples were selected for heat treatment. For the stabilization process, the sample was placed in a horizontal three-zone tube furnace. The stabilization temperature was determined experimentally. The optimal stabilization temperature is 250 °C. Further, the samples were carbonized at a temperature of 700°C in an argon atmosphere (500 mbar). The carbonation temperature was also determined experimentally. The obtained samples were examined by the SEM method. The study of the samples was conducted at the National nanotechnology laboratory of open type with a microscope Quanta 3D 200i.

2. Results and discussion

To determine the effect of the parameters of various stages of the experiment on the diameters of nanofibers, histograms of the distribution of diameters were constructed. Figure 2 shows the picture, the SEM image and the histogram of diameters distribution of the synthesized carbon nanofibers a value of PAN concentration of 8%. They are shown in different colors: white (after synthesis), brown (after the stabilization process at a temperature of 250 ° C) and black (after the carbonization process at a temperature of 700 ° C).

From the histogram data, it follows that the sample after synthesis is dominated by nanofibers with a diameter of 300-400 nm, the average diameter of which is 369 nm. After the stabilization process, the diameter of the fibers is reduced by a significant number the average diameter size is 298 nm. It is also seen that after the carbonation process, the diameter of the fibers decreases. The

average size of nanofibers after the carbonation process is 242 nm. Histogram analysis shows that the distribution of nanofibers by diameter is Gaussian with a mean square deviation of $\sigma = 25$ nm.

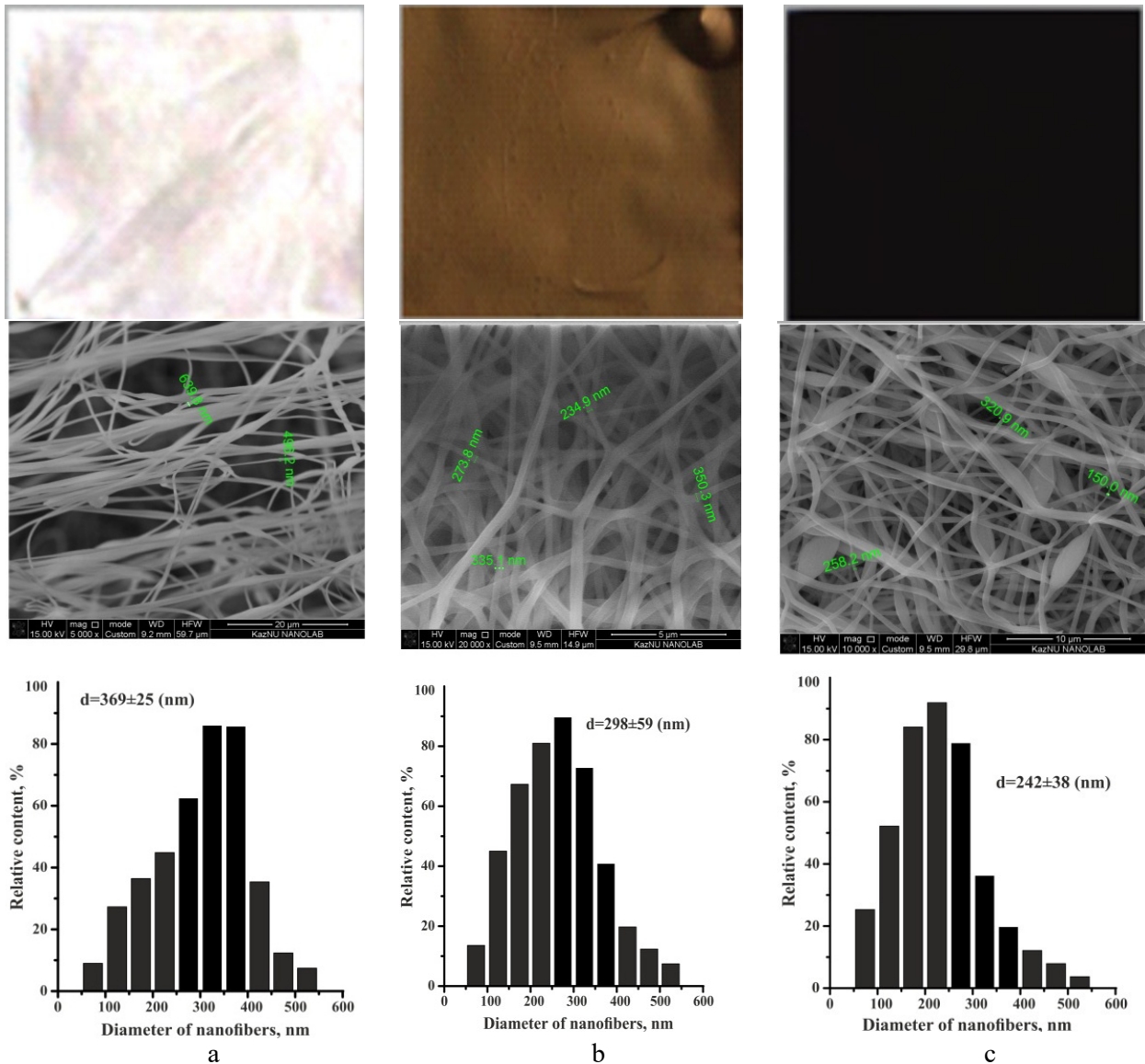


Fig.2. Photographs, SEM images and histograms distribution of synthesized fiber diameters at the value of PAN 8 % concentration: a – after synthesis, b – after the stabilization, c – after the carbonation

The results obtained from SEM and distribution of diameters showed that the average diameter of the stabilized and carbonized PAN nanofibers was significantly reduced. Analysis of literature data showed that the stabilization and carbonization process carried out significantly at high temperatures. Experimentally we determined the lower temperature limit for the stabilization and carbonization process. A series of experiments were carried out for check the repeatability of the results.

Figure 3 shows the SEM images after carbonation at a temperature of 700°C and a histogram of the distribution of nanofiber diameters at different values of PAN concentrations.

The results show that as the concentration of PAN decreases, the diameter of the nanofibers decreases. Thus, it was determined that the optimal concentration value for the synthesis of nanofibers with a minimum diameter is 6%

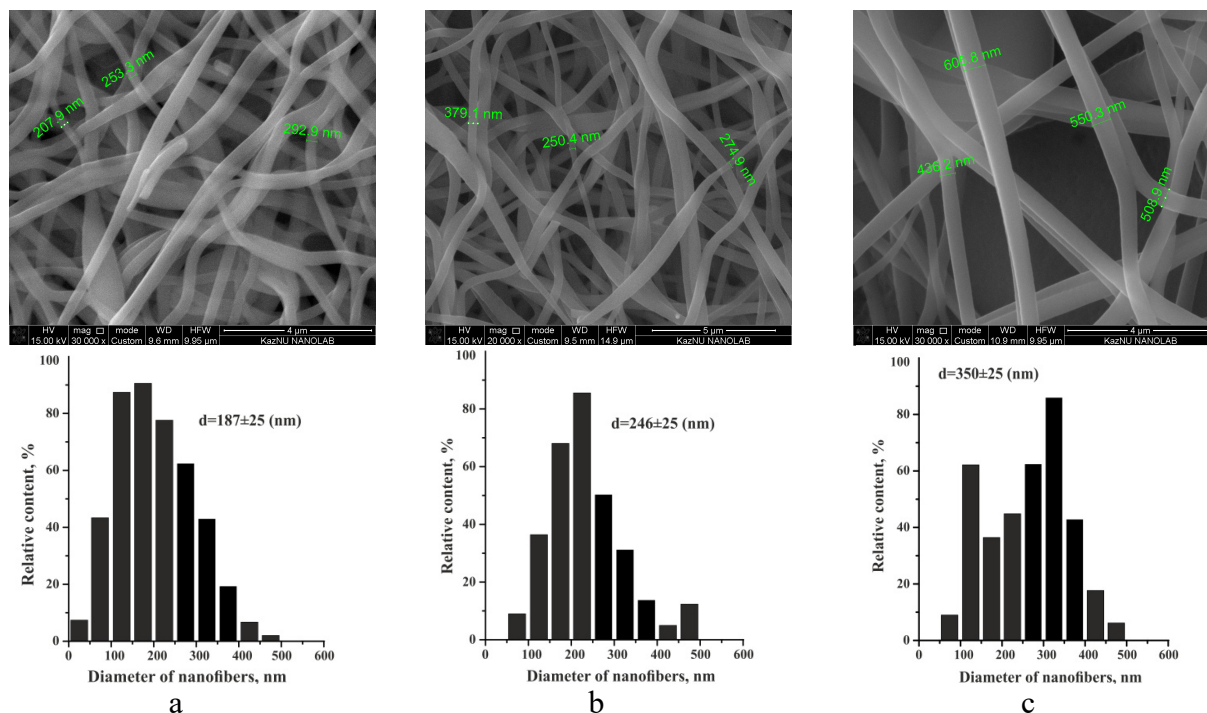


Fig.3. A histogram of the distribution of nanofiber diameters and SEM images after carbonation at different values of PAN concentrations (a) - 6%; b) - 8%; c) - 10%

Conclusion

During the research, trial experiments were conducted on the synthesis of carbon fibers by electrospinning based on PAN. The obtained samples were examined by the SEM method. According to the SEM analysis, the obtained samples have a homogeneous structure. The resulting nanofibers have a fairly large diameter spread from several tens to several hundred nanometers.

The optimal PAN concentration was determined for the synthesis of nanofibers with a minimum diameter. Further research will be aimed at determining the optimal combinations of technological parameters of synthesis, in order to obtain the necessary carbon nanofibers. For a more detailed analysis of the structure of the obtained structures, additional studies should be carried out using the methods of Raman scattering, X-ray fluorescence analysis, and transmission electron microscopy and electron diffraction.

Acknowledgements

The work was carried out with a partial financial support grant from the Science Committee of Ministry of Education and Science Republic of Kazakhstan. Grants No. AP05132865

REFERENCES

- 1 Li D., Wang Y., Xia Y. Electro spinning nanofibers as uniaxially aligned arrays and layer by-layer stacked films. *Adv. Mater.* 2004, Vol. 16, No. 4, pp. 361 – 366.
- 2 Teo WE., Ramakrishna S. A review on electrospinning design and nanofibre assemblies. *Nanotechnology*, 2006, Vol. 89, pp. 395 – 407.
- 3 Fang J., Zhang Li, Sutton D., Wang X., Lin T. Needleless Melt-Electrospinning of Polypropylene Nanofibres. *Journal of Nanomaterials*. 2012, Vol. 2012, pp. 1 – 9.
- 4 Chen D., Liu T., Zhou X., Chauhari W., Tjiu H. How Electrospinning Fabrication of High Strength and Toughness Polyimide Nanofiber Membranes Containing Multiwalled Carbon Nanotubes. *Physical chemistry*. 2009, Vol. 113, No. 29, pp. 9741 – 9748.
- 5 Lyons J., Ko F. Melt Electrospinning of Polymers: A Review. *The Polymer Science Monthly*. 2005, Vol. 30, No. 6, pp. 170 – 178.

DOI 10.31489/2020No1/39-45

UDC 539.125.5

STUDY OF WATER INFILTRATION INTO CEMENT-BASED MORTARS USING REAL-TIME THERMAL NEUTRON RADIOGRAPHY

Nazarov K.M.^{1,2*}, Kichanov S.E.¹, El Abd A.³, Taman M.⁴, Kozlenko D.P.¹

¹ Frank Laboratory of Neutron Physics, Joint Joint Institute for Nuclear Research, Dubna, Russia, knazarov@jinr.ru

² Faculty of Physics and Technology, L.N. Gumilyov Eurasian National University, Nur-Sultan, Kazakhstan

³ Reactor Physics Department, Nuclear Research Center, Atomic Energy Authority, Cairo, Egypt

⁴ Department of Structural Engineering, Faculty of Engineering, Tanta University, Tanta, Egypt

Water absorption into cement mortar with different water to cement ratio was studied using neutron radiography in order to assess the durability and stability of these mortars. While the samples absorb water, neutron radiography images were acquired regularly as the absorption time elapses. The time evolution of water front position or penetration depth and the water content distribution along the flow direction were determined based on the specific differences in the interactions of neutrons with various components of the cement mortars and absorbed water. The obtained results were discussed in terms of the capillary theory to obtain the characteristic parameters of water propagation in the cement mortars. It's shown that neutron radiography is a powerful method to study a moisture transport in porous media.

Keywords: cement mortars, neutron radiography, moisture transport, water absorption.

Introduction

Cement mortars are key elements in the construction of building materials, being widely used in different formulas. The operation time of cement-based mortars and concretes strongly depends on the presence of water inside these materials [1, 2]. Water transport in porous media such as cement mortar is a crucial process for their durability and stability [3, 4]. Because of water transport inside mortars and concretes materials, the chemical aggressive compounds can be penetrated into them, and accelerate the damage process of these materials [5]. In particular, steel corrosion in reinforced concrete under the moisture content can lead to the local critical destruction of massive concrete construction [5, 6]. Therefore, the desire to understand the mechanisms of water absorption into cement mortars lead to control of this process by using destructive and non-destructive experimental methods for improving their service life and durability [7-10]. These studies and obtained results are of high value being a base for optimizing the cement materials formulas if required. One of the non-destructive methods is neutron radiography [10, 11]. This method is a powerful tool for non-destructive analysis, which has many applications in the studies of water absorption and penetration in porous building materials including mortar, concrete, stones, and bricks [12-15]. Neutron radiography provides additional benefits to study moisture transport and its spatial distribution inside cement material due to the strong neutron attenuation by the hydrogen-contained matter like water.

In the present paper, the results of neutron radiography experiments performed on three types of cement mortars with different water to cement (w/c) ratios are highlighting the time evolution of waterfront inside the studied cement-based materials.

1. Sample preparation

Cement; Ordinary Portland cement (CEM I 42.5N) was used in the present experimental work. The cement specific gravity and specific surface area were 3.13 and 3394 cm²/gm, respectively. The

chemical compositions of cement matrix are listed in Table 1. The initial and the final setting times were performed according to [16] and the recorded times were 85 min and 240 min, respectively.

Sand; standard sand [17] was used for all mortar samples. Table 2 lists the grading of the standard sand used. The silica and moisture content of the used sand were not less than 98% and less than 0.2%, respectively.

Water; Tap water with pH value about 7.2 and complied with the limits of [17] was used.

Table 1. The chemical composition of the cement used for the preparation of cement mortar.

Component	Content, %
SiO ₂	19.6771
CaO	61.138
MgO	2.4444
Fe ₂ O ₃	5.6329
Al ₂ O ₃	3.879
Na ₂ O	0.4269
K ₂ O	0.1672
Cl	0.0331
SO ₃	3.0873
Loss of ignition	3.5003
Total	99.9865

Table 2. The grading of the standard sand.

Sieve size, mm	% retained, cumulative
2	0
1.6	7±5
1	33±5
0.5	67±5
0.16	87±5
0.08	99±1

Three mortar mixtures were mixed with different water/cement (W/C) ratios of 0.42, 0.45 and 0.65. The binder to sand ratio was kept constant of 1/3 as listed in Table 3. Each mix was mixed mechanically according to [17]. After mixing, the mortar was cast in moulds of 40×40×160 mm in dimension and kept in moist cabin for 24 hours. For each mix, 6 prisms of the dimension of 40×40×160 mm were cast. After that the specimens were demolded and kept in water of temperature of 25 ± 2 C° till the test.

For each fresh mortar mix, the flow test was performed according to [18]. The recorded flow percentage was measured after the standard number of shaking cycles of 25. Table 3 lists the flow ratio for the three mixes. It can be noticed that, the W/C ratio has a positively effect on the flow percentage of the fresh mortar where, the W/C ratio of 0.65 increased the flow to about 735% compared to that of 0.42 W/C ratio.

Table 3. The results of the tests for flow and compressive strength of samples.

Sample	Cement	Sand	Water	Flow (%)	Compressive strength (MPa)	
					Age of 2 days	Age of 28 days
#1	1	3	0.42	21.4	26.4	48.0
#2	1	3	0.45	73.8	22.6	52.8
#3	1	3	0.65	178.6	14.4	35.0

The compressive and flexural strength tests of the mortar samples were carried out at 2 and 28-days ages according to [17]. The results of the compressive strength were recorded in Table 3. It can be noticed that, the lower the water/ cement ratio, the higher the compressive strength for the two ages of tests.

2. Experimental methods

Three mortar samples were chosen for the neutron radiography experiments. We introduce the notation of the studied samples as Sample#1, Sample#2 and Sample#3, which corresponds to water/cement (w/c) ratios of 0.42, 0.45, and 0.65, respectively. The dry cement mortars were covered with a special type of acrylic paint from all sides except their ends to prevent evaporation and to allow water to flow in one dimension during the absorption process.

The experiments of neutron radiography were performed at the neutron radiography and tomography facility [19, 20] and placed on beamline 14 of the IBR-2 high-flux pulsed reactor. Neutron radiography images have been collected by a CCD-based detector system with a maximum field of view of 20×20 cm. The imaging data were corrected by subtracting the camera dark current image and normalizing to the image of the incident neutron beam using the Image J software [21].

The studied samples were placed in a container with water. The neutron radiography images were collected with duration of 30 seconds per frame and a delay between frames of 47 sec. Exposure starts 247 seconds after specimens have been placed in water. For 4.5 hours, the 202 radiography images were collected. Each image corresponds to the time of a duration of the capillary water transport inside the studied cement mortars. The small cadmium foils were fixed on the studied cement samples for an additional correction for scattered neutrons.

The basic calculation for the time evolution of the water front positions in the cement mortars was performed based on previous works [11, 12, 22].

3. Results and discussions

The result of signal generation based on the proposed analytical model (Equation (4)) in the time and frequency domains are shown in Fig. 2a and 2b. The direct signal propagates over the shortest distance and has greater energy characteristics than the reflected ones.

Examples of the neutron radiographic images of the cement mortars obtained at different times of the capillary water absorption are shown in Figure 1. Because the neutron attenuation coefficient of water is greater due to the large incoherent neutron scattering cross section, waterfront contrasts well with the cement materials in the neutron radiography images (Figure 1).

It can be seen that the water fronts are irregular and have complex shapes which can be attributed to the inhomogeneous structure of the samples resulting from manufacturing process and may be related to surface cracks, which decrease with increasing distance from the surface [11, 12]. As the absorption time elapses, the waterfronts proceed into the samples however, with different rates.

The water content distributions along the flow direction x as a function of the absorption time were extracted from the acquired neutron images (simply water profiles, $\theta(x, t)$) according to

$$\theta(x, t) \approx \ln\left(\frac{I_{dry}}{I_{dry+wetted}}\right), \quad (1)$$

where I_{dry} and $I_{dry+wetted}$ are total transmitted neutron fluxes (intensities or brightness) for the dry and wetted sample, respectively.

The procedures used to correct for neutron scattering using Cd strip will be discussed in a forthcoming paper. A rectangular area was drawn along the flow direction for every image obtained (Fig. 1). The neutron intensities extracted from the dry and wetted sample images altogether with Eq. 1 were used to determine the water profiles. The profiles determined for Sample #1, Sample #2 and Sample #3 are shown Figs. 2a, 2b and 2c, respectively.

The results shown in Fig. 2 show that as the absorption time increases, water profiles migrate into deeper distances in the samples. The process of water absorption into sample #1(w/c=0.42) is the slowest in comparison with the other samples and it is hardly to recognize any signs of water. At the largest absorption time (Fig. 2a), sample #1 started to absorb too small amounts of water.

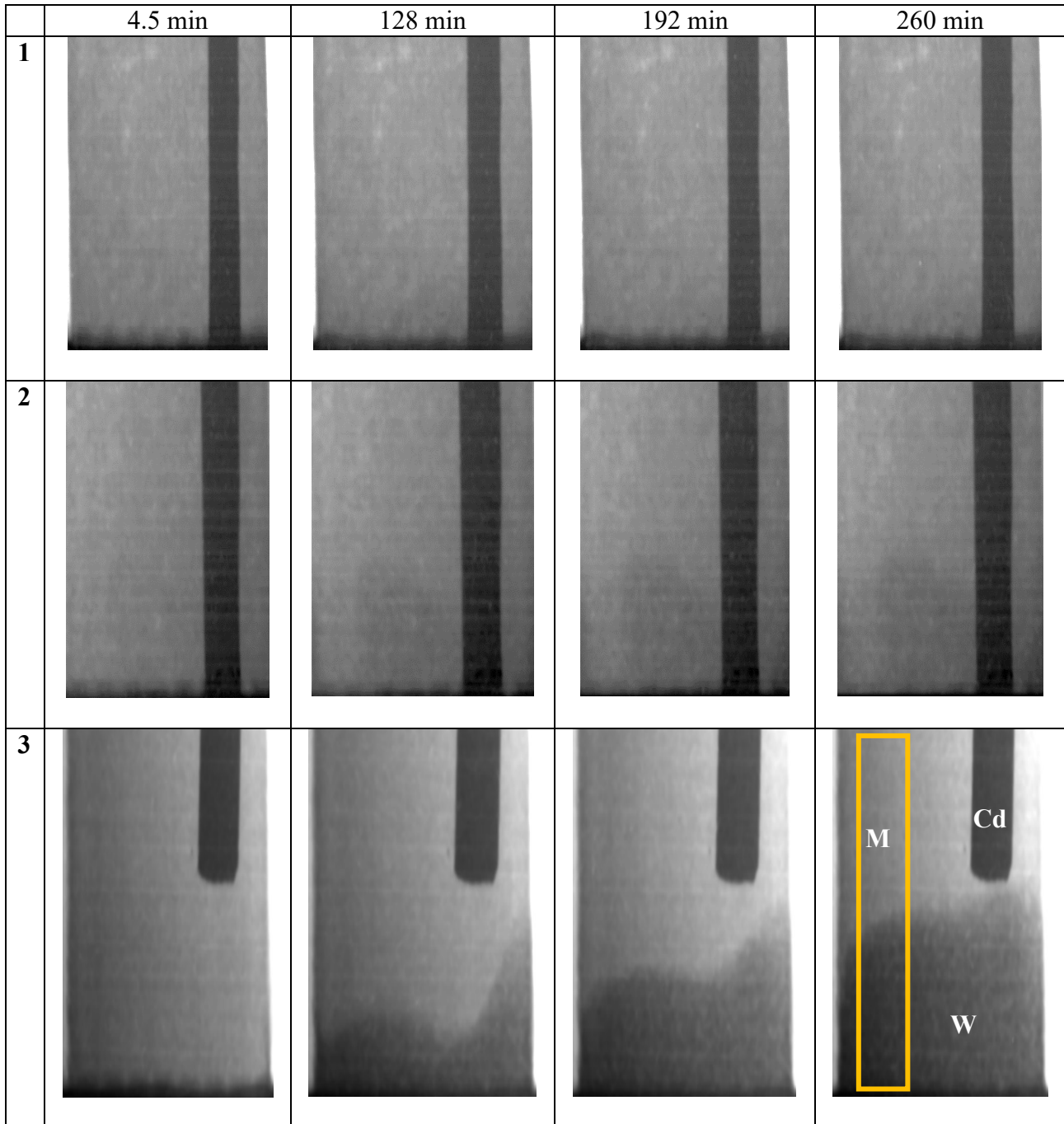


Fig.1. The neutron radiography images of the cement mortars of Sample #1, Sample# 2 and Sample#3 for the different exposure times.

On Fig. 1 the gray regions correspond to neutron attenuation in the cement materials. The darker areas are high neutron attenuate regions of penetrating water. The black stripe is cadmium foil shadow. The “M”, “W” and “Cd” mark the mortar, water and cadmium materials, respectively. The yellow bar marks the region used to calculate the water profiles.

It is noticed from the shape of the water profiles for sample #2 ($w/c=0.45$) and sample#3 ($w/c=0.65$) that the water contents are slightly decrease with distance along the flow direction till the water front regions. Additionally, sharp fronts characterize these samples. As the w/c increases, the porosity increases and hence the water absorption increases [22, 23]. Thus, water absorption by sample #3 is higher than that of sample #2. Namely, the amount of water absorbed by sample #3 is higher than that of sample #2.

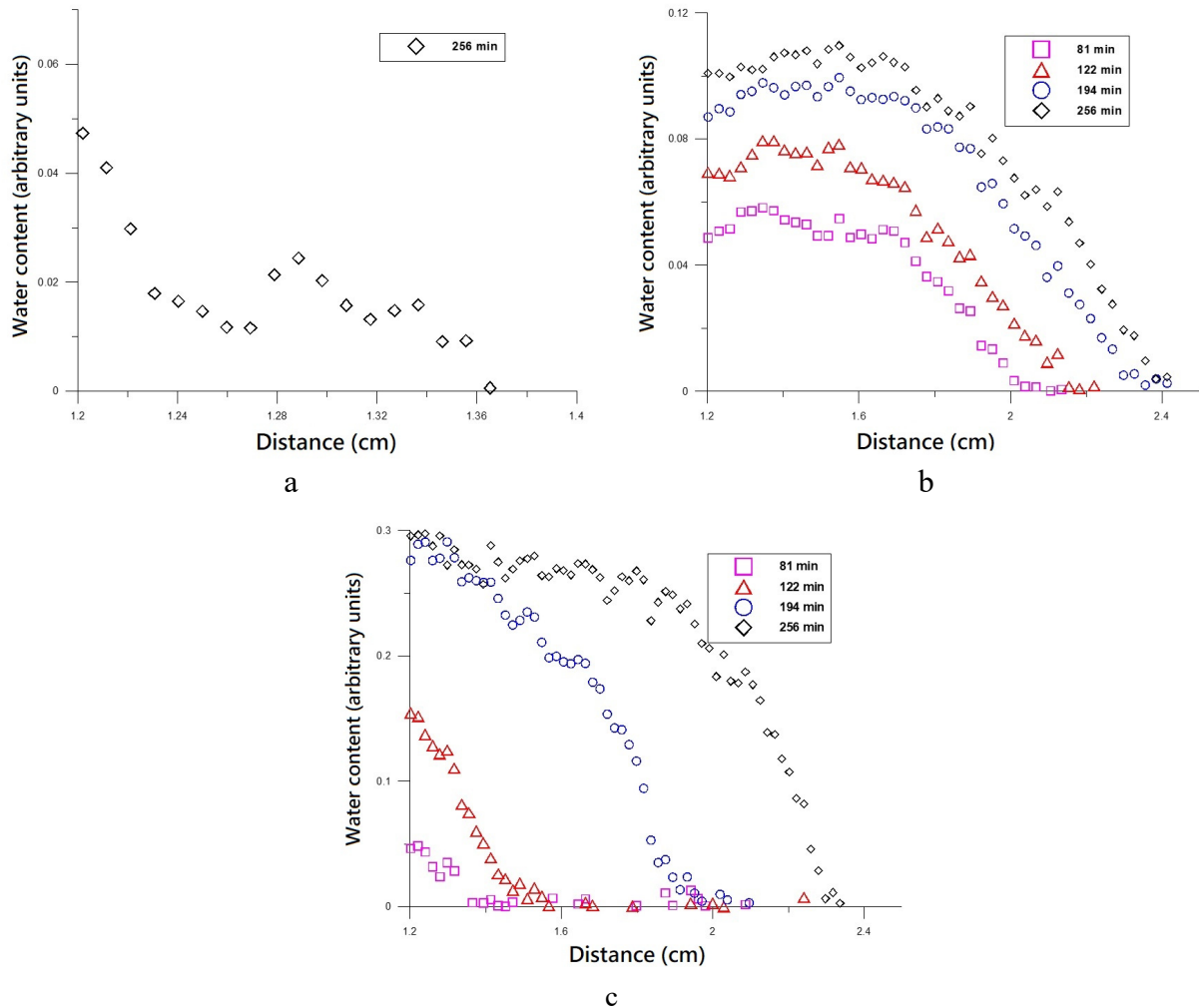


Fig.2. Water front profile for Sample: a) #1, $w/c=0.42$; b) #2, $w/c=0.45$; c) #3, $w/c=0.65$

Water front positions (penetration depth) were determined from the water profiles of the investigated samples. The water penetration into cement mortar samples can be estimated in terms of the capillary theory [12, 22, 24, 25]. According to this theory the penetration depth (water front position) as a function of time can be described by means of the following simple equation [10, 11]:

$$x(t) = B * \sqrt{t}, \quad (2)$$

where $x(t)$ stands for the penetration depth at time t and B is the coefficient of water penetration.

The coefficient of water penetration B was first termed the sorptivity [26]. It lumps the physical parameters of both the flowing liquid and the porous medium such as viscosity, surface tension contact angle and the radii of the porous medium [27]. The water penetration depths were determined from the water profiles. The penetration depth as a function of square root of time in hours is shown in Figure 3. As can be seen, the water front positions for mortar samples with \sqrt{t} are varied, however, with a different behavior. It is observed that the water penetrated distances for sample #2 are higher than that of sample#3 – it seems that there is a sudden jump of water inside sample #2, once water touches its immersed end.

During the initial period of water absorption, water fronts proceed quickly in sample #2 than in the advanced period. This is indicated by the slopes of the straight fit lines. However, the situation for sample #3 is different; water absorption during the initial period is slower than the advanced one. The calculated coefficients of water penetration B for the Sample #2 are $6.18 \text{ mm/h}^{1/2}$ and 4.48

mm/h^{1/2} for the initial and advanced periods of water absorption, respectively. The corresponding values for sample #3 are 7.23 mm/h^{1/2} and 15 mm/h^{1/2}.

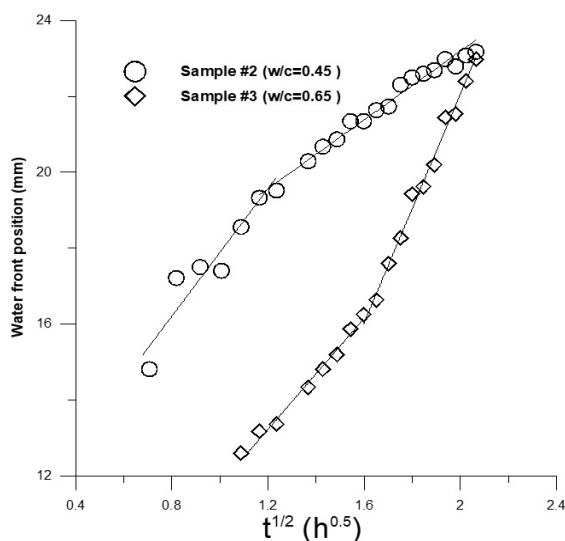


Fig.3. The water front positions versus square root of absorption time for sample #2 and #3 along with straight line fits

The initial and advanced periods of water absorption characterizing the mortar samples investigated in this work were previously observed for some mortar samples in [28]. Additionally, the calculated values of water penetration B lie in the ranges reported in [11, 28]. As the W/C ratio increases, both the flow percentage of the fresh mortar and water absorption (water penetration B) increase, however the corresponding compressive strength decreases.

Conclusion

The real-time neutron radiography method and the analytical procedures used have proven to be effective for studying the processes of moisture transfer in cement mortars. In our research, we observed that different ratios of water/cement lead to dramatic changes in the mechanisms of moisture absorption inside the cement mortar samples.

Firstly, it should be correlated with the features of the structure of cement mortars, where an interface between aggregates and grains of the cement paste can form some dominant ways for the water penetration. The different interactions between those mortars components lead to damages, cracks or inner voids in the cement materials. Secondly, the faster water penetration in the first hours of the experiment corresponds to cracks in the side edges of studied cement mortars because of the mechanical treatments. These external cracks can be paths of the dominant infiltration of water into the thickness of the cement mortar, where the described above type of the pores and capillaries dominants.

REFERENCES

- 1 Phillipson M.C., Baker P.H., Davies M., et al. Moisture measurement in building materials: an overview of current methods and new approaches. *Build. Serv. Eng.Res.T.* 2007, Vol. 28, No. 4, pp. 303-316.
- 2 Abd A.El, Kichanov S.E., Taman M., Nazarov K.M. Penetration of water into cracked geopolymer mortars by means of neutron radiography. *Constr. Build. Mater.* 2020, Vol. 256, pp.119471.
- 3 Abd A.El, Kichanov S.E., Taman M., et al. Determination of moisture distributions in porous building bricks by neutron radiography. *Applied Radiation and Isotopes.* 2020, Vol. 156, No. 108970.
- 4 Angst U. M., Hooton R. D., Marchand J., et al. Present and future durability challenges for reinforced concrete structures. *Mater Corros.* 2012, Vol. 63, No.12, pp. 1047–1051.

- 5 Müller H. S., Haist M., Vogel M. Assessment of the sustainability potential of concrete and concrete structures considering their environmental impact, performance and lifetime. *Constr. Build. Mater.* 2014, Vol. 67, pp. 321–337.
- 6 Wang K., Jansen D.C., Shah S.P., et al. Permeability study of cracked concrete. *Cem. Conc. Res.* 1997, Vol.27, pp. 381 – 393.
- 7 Gummerson R.J., Hall C., Hoff W.D., et al. Unsaturated water flow within porous materials observed by NMR imaging, *Nature.* 1979, Vol. 281, pp. 56–57.
- 8 Baker P.H., Bailly D., Campbell M., et al. The application of x-ray absorption to building moisture transport studies. *Measurement.* 2007, Vol. 40(9-10), pp. 951–959.
- 9 Zhang P., Wittmann F.H., Zhao T. J., et al. Observation and quantification of water penetration into frost damaged concrete by neutron radiography. *Restoration of Buildings and Monuments.* 2010, Vol. 16, pp. 195–210.
- 10 Zhang P., Wittmann F.H., Lura P., et al. Application of neutron imaging to investigate fundamental aspects of durability of cement based materials: A review. *Cem. Conc. Res.* 2018, Vol. 108, pp. 152–166.
- 11 Anderson S., McGreevy R.L., Bilheux H.Z. *Neutron Imaging and Applications: A Reference for the Imaging Community.* Springer US, New York, Edition 1, 2009, p. 341.
- 12 Lehmann E.H., Kaestner A., Gruenzweig C., et al. Materials research and non-destructive testing using neutron tomography methods. *Int. J. Mater. Res.* 2014, Vol. 105, pp. 664-670.
- 13 Perfect E., Cheng C.-L., Kang M., et al. Neutron imaging of hydrogen-rich fluids in geomaterials and engineered porous media: A review, *Earth-Sci. Rev.* 2014, Vol. 129, pp. 120-135.
- 14 Kichanov S.E., Kenessarini M., Balasoiu M., et al. Studies of the Processes of Hardening of Cement Materials for the Storage of Aluminum Radioactive Waste by Neutron Radiography. *Phys. Part. Nuclei Lett.* 2020, Vol. 17, No. 1, pp.73–78.
- 15 Kichanov S.E., Nazarov K.M., Kozlenko D.P., et al. Neutron tomography studies of cement-based materials used for radioactive waste conditioning, *Rom. J. Phys.* 2019, Vol. 64, No. 803.
- 16 BS EN196-3: Methods of Testing cement – part 3: Determination of Setting Times and Soundness. BSI Group, London, UK, 2005, 18p.
- 17 BS EN, 96-1: Methods of Testing cement: Determination of Strength. BSI Group, London, 2005, 36p.
- 18 ASTM C 230 /C 230M-14, Standard Specification for Flow Table for Use in Tests of Hydraulic Cement. ASTM International, West Conshohocken, PA, 2014, p. 6.
- 19 Kozlenko D.P., Kichanov S.E., Lukin E.V., et al. Neutron Radiography Facility at IBR-2 High Flux Pulsed Reactor: First Results. *Physics Procedia.* 2015, Vol. 69, pp. 87 – 91.
- 20 Kozlenko D. P., Kichanov S. E., Lukin E. V., et al. Neutron radiography and tomography facility at IBR-2 reactor. *Phys. Part. Nuclei Lett.* 2016, Vol. 13, pp. 346–351.
- 21 Schneider C. A., Rasband W. S., Eliceiri K.W. NIH Image to Image J: 25 years of image analysis. *Nat. Methods.* 2012, Vol. 9(7), pp. 671–675.
- 22 Hall C. Water movement in porous building materials—I. Unsaturated flow theory and its applications. *Build. Environ.* 1977, Vol. 12, pp. 117-125.
- 23 Brew D. R. M., De Beer F.C., Radeb M.J., et al. Water transport through cement-based barriers - A preliminary study using neutron radiography and tomography. *Nucl. Instrum. Meth. A.* 2009, Vol. 605, pp.163–166.
- 24 Singh S.B., Munjal P., Thammishetti N. Role of water / cement ratio on strength development of cement mortar. *J. Build. Eng.* 2015, Vol. 4, pp. 94–100.
- 25 Philip J.R. Theory of infiltration. *Advances in Hydrosience.* 1969, Vol. 5, pp. 215 – 296.
- 26 Philip J.R. The theory of infiltrate Sorptivity and algebraic infiltration. *Soil Sci.* 1957, Vol. 84(3), pp.257–264.
- 27 Zhao Y., Xue S., Han S., et al. Effects of microstructure on water imbibition in sandstones using X-ray computed tomography and neutron radiography *J. Geophys. Res. Solid Earth,* 2017, Vol. 122, pp. 4963–4981.
- 28 Lucero C.L. Quantifying moisture transport in cementitious materials using neutron radiography. 2015, Purdue University, Open Access Theses, pp. 132.

DOI 10.31489/2020No1/46-53

UDC 538.971

INVESTIGATION OF THE EFFECT OF EXPOSURE TO HEAVY Xe^{22+} IONS ON THE MECHANICAL PROPERTIES OF CARBIDE CERAMICS

Kadyrzhanov K.K.^{1*}, Tinishbaeva K.¹, Uglov V.V.²

¹L.N. Gumilyov Eurasian National University, Nur-Sultan, Kazakhstan, kayrat.kadyrzhanov@mail.ru

²Belarusian State University, Minsk, Belarus

The paper presents the results of a study of the effect of irradiation with heavy Xe^{22+} ions with an energy of 440 keV and irradiation fluences of 10^{14} , 5×10^{14} , 10^{15} ion/cm² on the properties of ceramics based on silicon carbide (SiC). The choice of the type of irradiation and dose load is due to the possibility of modeling radiation damage to the surface layer with a thickness of 200 nm as a result of the effect of overlapping defective areas. The scientific novelty of the results obtained consists in systematic studies of the stability of the mechanical and strength properties of the surface layer of carbide ceramics to radiation damage. In the course of the studies, it was found that in the case of irradiated ceramics, the damage depth exceeds the estimated ion mean free path by 20-30%, depending on the irradiation fluence. The main mechanism of radiation damage is an increase in the dislocation density of defects and the formation of regions of disordering in the case of large doses. As a result of the simulation of accelerated aging processes, it was found that for irradiated samples the decrease in crack resistance does not exceed 10%. Studies have shown high values of the stability of silicon carbide ceramics to radiation damage to the surface layer.

Keywords: ceramic, mechanical properties, defects, Silicon Carbide, heavy ions, distortion, degradation, radiation resistance

Introduction

The current state of energetics in the world requires cardinal decisions in the field of improving the reliability of nuclear installations, as well as a significant increase in the life of nuclear reactors. One of the solutions in this direction is the use of new classes of structural materials with improved mechanical, strength properties, with a high melting point, radiation and corrosion resistance, etc. [1-4]. The most suitable materials with characteristics corresponding to these requirements are ceramics based on oxides [5-8], nitrides [9-12], carbides [13-15], etc. The interest in this class of materials is due not only to the great potential for practical applications in the nuclear industry, space technology, aircraft manufacturing, microelectronics, but also to the acquisition of new fundamental knowledge in the theory of radiation defects in solids, in particular, in carbide, oxide or nitride ceramics [16-20]. Obtaining new knowledge will allow significant progress in predicting the life of this class of materials in the new generation of GenIV reactors [21-25]. When structural materials are used in nuclear reactors, the surface layers of the first wall of the reactor are exposed to large doses of radiation that can cause amorphization of the crystal structure and subsequent destruction of the surface layer, which can lead to catastrophic consequences. The processes of amorphization and degradation that occur during irradiation are caused by the accumulation of point defects in the structure with the subsequent formation of cluster defects and disordering regions, which contain a large number of stresses and distortions. In the case where the concentration of structural distortions is sufficiently high, peeling and partial delamination processes can be initiated in the surface layer, which leads to a sharp deterioration of not only structural properties, but also mechanical and heat-conducting, which leads to a decrease in the life of materials and its destruction [26, 27]. The use of ceramic materials can significantly increase the service life, due to

the high degree of resistance to structural changes that occur during irradiation. Moreover, despite a large number of works on this topic [8-19], interest in studying the processes of radiation damage to surface layers, as well as the effect of irradiation on the mechanical properties and wear resistance of ceramics, is still relevant and requires more and more attention to itself. Among the variety of ceramic materials, silicon carbide and its various structural modifications are considered the most promising, the interest in which is due to structural and mechanical characteristics, as well as its wide range of applications in various industries and technics [28-30]. However, there are few works devoted to the study of mechanical changes in the surface layer as a result of irradiation, despite the huge interest in this topic. Based on the foregoing, the main purpose of this work is to study the influence of the degradation of the surface layer of SiC ceramics on the mechanical and strength properties as a result of the accumulation of defects during irradiation.

1. Experimental part

The study of mechanical properties, including wear resistance and strength depending on the radiation dose, was carried out on samples of commercial polycrystalline silicon carbide (SiC) ceramics with potential applications as the basis for structural materials for nuclear power.

The initial samples were irradiated with a DC-60 heavy ion accelerator with low-energy Xe^{22+} ions with an energy of 440 keV and irradiation fluences of 10^{14} , 5×10^{14} , 10^{15} ion/cm². The choice of radiation doses is due to the modeling of the effects of overlapping cascade defects resulting from elastic and inelastic collisions, the number of which for the selected doses varies from 100 to 1000 multiple overlaps. Figure 1 presents the results of modeling the irradiation effect using the Stopping and Range of Ions in Matter (SRIM) Pro 2013 program code, which clearly shows that in the case of collisions, a large number of secondary defects are observed that can create a branched defective structure.

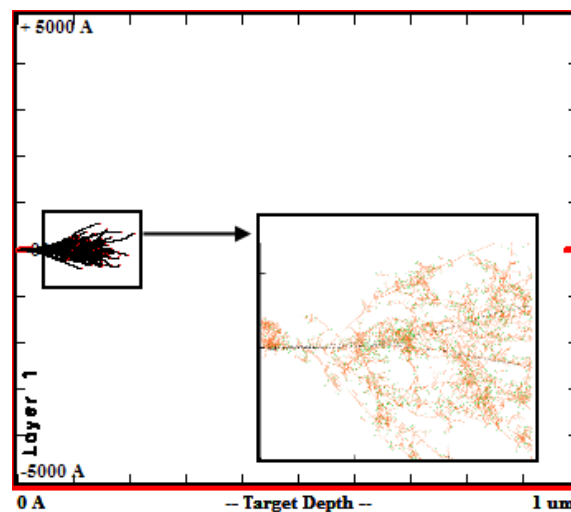


Fig.1. Xe^{22+} ion paths in SiC ceramics

The study of changes in morphological features before and after irradiation was carried out using scanning electron microscopy and atomic force microscopy.

Table 1. SRIM Outputs / Xenon in SiC ceramic

Sample	Projected range, nm	Vacancies /ion	dE/dx_{elect} , 10^3 keV/ μm	dE/dx_{nucl} , 10^3 keV/ μm
SiC irradiated Xe^{22+} , 440 keV	190 \pm 20	5300 \pm 100	1.077	2.821

Strength characteristics, as well as the dynamics of changes in the mechanical properties of nitride ceramics before and after irradiation, were determined using the depth hardness method, as well as tests for wear resistance at a load of 200 N, bending strength, and impact strength before and after irradiation [14]. Assessment of resistance to low-temperature degradation of the surface microstructure, as well as the formation of microcracks, was evaluated by aging tests, under accelerated degradation conditions, obtained by modeling the external effects of water vapor at a temperature of 150°C and a pressure of 2.2-2.3 atm. According to the proposed methodology, 1 hour of testing is 4-4.5 years of aging and degradation under normal conditions.

2. Results and Discussion

Figure 2 shows the results of changes in the morphology of the surface layer of carbide ceramics during irradiation with various fluences obtained using the atomic force microscopy method. According to the data presented, the ceramic surface in its initial state does not contain a large number of structural defects, such as hillocks, elevations or microcracks. The degree of roughness of the ceramic in the initial state does not exceed 3-5 nm. For irradiated samples, the formation of defective regions in the form of sphere-like hillocks is observed, as well as the presence of regions with pronounced elevation differences. In this case, with an increase in the irradiation fluence, the density of these inclusions and their sizes increase, which indicate the occurrence of disordered regions and structural distortions in the surface layer, which leads to partial extrusion of structural defects near grain boundaries with subsequent formation of hillocks. Also, the degradation of the surface layer at a fluence of 10^{15} ion/cm² can be due to exfoliation due to the high concentration of defects in the structure due to their accumulation.

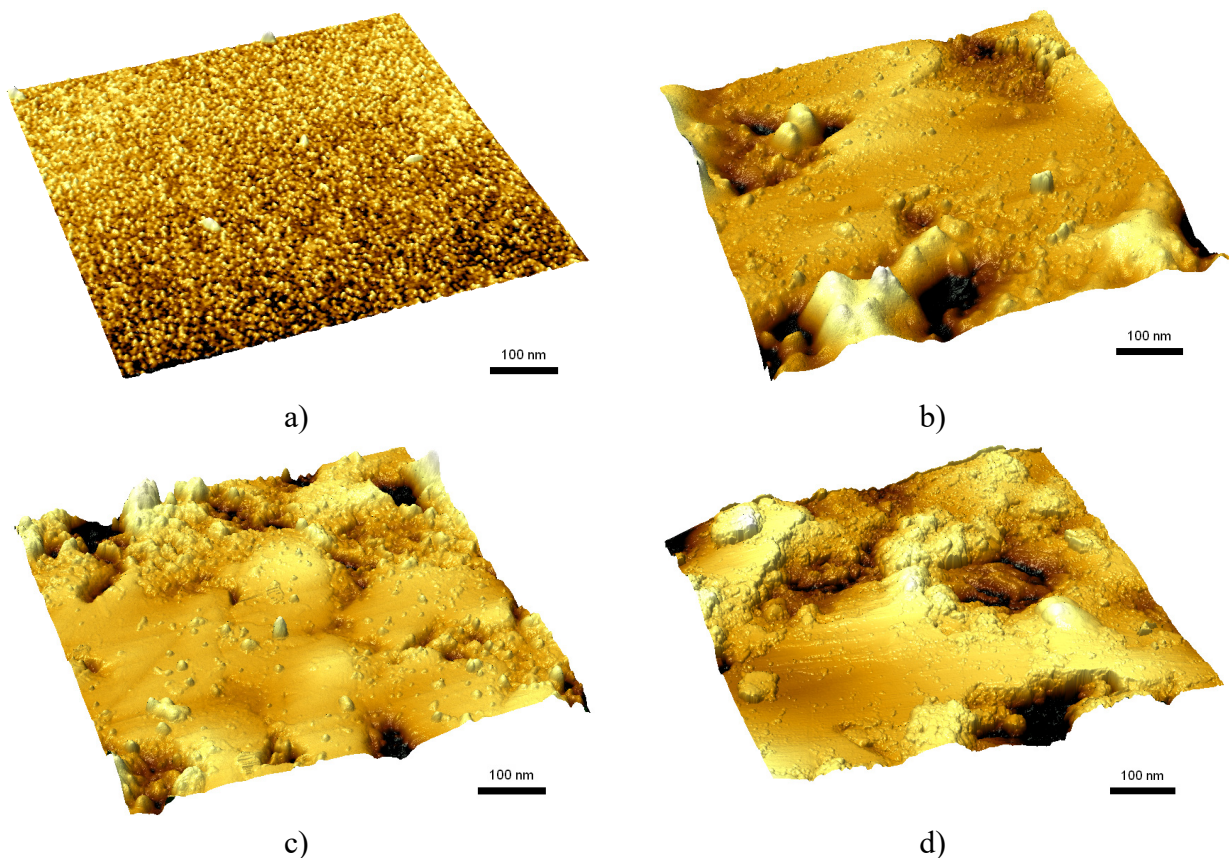


Fig.2. 3D atomic force microscopy (AFM) images of ceramics before and after irradiation:
a) Initial sample; b) 10^{14} ion/cm²; c) 5×10^{14} ion/cm²; d) 10^{15} ion/cm²

Partial degradation of the surface layer due to the accumulation of defects due to the effect of cascade overlaps can lead to a significant change in the mechanical properties and wear resistance of ceramics, since the formation of anisotropic defect regions near grain boundaries, as well as the partial destruction of crystalline and chemical bonds, followed by the formation of initially knocked out atoms, may lead to distortions and deformations in the structure. Table 2 presents the results of changes in strength characteristics, such as the value of bending strength and impact strength before and after irradiation, as well as a change in the dislocation density, porosity and density of ceramics during irradiation.

Table 2. Data of strength characteristics.

Parameter	Initial sample	10^{14} ion/cm ²	5×10^{14} ion/cm ²	10^{15} ion/cm ²
Three-point bending strength, MPa	178±4	173±4	168±5	143±9
Impact toughness, kJ/mm ²	1.35±0.13	1.31±0.11	1.24±0.12	1.12±0.09
Dislocation density, 10^{15} unit/cm ²	0.14	0.17	0.25	0.62
Porosity, %	0.606	0.656	0.945	2.351
Density, g/cm ³	3.196	3.165	3.121	3.014

According to the data presented, the greatest change in strength characteristics is observed at a fluence of 10^{15} ion/cm², which is characterized by the presence of a large number of defects as a result of overlapping cascades of secondary defects, which lead to a strong disordering of the structure with a sharp increase in the dislocation density by more than 4 times compared to the initial sample, and an increase in porous inclusions characterizing defective regions in the crystal lattice. An increase in porosity, as well as dislocation density, caused by grain crushing processes as a result of deformation initiated by irradiation, leads to a decrease in the density of ceramics. A decrease in density indicates a degradation of the ceramic structure during irradiation, and an increase in the dislocation density due to grain crushing can explain the degradation of the surface layer with an increase in the irradiation fluence.

Figure 3 presents the results of changes in the coefficient of dry friction depending on the dose of radiation and the number of tests.

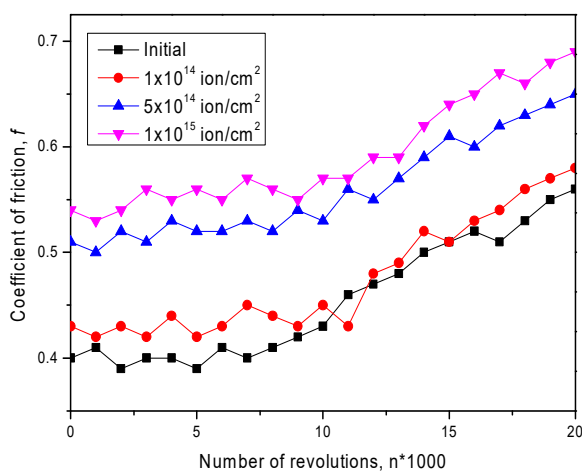


Fig.3. Dependence of the coefficient of dry friction on the dose.

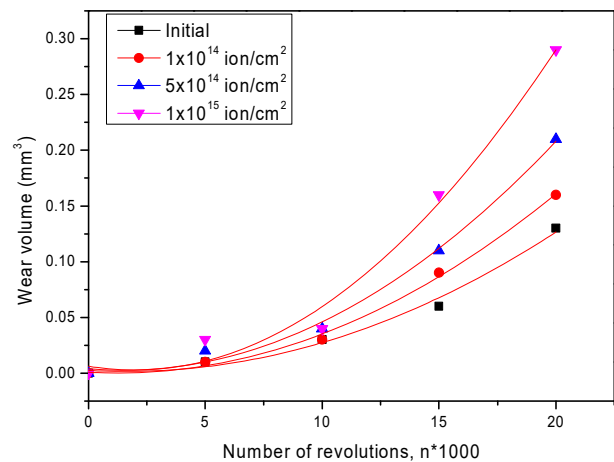


Fig.4. The dynamics of changes in volume loss during wear, depending on the dose.

As can be seen from the data presented, the dry friction coefficient for the initial sample is 0.4-0.41 and remains for 8000-10000 cycles, which indicates a high degree of wear resistance.

For irradiated samples with a dose of 10^{14} ion/cm², a slight increase in the coefficient at the initial stage is observed, while the nature of the change in the value during the tests is comparable with the initial samples. For samples irradiated with doses of 5×10^{14} and 10^{15} ion/cm², an increase in the dry friction coefficient is observed, which is due to a change in the surface morphology, as well as its partial degradation, which leads to deterioration of friction. It should be noted that the nature of the change in the value of wear resistance during testing is comparable with the original sample. Figure 4 shows the results of changes in the amount of wear during testing, according to which the largest changes in volume loss occur after 10,000 cycles. Moreover, for samples irradiated with a dose of 10^{15} ion/cm², the volume loss is maximum and exceeds losses in the initial state by 2.5-2.7 times.

Surface degradation due to irradiation is directly related to a decrease in the hardness of the surface layer. Figure 5 presents the results of a change in the microhardness along the depth of the sample in order to determine the maximum depth of the damaged layer. According to the data presented, for samples irradiated with a dose of 10^{14} ion/cm², the decrease in the microhardness is insignificant, with the depth of the damaged layer being 200-250 nm, while the ion path length is not more than 200 nm.

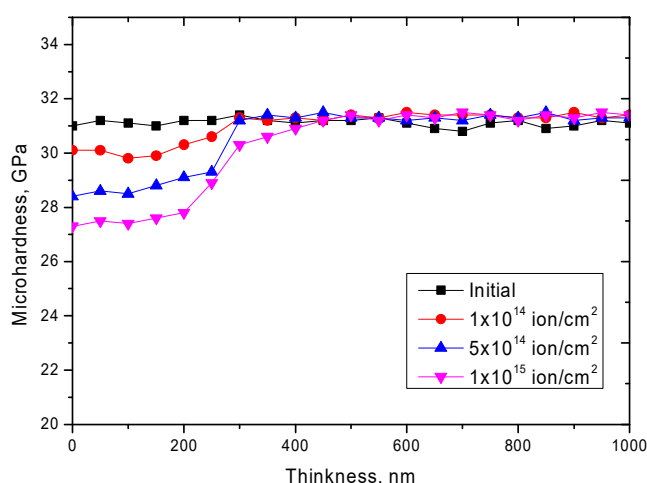


Fig.5. The dependence of changes in microhardness on the dose of radiation.

The increase in the depth of the damaged region is due to the cascading effects of the propagation of defects capable of penetrating to a depth exceeding the maximum mean free path of ions in the ceramic. Also, an increase in the depth of damage may be due to the fact that during irradiation a decrease in the density of ceramics is observed as a result of degradation and the formation of anisotropic porous inclusions, which leads to an increase in the mean free path of ions. In the case of an increase in the radiation dose, not only a decrease in the micro-hardness of the near-surface layer is observed, but also an increase in the depth of the damaged zone, which confirms the previously made assumption about the effect of changes in the density of ceramics on the mean free path of ions.

Figure 6 presents the results of a study of the resistance of ceramics to low-temperature degradation under accelerated aging processes, which are used to simulate temporary aging processes for a long time. As can be seen from the presented data (see Figure 6), for irradiated samples, in contrast to the initial sample, aging occurs linearly, while for the initial samples during the first 10 hours the crack resistance is almost unchanged, which indicates a high resistance of ceramics to cracking. Moreover, according to the data presented in the diagram of Figure 7, the decrease in crack resistance as a result of irradiation does not exceed 2-3% of the initial value,

which indicates a high resistance to degradation and crack formation. Moreover, both in the case of the initial sample and in the case of irradiated samples, the decrease in crack resistance after 30 hours of life tests does not exceed 8-10%, which confirms the high resistance to temporary degradation of ceramics.

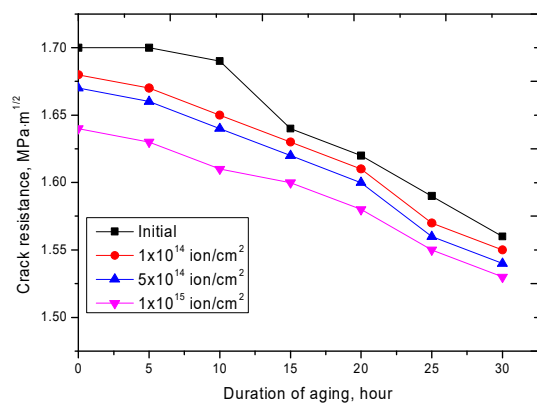


Fig. 6. A graph of the dependence of the crack resistance on the aging time of the samples before and after irradiation.

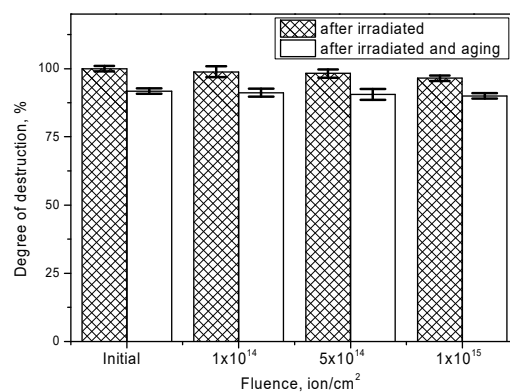


Fig. 7. Diagram of changes in the degree of destruction of ceramics before and after tests.

The data obtained are in good agreement with the previously presented studies of the radiation resistance of ceramics and thin-film coatings [31-34]. For example, the results of mechanical resistance to irradiation have a good correlation with the results of resistance to low-energy irradiation with He ions of thin-film structures based on ZrSiN [31], where it was shown that irradiation with high doses can lead to partial embrittlement and degradation of the surface layer. However, unlike oxide ceramics based on zirconium oxide (ZrO₂) [33] in which phase transformation processes are observed upon irradiation with low-energy Kr ions, no such effects were observed in the case of the studied ceramics.

In total, the presented results of changes in the strength of carbide ceramics as a result of irradiation with Xe²²⁺ ions with doses of 10¹⁴, 5x10¹⁴, 10¹⁵ ion/cm² can be further used not only from a fundamental point of view, as an addition to the theory of radiation damage to ceramics, but also from the practical side, as the results radiation resistance and modeling the effects of ionizing radiation on structural materials.

Conclusion

The paper presents the results of a study of the mechanical strength, wear and crack resistance of SiC-based ceramics before and after irradiation with heavy Xe²²⁺ ions with an energy of 440 keV and irradiation fluences of 10¹⁴, 5x10¹⁴, 10¹⁵ ion/cm². The choice of radiation doses is due to the modeling of the effects of overlapping cascade defects resulting from elastic and inelastic collisions, the number of which for the selected doses varies from 100 to 1000 multiple overlaps.

According to changes in mechanical properties, the largest change in strength characteristics is observed at a fluence of 10¹⁵ ion/cm², which is characterized by the presence of a large number of defects as a result of overlapping cascades of secondary defects, which lead to a strong disordering of the structure with a sharp increase in the dislocation density by more than 4 times compared to the initial sample, and an increase in porous inclusions.

During the study of the microhardness of ceramics before and after irradiation, it was found that in the case of irradiated ceramics, the damage depth exceeds the estimated ion path by 20-30%, depending on the irradiation fluence. The increase in the depth of the damaged area is due to a decrease in density as a result of the cascade effects of the propagation of defects that can penetrate to a depth exceeding the maximum mean free path of ions in the ceramic.

It was found that both in the case of the initial sample and in the case of irradiated samples, the decrease in crack resistance after 30 hours of accelerated degradation life tests simulating the aging effect does not exceed 8-10%, which confirms the high resistance to temporary degradation of ceramics. The obtained results will make a significant contribution to the development of the modern theory of radiation damage in ceramic materials applicable in nuclear energy.

REFERENCES

- 1 Guérin Y., Was G. S., Zinkle S. J. Materials challenges for advanced nuclear energy systems. *Mrs Bulletin*. 2009, Vol. 34, No.1, pp. 10 – 19.
- 2 Gladkikh T., et al. Changes in optical and structural properties of AlN after irradiation with C²⁺ ions of 40 keV. *Vacuum*. 2019, Vol. 161, pp. 103 – 110.
- 3 Kaliekperov M., et al. The study of changes in structural properties of Cu films under ionizing radiation. *Materials Research Express*. 2018, Vol. 5, No.5, pp. 055008.
- 4 Chronos A. et al. Nuclear waste form materials: Atomistic simulation case studies. *Journal of nuclear materials*. 2013, Vol. 441, No. 1 – 3, pp. 29 – 39.
- 5 Ryskulov A.E., et al. The effect of Ni¹²⁺ heavy ion irradiation on the optical and structural properties of BeO ceramics. *Ceramics International*. 2020, Vol. 46, No. 4, pp. 4065 – 4070.
- 6 Zdorovets M. V., Kozlovskiy A. L. Study of the stability of the structural properties of CeO₂ microparticles to helium irradiation. *Surface and Coatings Technology*. 2020, Vol. 383, pp. 125286.
- 7 Kozlovskiy A., et al. Structure and corrosion properties of thin TiO₂ films obtained by magnetron sputtering. *Vacuum*. 2019, Vol. 164, pp. 224 – 232.
- 8 Raj B., Mudali U. K. Materials development and corrosion problems in nuclear fuel reprocessing plants. *Progress in Nuclear Energy*. 2006, Vol. 48, No. 4, pp. 283 – 313.
- 9 Dukenbayev K., et al. Investigation of radiation resistance of AlN ceramics. *Vacuum*. 2019, Vol. 159, pp. 144 – 151.
- 10 Kozlovskiy A. L., et al. Radiation resistance of thin TiN films as a result of irradiation with low-energy Kr¹⁴⁺ ions. *Ceramics International*. 2020, Vol. 46, No. 6, pp. 7970 – 7976.
- 11 Kozlovskiy A., et al. Optical and structural properties of AlN ceramics irradiated with heavy ions. *Optical Materials*. 2019, Vol. 91, pp. 130 – 137.
- 12 Féron D. Overview of nuclear materials and nuclear corrosion science and engineering. *Nuclear Corrosion Science and Engineering*. Woodhead Publishing, 2012, pp. 31 – 56.
- 13 Zdorovets M. V., Kurlov A. S., Kozlovskiy A. L. Radiation defects upon irradiation with Kr¹⁴⁺ ions of TaC_{0.81} ceramics. *Surface and Coatings Technology*. 2020, Vol. 386, pp.125499.
- 14 Tinishbaeva K., et al. Implantation of low-energy Ni¹²⁺ ions to change structural and strength characteristics of ceramics based on SiC. *Journal of Materials Science: Materials in Electronics*. 2020, Vol.31, No. 3, pp. 2246 – 2256.
- 15 Ferraris M., et al. Joining of SiC-based materials for nuclear energy applications. *Journal of nuclear materials*. 2011, Vol. 417, No. 1-3, pp. 379 – 382.
- 16 Le Brun C. Molten salts and nuclear energy production. *Journal of nuclear materials*. 2007, Vol.360, No. 1, pp. 1 – 5.
- 17 Kozlovskiy A., et al. Investigation of the influence of irradiation with Fe⁷⁺ ions on structural properties of AlN ceramics. *Materials Research Express*. 2018, Vol. 5, No. 6, pp. 065502.
- 18 Singh V.P., Badiger N. M. Gamma ray and neutron shielding properties of some alloy materials. *Annals of Nuclear Energy*. 2014, Vol. 64, pp. 301 – 310.
- 19 Zinkle S.J., Hodgson E. R. Radiation-induced changes in the physical properties of ceramic materials. *Journal of nuclear materials*. 1992, Vol. 191, pp. 58 – 66.
- 20 Zdorovets M.V., et al. Helium swelling in WO₃ microcomposites. *Ceramics International*. 2020, Vol.46(8A), pp. 10521 . 10529.
- 21 Wray P. Materials for nuclear energy in the post-fukushima era. *American Ceramics Society Bulletin*. 2011, Vol. 90, No. 6, pp. 24 – 28.
- 22 Zdorovets M., et al. Defect formation in AlN after irradiation with He²⁺ ions. *Ceramics International*. 2019, Vol. 45, No. 7, pp. 8130 – 8137.
- 23 Weber W.J., et al. Materials science of high-level nuclear waste immobilization. *MRS Bulletin*. 2009, Vol. 34, No. 1, pp. 46 – 53.

-
- 24 Kozlovskiy A., et al. Influence of He-ion irradiation of ceramic AlN. *Vacuum*. 2019, Vol.163, pp. 45 – 51.
- 25 Trukhanov A.V., et al. Control of structural parameters and thermal conductivity of BeO ceramics using heavy ion irradiation and post-radiation annealing. *Ceramics International*. 2019, Vol. 45, No.12, pp.15412 – 15416.
- 26 Katoh Y., et al. Radiation effects in SiC for nuclear structural applications. *Current Opinion in Solid State and Materials Science*. 2012, Vol. 16, No.3, pp. 143 – 152.
- 27 Zhang Z. H. et al. Processing and characterization of fine-grained monolithic SiC ceramic synthesized by spark plasma sintering. *Materials Science and Engineering: A*. 2010, Vol. 527, No. 7 – 8, pp.2099 – 2103.
- 28 Li M. et al. The critical issues of SiC materials for future nuclear systems. *Scripta Materialia*. 2018, Vol. 143, pp. 149 – 153.
- 29 Katoh Y. et al. SiC/SiC composites through transient eutectic-phase route for fusion applications. *Journal of Nuclear Materials*. 2004, Vol. 329, pp. 587 – 591.
- 30 Naslain R. R. SiC-matrix composites: Nonbrittle ceramics for thermo-structural application. *International Journal of Applied Ceramic Technology*. 2005, Vol. 2, No. 2, pp. 75 – 84.
- 31 Uglov V. V., et al. Surface blistering in ZrSiN nanocomposite films irradiated with He ions. *Surface and Coatings Technology*. 2020, p. 125654.
- 32 Uglov V. V., et al. Size effect in AlN/SiN multilayered films irradiated with helium and argon ions. *Nuclear Instruments and Methods in Physics Research Section B: Beam Interactions with Materials and Atoms*, 2018, Vol. 435, pp. 228-235.
- 33 Chauhan V., Kumar R. Phase transformation and modifications in high-k ZrO₂ nanocrystalline thin films by low energy Kr⁵⁺ ion beam irradiation. *Materials Chemistry and Physics*, 2020, Vol. 240, p. 122127.
- 34 Kumar V., Kumar R. Low energy Kr⁵⁺ ion beam engineering in the optical, structural, surface morphological and electrical properties of RF sputtered TiO₂ thin films. *Optical Materials*, 2019, Vol.91, pp. 455-469.

DOI 10.31489/2020No1/54-58

UDC 530.1; 538.97; 539.216.1; 539.216.2; 539.23

ELECTRICAL PROPERTIES OF SILICON NANOWIRES UNDER AMMONIA ADSORPTION CONDITIONS

Dikhanbayev K.K.¹, Bondarev A.I.², Ikramova S.B.¹, Shabdan E.¹

¹ National Nanotechnology Open Laboratory, Almaty, Kazakhstan, dkadyrian@mail.ru

² al-Farabi Kazakh National University, Almaty, Kazakhstan

When monitoring the environment, measurements of the concentration and composition of the gas phase of various substances are of great importance. To solve such problems, resistive-type semiconductor sensors are of interest. The proposed sensors based on silicon nanowires have several advantages: high sensitivity and possibility to work at room temperature. This in turn simplifies the design and reduces the cost of the sensors. All this indicates the relevance of the investigated gas sensor.

Keywords: silicon, nanowires, electrical properties, metal-assisted chemical etching, current-voltage characteristics, sensor.

Introduction

This work aims to create a new type of gas-sensitive material based on hetero-structured the p-Si/SiNWs (p type Silicon/Silicon nanowires). Finding new materials for gas sensors is particularly relevant for monitoring environment, in medicine, automotive industry and subways etc. [1-2]. To solve the various problems of determining the composition of gas phase, the resistive-type semiconductor gas sensor has attracted great interest [3]. The working principle of such sensors is based on the effect of changing the electrical conductivity of semiconductor materials in the presence of trace amounts of oxidizing gases or reducing agents. Silicon nanowire-based sensors have the following advantages: high sensitivity, compactness, low cost, and the ability to integrate into modern information systems.

In the conventional resistive type gas sensors, the gas sensitivity mechanism includes surface chemisorption process with the change of the carrier concentration in the volume of semiconductor. Overall changes in the electrical conductivity of semiconductor materials (for example, the use of tin dioxide [4] with conductivity and light transmission) can form a sensory response. It is promising to create local interfaces between materials such as silicon nanostructures with various electronic properties [5-6]. In such a system, the chemical absorption process will determine the energy barrier height of the carriers at the nanostructure boundary which will lead to gas sensitivity. The literature [7] contains data on the gas-sensitive characteristics of metal-semiconductor heterojunctions (heterostructures), and its mechanism of action is related to changes in the Schottky barrier height at the hetero-interface. For such materials, high sensitivity value for hydrogen is obtained.

The aim of this work is to study the characteristics of changes in the chemical composition on the resistive properties and surface structures of silicon nanowires and sensitivity to ammonia, as well as the photosensitivity of silicon nanowires in the process of adsorption and in the absence of ammonia.

1. Experimental methods

Initially, p-type single crystal silicon was used, which was doped with boron, and the resistivity was 10 Ohm · cm. Silicon nanowires (SiNWs) layer to the p-layer is mainly obtained by metal-

assisted chemical etching (MACE). In this method an HF: H₂O₂ electrolytes used, initially depositing a silver or silver coating on the silicon surface, and then subsequently etching it with metal particles. Etching is carried out in the absence of power requiring very little time and is simple to manufacture. The mechanism of this wet etching of silicon is very different from the conventional electrochemical anodization in porous silicon [8-9]. Finally, strips of component with a SiNWs/p-Si structure were manufactured with a size of (1x10) mm².

Nanostructured silicon nanowires using a transmission electron microscope examination is shown in Figure 1. Analysis of the results of silicon nanowires on SEM microstructures showed that the half-width of nanowires is 20-50 nm, but the presence of ammonia on the surface significantly affects the surface morphology of silicon nanowires, the roughness is about 200 nm. Furthermore, the roughness height of the plate (in the inset of Figure 2) was about 50 nm. The nanostructured sample of the gas sensor prepared in this way was tested for the conductivity of the porous structure based on the presence of steam in the atmosphere of ammonia. The samples were tested in a specially designed light-protective box measuring 10×10×10 cm³. The design of the sensor structure with SiNWs/p-Si is shown in Figure 2.

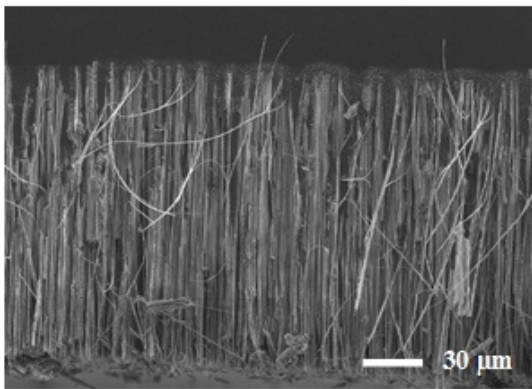


Fig. 1. SEM image of a cross section of a silicon nanowire formed by chemical wet etching.

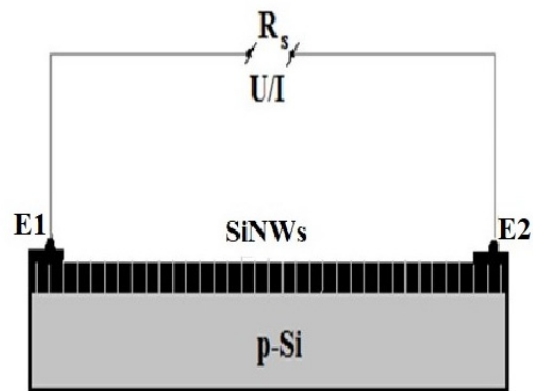


Fig. 2. Sensor Design.

4. Discussion of results

The changes of overall resistance R_s during gas adsorption on the surface of silicon nanowires through electrodes E1 and E2 was observed with the ohmmeter, the I/V characteristics of the silicon nanowires were measured on an NI ELVIS II⁺ (1000 Ms/S Oscilloscope) characterizer. I/V characteristics are shown in Figure 3 in the presence of ammonia vapors with illumination and without ammonia and no illumination. The volume resistance measured via contacts E1 and E2 is 24 kOhm. It can be seen that in the presence of ammonia vapors, the reverse currents of the left branch of the I/V characteristics increase; when illuminated with light, the forward bias with ammonia (blue line) increases significantly compared to nanowires without ammonia. However, the highest volume resistance of the SiNWs sample is about 36 kOhm with the introduction of ammonia vapor, the reverse branch of the I/V characteristic showed a high sensitivity to ammonia impurities. The increases in 6 times in sensitivity is shown in Figure 4. An increase in the SiNWs bulk resistance to 45 kOhm leads to an increase in the reverse and forward bias of the electrical characteristic; for a pure SiNWs (green curve), a forward bias expands the space charge region to 5 V, then increases, similar to the rectifying property of a conventional diode. When exposed to ammonia, the sensitivity of forward and reverse currents increases significantly, however, with the advent of forward bias, the space charge region appears and then increases linearly. Exposure to light dramatically increases reverse and forward bias currents by a factor of 5 compared to the original SiNWs without ammonia. Therefore, the measurement of the sensitivity of the SiNWs structure to the gas vapors presence on the surface layer was determined by the change in resistance

caused by the charge carrier dispersion in the darkness and under LED lighting as a function of time, as well as due to an increase in the reverse and forward bias currents of the I/V characteristics.

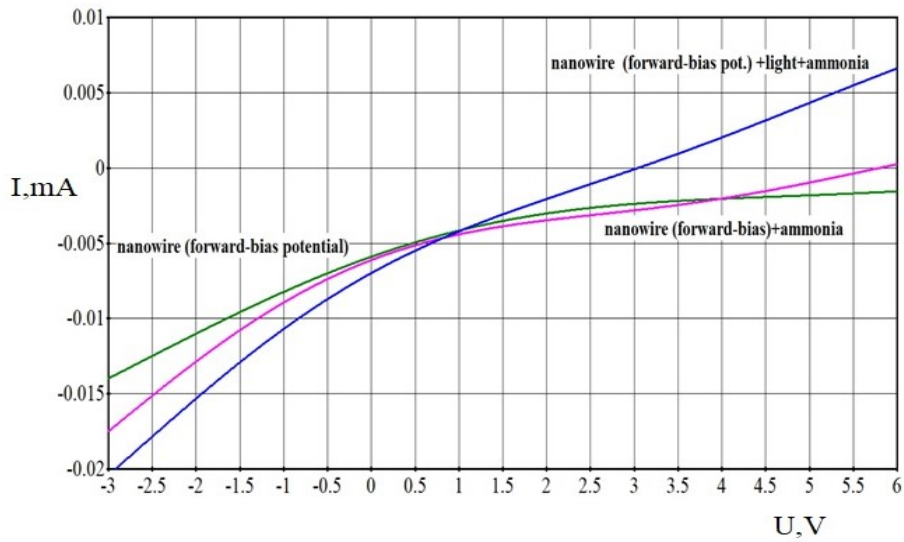


Fig. 3. Electrical characteristics of silicon nanowires

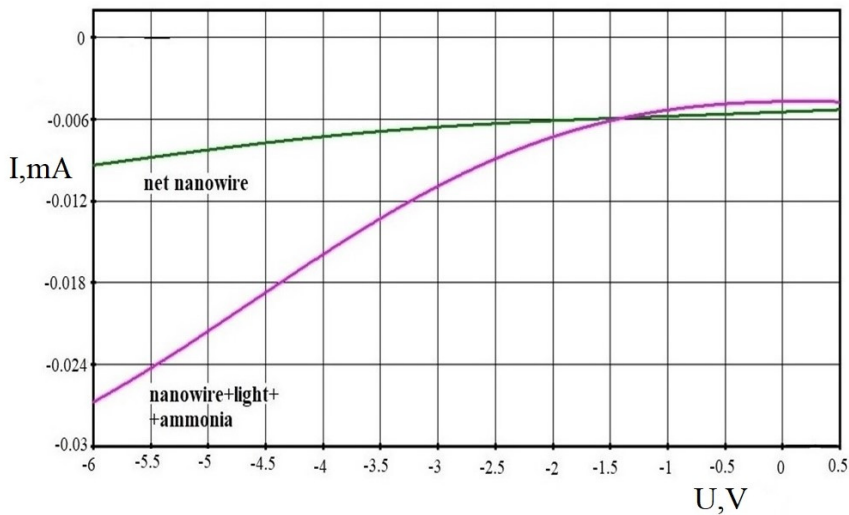


Fig. 4. I-V reverse branch of SiNWs

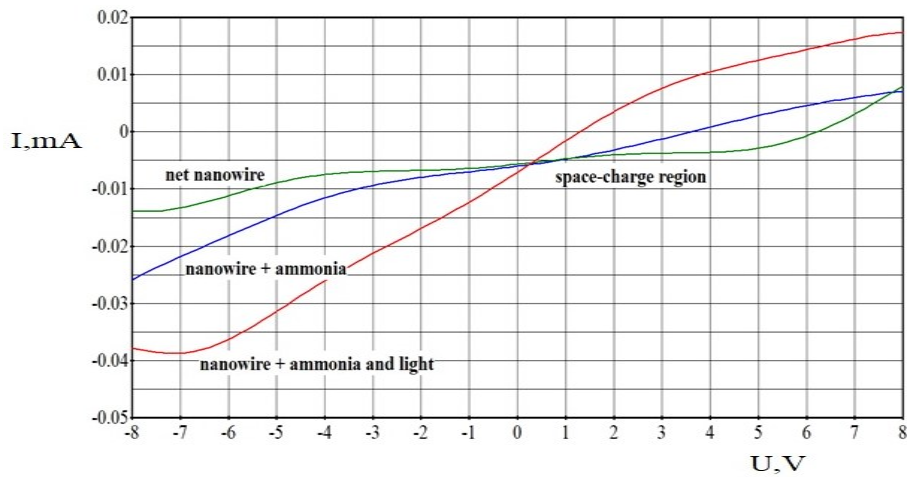


Fig.5. I-V reverse branch of SiNWs.

Parameters used to change ammonia vapor sensitivity without and with LED lighting are shown in Figure 6. The change in silicon nanowire resistance in the presence of ammonia vapor in the atmosphere with and without illumination depending on time is shown in Figure 6. After entering ammonia vapor, the measuring box was opened after 5 minutes and the concentration of ammonia vapor slowly was decreased due to vapor diffusion into the surrounding atmosphere.

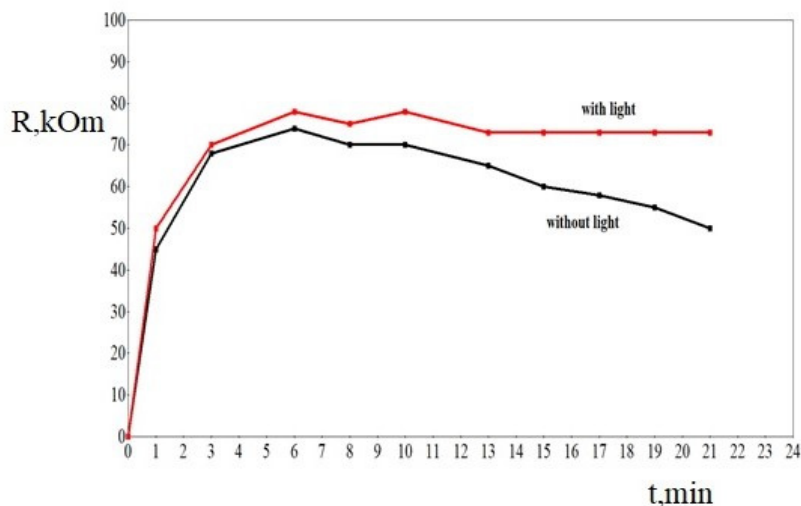


Fig.6. Changes in the resistance of the SiNWs in the presence of ammonia vapor in the atmosphere without/with LED lighting depending on time

A significant change in the resistance of the spreading layer was detected in an atmosphere of ammonia vapor. Furthermore, when lighting was observed, the resistance was observed to recover very slowly from the original value (without ammonia). In contrast, the recovery is much faster in the absence of lighting, which indicates a higher sensitivity to low concentrations of ammonia in the atmosphere when illuminated. It is important to note that although the SiNWs/p-Si structure is an isotype p-type transition; its photoelectric properties are not only very sensitive to the presence of ammonia, but also very sensitive when illuminating the surface of silicon nanowires.

In addition, the chemical etching of the silicon surface of the metal-assisted sensitive layer will lead to an increase in effective surface area, an increase in surface state density, and a formation of deep energy level in the semiconductor band gap caused by atoms of the electrode material and dislocations, which together will allow us to vary the sensitivity and selectivity of the sensory gases.

We have shown that the gas sensitivity and photosensitivity of silicon nanoparticles can be controlled not only by the direct branch of the I/V characteristics, but also by its reverse branch of the curve. We found that this dependence was repeated during the measurement of the I/V characteristics of the samples over five measurements; however, the space charge region at the interface between the SiNWs and crystalline silicon changed with increasing bulk resistance of silicon nanoparticles.

The accuracy of the measurement results of the I/V characteristic depends on the porosity of silicon nanowires and the influence of the environment on the structure of nanoscale filaments aging with storage time in the air, as a result of oxidation, the crystallite size decreases due to the quantum-size effect. However, this effect does not affect the formation of the I/V characteristics.

The novelty of the work is that, for the first time, silicon nanowires obtained by wet chemical etching of the surface of crystalline silicon were used as a sensor device. It was shown for the first time that gas and photosensitivity can be determined from the deviation of the branch of the reverse currents of the I/V characteristic. In addition, from the I/V characteristics, with an increase in the volume resistance of nanostructures, the space charge region (from the straight branch) expands, current rectification occurs at high voltages (for example, in Figure 3).

Conclusion

Earlier, the authors studied sensors based on porous silicon [10-11], and other coatings of the SnO₂ [12-13] and ZnO [14] type, etc. We presented samples of silicon nanowires (SiNWs) and examined sensors of a gas-sensitive element in which nanowires were surrounded by silicon and silver oxides, since on the surface nanowires are passivated by silver nitride. This fact also indicates the photoelectric properties of the sensor device. Silicon nanowires structure has been formed by metal-assisted chemical etching with size of 20 - 50 nm. The shape of the silicon nanowires shown the different diameters of silicon rod nanowires which measured by the SEM.

The forms of silicon nanowires measured in a transmission electron microscope are silicon rod nanowires with different diameters. The effect of ammonia vapor on the electrical properties of the silicon nanowire is shown for the different layer resistance of nanowires. The results showed that the presence of ammonia in SiNWs significantly increases the sensitivity of the reverse and forward branching of features without the need to illuminate the nanowire surface. In particular, the sensitivity to ammonia increased 6 times when illuminated by LED lights.

It was found that with an increase in the etching time for silicon nanowires, the space charge volume in the SiNWs increases which determines the threshold voltage at which the direct voltage of the direct branch of the electrical characteristic increases, and this threshold is 5 V. The relative change in the layer resistance as a function of the time of exposure to ammonia vapor was measured, and when ammonia vapor was removed in the darkness and with light. It is shown that when ammonia vapors are removed without illuminating the sensitivity, the SiNWs slowly decreases to 50% during 22 minutes.

Acknowledgements

This research is supported by Ministry of Education and Science of the Kazakhstan Republic (Grant number is AP05132854).

REFERENCES

- 1 Buturlin A.I. et al. Gas-sensitive sensors based on metal oxide semiconductors. *Foreign Electronic Technology*, 1983, No.10, pp. 3 - 39. [in Russian]
- 2 Dey A. Semiconductor metal oxide gas sensors: A review. *Materials Science and Engineering: B*, 2018, Vol. 229, pp. 206–217.
- 3 Fau P., Sauvan M., Trautweiler S., et al. Nanosized tin oxide sensitive layer on a silicon platform for domestic gas application. *Sensors and Actuators*. 2001, Vol.78, pp. 83–88.
- 4 Barsan N., Weimar U, Understanding the fundamental principles of metal oxide based gas sensors; the example of CO sensing with SnO₂ sensors in the presence of humidity. *Journal of Physics: Condensed Matter*. 2003, Vol. 15, No. 20, pp. 813 – 839.
- 5 Vashpanov Yu.O., Smyntyna V.A. *The adsorption sensitivity of semiconductors*. Odessa, 2005, 216p.
- 6 Oleksenko L.P., et al. Study of influence of palladium additives in nanosized tin dioxide on sensitivity of adsorption semiconductor sensors to hydrogen. *Sensors and Actuators B: Chemical*. 2014, Vol. 196, pp. 298–305.
- 7 Sechenov D.A., Zakharov A.G., Nabokov G.M. Electrophysical properties of MIS structures formed on silicon with a high dislocation density. *News of higher educational institutions of the Ministry of Higher and Secondary Special Education of the USSR. Physics*. 1977, No. 9, pp. 137 – 143. [in Russian]
- 8 Maccagnani P., Dory L., Negrini P. Thermo-Insulated Microstructures Based on Thick Porous Silicon Membranes. *Proc. of the 13th European Conf. on Solid-State Transducers*. Netherlands, 199, pp. 817 – 820.
- 9 Simon I., Barsan N., Bauer M., Weimar U. Micromachined metal oxide gas sensors: opportunities to improve sensor performance. *Sensors and Actuators B: Chemical*. 2001. Vol.73, pp. 1–26.
- 10 Kayahan E. Porous silicon based CO₂ sensors with high sensitivity. *Optik*. 2018. Vol. 164, pp. 271–276.
- 11 Baratto C., et al. Multiparametric Porous Silicon Sensors. *Sensors*. 2002. Vol. 2, pp. 121-126.
- 12 Phan Hong P., Chu Manh H., Van Toan N., et al. One-step fabrication of SnO₂ porous nanofiber gas sensors for sub-ppm H₂S detection. *Sensors and Actuators A: Physical*. 2019. Vol. 303, pp. 111722.
- 13 Wu Q.H., Li J., Sun S.G. Nano SnO₂ gas sensors. *Current Nanoscience*. 2010. No. 5, Vol. 6, pp. 525-538.
- 14 Dwiputra M.A., Fadhila F., et al. The Enhanced Performance of Capacitive-type Humidity Sensors Based on Heterostructure ZnO Nanorods/WS₂ Nanosheets. *Sensors and Actuators B: Chemical*. Vol. 310, pp. 127810.

DOI 10.31489/2020No1/59-64

UDC 62-1/-9

IMPACT OF THE DETONATION GAS SPRAYING MODE ON THE PHASE COMPOSITION AND ADHESIONAL STRENGTH OF Ti-Si-C COATINGS

Rakhadilov B.K.¹, Buitkenov D.B.^{1*}, Wieleba W.², Kylyshkanov M.K.¹, Yerbolatuly D.¹¹ S. Amanzholov East Kazakhstan State University, Ust-Kamenogorsk, Kazakhstan, buitkenovd@mail.ru² Wroclaw University of Science and Technology, Wroclaw, Poland

The work considers the research results of the phase composition and strength characteristics of detonation coatings based on Ti-C-Si, which obtained for different values of the volume of filling the detonation barrel with an explosive acetylene-oxygen mixture. It was determined that with an increase in the volume of filling the detonation barrel with an explosive mixture up to 70% of the coating are mainly consist of TiC phases. Since Ti_3SiC_2 powder heated to high temperatures partially decomposes into TiC as a result of high-speed shock interaction. The results of X-ray phase analysis showed that a low degree of decomposition of Ti_3SiC_2 can be achieved under filling the barrel with an explosive mixture of 50% and 60% and the coatings mainly consist of Ti_3SiC_2 phases with a low TiC content. This is due to the fact that the heating temperature of the sprayed powder increases with increasing in the degree of filling of the detonation barrel with an explosive acetylene-oxygen mixture. It was determined that an increase in the volume content of the TiC phase in the coating composition leads to a decrease in the hardness of the Ti-C-Si coating. The results of the research of the adhesive strength of coatings showed that the effect of the volume of filling the detonation barrel with an explosive mixture on the adhesive strength is negligible. Moreover, all coatings based on Ti-C-Si, obtained by the detonation method, showed good adhesive strength.

Keywords: detonation spraying, titanium carbosilicide, steel, phase, adhesion.

Introduction

The creation of wear-resistant coatings on rubbing surfaces is one of the most effective and economical time-tested areas for increasing the durability of parts operating in conditions of contact wear. Detonation spraying [1,2] and HVOF-spraying [3] among the coating methods have obvious superiority compared to plasma spraying and other spraying methods due to the high speed of flight of particles and lower operating temperature. Detonation spraying of coatings from powders is based on the use of the energy of the explosion of a fuel-oxygen mixture and is known as a promising method for producing coatings from various materials with good adhesion [4]. A higher particle velocity allows a higher density and adhesion strength of the detonation coating. A key advantage of the detonation spraying method is the ability to precisely control the amount of explosive gas mixture used for each shot of detonation gun, which allows you to change the degree of thermal and chemical effect of detonation products on the particles of the sprayed powder [5,6]. Chemical interactions can occur between the individual phases of the composite particles depending on the composition of the acetylene-oxygen explosive mixture, on the O_2/C_2H_2 ratio, and on the nature of the gas carrier [7,8]. Therefore, recently, it has become increasingly interesting to obtain detonation coatings from binary and ternary phases belonging to the Ti-Si-C system. Nanocomposites based on Ti-Si-C are especially relevant, since it is shown that these nanocomposites combine known mechanical strength and low friction coefficient with high conductivity and low contact resistance [9-11]. The question of how to deposit coatings with high adhesive strength based on Ti_3SiC_2 is still open by considering their tribological application.

In connection with the foregoing, the aim of this work is to study the impact of detonation gas spraying on the phase composition, adhesive strength and hardness of Ti-Si-C coatings.

1. Materials and methods of research

Ti₃SiC₂ coatings were obtained by the method of detonation spraying on the surface of U9 steel. The chemical composition of the powder: Ti - 74 wt.%; SiC - 20 wt.%; C - 6.0 wt.%. The particle size of the powder is up to 40 μm. U9 steel was sandblasted in order to improve the adhesion strength of the coatings before applying the coatings. The distance between the treated surface of the sample and the detonation barrel was 500 mm. The diameter of the straight barrel was 20 mm.

The CCDS2000 detonation complex was used to obtain coatings, which has a system of electromagnetic gas valves that regulate the supply of fuel and oxygen, as well as control the purge of the system (Figure 1). An acetylene-oxygen mixture was used as a combustible gas, which is the most popular fuel for detonation spraying of powder materials. Spraying was carried out at a ratio of acetylene-oxygen mixture O₂/C₂H₂ = 1.856. The volume of filling the barrel with an acetylene-oxygen mixture was varied from 50% to 70%. Nitrogen was used as a carrier gas.

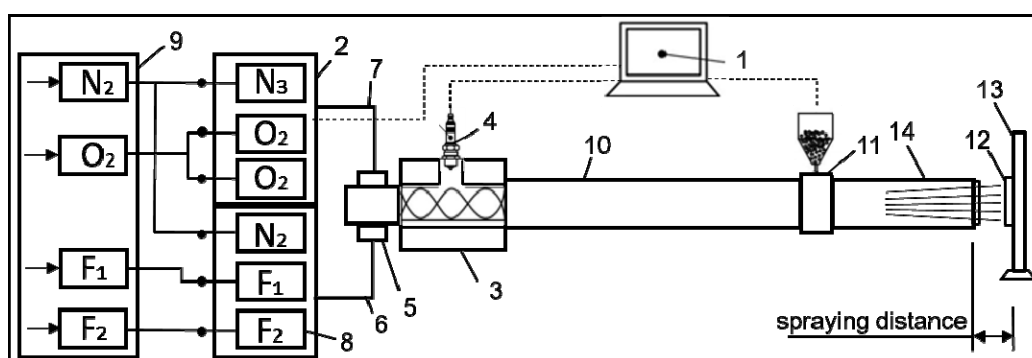


Fig.1. Principled schematic diagram of the CCDS2000 detonation complex:

- 1 - control computer, 2 - gas distributor, 3 - mixing-ignition chamber, 4 - spark plug, 5 - barrel valve, 6 - fuel line, 7 - oxygen line, 8 - gas valves, 9 - gas supply unit, 10 - indicated part of the barrel, 11 - powder dispenser, 12 - workpiece; 13 - manipulator, 14 - the muzzle of the barrel

The research of phase composition of the samples was studied by X-ray diffraction analysis on X'PertPro diffractometer by using CuK α -radiation[12]. The survey was carried out in the following modes: tube voltage $U = 40$ kV; tube current $I = 20$ mA; exposure time 1s; survey step 0.02° . The scratch tester CSEM MicroScratchTester was used to study the adhesion characteristics of coatings by the "scratch" method. Scratch testing was carried out at a maximum load of 30 N, the rate of change of normal loading on the sample - 29.99 N/min, the indenter displacement rate - 9.63 mm / min, the scratch length - 10 mm, and the tip curvature radius - 100 μm.

Nanoindentation is a universal method for identifying patterns of the mechanical behavior of materials in the surface layers of coatings. The mechanical properties (Young's modulus, hardness) were investigated using a NanoScan-4D Compact compact nanohardness meter for the resulting coatings. Experiments were carried out at a load of 200 mN. The load – unload rate was 3mN / min. The dependence of the penetration depth on the applied force at the stages of loading and unloading was determined by the Oliver – Farr method [13].

2. Research results and its discussion

Figure 2 presents the diffraction patterns of Ti₃SiC₂ powder and Ti-Si-C system coatings obtained with a barrel filling volume of 50% to 70%. The results of x-ray phase analysis of the powder showed that the powder consists of the phases Ti₃SiC₂ and TiC. A decrease in the intensity of Ti₃SiC₂ diffraction lines and an increase in TiC intensity are observed in the diffraction patterns of Ti-Si-C coatings, which indicates partial decomposition of the Ti-Si-C system and is consistent with the data [14]. A decrease in the intensity of diffraction lines in the Ti-Si-C system is observed

after detonation sputtering due to deintercalation of silicon from Ti- Si-C lattice layers [15-18], since silicon planes have weak bonds with Ti-C planes. This fact can be explained that the Ti-Si-C system lost a certain amount of silicon due to its high “volatility” as a result of detonation deposition [19]. The results of X-ray phase analysis showed that a low degree of decomposition of Ti_3SiC_2 can be achieved with a 50% and 60% filling volume of the barrel of the explosive mixture. A decrease in the intensity of diffraction peaks of Ti_3SiC_2 With an increase in the volume of filling the detonation barrel by 70% is observed as a result of decomposition of the powder into TiC. Ti_3SiC_2 powder decomposes due to high-speed shock interaction of heated to high temperatures in a detonation wave stream.

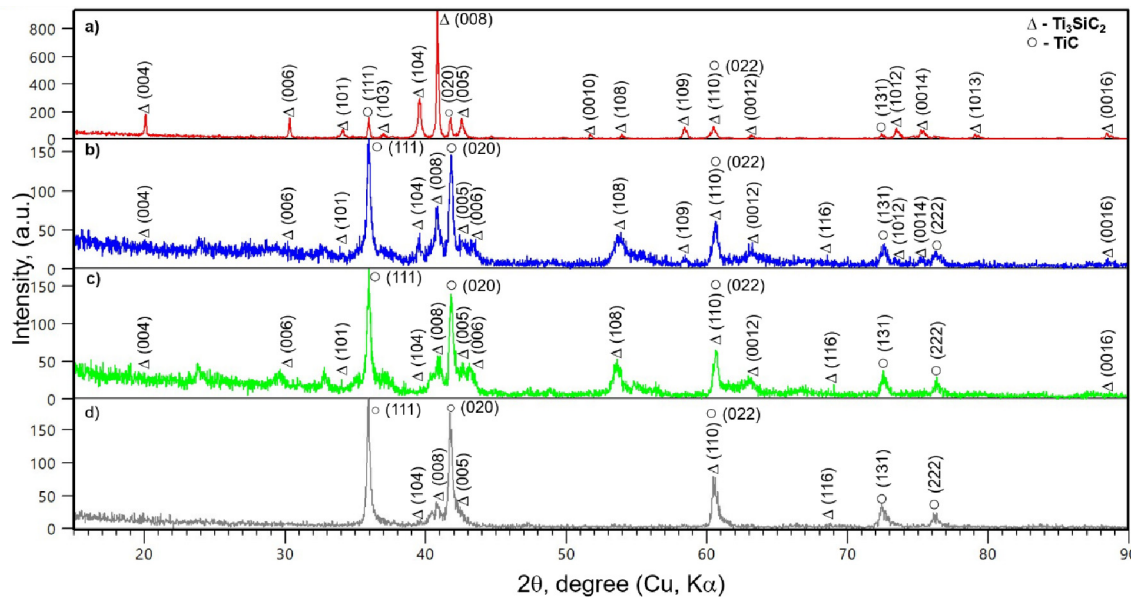


Fig. 2. Diffraction pattern of Ti_3SiC_2 powder (a) and Ti-Si-C coatings obtained at different volumes of filling the detonation barrel with an acetylene-oxygen mixture: 50% (b), 60% (c) and 70% (d)

One of the main factors determining the quality of the coating is adhesion. Figure 2 shows the results of testing the adhesion strength of coatings by scratch testing. The moment of adhesive or cohesive destruction of the coating was recorded after testing visually using an optical microscope equipped with a digital camera, as well as by changing two parameters: acoustic emission and friction force. It should be noted that not all recorded events associated with the destruction of the coating describe the actual adhesion of the coating to the substrate. Registration of various parameters during the testing process allows you to record the various stages of coating failure. So, L_{c1} denotes the moment of the appearance of the first crack, L_{c2} - peeling of the coating areas, L_{c3} - plastic abrasion of the coating to the substrate [20].

We can find that the intensity of crack formation and their development in the sample upon scratching by the type of change in the amplitude of acoustic emission (AE). It can be seen that the first crack is formed at a load of $L_{c1} = 12$ N. Further, the process continues with certain cyclicity for Ti-Si-C coatings obtained with a detonation barrel filling volume of 50% and 60%. Each formation of a chevron crack (Figures 3a, 3b) is accompanied by a corresponding peak in acoustic emission. The partial abrasion of the coating to the substrate was judged by a sharp change in the growth rate of the friction force. This occurred at a load of $L_{c3} = 29$ N, which is also confirmed by visual observations fixing the color change of the sample material at the bottom of the scratch (Figures 3a, 3b). Such a value of L_{c3} indicates a high adhesive strength of adhesion of the coatings to the substrate. The appearance of chevron cracks (Figures 3c) is observed at a load of $L_{c1} = 8$ N for a Ti-Si-C system coating obtained with a 70% fill volume. It can be argued that the cohesive fracture of the sample coating occurs at 8 N, and its adhesive failure at 26 N according to the results of

adhesive tests. This is explained by the fact that the Ti-C system has a higher rigidity; therefore, it is natural to expect minimal elastic and intense plastic deformation during adhesive testing [21].

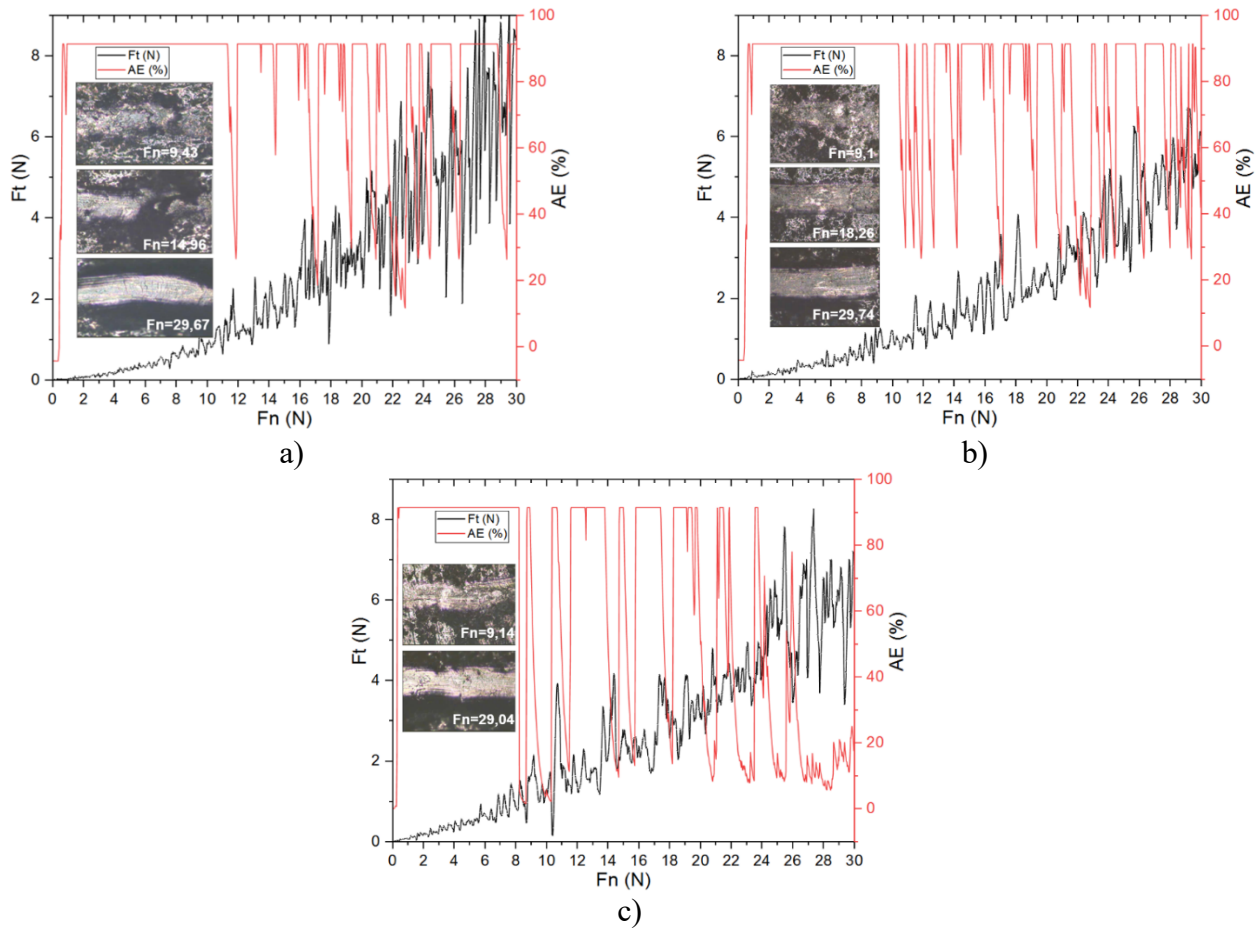


Fig. 3. Results of a scratch-test of Ti-Si-C coatings obtained at different volumes of filling the detonation barrel with an acetylene-oxygen mixture: a) 50%, b) 60% and c) 70%.

The research results of the mechanical characteristics of the obtained coatings were carried out by the Oliver-Farr method. Typical dynamic loading-unloading diagrams are shown in Fig.4.

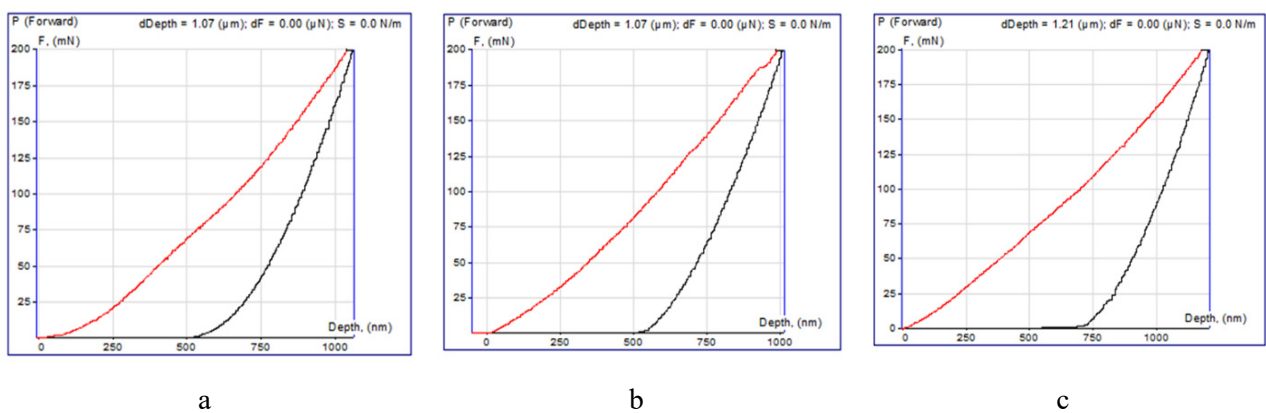


Fig. 4. Load-unloading curves for Ti-Si-C coatings obtained at different volumes of the detonation barrel fillings: a) 50%, b) 60% and c) 70%.

An analysis of the loading and unloading curves shows that the penetration depth of the nanoindenter in the case when the detonation shaft is filled with acetylene-oxygen mixture by 50% and 60% less than 70% filling. We can conclude that the elastic stiffness of the coatings during filling is 70% (Figure 4 c) higher than the others (Figures 4a and 4b) according to the analysis of the indentation curves. According to the results of X-ray phase analysis, a coating with a high TiC phase content is formed with an increase in the volume of filling of the detonation barrel with an acetylene-oxygen mixture by 70%. Thus, the results of nanoindentation and scratch testing are agreed in a good way and confirm the TiC formation, which has a higher rigidity than Ti_3SiC_2 . The values of hardness and elastic modulus of the test samples obtained from the analysis of the load-unloading curve are shown in table 1. Coatings with a high Ti_3SiC_2 content have a higher hardness compared to the coating with the predominant TiC phase as can be seen from Table 1.

Table 1. Results of nanoindentation

Coatings	Occupancy, %	H_{IT} , GPa	E_{eff} , GPa
Ti-Si-C	50	10.07 ± 1.63	232.36 ± 51.61
	60	10.01 ± 2.31	245.96 ± 44.05
	70	7.51 ± 0.50	198.99 ± 17.70

Conclusion

An experimental study of the impact of the detonation gas filling mode on the phase composition and strength characteristics of Ti-Si-C system coatings was carried out in this work. It is shown that the phase composition of detonation coatings can be significantly changed relative to the phase composition of the initial powders, depending on the volume of filling the detonation barrel with an explosive acetylene-oxygen mixture. It was determined that coating mainly consist of TiC phases under increasing in the volume of filling of the detonation barrel with an explosive mixture up to 70%, since the Ti_3SiC_2 powder partially decomposes into TiC in the detonation wave stream due to the high-speed shock interaction of heated to high temperatures. The results of X-ray phase analysis showed that a low degree of decomposition of Ti_3SiC_2 can be achieved when filling the barrel with an explosive mixture of 50% and 60% and the coatings mainly consist of Ti_3SiC_2 phases with a low TiC content. It is connected due to the fact that the heating temperature of the sprayed powder increases under increasing in the degree of filling of the detonation barrel with an explosive acetylene-oxygen mixture. High temperature helps decompose Ti_3SiC_2 powder into TiC. It was determined that an increase in the volume content of the TiC phase in the composition of the coatings leads to a decrease in the hardness and cohesive strength of the Ti-C-Si coatings. The research results of the adhesive strength of coatings showed that the impact of the volume of filling the detonation barrel with an explosive mixture on the adhesive strength is negligible. Moreover, all coatings based on Ti-C-Si, obtained by the detonation method, showed good adhesive strength.

Acknowledgements

The results obtained with the support of program-targeted financing of the Ministry of Education and Science of the Republic of Kazakhstan, grant BR05236748 are used in this article.

REFERENCES

- 1 Ulianitsky V., Shtertser A., Zlobin S., Smurov I. Computer-controlled detonation spraying: from process fundamentals toward advanced applications. *J. Therm. Spray Technol.*, 2011, Vol. 20, pp. 791–801.
- 2 Ulianitsky V., Batraev I., Dudina D., Smurov I. Enhancing the properties of WC/ Co detonation coatings using two-component fuels. *Surf. Coat. Technol.* 2017, Vol. 318, pp. 244–249.

3 Murthy J. K. N. & Venkataraman B. Abrasive wear behaviour of WC–CoCr and Cr₃C₂–20(NiCr) deposited by HVOF and detonation spray processes. *Surface and Coatings Technology*, 2006. Vol. 200, No.8, pp. 2642–2652.

4 Ulyanitsky V.Y., Nenashev M.V., Kalashnikov V.V., et al. Experience in research and application of detonation coating technology. *Bulletin of the Samara Scientific Center of the Russian Academy of Sciences*, 2010 Vol. 12, No. 1 (2), pp. 569-575.

5 Batrayev I. S., Prokhorov E. S., Ulyanitsky V. Y. Acceleration and heating of powder particles by gas detonation products in channels with a conical transition. *Combustion and Explosion Physics*, 2014, Vol. 50, No. 3, pp. 78-86

6 Nikolayev Y. A., Vasiliev A. A., et al. Gas detonation and its application in engineering and technology (review). *Combustion and Explosion Physics*, 2003, Vol. 39, No. 4, pp. 22–54.

7 Dudina D.V., Batraev I.S., Ulyanitsky V.Yu., Korchagin M.A., Possibilities of the computer-controlled detonation spraying method: a chemistry viewpoint. *Ceram. Int.*, 2014, No. 40, pp. 3253–3260.

8 Ulyanitsky V., Shtertser A., Zlobin S., Smurov I., Computer-controlled detonation spraying: from process fundamentals toward advanced applications. *J. Thermal Spray Technol.*, 2011, Vol. 20, pp.791–801.

9 Barsoum M.W. *MAX-phases: Properties of machinable ternary carbides and nitrides*. Wiley, 2013. 436 p.

10 Sun Z. M. Progress in research and development on MAX phases: a family of layered ternary compounds. *Int. Mater. Reviews*.2011, Vol. 56, pp. 143–166.

11 Sonestedt M., Frodelius J., Palmquist J. P., Högberg H., Hultman L., Stiller K. Microstructure of high velocity oxy-fuel sprayed Ti₂AlC coatings. *J. Mater. Sci.*, 2010, Vol.45, pp.2760–2769.

12 Buitkenov D., Rakhadilov B., Erbolatuly D., Sagdoldina Zh. Influence of Heat Treatment on the Phase Composition and Microhardness of Coatings Based on Ti₃SiC₂/TiC, *Key Engineering Materials*, 2020, Vol.839, pp. 137 – 143.

13 Useinov A. et al. Investigation of properties of thin coatings in dynamic mode mechanical analysis using a scanning nanohardometer "NanoScan-4D". *NANOINDUSTRY*, 2016, No. 1, pp. 80-87.

14 Trache R. Puschmann R., Leyens C., et al. Thermally sprayed Ti₃SiC₂ and Ti₂AlC MAX-phase coatings. *Proceeding of the Int. Thermal Spray Conf., ASM International*, 2013, pp. 74–78.

15 Barsoum, M.W., El-Raghy T., Rawn C.J., et al. Thermal properties of Ti₃SiC₂. *J. Phys. Chem. Solids.*, 1999, Vol.60, pp. 429–439

16 Zhou Y., Gu W.: Chemical reaction and stability of Ti₃SiC₂ in Cu during high-temperature processing of Cu/Ti₃SiC₂ composites, *Z. Metallkd*, 2004, No. 1(95), pp. 50 – 56.

17 Barsoum M. W. The M_{N+1}AX_N phases: A new class of solids: Thermodynamically stable nanolaminates. *Prog. Solid St. Chem.*, 2000, Vol. 28, Issues 1–4, pp. 201 – 281.

18 Barsoum M. W., El-Raghy T., Radovic M. Ti₃SiC₂: a layered machinable ductile carbide: *Interceram.*, 2000, No. 49(4), pp. 226-223.

19 Rakhadilov B.K., Buitkenov D.B., Tuyakbaev B.T., Sagdoldina Zh.B., Kenesbekov A.B. Structure and properties of detonation coatings based on titanium carbosilicide. *Proceeding of the 9th International Conference on Key Engineering Materials*. Oxford, United Kingdom, 2019, pp. 301 – 306.

20 Shtansky D.V., Petrzhek M.I., Bashkova I.A., et al. Adhesion, friction, and deformation characteristics of Ti–(Ca, Zr)–(C, N, O, P) coatings for orthopedic and dental implants. *Solid State Physics*, 2006, Vol. 48, No. 7, pp. 1231 – 1238.

21 Andrievskii R. A., Spivak I. I., Strength of refractory compounds and materials based on them. *Guide. Metallurgy*, Chelyabinsk, 1989, pp. 368. [in Russian]

DOI 10.31489/2020No1/65-72

UDC 538.1: 548

INFLUENCE OF HEXAGONAL SYMMETRY STRESSES ON DOMAIN STRUCTURE AND MAGNETIZATION PROCESS OF FeBO₃ SINGLE CRYSTAL

Sharipov M.Z., Hayitov D.E., Raupova I.B., Sadikova M.I.

Bukhara Engineering Technological Institute, Bukhara, Uzbekistan, m.z.sharipov@rambler.ru

The magneto-optical method was used to study the effect of mechanical stresses on the domain structure, the magnetization process, and the main magnetic characteristics of the FeBO₃ crystal. It is shown that the presence of mechanical stresses of C₃ symmetry in the basal plane of the FeBO₃ crystal leads to a rearrangement of its domain structure from 180 to 120 degrees, in which, unlike the usual domain structure, the spontaneous magnetization vector smoothly changes its azimuth in the basal plane along the direction domain boundaries. It was found that the appearance of a 120-degree domain structure leads to a substantial increase in magnetic anisotropy in the basal plane of a strained crystal, which leads to a change in its magnetic susceptibility and magnetization curve.

Keywords: single crystal, domain structure, magnetic field, temperature, thermodynamic theory, magneto-optics, mechanical stresses.

Introduction

The light-plastic weak ferromagnet, iron borate, is transparent in the visible region of the spectrum of electromagnetic waves, which, using magneto-optical methods, can conveniently and visually study the magnetic state and the magnetization process of this class of magnets. At temperatures below T_N , a stable domain structure (DS) arises in FeBO₃, which determines the process of technical magnetization of the crystal. In contrast to [1,2], where the experiments were carried out under conditions of uniform uniaxial crystal stress, the results of studies of the effect of inhomogeneous mechanical stresses on FeBO₃ DS are presented below. Transparent weak ferromagnets are (primarily due to the high mobility of domain walls) a promising medium for the elemental base of various devices of optical communication technology [3]; in addition to purely scientific interest, these studies were also stimulated by applied problems. Such problems inevitably arise when developing the design of one or another functional element of the device, when it is necessary to take into account possible changes in the main characteristics (magnetic susceptibility, coercive force, etc.) of the used magnetic material under the action of mechanical stresses caused, for example, by deformation of the attachment points of the functional element when the ambient temperature changes. The following are the results of studies of the effect of low-symmetric mechanical stresses on DWs and the magnetization process of this weak ferromagnet.

1. Examples and experimental technique

Samples of nominally pure (pure) iron borate single crystals were used as objects of study in the work. The synthesized crystals had the form of plates with a thickness of ~ 50 - 70 μm with transverse dimensions ~ 3~5 mm², the developed planes of which coincided with the basal (with the (111) plane). The crystals had surfaces of sufficiently high optical quality and did not require further polishing. For experiments, crystal samples were taken, the developed faces of which had a shape close to a regular hexagon. The orientation of the samples in the basal plane was carried out according to the natural faceting of the crystals.

To create mechanical stresses in the crystal, the test sample was glued (BF-2 glue) to the copper washer in a predetermined manner (with its three angles) so that its center coincided with the center of the washer (Fig. 1), after which the washer with the sample was glued to the cryostat coolant. As the temperature decreases from room temperature, the washer deforms (its diameter decreases), which is transmitted to the sample, causing its elastic stresses. We do not know the coefficient of linear expansion of iron borate, however, as shown by our measurements, in this case the crystal is compressed in the basal plane along the radii of the washer.

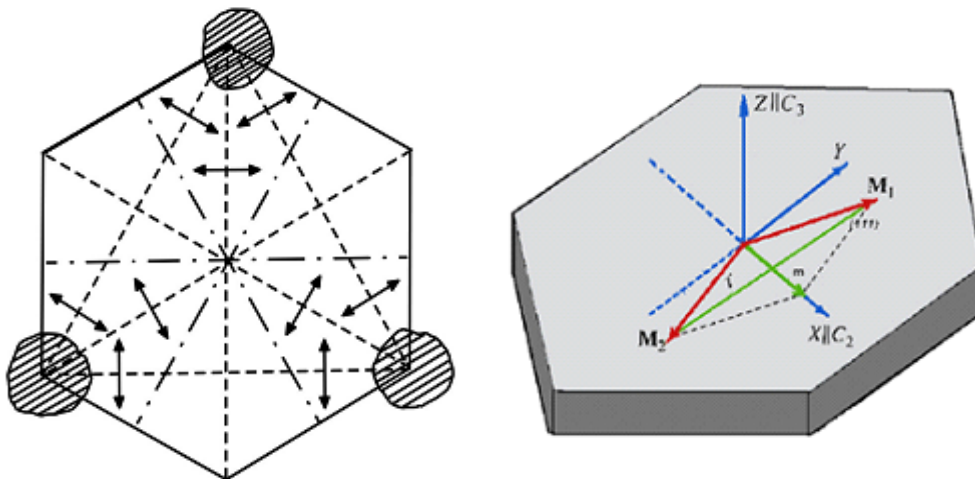


Fig.1. Schematic representation of the investigated sample: shaded areas - droplets of glue with which the crystal is glued to a copper washer; dashed lines - the main directions of emerging stresses; dash - dotted lines - directions of C_2 axes; double arrows indicate the preferred orientation of the vectors \mathbf{m} in various regions of the crystal. On the right is the relative arrangement of the magnetizations of the \vec{M}_1 and \vec{M}_2 sublattices, as well as the vectors $\vec{m} = \vec{M}_1 + \vec{M}_2$ and $\vec{l} = \vec{M}_1 - \vec{M}_2$ in the basal plane of iron borate in the weakly ferromagnetic state.

The effect on the magnetic properties (domain structure, low-frequency magnetic susceptibility and magnetic hysteresis accompanying the process of technical magnetization) of the light-ferrous iron borate ferromagnet was studied under the influence of C_3 symmetry stresses. The experimental results were carried out on an “unstressed” crystal and on a strained crystal, and also these results were compared with each other. Initially, the sample was placed in a mandrel of a sheet of thick paper about $10\ \mu\text{m}$ thick more than the thickness of the sample, in which a through hole was cut out according to the shape of the sample. The mandrel with the sample was glued around the perimeter between two $0.5\ \text{mm}$ thick copper washers with central holes $1.5\ \text{mm}$ in diameter, after which the whole structure was glued (using silicone vacuum grease) to the copper cold conductor of a nitrogen optical cryostat.

To study the effect of mechanical stresses on the magnetic state of iron borate, a magneto-optical technique for visualizing its DS was used. Images of domains were observed under a polarization microscope with an increase of $\sim 30\text{--}40\times$ [4]. The contrast of the obtained DS images arose due to different sizes and/or differences in the sign of the Faraday rotation angle for light transmitted through neighboring domains with different orientations of the vector \mathbf{m} . The domain structure of the sample and its evolution under the influence of a magnetic field and temperature was observed visually and recorded with a digital camera docked with a computer, or could be photographed using a photodetector. The process of technical magnetization was studied on the basis of hysteresis loops of the Faraday Effect that arose during magnetization reversal of a crystal in a quasistatic magnetic field that develops in time at a speed of $\approx 1\ \text{Oe/s}$.

Since the vector \mathbf{m} lies in the plane of the sample and, therefore, the Faraday effect is possible only when the projection of the magnetization vector on the direction of light propagation appears, in all experiments the sample was oriented so that the normal to its plane formed an angle of $\sim 10^\circ$ with the direction of incident light.

2. Discussion of experimental results

The crystal symmetry of FeBO_3 (space group D_{3d}^6) allows the existence of 60, 120, and 180° domain walls in the basal plane [5-12]. However, according to experiments [2, 3], temperature 180° domain structure is realized in thin FeBO_3 plates, which ensures a minimum of magnetoelastic energy. It's the main contribution to the thermodynamic potential of the crystal at $H = 0$ [11]. Moreover, in stress-free crystals, domains form layers parallel to the basal plane along the thickness of the crystal with a Néel type domain boundary oriented along the C_2 axes, which are FeBO_3 easy magnetization axes (the domain boundary between domain layers is a Bloch type) [11]. As can be seen from Fig. 2a, just such a (two-layer) domain structure exists in the studied crystal at room temperature¹. As the temperature decreases, the domain structure of the crystal continues to remain two-layer, however, the domain configuration gradually changes, acquiring at $T \sim 250$ K the form shown in Fig. 2 b, which remains practically unchanged up to the minimum attainable in the experiment $T = 90$ K.

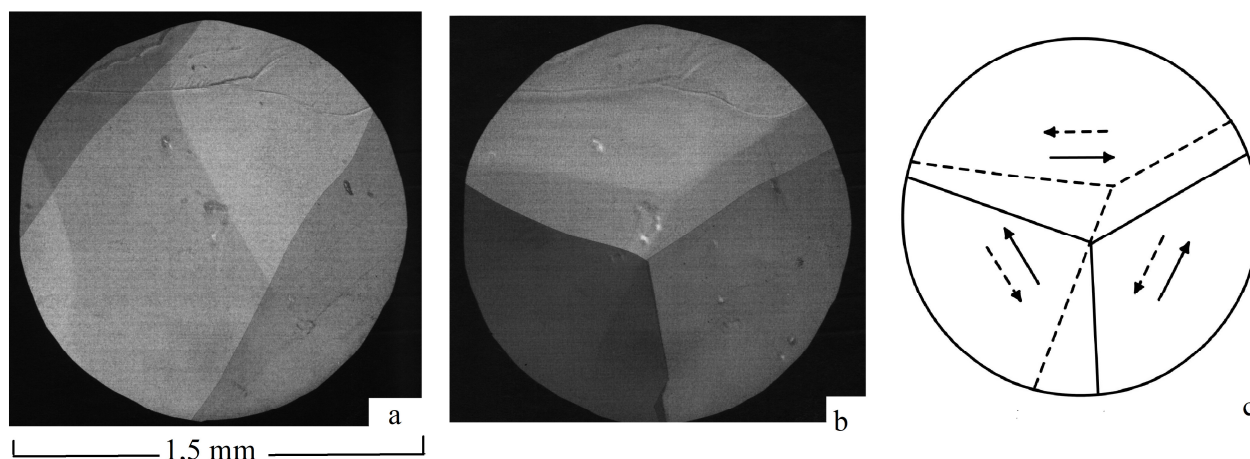


Fig. 2. The domain structure of a weak ferromagnet of iron borate obtained from the central part at a zero magnetic field: a - $T = 295$ K, b - $T = 90$ K; c - orientation geometry of the vector \mathbf{m} in domains at $T = 90$ K.

The preferred orientation of the vector \mathbf{m} in the crystal was determined by the reaction of the domain structure to an external magnetic field applied along different directions in the basal plane: with an increase in the field, the areas of domains in which the vector \mathbf{m} makes an acute angle with the direction \mathbf{H} grow due to domains with an energetically less favorable orientation \mathbf{m} (Fig. 3 a, b). The research results show that during compression of the light-weight ferromagnet of iron borate in the basal plane, the vector \mathbf{m} changes its orientation perpendicularly, and when stretched - parallel to the direction of stresses. In the stressed state, the spatial distribution of the ferromagnetism vector \mathbf{m} in the domain structure is represented by the diagram in Fig. 2 c. The resulting diagram shows that the iron borate sample is compressed, i.e. the linear expansion coefficient in FeBO_3 is less than the linear expansion coefficient of copper in the entire studied temperature range.

Based on Fig. 2b, it can be concluded that the created stresses induce the so-called rotating anisotropy in a weak ferromagnet of iron borate, where the axis rotates in the basal plane. This leads

¹ All images of the domain structure presented in the work were obtained when the sample was rotated around the Y axis by an angle of $\sim 10^\circ$ (the axes of the laboratory coordinate system are shown in Fig. 1).

to a change in the boundary of its DS from 180° to $\sim 120^\circ$ DS. In this case, each domain is divided by the thickness of the crystal into two layers with antiparallel vectors \mathbf{m} (due to the different thickness of the domain layers, the resulting Faraday rotation in each domain is nonzero, which ensures the magneto-optical contrast of the domain structure shown in Fig. 2). Note that, in contrast to the usual 120-degree domain structure, where the angle between the vectors \mathbf{m} in neighboring domains is constant along the domain wall, in the observed domain structure of the “glued” sample due to the spatial heterogeneity of the arising stresses (see Fig. 1), the orientation of the vectors \mathbf{m} in both sides of the domain wall change along its length (it is obvious that the direction of the local vector \mathbf{m} in the domains at $H = 0$ is determined by the competition between the exchange and magnetoanisotropic interactions).

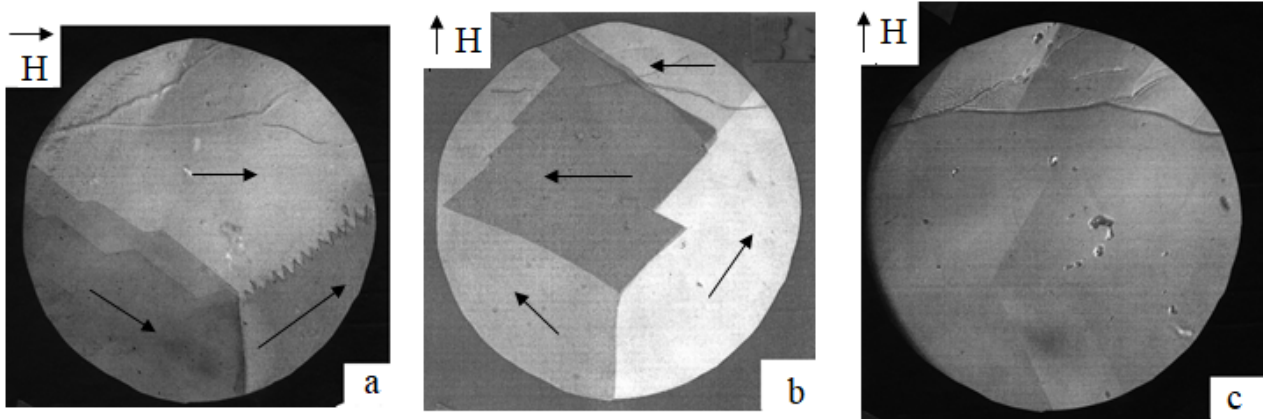


Fig. 3. Images of the central part domain structure of the stressed FeBO_3 crystal obtained at $T = 90$ K: a) - $H = 0.5$ Oe ($\vec{H} \parallel \vec{X}$), b) - $H = 0.5$ Oe ($\vec{H} \perp \vec{X}$), c) - $H = 1.5$ Oe ($\vec{H} \perp \vec{X}$). The arrows indicate the preferred direction of the vector \mathbf{m} in the domains; the arrow in the upper corner indicates the direction of magnetization.

The physical concepts of the magnetization of a crystal with domains prove that induced mechanical stresses increase its heterogeneity, and also cause an increase in the coercive force H_c [7], which we observed experimentally. As shown in fig. 4 at temperature $T = 90$ K the field dependence $F(H)$, i.e. hysteresis loops of the “glued” sample are characterized by high coercivity. In the quasistatic mode of magnetic field sweep, the shape of the magnetic hysteresis loop changes depending on the direction of magnetization, as can be seen from Fig. 4, the dependence $F(H)$ of the “glued” sample, observed at ($\vec{H} \perp \vec{X}$), when reaching saturation, has an almost “hysteresis-free” quasilinear section that is absent in the analogous curve obtained at ($\vec{H} \parallel \vec{X}$).

To interpret the results of studies of the field dependence of the Faraday Effect in stressed FeBO_3 , we turn to Fig. 3, which shows the evolution of its domain structure in a weak magnetic field. From fig. 3 a, b that, when applying the field, first of all (due to the insignificant thickness of the sample) the boundaries between the domain layers disappear, as a result of which the domain structure becomes end-to-end with the orientation \mathbf{m} in each domain, which corresponds to the most energetically favorable of the two possible at $H = 0$ (see Fig. 3 a, b). Further growth of H leads to a displacement of the domain wall in the basal plane of the crystal under the action of pressure P [12]

$$P = mH(\cos \theta_1 - \cos \theta_2), \quad (1)$$

where θ_1, θ_2 are the angles that the vector \mathbf{m} makes up with \mathbf{H} on both sides of the domain wall.

As shown in Fig. 3 *a, b*, with a perpendicular and parallel position of the magnetic field, one of the domain walls does not act on the magnetic field, due to the equality of angles θ_1 and θ_2 , therefore, the magnetization of the crystal occurs mainly due to the displacement of two other domain walls. If we assume that the direction \mathbf{m} in each domain does not change over the entire area of the domain, then substituting the values of the angles between the vectors \mathbf{m} and \mathbf{H} in (1), for the pressure acting on these domain walls, we obtain:

$$|P(\vec{H} \parallel \vec{X})| = mH |\cos 0^\circ - \cos 60^\circ| = \frac{1}{2} mH ,$$

$$|P(\vec{H} \perp \vec{X})| = mH |\cos 90^\circ - \cos 30^\circ| = \frac{\sqrt{3}}{2} mH ,$$

then, *ceteris paribus*, to start an irreversible displacement of domain walls at $(\vec{H} \perp \vec{X})$ the field is required approximately 1.7 times less than at $(\vec{H} \parallel \vec{X})$. Taking into account the relation $H_c \propto \frac{1}{P}$ [9], from the last it follows:

$$H_c(\vec{H} \parallel \vec{X}) \approx 1.7 H_c(\vec{H} \perp \vec{X}),$$

which correlates with the experimental results (according to the graphs $F(H)$ presented in Fig. 4,

$$\frac{H_c(\vec{H} \parallel \vec{X})}{H_c(\vec{H} \perp \vec{X})} \approx 1.5).$$

The difference between the values of $H_c(\vec{H} \parallel \vec{X})$ and $H_c(\vec{H} \perp \vec{X})$, less pronounced in comparison with the experimentally derived from (1), can probably be attributed to the already mentioned change in the angle between the vectors \mathbf{m} in neighboring domains along domain walls.

So, for example, from a comparison of Fig. 1 and Fig. 3 *a, b*, it can be seen that in the middle part of the formed domain walls the angles between the vectors \mathbf{m} on both sides of the domain walls are $\sim 180^\circ$, and therefore, in these sections of the domain walls, the ratio between $|P(\vec{H} \parallel \vec{X})|$ and $|P(\vec{H} \perp \vec{X})|$ it turns out to be the opposite of what was obtained above.

From fig. 3 *a, b*, we can conclude that at the final stage of the process of displacement of domain walls (when domain walls disappear and the crystal transitions to a single domain state) at $(\vec{H} \parallel \vec{X})$, the vector \mathbf{m} over the entire area of the sample is approximately parallel to \mathbf{H} , while at $(\vec{H} \perp \vec{X})$ the vectors \mathbf{m} and \mathbf{H} form a sharp angle between themselves. In the latter case, the further magnetization of the crystal, obviously, occurs by turning the vector \mathbf{m} towards \mathbf{H} . This causes the appearance of a “hysteresis-free” quasilinear region on the $F(H)$ curve observed during magnetization of strained FeBO_3 along the Y axis (Fig. 4). Fig. 3 *c* illustrates the magnetic state of the sample at this stage of the magnetization process.

It is known that, at a sufficiently fast change in the value of magnetization of iron borate in the basal plane occurs exclusively by rotation vector \mathbf{m} . Based on this fact, it can be assumed that in our experiments when the magnetization is reversed, the sample \mathbf{m} in the alternating magnetic field with a frequency of $\nu = 95$ Hz rotates the vector \mathbf{m} in the domains toward \mathbf{H} .

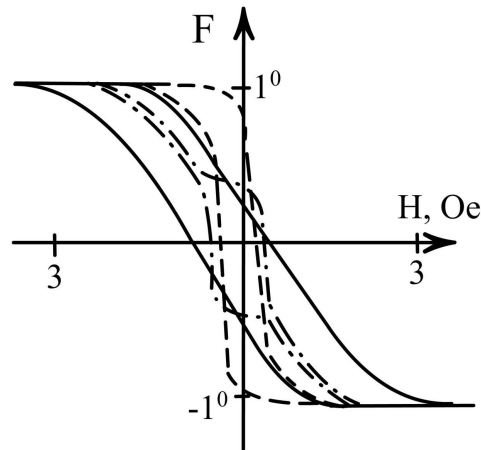


Fig.4. Field dependence of the Faraday Effect in FeBO_3 . The dashed line is the $F(H)$ dependence for the “unstressed” crystal, the solid and dashed lines are the $F(H)$ dependences for the “glued” sample, observed at $T = 90$ K with the field orientation $(\vec{H} \parallel \vec{X})$ and $(\vec{H} \perp \vec{X})$, respectively.

Therefore, the shape of the dynamic hysteresis loop is practically independent (in contrast from the $F(H)$ curves observed under the quasistatic magnetization regime) from the orientation of \mathbf{H} in the basal plane of the crystal.

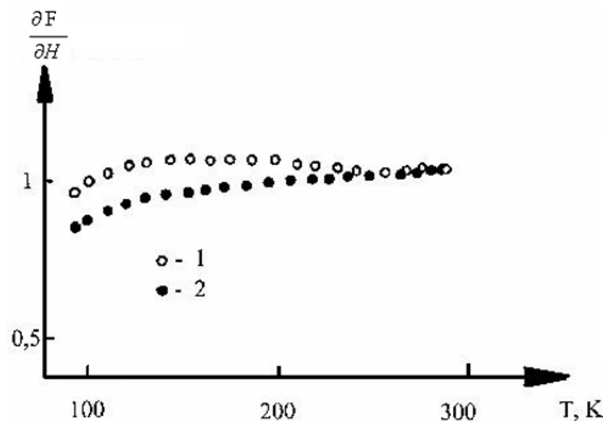


Fig. 5. Temperature dependence of the magneto-optical susceptibility of FeBO_3 : 1 - “glued” sample, 2- “unstressed” crystal.

From the graphs presented in Fig. 5, it can be seen that at $T < 250$ K the value $\frac{\partial F}{\partial H}$ for the “unstressed” crystal decreases monotonically with decreasing temperature, while for the “glued” sample the $\frac{\partial F}{\partial H(T)}$ dependence has a more complex form. It was established that the initial magnetic susceptibility χ in FeBO_3 is determined by the reversible shift of the Bloch domain walls separating the domains along the thickness of the crystal (therefore, the anisotropy of χ , and hence the anisotropy of the $\frac{\partial F}{\partial H}$ quantity, is absent in the basal plane of the crystal).

$$\text{In this case } \chi \propto \frac{m^2}{K}$$

($K = \frac{H_a}{M_s}$ – in-plane anisotropy constant). From the known data on the dependences $m(T)$ and $K(T)$, it follows that at $T < 290$ K, with decreasing temperature, m^2 increases more slowly than the constant K , which determines the form of the dependence of the $\frac{\partial F}{\partial H(T)}$ “unstressed” crystal (Fig. 5).

Turning to Fig. 1, one can notice that in the central part of the crystal the magnitude of the arising stresses is relatively small, and the directions of the stress vectors are least defined (the radius of “curvature” of the anisotropy axis is maximum). If we do not take into account the exchange interactions, it follows from the latter that in the central part of the “glued” sample all possible orientations \mathbf{m} in the basal plane are approximately equivalent from the energy point of view. Obviously, this circumstance facilitates the rotation of the vector \mathbf{m} under the action of the field in the basal plane of the crystal. Consequently, in stressed FeBO_3 , the process of the displacement of the Bloch domain boundary along its thickness begins in a weaker magnetic field, which is likely to determine a certain increase in the magneto-optical susceptibility of the “glued” sample (Fig. 5)¹

Conclusion

It is shown that the presence of mechanical stresses of C_3 symmetry in the basal plane of the FeBO_3 crystal leads to a rearrangement of its domain structure from 180 to 120 degrees, in which, unlike the usual domain structure, the spontaneous magnetization vector smoothly changes its azimuth in the basal plane along the direction domain boundaries.

It was found that the appearance of a 120-degree domain structure leads to a substantial increase in magnetic anisotropy in the basal plane of a stressed crystal, which leads to a change in its magnetic susceptibility and magnetization curve.

Acknowledgments

The authors are grateful to doctor of phys.-math. sci., prof. Sokolov B.Yu., doctor of phys.-math. sci., prof. Djuraev D.R. and prof. Zhumaev M.R. for the discussion of the results. The work was carried out with the financial support of the Ministry of Innovation Development of the Republic of Uzbekistan in the framework of project OT-Φ2-64 “Fluctuation and parametric phenomena in condensed and nanoscale systems”.

REFERENCES

- 1 Bogdanova Kh.G., Golenishchev-Kutuzov V.A., Medvedev L.I., et al. Weak distortions of the magnetic structure of iron borate. *Sov. Phys. JETP*. 1989, Vol. 68, No. 2. pp. 345-349.
- 2 Lacklison D.E., Chadwick J., Page J.L. Photomagnetic effect in ferric borate. *J. Phys. D: Appl. Phys.* 1972, Vol. 5, pp. 810 – 821.
- 3 Scott G.B. Magnetic domain properties of FeBO_3 . *J. Phys. D: Appl. Phys.* 1974, Vol. 7, No.11, pp.1574 – 1587.
- 4 Boidedaev S.R., Dzuraev D.R., Sokolov B.Yu., Sharipov M.Z. Magneto-optical method of investigation of the magnetic inhomogeneity of easy-plane antiferromagnets with a weak ferromagnetism. *Optics and Spectroscopy*, 2008, Vol. 104, No. 4, pp. 604–609.

¹ Considering the heterogeneity of the crystal stresses, in this case it is more correct to speak not about the displacement of the Bloch domain wall in the field H as a whole, but about its bending, similar to the deformation of a flat elastic membrane under the action of a force applied normally to the plane of the membrane in the center of the membrane.

5 Sharipov M.Z., Mirzhonova N.N., Hayitov D.E. Effect of inhomogeneous radially directed mechanical stresses on the domain structure of a FeBO_3 single crystal. *Eurasian Physical Technical Journal*, 2019, Vol.16, No.1(31), pp. 35 – 41.

6 Sharipov M.Z., Dzhuraev D.R., Sokolov B.Yu., Kurbanov M. Modulated magnetic structure of an inhomogeneously stressed single crystal FeBO_3 . *Ukr. J. Phys.* 2010. Vol. 55, No. 6. pp. 706 – 711.

7 Sokolov B.Yu., Sharipov M.Z. Influence of the biaxial mechanical stress on the domain structure of holmium yttrium garnet ferrite. *Russian Physics Journal*. 2014, Vol. 57, No 8, pp. 1001 – 1007.

8 Sharipov M.Z., Hayitov D.E., Rizoqulov M.N., Islomov U.N., Raupova I.B. Domain structure and magnetic properties of terbium ferrite-garnet in the vicinity of the magnetic compensation point. *Eurasian Physical Technical Journal*. 2019. Vol. 16, No. 2(32), pp. 21 – 25.

9 Sokolov, B.Y., Sharipov, M.Z. Magneto-optical properties of the iron garnet $\text{Tb}_3\text{Fe}_5\text{O}_{12}$ near the magnetic compensation temperature. *Physics of the Solid State*, 2014, Vol.56, No. 5, pp. 975 – 979.

10 Sokolov B.Yu., Sharipov M.Z. Low – frequency resonance of domain walls in the iron garnet $\text{Tb}_3\text{Fe}_5\text{O}_{12}$ near the magnetic compensation point. *Journal of Experimental and Theoretical Physics*. 2013, Vol. 116. No 5. pp. 775-779.

11 Farztdinov M.M. *Physics of magnetic domains in antiferromagnets and ferrites*. Moscow, Nauka, 1981, 156 p. [in Russian]

12 Tikadzumi S. *Physics of ferromagnetism*. Moscow, Mir, 1987, 420 p. [in Russian].

Article accepted for publication 28.04.2020

DOI 10.31489/2020No1/73-76

UDC29.19.04, 29.19.21

TIME-RESOLVED LUMINESCENCE EXCITED WITH N₂ LASER OF YAG:CE CERAMICS FORMED BY ELECTRON BEAM ASSISTED SYNTHESIS

Karipbayev Zh.^{1,2}, Alpyssova G.^{1*}, Mussakhanov D.², Lisitsyn V.², Kukenova A.¹, Tulegenova A.³

¹L.N. Gumilyov Eurasian National University, Nur-Sultan, Kazakhstan, gulnur-0909@mail.ru

²National Research Tomsk Polytechnic University, Tomsk, Russia

³al-Farabi Kazakh National University, Almaty, Kazakhstan

In this paper, an attempt to synthesize the phosphor using powerful hard radiation fluxes. White light-emitting diodes (LEDs) are considered a good lighting devices due to their unsurpassed qualities, such as energy saving and long service life. The synthesized ceramics has the characteristic properties of YAG: Ce, YAGG: Ce phosphors. In total, 10 types of phosphors were chosen for research. Phosphors differed in the presence of Ce₂O₃ and gadolinium ions incorporated as a modifier.

Keywords: white LEDs, yttrium-aluminum garnet, phosphor, ceramics, synthesis in the radiation field.

Introduction

On YAG:Ce based phosphors are the most promising for use in LEDs [1-2]. Phosphors are crystalline multicomponent systems [3-4]. The synthesis of YAG:Ce phosphors is carried out by different methods: solid-state reactions, [5], laser ablation [6], sol-gel method [7], hydrothermal [8], pyrolytic spraying [3], coprecipitation [9], using combustion [10] and others. The most common is the synthesis using solid-phase reactions. But this method, as well as the others listed, requires to use a high temperatures. The melting points of the components are from 2455 °C in Y₂O₃ to 2075 °C in Al₂O₃. Therefore, the reproducibility of the synthesis results is low: the elemental composition of microcrystals differs significantly from that included in the mixture, the composition of different batches of phosphor even during synthesis under the same conditions, and the same initial composition of the mixture are changes [11-13]. This also affects to the luminescent properties of phosphors. Therefore, work is constantly ongoing to improve synthesis technologies. In this work, we present the results of studies YAG:Ce based phosphors synthesized in a radiation field.

1. Experimental technique

The samples were synthesized by high-power electron beam generated electron accelerator ELV-6. The possibility of using such a method was first demonstrated in [13-14]. Synthesis in the radiation field should obviously contribute to the occurrence of solid-phase reactions. In the present work, phosphors of different compositions were synthesized with a Y₂O₃ charge content of 22 to 36 wt%, Al₂O₃ ~56 to 62 wt%, Ce₂O₃ ~4.8 to 9.1 wt%, and Gd₂O₃ ~0 to 12 wt% (Table 1).

The structure and elemental composition of these samples were described in [15]. The luminescence spectra of samples and the luminescence excitation spectra were measured using an Cary Eclipse (Agilent) fluorescence spectrophotometer. The photoluminescence kinetics was registered by a Hamamatsu PMT through a monochromator when excited by a nitrogen laser at a wavelength of 337 nm.

Table 1. The initial composition of the synthesized samples

No.	Compositions	Sample number
1	Al ₂ O ₃ (59.5%) + Y ₂ O ₃ (35.7%)+ Ce ₂ O ₃ (4.8%)	1
2	Al ₂ O ₃ (56.8%) + Y ₂ O ₃ (34.1%)+ Ce ₂ O ₃ (9.1%)	2
3	Al ₂ O ₃ (59.5%) + Y ₂ O ₃ (23.8%) + Gd ₂ O ₃ (11.9%) + Ce ₂ O ₃ (4.8%)	3
4	Al ₂ O ₃ (56.8%) + Y ₂ O ₃ (22.7%)+ Gd ₂ O ₃ (11.4%) + Ce ₂ O ₃ (9.1%)	4
5	Al ₂ O ₃ (56.8%) + Y ₂ O ₃ (34.1%)+ Ce ₂ O ₃ (9.1%)	5
6	Al ₂ O ₃ (59.5%) + Y ₂ O ₃ (23.8%)+ Gd ₂ O ₃ (11.9%) + Ce ₂ O ₃ (4.8%)	6
7	Al ₂ O ₃ (59.5%) + Y ₂ O ₃ (35.7%)+ Ce ₂ O ₃ (4.8%)	7
8	Al ₂ O ₃ (56.8%) + Y ₂ O ₃ (34.1%)+ Ce ₂ O ₃ (9.1%)	8
9	Al ₂ O ₃ (56.8%) + Y ₂ O ₃ (22.7%)+ Gd ₂ O ₃ (11.4%) + Ce ₂ O ₃ (9.1%)	9

2. Results and Discussion

The synthesized samples were ceramic balls with a diameter of 3-6 mm of a characteristic yellow color. The samples were crushed into powder, photoluminescence spectra were measured upon excitation by laser radiation λ 337 nm. Excitation spectra and decay kinetics were also measured. It was established that the main luminescent characteristics of the synthesized ceramic samples are mainly similar to those known for the solid-phase synthesis of phosphors obtained by traditional methods [16]. Fig. 1 shows the results of study the luminescence spectra of powdered samples of different compositions; the luminescence spectra have the form of a monopole by exciting on 337 nm.

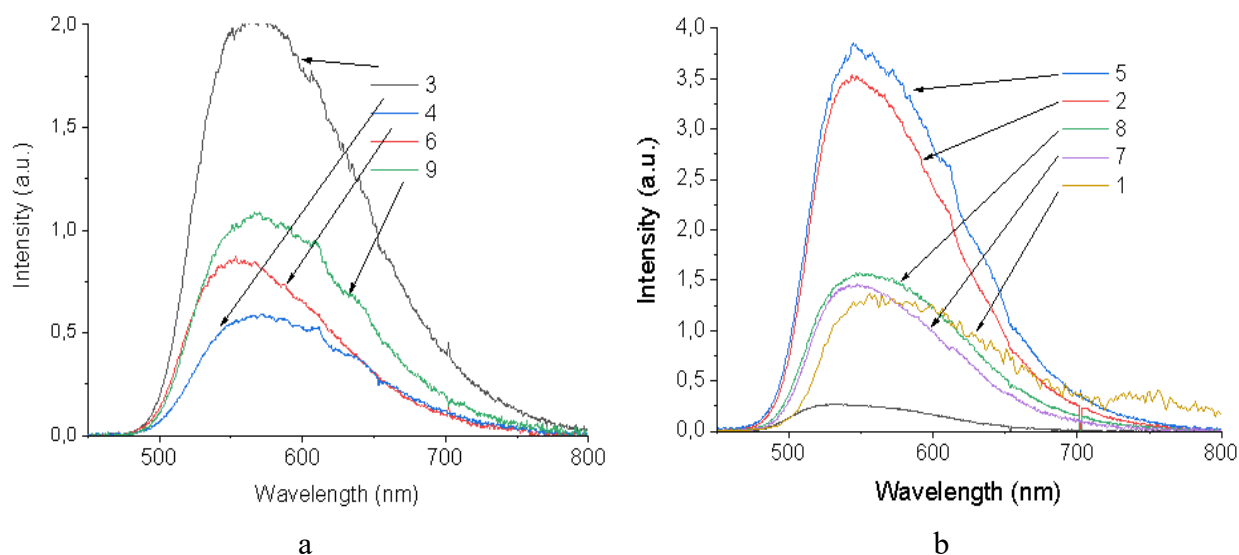


Fig. 1. Luminescence spectrum of YAG (a) and YAGG (b) ceramics samples excited by 337 nm.

A comparison of results of measuring the characteristics of the spectra gives the following. There is a large variation in the positions and half-widths of the luminescence bands. In YAG:Ce ceramic samples the positions of bands are in the range from 546 to 563 nm, the half-width is from 0.42 to 0.49 eV. In YAGG:Ce from 548 to 570 nm and from 0.44 to 0.48 eV, respectively. In general, tendency is: the entering of gadolinium leads to a band shift to the red region. The wide variation in the band characteristics is explained by the following. In strongly defective systems, which are YAG:Ce ceramics samples, the luminescence center is an element of a nanod defect, a complex defect [17]. Nanod defect is formed during the synthesis. The formation does not have time

to complete at a high rate of ceramic synthesis. Therefore, small differences in the synthesis conditions, primarily during the preparation of mixtures, can lead to deviations in the structure of the nanodefekt. This is manifested in a change in the characteristics of the spectrum due to differences in environment of luminescence center. The maxima position, the half-width of the spectra, the kinetic parameters at a wavelength of registration of 540 nm pulsed photoluminescence are presented in table 2.

Table 2. The maxima position, the half-width of the spectra, the kinetic parameters at a wavelength of registration of 540 nm

Sample number	$\lambda_{\text{ex}}=337 \text{ nm}$		Photoluminescence kinetics parameters at $\lambda = 540 \text{ nm}$			
	$\Delta E, \text{ eV}$	λ_{max}	$\tau_1, \text{ ns}$	A_1	$\tau_2, \text{ ns}$	A_2
1	0.494371	563	38.78	0.51	70	0.6
2	0.427453	545			62.34	
3	0.477145	570	28	0.5	64.29	0.6
4	0.459989	548	21.44	0.85	60	0.37
5	0.441487	546			65	
6	0.441029	554	29	0.4	62	0.69
7	0.422713	548			67.71	
8	0.456703	550			70	
9	0.484883	570	37.16	0.475	68.37	0.6

Figure 2 (a,b) shows the results of study of the luminescence decay kinetics of synthesized ceramic samples after excitation by a nanosecond laser measurement pulse at 337 nm.

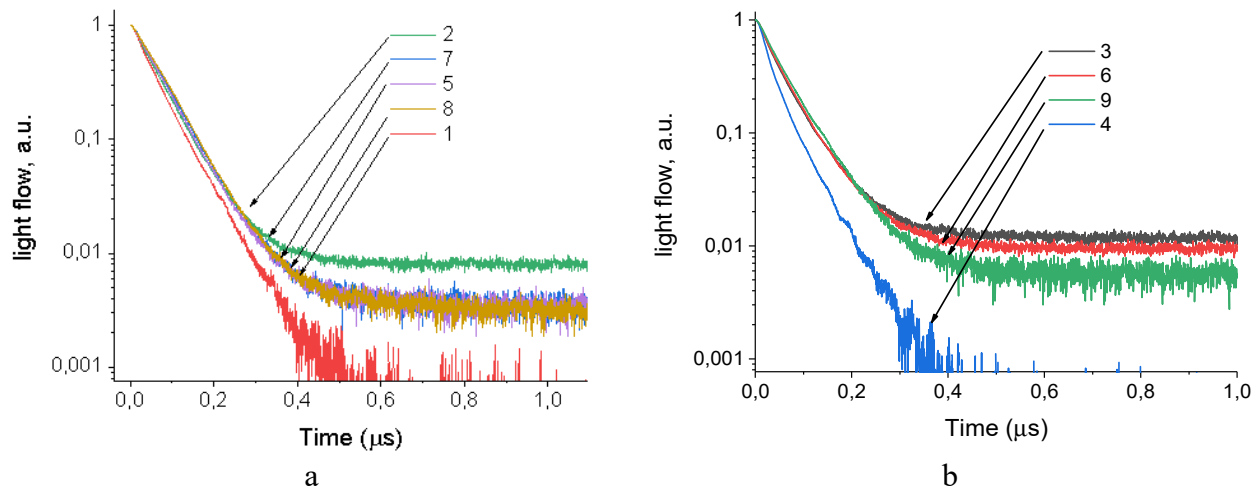


Fig. 2. Photoluminescence kinetics of YAG ceramics excited by a 337 nm nitrogen laser

In the majority of studied ceramic samples, at least two stages of decay with characteristic times $\sim \text{ns}$ and long in the microsecond range take place. For some samples, the decay pattern is described by a single exponent. There is a difference in the decay amplitude ratios in the first stage

Conclusion

The luminescent characteristics of YAG: Ce ceramic samples synthesized in a radiation field were studied. In general terms, the spectral and kinetic characteristics of ceramics luminescence are similar to those known for YAG: Ce phosphors and ceramics obtained using the solid-state reaction method. Therefore, the radiation method for the synthesis of luminescent ceramics which differ

fundamentally from the existing one, can be considered as an alternative. It was shown that the luminescence characteristics of the synthesized samples have a large variation. This is explained in the framework of the notion that the luminescence center, cerium ion, are elements of nanodefects which formed during the synthesis. In the synthesis of samples, the radiation field, which takes 1 s, does not complete the formation of nanodefects. Subsequent annealing of the samples is required to complete their formation.

Acknowledgments

The work was carried out within the framework of the grant AP08052050 of the Ministry of Education and Science of the Republic of Kazakhstan. This research was supported by Tomsk Polytechnic University CE Program.

REFERENCES

- 1 Zehua Liu, Shuxing Li, et al. Composite ceramic with high saturation input powder in solid-state laser lighting. *Ceramics International*, 2018, Vol.44, pp. 20232–20238.
- 2 Țucureanu V., Munteanu D. Enhanced optical properties of YAG:Ce yellow phosphor by modification with gold nanoparticles. *Ceramics International*, 2019, Vol. 45, pp.7641-7648.
- 3 Barbaran J.H., Ghamsari M.S., Javaheri I., et al. Growth and spectral properties of Ce³⁺:YAG single crystal. *Journal of optoelectronics and advanced materials*, 2018. Vol. 20, pp. 431 – 434.
- 4 Murai S., Fujita K., Iwata K., Tanaka K. Scattering-based hole burning in Y₃Al₅O₁₂:Ce³⁺ monoliths with hierarchical porous structures prepared via the sol-gel route. *J. Phys. Chem: C*, 2011, Vol. 115, No.36, pp. 17676–17681.
- 5 Hakuta Y., Haganuma T., Sue K., et al. Continuous production of phosphor YAG: Tb nanoparticles by hydrothermal synthesis in supercritical water. *Materials Research Bulletin*, 2003, Vol. 38, pp. 1257-1265.
- 6 He G., Mei L., Wang L., Liu G., Li J. Synthesis and luminescence properties of nano-/microstructured Y₃Al₅O₁₂:Ce³⁺ microspheres by controlled glass crystallization. *Cryst. Growth. Des.*, 2011, Vol. 11, pp.5355–5361.
- 7 Karbowski M., Kepinski L., et al. Structural and luminescent properties of nano-sized NaGdF₄: Eu³⁺ synthesised by wet-chemistry route. *Journal of Alloys and Compounds*, 2004, Vol. 380, pp. 315 – 320.
- 8 Huczko A. Fast combustion synthesis and characterization of YAG:Ce³⁺ garnet nanopowders. *Phys. Status Solidi B*, 2013, Vol. 250, No.12, pp. 2702–2708.
- 9 Xianqiang Chen, et.al. Highly transparent ZrO₂-doped (Ce,Gd)₃Al₃ Ga₂O₁₂ ceramics prepared via oxygen sintering. *Journal of the European Ceramic Society*, 2015, Vol. 35, pp. 3879-3883.
- 10 Dantelle G., Salaiin M., Bruyere R., et al. Luminescent coatings prepared from optimized YAG:Ce nanoparticles. *Thin Solid Films*, 2013, Vol. 543, pp. 36-42.
- 11 Lisitsyn V.M., Lisitsyna L., Dauletbekova A., et al. Luminescence of the tungsten-activated MgF₂ ceramics synthesized under the electron beam. *Nuclear Instruments and Methods in Physics Research Section B: Beam Interactions with Materials and Atoms*, 2018, Vol. 435, pp. 263-267.
- 12 Lisitsyn V.M., Golkovskii M.G., Lisitsyna L., et al. MgF₂-Based Luminescing Ceramics. *Russian Physics Journal*, 2019, Vol. 61, Issue 10, pp. 1908–1913.
- 13 Lisitsyn V.M., Golkovskii M.G., Musakhanov D.A., et al. YAG based phosphors, synthesized in a field of radiation. *Journal of Physics: Conference Series*, Vol. 1115, Issue 5, pp.052007.
- 14 Musakhanov D.A., Tulegenova A.T., Lisitsyn V.M., et al. Structural and luminescent characteristics of YAG phosphors synthesized in the radiation field. *IOP Conf. Series: Materials Science and Engineering*, 2019. Vol. 510, pp. 012031.
- 15 Nie, Lijun Xu, Mingfu Zhang Microstructures, optical properties and application in WLEDs of large- size YAG:Ce³⁺-Al₂O₃eutectic grown by HDS method. *Journal of Alloys and Compounds*, 2019, Vol. 782, pp. 348-354.
- 16 Wagner A., Ratzker B., Kalabukhov S., et.al. Residual porosity and optical properties of spark plasma sintered transparent polycrystalline cerium -doped YAG. *Journal of the European Ceramic Society*, 2019, Vol. 39, pp. 1436-1442.
- 17 Alpysova G., Mussakhanov D., Karipbayev Zh, et.al. Luminescence spectra of YAG:Ce phosphors synthesized in a field of radiation. *HTRA-2019 IOP Conf. Series: Materials Science and Engineering*, 2020, Vol. 754, pp. 012014.

DOI 10.31489/2020No1/77-84

UDC 621.311.25:621.548:551.55-026.51

DYNAMIC WIND SPEED MODEL FOR SOLVING WIND POWER PROBLEMS

Obukhov S.G.¹, Plotnikov I.A.¹, Masolov V.G.²¹ National Research Tomsk Polytechnic University, Tomsk, Russia, igorplt@tpu.ru² "VDM-tehnika" LLC, Moscow, Russia, vdm-tech@mail.ru

This work is devoted to the development of a dynamic model of wind speed designed to solve the problems of wind power. The time model of wind is presented in the form of two components - constant and turbulent. The Kaimal spectral model recommended by IEC 61400-1:2005 is used to describe the turbulent component of wind speed. The initial data for the calculation of turbulence parameters are the class of wind power plant, which is determined by its location, the height of the axis of rotation of the wind wheel and the average wind speed for the specified time interval of simulation. Computer implementation of wind model is carried out on the basis of statistically independent sources of white noise acting on forming filters, output signals of which are summed. The analysis of the obtained results shows that the wind flow model implemented on the basis of the method of forming filters provides adequate modeling of the longitudinal component of wind speed and can be used to solve the problems of wind power engineering.

Keywords: wind power, wind model, spectral model, forming filters.

Introduction

The priority direction of the development of modern energy is the application of the improvement of environmentally friendly technologies for the production of electric energy. Wind power is one of the most popular and widely used renewable energy technologies. According to the International Renewable Energy Agency (IRENA), about 52 GW of wind-based generation was introduced in 2017, bringing the total installed capacity of wind power plants to about 539 GW [1]. According to Harvard University studies based on very conservative assumptions, by 2020 the installed capacity of wind power will reach 1000 GW, and in many technologically developed countries the share of wind power will be more than 30%. The rapid development of wind power is greatly facilitated by the efforts of scientists aimed at improving the technologies of component production and operation of wind power plants [2, 3].

One of the pressing tasks of increasing the energy efficiency of wind power plants is to find new and improve the known control algorithms [4-7]. The necessity to solve this problem is due to the fact that in order to extract the maximum available wind flow power, it is necessary to control the speed of wind turbine (WT) rotation according to certain laws in accordance with the dynamics of wind speed change. Given the high complexity of the problem identified, most researchers use mathematical computer modeling techniques to solve it. One of the most important components of the integrated mathematical model of WT required for research is the dynamic model of wind speed. The development of a dynamic model of wind speed is a difficult technical task due to the transient characteristics of wind speed data, which largely reflect turbulent dynamics in the atmosphere. The analysis of scientific papers on dynamic wind modelling for wind power has shown that the authors apply different techniques and methods, which differ mainly in describing the turbulent component of wind flow [8-10]. At the same time quality of wind models in this field of research is mainly determined by adequacy of display of dynamics of change of longitudinal component of wind flow and simplicity of computer implementation.

The purpose of this research was to develop a universal dynamic wind model to solve various wind power problems implemented in the Matlab/Simulink software complex.

1. Theoretical justification of dynamic wind model

Modern software complexes such as ANSYS, ARIMA and others [11, 12] allow to model stationary and non-stationary turbulent air flows in time and space. The main purpose of these software complexes is to model aerodynamic effects on structural elements of high-rise buildings. The use of complex multi-dimensional wind models built on the Navier-Stokes differential equations describing the movement of non-stationary airflow for the identified study tasks appears to be redundant, and wind models based on statistical distribution functions have become most common in wind power. Of greatest interest is the longitudinal component of wind speed, which ultimately determines the mechanical and output electrical power of the WT. Time fluctuations of major meteorological factors, such as wind speed, pressure, humidity, etc., contain components ranging from fractions of a second to at least hundreds of years. From the point of view of simulating the operating modes of the WT, time intervals ranging from seconds to several hours are of practical interest.

Micrometeorological variations in wind speed with periods ranging from a fraction of a second to minutes are determined by small-scale turbulence. Its energy spectrum in the surface layer of the atmosphere has a maximum in a period of about 1 min. In a meso-meteorological time interval with periods of minutes to hours, intense fluctuations of meteorological elements are relatively rare. It allows obtaining relatively stable average values of wind speed, temperature, etc., using averaging over periods of 10-20 min. Figure 1 shows the spectral distribution of horizontal wind speed constructed by Van der Hoven from measurements at the 125-metre meteorological tower at Brookhaven.

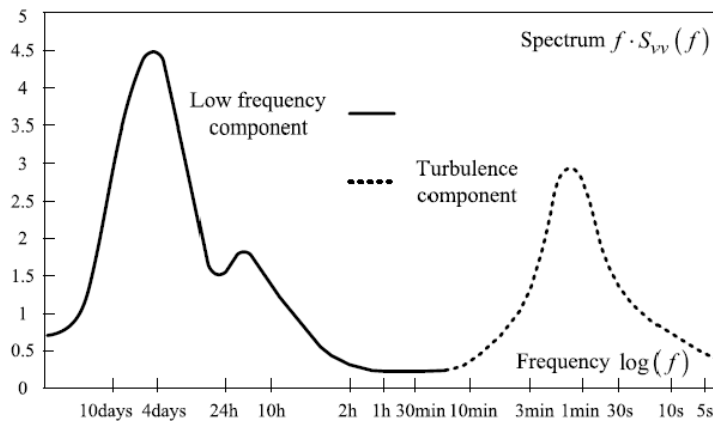


Fig.1. Horizontal wind speed spectrum

It can be seen from the graph that the frequency of the energy spectrum of the synoptic and daily fluctuations of wind speed differs significantly from the high-frequency fluctuations of turbulence, which allows to use independent time sampling for their mathematical description with subsequent superposition.

Under the assumptions taken, the time model of wind can be represented as an equation:

$$V(t) = \bar{V} + v(t), \quad (1)$$

where \bar{V} is the average speed of wind is 10 minute time interval; $v(t)$ is a dynamic or turbulent component of speed of wind.

For statistical description of the turbulent component of wind speed in wind power, empirical models of spectral density $S(f)$ are preferably used, the most famous of which are Davenport,

Karman and Kaimal functions [13]. To model the dynamic component of wind speed, the current work used the Kaimal spectral model recommended by the international standard [14].

According to the normal turbulence model, turbulent wind velocity fluctuations are assumed to be a stationary field of random vectors whose constituents have a Gaussian statistical distribution with zero mathematical expectation. The power spectral densities of the normalized components for the Kaimal model are described by the equation:

$$\frac{f \cdot S(f)}{\sigma^2} = \frac{4 \cdot f \cdot L / \bar{V}}{(1 + 6 \cdot f \cdot L / \bar{V})^{5/3}}, \quad (2)$$

where f is a frequency in Hz; $S(f)$ is unilateral range of a longitudinal component of a vector of speed; σ - means square deviation of a longitudinal component of a vector of speed; L - is integrated large-scale parameter of turbulence.

Spectral decomposition shows a stationary random function decomposed into harmonic oscillations of different frequencies f_1, f_2, \dots, f_k , with harmonics amplitudes being random values. According to Fourier's theorem any function with the period of π can be presented in the row form:

$$f(t) = A_0 + \sum_{k=1}^{\infty} A_k \cdot \cos(\omega_k t + \varphi_k), \quad (3)$$

where A_k is the amplitude of k -th harmonic oscillation; ω_k is the circular frequency of harmonic oscillation; φ_k is an initial phase k -th fluctuation; A_0 is the free member representing population mean of function on π interval.

On the other hand, the dispersion of a stationary random function is equal to the sum of the dispersions of all harmonics of its spectral decomposition:

$$D = \sigma^2 = \int_0^{\infty} S(f) \cdot df = \sum_{k=0}^{\infty} D_k = \sum_{k=0}^{\infty} S(f_k) \cdot \Delta f, \quad (4)$$

If the same set of frequencies is used for spectral decomposition of the function and Fourier series, it follows from (3) and (4) that the amplitude of the k -th harmonic oscillation of the Fourier series will be equal to the standard deviation of the corresponding harmonic of the spectrum:

$$A_k = \sqrt{D_k} = \sqrt{S(f_k) \cdot \Delta f}, \quad (5)$$

where Δf is the distance between adjacent frequencies.

For a final number of frequencies N , the equation for the longitudinal component of wind velocity determined at time interval T can be represented as follows:

$$V(t) = \bar{V} + \sum_{k=1}^N A_k \cdot \cos(\omega_k t + \varphi_k), \quad (6)$$

where \bar{V} is the wind speed averaged over a 10-minute time interval.

In expression (6) time of modeling of T corresponds to a half-cycle of the main harmonica: $T = \pi$, respectively number N determines the frequency of sampling of a temporary signal:

$$\Delta t = \frac{T}{N}; \quad \Delta \omega = \frac{\pi}{T}; \quad \Delta f = \frac{1}{2 \cdot T}; \quad t = k \cdot \Delta t \quad k=1 \dots N \quad f_k = \frac{k}{2 \cdot T} \quad (7)$$

Expressions (2) - (7) allow to construct a simulated time model of the longitudinal component of wind speed, if spectral parameters of turbulence are known. The size of spectral density for the corresponding frequency of f_k is defined from the equation (2), and the phase corner of φ_k represents a random number in the range from 0 to 2π . The spectral parameters of turbulence for the Kaimal model are determined in accordance with the requirements specified in IEC 61400-1:2005 [14], according to which all wind power plants in terms of turbulence intensity are divided into subclass A, B, C, each of which is characterized by its expected value of turbulence intensity of air flow at the height of the axis of the wind wheel I_{ref} .

Class A corresponds to WT with increased turbulence ($I_{ref}=0.16$) and is accepted for urbanized area where the roughness of the Earth's surface is $z_0>0.3$. Class B corresponds to more open area ($0.1<z_0<0.3$) and turbulence intensity for it is taken equal to $I_{ref}=0.14$. Class C is characterized by open area ($z_0<0.1$) with turbulence intensity $I_{ref}=0.12$, Table 1.

Table 1 -Basic Class Parameters WT

Class WT	I	II	III	S
$V_{ref}(m/c)$	50	42.5	37.5	Values of calculated parameters are assigned by a designer
A I_{ref}	0.16			
B I_{ref}	0.14			
C I_{ref}	0.12			

Wind speed in the surface layer of the atmosphere depends significantly on the roughness of the Earth's surface, consequently, the nature of the location of the WT and the height of its mast h will have a direct impact on the total generation of electric energy [15]. Most meteorological stations record wind parameters at a standard height of 10 m. To determine the average wind speed at other V_h altitudes, an approximate empirical formula can be used, which includes the value of the standard wind speed V_{10} , measured at an altitude of ten meters:

$$V_h = V_{10} \cdot \left(\ln \left(\frac{h}{z_0} \right) / \ln \left(\frac{10}{z_0} \right) \right), \text{ m/s} \quad (8)$$

where z_0 is the roughness of the Earth's surface, the numerical values from Table 2 [16].

$$\Lambda = \begin{cases} 0.7 \cdot Z & Z \leq 60 \text{ m} \\ 42 \text{ m} & Z > 60 \text{ m} \end{cases} \quad (9)$$

To calculate the integral scale parameter of the longitudinal component of the velocity vector L , the expression is used:

$$L = 8.1 \cdot \Lambda \quad (10)$$

The initial data for the calculation of turbulence parameters are the WT class, which is determined by its location, the height of the axis of rotation of the wind wheel Z and the average wind speed for a given simulation time interval \bar{V}_{hub} .

Table 2 - Parameters for calculation of vertical wind flow profile.

Type of terrain	Roughness of a surface, z_0 (m)	Class of roughness of a relief
Water surface	0.0001	0
Desert	0.0003	
Flat snow cover	0.001	
Airport runway	0.01	
Countryside with separate buildings and fences	0.05	1
Countryside with trees, forests, villages	0.1	2
Numerous trees, shrub	0.2	
Mountain area	0.3	3
The city	0.5	
Big cities, forest	1.0	

The software implementation of the above model is carried out in two stages. At the first stage values of amplitudes A_k and phase corners of φ_k of the corresponding harmonics of the modelled signal pay off, and at the second stage its synthesis is carried out. To fulfil the calculations, two numeric data arrays must be created: one with dimension $M1 [m, N]$, and second with $M2 [N, Nt]$.

The parameter m in the M1 array is determined by the number of calculated variables: $f_k, S(f_k), A_k$, etc. The value N defines the number of harmonic oscillations that are taken into account in the decomposition of the function. With a small value of N we obtain a low accuracy of calculation, a large value of N requires additional resources. For the solved class of tasks it seems quite acceptable to choose the number of harmonics taken into account, on the order of $N=50-100$. The Nt parameter corresponds to the specified number of process calculation points used for output. It is important to note that frequency synchronization adopted in model development requires certain ratios between N and Nt .

For example: the purpose of modeling is imitation of a longitudinal component of speed of wind on a time interval of $T_{\text{mod}}=100$ s with sampling $\Delta t=0.1$ s. If directly to accept page $T=100$ s, then at $N=50$ in expressions (7) we will receive $\Delta t=2$ s that much more exceeds a desirable interval of sampling. For this example it is necessary to determine the decomposition period as $T=\Delta t \cdot N$, then to calculate the parameter c which defines dimension of the output array $Nt=c \cdot N$ and number of cycles of calculation which need to be executed for its full filling:

$$c = \frac{T_{\text{mod}}}{T} \quad (11)$$

Figure 2 shows an example of simulating the longitudinal component of wind speed at a time interval of 40 seconds with a sampling of 0.1 s. The simulation was carried out under the following conditions: average wind speed $\bar{V} = 6.0$ m/s, turbulence intensity $I_{\text{ref}} = 0.16$, height of rotation axis of wind wheel $Z_{\text{hub}} = 15$ m.

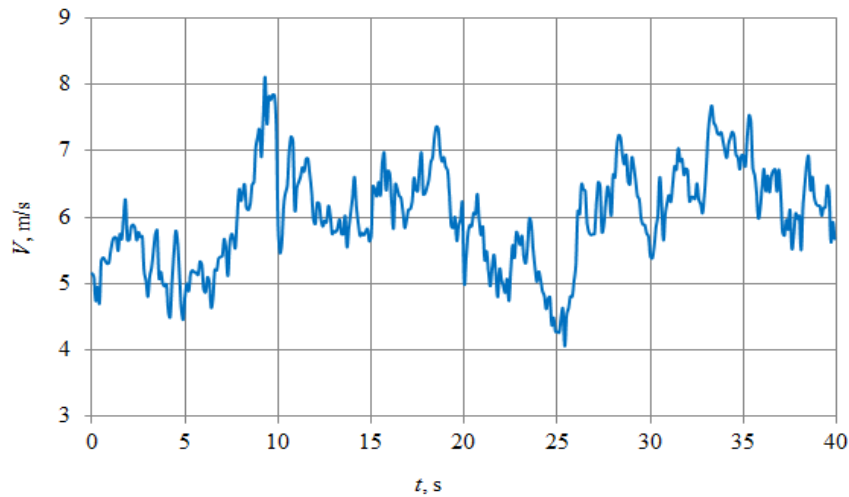


Fig.2. Results of simulation of the longitudinal component of wind speed

The simulation results are well consistent with the results of studies by other authors involved in the development of mathematical wind models for wind power [17-19].

A disadvantage of the above simulation method is that the spectral density $S(f)$ of the turbulent velocity component $v(t)$ is approximated by the sum of fractional-rational functions:

$$S(f) = \sum_{k=1}^N S_k(f), \quad (12)$$

that results in the need to create and store large number arrays in the RAM of the computer.

A forming filter method can be used As an alternative method of simulation of random variable. According to this method, the value of the random variable $v(t)$ having the spectral density $S(f)$ will be equal to the output signal of the transfer function link $W(s)$ when exposed to the white noise $h(t)$ with a single spectral density when the condition is:

$$S(f) = |W(s)|^2 \quad (13)$$

In practice, this method is implemented by selecting the family of frequency characteristics $W_k(s)$ at $k = 1 \dots N2$, at which the approximate equality is achieved:

$$S(f) = \sum_{k=1}^{N2} |W_k(s)|^2 \quad (14)$$

It should be noted that the $N2$ value is generally much smaller than N in equation (6), which provides significant savings in computing resources.

2. Implementation of dynamic wind model in MatLab/Simulink

Computer implementation of wind model is carried out on the basis of $N2$ statistically independent sources of white noise acting on $N2$ of forming filters, output signals of which are summed. The authors of the [18-20] have obtained a satisfactory approximation to the initial spectral density for the Kaimal distribution at the number of generating filters $N2 = 5$ in the frequency range up to 1 Hz, which is quite acceptable for wind power calculations. Transfer functions for the Kaimal distribution are as follows [15]:

$$\begin{aligned} W_1(s) &= \frac{\sqrt{270 \cdot D \cdot L \cdot V} \cdot s}{\frac{3}{2\pi} \cdot \frac{L}{V^2} \cdot s + 0.6L}, & W_2(s) &= \frac{\sqrt{2898 \cdot D \cdot \frac{L}{V}} \cdot s}{\frac{3}{2\pi} \cdot \frac{L^2}{V^2} \cdot s^2 + 3.15 \cdot \frac{L}{V} \cdot s + 1.2\pi}, \\ W_3(s) &= \frac{\sqrt{6300 \cdot D \cdot \frac{L}{V}} \cdot s}{\frac{3}{2\pi} \cdot \frac{L^2}{V^2} \cdot s^2 + 11.4 \cdot \frac{L}{V} \cdot s + 21.7\pi}, & W_4(s) &= \frac{\sqrt{9000 \cdot D \cdot \frac{L}{V}} \cdot s}{\frac{3}{2\pi} \cdot \frac{L^2}{V^2} \cdot s^2 + 43.5 \cdot \frac{L}{V} \cdot s + 315.4\pi}, \\ W_5(s) &= \frac{\sqrt{13200 \cdot D \cdot \frac{L}{V}} \cdot s}{\frac{3}{2\pi} \cdot \frac{L^2}{V^2} \cdot s^2 + 186 \cdot \frac{L}{V} \cdot s + 5766\pi}. \end{aligned} \quad (15)$$

In expression (15), the following variable designations are used: D is the dispersion of the longitudinal component of wind speed, m^2/s^2 ; L is the scale of the longitudinal component of atmospheric turbulence; V is the average wind speed at the level of the wind wheel hub, m/s. The wind model implemented as a subsystem in MatLab/Simulink is shown in Figure 3.

The primary initial wind flow simulation data are:

Z_0 – roughness of the Earth's surface, m; Z_{hub} – tower height of WT at the level of the hub, m; V – the average wind speed accepted for simulation, m/s.

The calculation sequence for preparing input data to the model dialog form is as follows:

1. The value of the Z_0 is determined from Table 2 and the specified location of the WT.
2. Taking into account the recommendations [21] in Table 1, class of WT and intensity of turbulence $I_{ref.}$ are determined.

3. Equation (9) determines the standard deviation of the longitudinal component of wind speed σ and its dispersion $D = \sigma^2$.

4. Equations (10), (11) determine the scale parameter of the longitudinal component of the speed vector L .

Figure 4 shows an example of simulating of a longitudinal component of wind speed over a time interval of 40 seconds with initial simulation data corresponding to Figure 2.

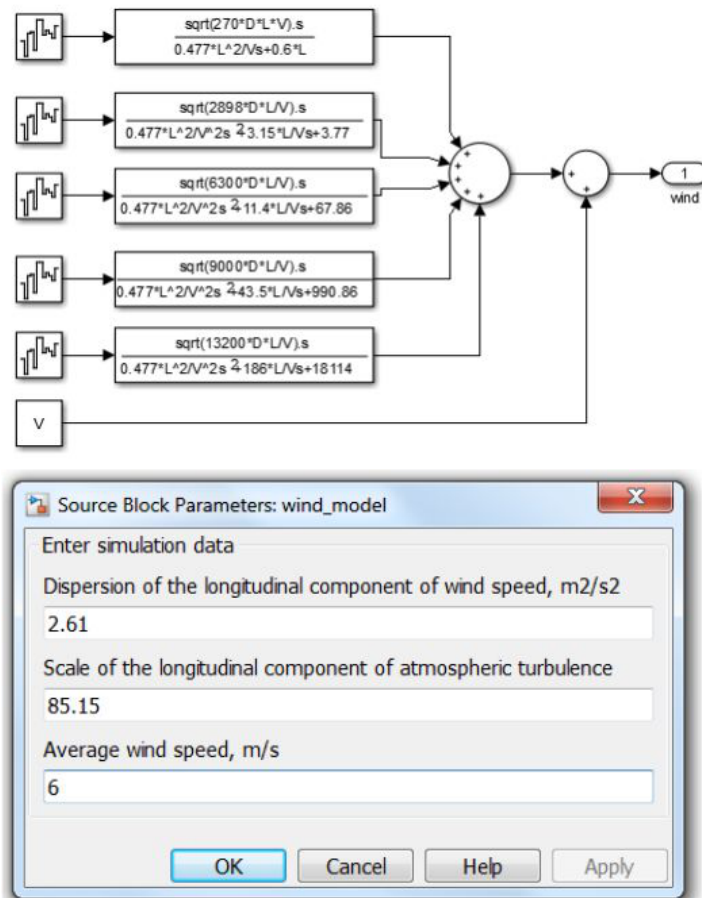


Fig. 3. Wind flow model with input parameters window

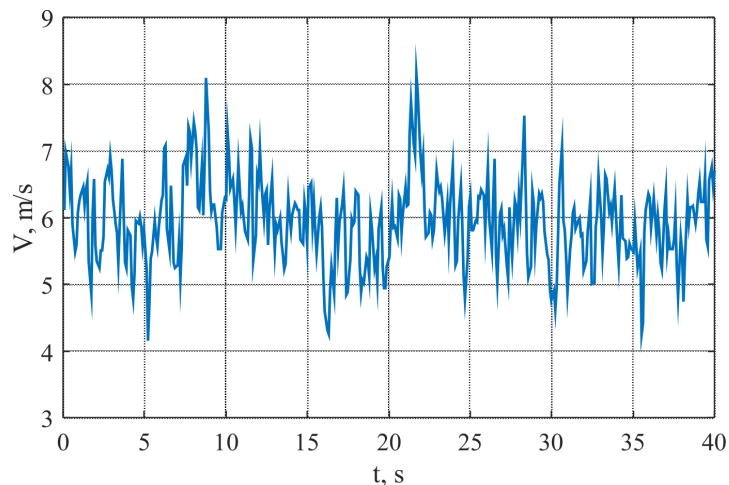


Fig. 4. Results of simulation of the longitudinal component of wind speed

The analysis of the obtained results shows that the wind flow model implemented on the basis of the method of forming filters provides adequate simulation of the longitudinal component of wind speed and can be used to solve the problems of wind power engineering.

Conclusion

As a result of the research a dynamic wind model has been developed and implemented in the MatLab/Simulink software complex, which can be used to solve a wide range of wind power problems: research of wind turbine performance during turbulence and stochastic changes in wind speed, development of effective algorithms for control of the operating mode of the WT, etc. The model is implemented in the form of a separate functional unit, which provides simplicity and convenience of its practical application.

Acknowledgements

The study was supported by the Ministry of Education and Science of the Russian Federation. The unique identifier is RFMEFI57617X0098 (agreement No. 14.576.21.0098 dated 26 September 2017).

REFERENCES

- 1 Renewables 2018 Global Status Rep ort. Renewable Energy Policy Network for the 21st Century. 2018. – 325 p. Available at: <http://www.ren21.net/> (accessed 20 October 2019).
- 2 Cherubini A., Papini A., Vertechy R., Fontana M. Airborne Wind Energy Systems: A review of the technologies. *Renewable and Sustainable Energy Reviews*, 2015, Vol. 51, pp. 1461–1476.
- 3 Goudarzi N., Zhu W.D. A review on the development of wind turbine generators across the world. *International Journal of Dynamics and Control*, 2013, Vol. 1, No. 2, pp.192–202.
- 4 Abdullah M.A., Yatim A.H., Tan C.W., et al. A review of maximum power point tracking algorithms for wind energy systems. *Renewable and Sustainable Energy Reviews*, 2012, Vol. 16, pp. 3220– 3227.
- 5 Guo R, DuJ., J. Wu, Y. Liu, The Pitch Control Algorithm of Wind Turbine Based on Fuzzy Control and PID Control. *Energy and Power Engineering*, 2013, Vol. 5, pp. 6-10.
- 6 Surzhikova O. Power supply of remote and almost inaccessible settlements. *IOP Conference Series: Materials Science and Engineering IOP*. 2015, Vol. 81, No 1 doi10.1088/1757-899X/81/1/012098
- 7 Bemš, J., Starý, O., Macaš, M., Žegklitz, J., Pošík, P. Innovative default prediction approach. *Expert Systems with Applications*, 2015, Vol. 42, No 17-18, pp. 6277-6285. doi: 10.1016/j.eswa.2015.04.053
- 8 Kerrouche K., Mezouar E., Boumediene A., et al. Modeling and Lyapunov-Designed based on Adaptive Gain Sliding Mode Control for Wind Turbines. *Journal of Power Technologies*, 2016, Vol. 96, No.2, pp.124–136.
- 9 Barbosa de Alencar D., De Mattos Affonso C., Limão de Oliveira R.C., et al. Different Models for Forecasting Wind Power Generation: Case Study. *Energies*, 2017, Vol. 10, No. 1976, pp. 1 – 27.
- 10 Sarsikeev Y, Lukutin B.V, Lyapunov D.Y., Surkov M.A., Obuhov S.G. Dynamic model of wind speed longitudinal component. *Advanced Materials Research*, 2014, Vol. 953-954, pp. 529-532.
- 11 Abo-Khalil A.G., Alyami S., Sayed K., Alhejji A. Dynamic Modeling of Wind Turbines Based on Estimated Wind Speed under Turbulent Conditions. *Energies*, 2019, Vol. 12, No. 1907, pp. 1–25.
- 12 Yunus K., Thiringer T., Chen P. ARIMA-Based Frequency-Decomposed Modeling of Wind Speed Time Series. *IEEE Transactions on Power System*, 2016, Vol. 31, pp. 2546–2556.
- 13 Smilden E., Sørensen A., Eliassen L. Wind Model for Simulation of Thrust Variations on a Wind Turbine. *Energy Procedia*, 2016, Vol. 94, pp. 306 – 318.
- 14 IEC 61400-1: 2005 Wind Turbines – Part 1: Design requirements. Available at: <https://webstore.ansi.org/Standards/IEC/IEC61400AmdEd2010?msclkid>
- 15 Kirpichnikova I.M., Matveyenko O.V. Computer simulation of wind pulsation depending on time. *International Scientific Journal for Alternative Energy and Ecology*, 2010, Vol. 4, No. 81, pp. 54–59.
- 16 Neammanee B., Sirisumrannukul S., Chatratana S. Development of a Wind Turbine Simulator for Wind Generator Testing. *International Energy Journal*, 2007, Vol. 8, pp. 21 – 28.
- 17 Gavrilin A., Moyzes B., Kuvshinov K., Vedyashkin M., Surzhikova O. Determination of optimal milling modes by means of shock-vibration load reduction on tool and peak-factor equipment. *Materials Science Forum*, 2019, Vol. 942, pp. 87 – 96. doi:10.4028/www.scientific.net/MSF.942.87
- 18 Hao H., Gu B., Yan R., Hui H. Simulation and Analysis of Direct-driven Wind Turbine. *International Journal of Online and Biomedical Engineering*, 2015, Vol. 11, No. 5, pp. 17 – 23.
- 19 Sakipova S.E., Tanasheva N.K. Modeling aerodynamics of the wind turbine with rotating cylinders. *Eurasian Physical Technical Journal*. 2019, Vol.16, No. 1(31), pp. 88 – 93. DOI: 10.31489/2019No1/88-93
- 20 Králík T., Bemš, J., Starý, O. Electricity markets integrations - What is the current status and future outlook of bidding zones reconfiguration? *Proc. of the 9th Intern. Scient.Symposium on Electrical Power Engineering, ELEKTROENERGETIKA 2017*, 237 – 240.
- 21 Erich Hau *Wind Turbines: Fundamentals, Technologies, Application, Economics*. 2-nd edition. Springer – Verlag Berlin Heidelberg. 2006, 783 p.

DOI 10.31489/2020No1/85-90

UDC: 532.517.4

CALCULATION OF THE END PLATES FRICTIONAL RESISTANCE EFFECT ON THE FLAT JET DYNAMICS

Toleuov G.K., Isataev M.S., Seydulla Zh.K.* , Zulfukharova E.M., Masina M.N.

al-Farabi Kazakh National University, Almaty, Kazakhstan, seydulla92@mail.ru

This article is a continuation of scientific research on the calculation of the effect of friction resistance of end plates on the aerodynamics of a flat jet. In the previous works, the resistance was calculated for a turbulent boundary layer. This paper shows the results of calculating the effect of friction resistance of end plates on the patterns of development of a flat free jet. A flow diagram of the jet between the end surfaces has been constructed. The resistance calculation for the laminar boundary layer has been carried out. The formula for calculation of the change in the maximum jet velocity in a first approximation has been derived. The comparison of the theoretical calculations with the experimental data has shown a good agreement.

Keywords: three-dimensional jet, flat jet, end plates, frictional resistance, boundary layer

Introduction

Over the last few decades, the dynamic and oscillatory response of a free three-dimensional jet flowing from a rectangular outlet cross-section nozzle, on the main and partially on the initial section of the current, have been subjected to detailed research [1-5]. Recently, attention has also been paid to the development of the vortex structure and its effect on the development of turbulent and mean flow properties on the initial, transition and main sections of a free jet stream. In experimental installations in the study of a plane jet, as a rule, in order to exclude the effect of finiteness of the rectangular nozzle height, the flow field is limited by end plates installed in parallel to the direction of flow, as a continuation of the end walls of the rectangular nozzle outflow section. As we see here, due to the influence of the end walls, instead of a three-dimensional jet, we obtain a plane jet bounded by these side walls.

It can be said that the new experimental and theoretical data obtained provide broad information about the effect of end walls and large-scale coherent vortices on the development of turbulent jets that flow from a rectangular nozzle. For example, in work [6] the effect of friction resistance of the end plates on the patterns of a plane free jet was experimentally investigated. Recently, much attention has been given to the study of coherent structures of the wall jets flow [7]. This field is an important target of research. It is also important to continue research on dynamic flow properties. In this paper, as a continuation of experimental studies shown in [6], a theoretical calculation of end plates friction resistance effect on the development patterns of a free plane jet is performed.

1. Calculation of friction resistance face end plates

Calculation of the resistance effect on the end walls. To calculate the effect of resistance of the end walls on the flat jet attenuation, we will look at the following jet flow scheme between end surfaces. Fig. 1 shows the jet flow schemes bounded by the end flat walls, in the xoy plane. In the xoy plane the jet, as in the ordinary free jet, has an initial ("i" index), a transition ("t" index) and main sections and lateral free mixing boundaries, the nozzle width in the axis direction is $2b$. In the

xoz plane, the $2h$ high jet flowing from the nozzle is bounded by the end plates from the sides in the direction of the oz axis. On the first section of the jet, after leaving the nozzle along the end walls, a laminar or turbulent boundary layer develops with a uniform profile along the z axis between the boundaries of the boundary layers. The development of these boundary layers is similar to the boundary layer when the plate is flowed past by a uniform flow. At the end of the 1-section, the boundary layers are joined on the jet axis and the 2-section of the jet begins, in which the flow in the xoz plane is analogous to the flow in a flat channel. Accordingly, the development of the boundary layer and the flow on the first section are analogous to the flow past the plate by a uniform flow, while in the second section it is analogous to a flow in a flat channel. The geometric parameter $\lambda=2h/2b$ characterizes the relative elongation of the outlet section of the nozzle.

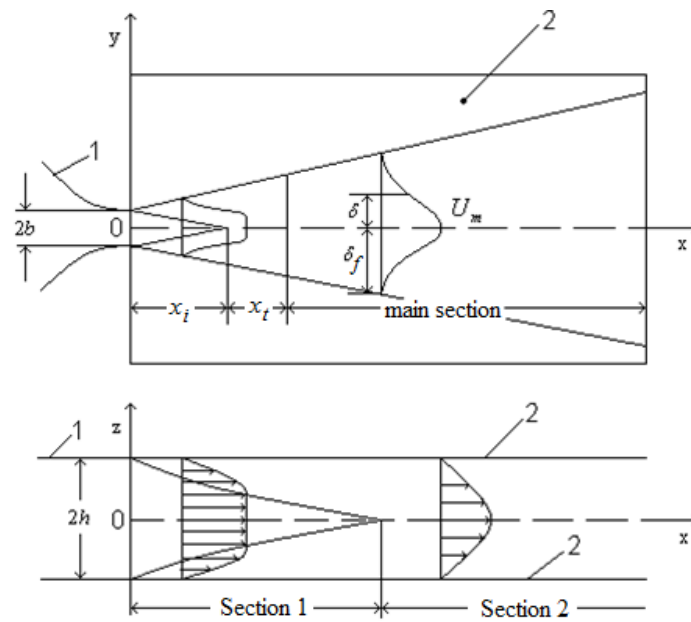


Fig.1. Diagram of a flat jet bounded by the end walls:

1 – nozzle; 2 – end plates. x, y, z – right angled Descartes coordinates; δ – current value of the boundary layer thickness; δ_c – free jet boundary layer thickness in y -direction. U_m – velocity on the jet axle

In view of the foregoing, on the first jet section we adopt the change in the boundary layer thickness along z on the end plates as the following dependences:

- for laminar flow

$$\delta_z = \frac{5.0 \times x}{\sqrt{\frac{U_m \times x}{\nu}}} \quad (1)$$

for a turbulent boundary layer

$$\delta_z = \frac{0.37 x}{\left(\frac{U_m \times x}{\nu}\right)^{1/5}} \quad (2)$$

Here x is the longitudinal coordinate, U_m is the velocity at the jet axis, ν is kinematic viscosity, and $\frac{U_m \times x}{\nu}$ – we adopt as a Reynolds number $Re_{mx} = \frac{U_m \times x}{\nu}$.

The length of the first section is determined from the condition of $x=x_l$ with $\delta_z = h$. Thus, in order to determine walls resistance, we can use the following formulas from the paper [6]:

$$\xi = \frac{16}{\text{Re}}, \text{Re} = \frac{U_m \times 2h}{\nu} \quad (3)$$

$$C_f = \frac{0.664}{\sqrt{\text{Re}_{mx}}}, \text{ or } C_f = \frac{0.0576}{\left(\frac{U_m \times x}{\nu}\right)^{0.2}}$$

After the boundary layers come in contact for the second flow section, we apply the law of resistance in a flat channel with ξ hydraulic resistance coefficient for laminar flow:

$$\xi = \frac{16}{\text{Re}}, \text{Re} = \frac{U_m \times 2h}{\nu} \quad (3a)$$

For turbulent flow:

$$\xi = \frac{0.3164}{\text{Re}^{\frac{1}{4}}}, \text{Re} = \frac{U_m \times d_r}{\nu}, \quad (4)$$

where $d_r = \frac{4F}{\vartheta}$ is hydraulic diameter, defined as the ratio of the quadruple section area of channel F to its perimeter ϑ .

Below we provide an approximate calculation of the change in the total jet momentum under the effect of end walls resistance in the laminar jet flow.

2. Calculation of resistance at a laminar boundary layer

In the presence of end walls resistance, the total jet momentum is not conserved and decreases along the length of the jet [6]:

$$\frac{dK}{dx} = -2 \int_{-\delta_f}^{\delta_f} \tau_w dy, \quad (5)$$

where K is the total flow momentum in any jet section, τ_w is the frictional stress on the wall at a y distance from the symmetry plane, and δ_f is the total half-width of the jet equal to the distance from axis to the outer boundary at $U = 0$.

Considering the jet between closely spaced plates with the Reynolds number being $\text{Re}_0 = \frac{U_0 b}{\nu} < 10^3$ (0 index is the value of the elongation parameter at the nozzle edge) and $\lambda < 1$; the first section length is small and the boundary layers on the walls contact at the axis already at a distance of $\frac{x_1}{b} < 10$. Therefore, for approximate calculation, we could adopt the profiles both along z axis and along y axis established from the end or from the nozzle exit; the plate resistance is calculated using the laminar boundary layer model.

For simplicity, we assume that along oy axis the velocity profile of the jet corresponds to the polynomial [6], and along oz axis – to the parabolic profile in the flat channel:

$$\frac{U}{U_1} = 1 - \frac{z^2}{h^2}, \quad (6)$$

where U_1 is the velocity value in the jet section with coordinates x, y at $z=0$, U is longitudinal velocity. The polynomial is represented as follows:

$$\frac{U_1}{U_m} = 1 - 6\eta^2 + 8\eta^3 - 3\eta^4, \quad (7)$$

where U_1 is the velocity at the boundary of the wall boundary layer at a distance of δ_z from the wall at the appropriate distances $\eta = \frac{y}{\delta_f}$ from zox plane in this section.

We use (7) in (6), then along the jet section the velocity distribution will look as follows:

$$\frac{U}{U_m} = \left(1 - \frac{z^2}{h^2}\right) (1 - 6\eta^2 + 8\eta^3 - 3\eta^4), \quad (8)$$

Total jet momentum in this section is as follows:

$$K = 4 \int_0^h \int_0^{\delta_f} \rho U^2 dy dz = 1.579 h \delta_f \rho U_m^2, \quad (9)$$

where ρ – is the liquid (gas) density.

Friction resistance of the walls on a section with dx length:

$$= \frac{16.576 U_m}{\text{Re}_0 \lambda U_0} \rho U_0^2 \delta dx \int_0^{\delta_f} \tau_w dy = 4 dx \int_0^{\delta_f} \frac{24}{<U_1> 2h} \rho \frac{<U_1>^2}{2} dy =, \quad (10)$$

where τ_w is the frictional stress on the wall at a distance y from the plane of symmetry.

We use (9) and (10) in (5) and after generation we obtain the following:

$$\int_1^{\frac{U_m}{U_0}} d\left(\frac{U_m}{U_0}\right) = -\frac{1}{2} \int_0^{\frac{x}{b}} d\left(\frac{x}{b}\right) - \frac{5.25}{\text{Re}_0 \lambda^2} \int_0^{\frac{x}{b}} d\left(\frac{x}{b}\right) \frac{U_m}{U_0}, \quad (11)$$

where $\text{Re}_0 = \frac{U_0 \times 2b}{\nu}$, here U_0 – is an initial flow velocity.

In the right part of (11) we use the null approximation solution

$$\int_1^{\frac{U_m}{U_0}} d\left(\frac{U_m}{U_0}\right) = \frac{U_m}{U_0},$$

and after integration and exponentiation we obtain the following:

$$\frac{U_m}{U_0} = \frac{N}{\sqrt{\frac{x}{b} + \frac{x_0}{b}}} \exp\left[-\frac{10.50}{\text{Re}_0 \lambda^2 N} \sqrt{\frac{x}{b}}\right] = \frac{N}{\sqrt{\frac{x}{b} + \frac{x_0}{b}}} \exp\left[-a \sqrt{\frac{x}{b}}\right], \quad (12)$$

where x_0 – is the pole distance, $a = \frac{10.50}{\text{Re}_0 \lambda^2 N}$.

In order to obtain a solution in the second approximation (12), we again use in the right part (11) and integrate. As a result, we obtain the following solution:

$$\ln \frac{U_m}{U_0} = -\frac{1}{2} \ln \frac{x}{x_i} - \frac{2}{a^2} \left[\exp[a\sqrt{x}] \times \left(\frac{1}{2} a^2 x - a\sqrt{x} + 1\right) - 1 \right] \quad (13)$$

where x_i – is the initial section length.

After (13) exponentiation we obtain:

$$\frac{U_m}{U_0} = \sqrt{\frac{x_i}{b}} \times \exp \left[-\frac{2}{a} \left[\exp[a\sqrt{x}] \times \left(\frac{a^2}{2} x - a\sqrt{x} + 1 \right) - 1 \right] \right] \quad (14)$$

In case of the values of $\frac{x}{b} \leq 100$ and $a\sqrt{x} \ll 1$ the function (14) can be represented as a following series:

$$\frac{U_m}{U_0} \approx \frac{N}{\sqrt{\frac{x}{b} + \frac{x_0}{b}}} \times \exp \left[-a \left(\frac{x\sqrt{x}}{3} + \frac{ax^2}{2} \right) \right] \quad (15)$$

3. Discussion of results

Calculation comparison for (15) with the experimental data is shown in Fig. 2 for a jet at $\lambda=0.62$, $U_0=9.2$ and 44.1 m/s.

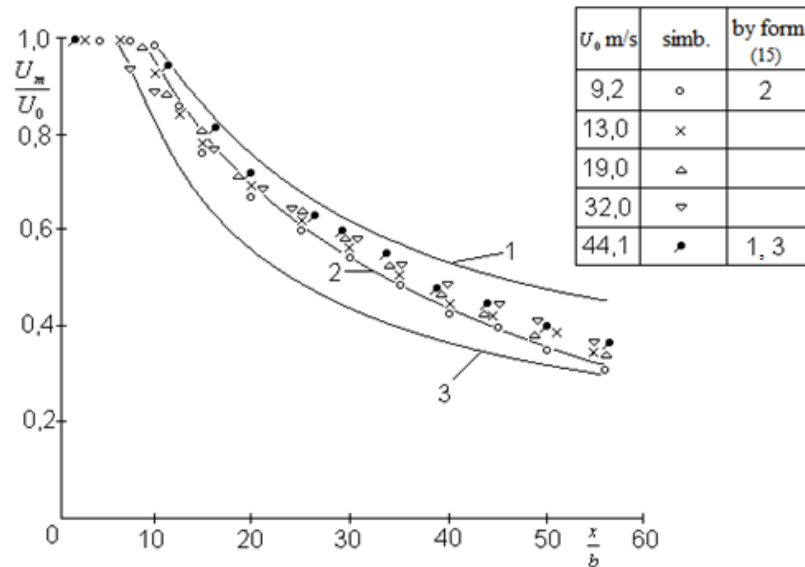


Fig.2. Dependence of $\frac{U_m}{U_0}$ on the distance from nozzle when $\lambda=0.62$.

Lines 1 and 2 calculation based on (15); line 3 calculation based on [6].

The same figure also provides calculations for the turbulent boundary layer from work [6] using the following formula:

$$\frac{U_m}{U_0} = \frac{N}{\sqrt{\frac{x}{b} + \frac{x_0}{b}}} \times \exp \left\{ -\frac{0.1481}{A} \left(\frac{x}{b} \right)^{0.9} + \frac{0.01372}{A^2} \left(\frac{x}{b} \right)^{1.8} - \frac{0.00288}{A^3} \left(\frac{x}{b} \right)^{0.27} \right\} \quad (16)$$

where $A = \lambda \text{Re}_0^{0.2} N^{0.2}$.

As can be seen, formula (15) much better corresponds to the experience data with $\lambda=0.62$, whereas the formula for the turbulent boundary layer is in better agreement with the experimental data with $\lambda > 1$ [6].

Conclusions

A jet flow diagram was constructed between the confining end walls. In the xoy plane, the jet propagates as a free jet. In the xoz plane in the first section, the boundary layer formed on the end walls is similar to the boundary layer when flowing past the plate as a uniform flow, and in the second section, when the boundary layers close on the axis of the flow, the flow is analogous to the flow in a flat channel. The paper shows the results of calculation of end plates friction resistance effect on the development patterns of a free flat jet. The resistance is calculated for a laminar boundary layer. A calculation formula is obtained that describes the change in the maximum jet velocity in the initial approximation. The results of calculation are compared with the experimental data.

REFERENCES

- 1 Abramovich G.N., Girshovich T.A, Krashennnikov S.I., Sekundov A.N., Smirnova I.P. *The Theory of Turbulent Jets*. The MIT Press, Cambridge, Massachusetts, 1984, 684p.
- 2 Quinn W.R. Turbulent free jet flows issuing from sharp-edged rectangular slots: the influence of slot aspect ratio. *Exp. Thermal Fluid. Sci.* 1992, No.5, pp. 203 – 215.
- 3 Faghani E., Maddahian R., Faghani P., et al. Numerical investigation of turbulent free jet flows issuing from rectangular nozzles: the influence of small aspect ratio. *Archiv. Appl. Mech.*, 2010, No. 80(7), pp. 727 – 745.
- 4 Inguva, V., Graceffa, R., Schulz, J., Bilsel, O., Perot, B.J. Creating round focused micro-jets from rectangular nozzles. *Journal of Mechanical Science and Technology*. 2019, Vol. 33, Issue 9, pp.4281 – 4289.
- 5 Hao, W.U., Yongpeng, O., Qing, Y.E. Experimental study of air layer drag reduction on a flat plate and bottom hull of a ship with cavity. *Ocean Engineering*. 2019, Vol 183, pp. 236 – 248.
- 6 Isataev S., Toleuov G., Isataev M., Ospanova Sh., Bolysbekova Sh. Impact of frictional resistance of end plates on flat jet attenuation. *Journal of engineering and applied Sciences*. 2015, No.10, pp. 76 – 79.
- 7 Lhendup Namgyal and Hall Joseph W. Coherent streamwise vortex structures in the near-field of the three-dimensional wall jet. *J. Fluid Eng.* 2013, No. 135(6), pp. 120 – 126.

Article accepted for publication 20.02.2020

DOI 10.31489/2020No1/91-97

UDC 621.928.37

STUDY OF SOME FEATURES OF THE LASER OPTICAL-ACOUSTIC METHOD FOR TECHNICAL DIAGNOSTICS OF HEAT AND POWER ENGINEERING OBJECTS

Sharifov D.M.¹, Sakipov K.E.¹, Merzadinova G.T.¹, Kaliyeva Zh.E.^{1,2}, Userbaev M.T.³

¹L.N. Gumilyov Eurasian National University, Nur - Sultan, Kazakhstan

²Institute of Scientific, Technical and Economic Research, Nur - Sultan, Kazakhstan

³S.Seifullin Kazakh AgroTechnical University, Nur - Sultan, Kazakhstan

The article presents the diagnosis of heat power facilities. The distinguishing features of the applied method are shown in solving a number of technologically important diagnostic problems, in particular: quality control of pipe welds, determination of residual stress, structural, mechanical, elastic properties of materials. The physical foundations of the laser optoacoustic method for exciting ultrasonic waves are theoretically investigated. It is shown that this method is based on laser thermo-optical excitation of broadband ultrasonic signals in a test object. Absorbed in a thin surface layer of the object under study, the laser pulse excites a broadband ultrasonic pulse. Propagating in an object, an excited ultrasonic pulse (either a transmitted or scattered ultrasonic signal with a high temporal resolution is recorded) carries information about the object under study.

Keywords: Laser optical-acoustic method, heat-power objects, defects.

Introduction

By definition, heat and power facilities are a complex of interconnected technological equipment (machines, installations, mechanisms, automation and control systems, engineering networks, etc.) intended for generating and transporting heat energy to the consumer. Characteristic features of heat-power objects are that they are under constant external influences (temperature, pressure and other physical loads) throughout almost their entire life cycle. Therefore, the safety and reliability of their operation largely depends on timely and high-quality technical diagnostics. As a rule, the structural foundations of many of these objects are made up of metal materials (screen pipes of boiler plants, discharge plants, steam generators, pipes and shut-off valves, etc.), which are especially exposed to high temperature and pressure differences.

It is known that the formation of defects and destruction of metal parts almost always begins with the formation of microcracks on the surface or deep under the surface of the material. The presence of a concomitant tensile stress on the surface of the studied objects leads to the growth of cracks and thus their further destruction. It is known that the formation of defects and destruction of metal parts almost always begins with the formation of microcracks on the surface or deep under the surface of the material. The presence of a concomitant tensile stress on the surface of the studied objects leads to the growth of cracks and thus their further destruction. Compressive stresses, though, prevent the growth of cracks, but contribute to their formation. If, in addition to the stresses arising from workloads, there are also so-called residual stresses in the metal that arose as a result of special processing or previous operation and remain in the absence of workloads, these stresses are summed up. Therefore, to study the suitability and increase the service life of metal products, it is very important to determine the sign and value of residual stresses in the product [1]. From this point of view, the use of more effective methods of technical diagnostics (TD) and non-destructive testing (NDT) of heat and power facilities plays a key role in the implementation and solution of tasks for the safety and reliability of their operation.

As shown by the research on the technical condition of heat power facilities (for the main sources of heat – boiler equipment, heat networks, heat points, etc.) [1-16]. In the context of the regions of the Republic of Kazakhstan, currently more than half of them have long worked out their operating resources and need major repairs or complete replacement. In this regard, it becomes necessary to solve the problem of creating systems for monitoring, diagnostics and monitoring of these objects in order to prevent and reduce the risk of an accident. It is revealed that the frequency and nature of the level of accidents, damage to boilers (including Autonomous, low-power), heating networks, heat points and other auxiliary equipment, in the vast majority of the overall picture of the state of objects is similar and is primarily associated with:

- wear and tear of equipment due to the expiration of its service life (up to 65-70%);
- leaks (micro-cracks) in the boiler sections and heat exchanger tubes;
- accumulation of scale and sludge in boilers and furnaces;
- formation of scale and leaks on the front and screen pipes of the boiler;
- a violation of the rules of operation and safety;
- exceeding the permissible values of the coolant pressure;
- non-compliance with modern conditions or poor-quality standards and operating rules (both for metal and polymer bases) of heat pipelines;
- lack of specialized diagnostic laboratories and automated systems of regular monitoring for early diagnostics and assessment of the technical condition of these facilities.

1. A brief comparative analysis of the available methods of technical diagnostics and non-destructive testing.

Currently, the following main methods of technical diagnostics and non-destructive testing of various technological objects are identified [11]: Visual and measuring; Ultrasonic; Acoustic emission; Radiation; Magnetic, Eddy current, Penetrating substances (capillary and leak detection), Vibrodiagnostic, Electric, Thermal, Optical and spectroscopy.

As a rule, each of these methods has its advantages and disadvantages, depending on the specific purpose and task of diagnostics. Also, the physical properties of materials and characteristics of research objects are of crucial importance when choosing a specific of NDT methods. Of course, when several methods are used to diagnose objects simultaneously, the probability of determining their real state increases. Depending on the spatial location of possible defects, they can be divided into surface, subsurface with a depth of 0.5 to 1.0 mm and internal with a depth of more than 1.0 mm. Almost all methods are applicable for detecting surface defects, but as a rule, the most effective are visual-optical, magnetic powder and capillary, and for detecting subsurface defects – radiation, ultrasonic, eddy current, and magnetic powder. As practice shows, in the field of heat power engineering, optical, thermal and acoustic (ultrasonic) methods have received the greatest distribution (more than half in relation to other methods of non-destructive testing) [15].

Standard methods and diagnostic technologies based on the above methods are used for thermal power facilities (when examining the quality of welds, seams, joints, and the structural composition of the material). For example, for welded joints and metal structures, this technique is called styloscopy - the simplest type of qualitative spectral analysis for the presence of alloying elements in various metals and alloys. Such a diagnostic procedure is mandatory (according to State Standard 7122-81) for all heating metal surfaces (boiler installations, pipelines, etc.) and welded joints. This method allows you to clearly determine the presence of a certain composition of alloying elements in metal and alloys. In this way, you can control the quality and brand of the welding structure used. The device for stylescope diagnosis and study of spectra is called stylescope. Also, based on the method of capillary flaw detection, the method of color flaw detection (State Standard 18442-80), which is designed to detect surface and through defects,

determine their location or extent (for extended defects of some types) and their orientation on the surface of the object under study. The essence of this method is the penetration of a liquid indicator into the defect, which is well wetting the test material, on the visual study of the material surface and on the subsequent registration of indicator traces [16].

The laser optical-acoustic ultrasonic method includes the features of these methods and is therefore the most versatile, informative, sensitive and in many other parameters (high resolution, visualization, imaging, velocities etc.) superior to many traditional methods of NDT. In particular, in contrast to the traditional ultrasonic method of diagnostics, the parameters (space-time) of the probing pulse allow creating and registering ultrasonic waves of wide frequency bands with the laser OA ultrasonic method. In the end, these characteristics allow you to get better images when visualizing defects and avoid the so-called "dead zones" in the objects under study. As noted, of particular interest is the development of combined methods based on laser optical-acoustic and laser-ultrasonic, which, mutually complementing each other, allow us to obtain more complete information about the object [6].

Laser optical-acoustic (photoacoustic) ultrasonic (LOAU) method - as a method of non-destructive testing is relatively "new" compared to other traditional methods. As its name implies, it appeared as a "laser" after the discovery of lasers and thanks to its unique properties, lasers brought the optical-acoustic method to a completely new level of development. Numerous scientific publications and books [2-10, 13-14], regularly international conferences on photoacoustic and photo-thermal phenomena (ICPPP), as well as the issue of the specialized international scientific journal "Photoacoustic", which has a high rating (Impact factor, 5.25 for 2018), indicate the prospects for the development and application of the LOAU method as one of the most popular methods of technical diagnostics. In the previous works of the authors [9, 18], an analysis of the current state of this method was given and noted of great interest in the study of the fundamental thermo-physical properties (study of the thermal conductivity and thermal diffusivity) of various materials.

The purpose of this work is to evaluate the possibility of using the laser optical-acoustic ultrasonic method for technical diagnostics of various elements of heat-power objects.

2. Theoretical foundation of the LOAU diagnostic method

Laser opto-acoustic diagnostics is based on the photoacoustic effect, the essence of which is the excitation of acoustic waves in the ultrasonic range $f = 2 \times 10^4 \div 10^9 \text{ (Hz)}$ under the action of modulated or pulsed optical (often laser) radiation. Although the effect itself was discovered quite a long time ago (1880, by A. Bell), it received its second revival only after the discovery of lasers as sources of optical radiation with unique properties. It is the high intensity and correlation of spatio-temporal characteristics of lasers that allowed to excite acoustic waves of a fairly wide range, which together with the parallel level of development of signal processing technology contributed to the wide application and development of the OA method as a whole. Depending on the registration methods OA signals (in the frequency range), piezoelectric and microphone registration schemes are distinguished. As a rule, the piezoelectric OA method has a number of advantages: sensitivity (by several orders), frequency range, degree of visualization (imaging of the surface and subsurface defects), resolution, etc. Therefore, the piezoelectric OA method of registration is the most widely used in OA flaw detection. In the theoretical description of the OA diagnostic method, the thermo-optic (thermoplastics) mechanism for generating optical-acoustic signals is mainly considered. It is assumed that a monochromatic laser pulse with a wavelength of λ (or continuous with intensity modulation $f(t) = [1 + m \cos(\omega t)]$), falls on the surface ($z=0$) of the test sample (Fig.1.).

The test sample (blank) is considered opaque at the wavelength of laser radiation λ , i.e., it absorbs at least part of the energy of optical radiation. Further, in the zone of the laser pulse, due to the processes of thermodiffusion (change in the equilibrium state), on the surface and deep into the sample, the absorbed energy is converted into thermal energy, causing a local change in temperature

and, consequently, the thermodynamic and elastic properties of the sample, subsequently generating acoustic waves (OA signal) at the frequency of the incident optical radiation f . This process, as mentioned above, is called the thermo-optic mechanism for generating acoustic waves.

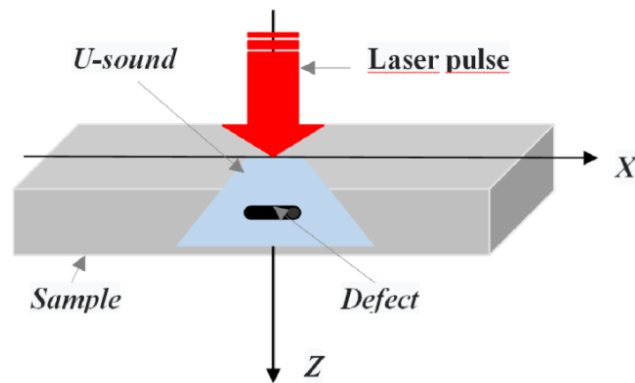


Fig. 1. Geometry of the problem

At the same time, all thermodynamic parameters of the test sample (object) are located far from the point of phase transitions. Theoretical equations describing the processes of thermo-optic excitation of acoustic waves in homogeneous isotropic solid-state materials are well-studied and well-known [2, 8, 13-14, 17]. They represent closed systems of wave equations for acoustic and temperature waves. Depending on the interaction of optical radiation (conditions of the input optical energy, parameters of the radiation source, optical and thermophysical properties of the object of study, etc.), the theoretical descriptions of the generation of OA signals may differ, although the physical essence of the effect remains. For example, for strongly or weakly absorbing optical radiation, the spatio-temporal heating regions and, accordingly, the processes of generating the OA signal change.

One of the important OA parameters is the length of thermal diffusion μ , which allows for varying the frequency of probing laser pulses f , to obtain and control the penetration depth of heat sources and the parameters of the excited ultrasonic radiation. It is related to the frequency of optical radiation modulation f and the thermophysical characteristics of the object of study as:

$$\mu = \left(\frac{2\chi}{\omega} \right)^{1/2}, \quad (1)$$

where, $\chi = \frac{k}{\rho C_p}$ is the coefficient of thermal conductivity (m^2/sec), k is the coefficient of thermal conductivity ($\text{W}/\text{m}\times\text{K}$), ρ is the density (kg/m^3), C_p is the heat capacity ($\text{J}/\text{kg}\times\text{K}$), and $\omega = 2\pi f$ (Hz) is the cyclic frequency.

For the thermal and power facilities (mostly a metal materials) the value of the optical absorption coefficient is sufficiently large ($\beta \approx 10^6 \text{sm}^{-1}$) and accordingly, the optical absorption thickness (light penetration depth) $d \approx 1/\beta$ is less. On the other hand, most metal materials are characterized by high values of the coefficient of thermal conductivity (thermal conductivity) and, accordingly, the length of thermal diffusion μ according to (1). This allows the conditions $d \ll \mu$ to be met. As shown by the analysis of optical-acoustic parameters [2] for most solid-state materials, up to the frequencies of 10^{11} Hz, the connection between heat and acoustic waves in the process of generating OA signals can be neglected, i.e. acoustic waves propagate adiabatically and thus heat waves do not have time to propagate over a distance of the order of the acoustic wave length during the oscillation period. These conditions allow us to solve the thermal and acoustic part of the problem separately. Therefore, to determine the temperature field $T(z=0, t)$, you can use the

original equations of thermal conductivity with the corresponding boundary conditions (equality of temperature and heat flows at the boundaries, $z=0$):

$$\begin{cases} \frac{\partial T_1}{\partial t} = \alpha_1 \Delta T_1 \\ \frac{\partial T_2}{\partial t} = \alpha_2 \nabla T_2 \end{cases}, \quad (2)$$

$$T_2|_{z=0} = T_1|_{z=0}, \quad \rho_2 c_2 \alpha_2 \frac{\partial T_2}{\partial z}|_{z=0} = \rho_1 c_1 \alpha_1 \frac{\partial T_1}{\partial z}|_{z=0} + I_0 f(t), \quad (3)$$

where the indices denote, respectively, a transparent 1 and an absorbing 2 medium, $I(t, z=0) = I_0 f(t)$ - intensity of laser radiation.

The equations for determining the generated acoustic field for the potential φ (vibrational velocity v), are systems of wave equations (4) with the right part describing the distributions of thermal sources defined by (2) and (3):

$$\begin{cases} \frac{1}{v_1} \frac{\partial^2 \varphi_1}{\partial t^2} - \Delta \varphi_1 = -\beta_1 \frac{\partial T_1}{\partial t} \\ \frac{1}{v_2} \frac{\partial^2 \varphi_2}{\partial t^2} - \Delta \varphi_2 = -\beta_2 \frac{\partial T_2}{\partial t} \end{cases}, \quad (4)$$

Here $p = \rho c v = \rho c(\text{grad}\varphi)$, $v = \text{grad}\varphi$ and β_1, β_2 - are the effective thermal expansion coefficients of these media.

Boundary conditions describing the continuity of pressure and vibrational velocity at the interface of two media have the form:

$$\rho_1 \varphi_1|_{z=0} = \rho_2 \varphi_2|_{z=0}, \quad \frac{\partial \varphi_2}{\partial z}|_{z=0} = \frac{\partial \varphi_1}{\partial z}|_{z=0}. \quad (5)$$

The systems of equations (2) and (4) with corresponding boundary conditions (3) and (5) represent a theoretical model of the processes of thermo-optic excitation of OA signals and usually have their own methods and approaches for analytical solution (spectral, green functions, Fourier transform, Laplace, etc.) [2, 13-14]. The results of theoretical analysis show that the shape of the OA signal profile will repeat the envelope of the laser pulse (for a short duration of the laser pulse), i.e. it will not contain fluctuations that are characteristic of acoustic pulses excited by piezoelectric method. This is one of its characteristic features, which allows you to successfully use it when solving diagnostic problems. The parameters of the LOAU signal depend on a number of physically important properties of the objects under study (optical, thermal, elastic, geometric dimensions and acoustics). Therefore, the OA signal is quite informative and in certain cases, depending on the object of research, it is used in solving various problems of diagnostics (properties of gases with microphone detection, liquids and solids, porous, multilayer, biomedical, etc.).

3. Application of the LOAU diagnostic method

One of the main objects of heat energy production, as noted above, is a boiler plant (BP), which is under constant temperature and pressure changes. Therefore, at the same time, the BP is the most likely source of accidents and malfunctions in heat power facilities. The objects of technical control are: heating surfaces of boiler installations, smoke pumps, blow fan, auxiliary equipment, walling, fuel supply systems, economizers, regenerative air heaters, gas pipelines, automation, fuel treatment systems in solid fuel CU (mill, coal feeders and conveyors), fittings and other elements. Also, currently in the Kazakhstan, more than half of the heat and power equipment

has developed an operational life, which is why the problem of creating control systems, technical diagnostics and monitoring of heat and power facilities is becoming more acute.

As a rule, low reliability of heating equipment leads to accidents and significant energy losses and, as a result, to high economic costs and a significant amount of repair and restoration work. It should be noted that the improvement of technical diagnostics methods and the search for innovative methods are becoming more relevant. Thus, complementing the capabilities of other traditional methods of technical diagnostics, LOAU flow detection is essentially innovative in this direction. The heat and power objects under investigation are mainly metal pipes of various diameters and thicknesses. Schematically, the principle of operation of LOAU flow detectors for quality control of welds is shown in figure 2. After absorption of the laser pulse in the OA source, an ultrasonic pulse (longitudinal acoustic waves with a known amplitude and frequency spectrum) is excited in it, i.e., a probing (reference) pulse, which then propagates in the sample under study and is registered using a specially designed broadband piezoelectric receiver that is in acoustic contact with the sample.

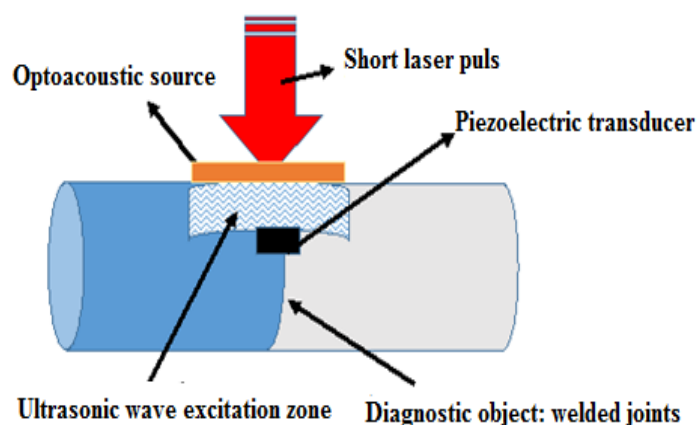


Fig.2. Principle of application of the LOAU flow detector

Currently, many authors have developed and patented a number of experimental and semi-industrial flow detectors based on laser OA excitation of broadband ultrasonic waves. For example, the ultrasonic laser multifunctional flaw detector UDL-2M is designed for ultrasonic examination of structural disorders of materials such as metals, composites, ceramics and plastics. As noted [17, 18], the generation of broadband acoustic pulses occurs due to the laser thermo-optic mechanism of ultrasound excitation. The thickness of the test samples can be 0.1 ... 70 mm, the cross dimensions - from 10 mm.

Conclusions

The analysis of the possibility of using the LOAU diagnostic method for the examination of various heat and power facilities is carried out. It is noted that this method has a number of characteristic advantages in comparison with other traditional methods of ultrasound control, which makes it possible to successfully apply it. In particular, high resolution (tens of microns), allowing visualization of defects, the absence of a "dead zone" in the considered area of the object, also the high sensitivity to the change of sign of the impedance environment that allows to distinguish the defects of porous and dense inclusions, microcracks, etc. Thus, the analysis shows that the LOAU method, complementing the traditional methods of technical diagnostics, can be successfully applied in the technical diagnostics of various heat and power facilities.

REFERENCES

- 1 Ovchinnikov V.V. *Weld defects and quality control of welds*. Moscow, 2017, 224 p. [in Russian]
- 2 Gusev V.E., Karabutov A.A. *Laser optoacoustics*. American Institute of Physics, 1993, 203 p.
- 3 Tam A.C. Pulsed-laser generation of ultrashort acoustic pulses: Application for thin-film ultrasonic measurements. *Appl. Phys. Lett.* 1984, Vol. 45, No. 5, pp. 510–512.
- 4 Bychkov A., Simonova V., Zarubinet V., et al. The Progress in Photoacoustic and Laser Ultrasonic Tomographic Imaging for Biomedicine and Industry: A Review. *Appl. Sci.* 2018, Vol.8, 1931, pp. 1 – 26.
- 5 Wang L.V. *Photoacoustic Imaging and Spectroscopy*. Boca Raton: CRC Press. 2009, 499 p.
- 6 Bychkov A.S. Combined optical-acoustic and laser-ultrasonic tomography of media with inhomogeneities of acoustic properties and induced heat sources. Diss. PhD, Moscow. 2019, 128 p.
- 7 Zakrzewski J., Chigarev N., Tournat V., Gusev V. Combined Photoacoustic–Acoustic Technique for Crack Imaging. *Int. J. Thermophys.* 2010, Vol. 31(1), pp.199-207.
- 8 Sylvain Mezil. *Nonlinear optoacoustics method for crack detection & characterization*. Diss. PhD, Universite du Maine, Le Mans, France, 2012, 176 p.
- 9 Merzadinova G. T., Sakipov K. E., Kalieva Z. E., et al. Laser optical-acoustic ultrasonic method of technical diagnostics of heat power facilities. *Proceeding of the 11th Intern. Scient. Conf. “Chaos and structures in nonlinear systems. Theory and experiment”*, Karaganda, 2019, pp. 336–339.
- 10 Pelivanov I.M., Kopylova D.S., Podymova N.B., Karabutov A.A. Optoacoustic method for determination of submicron metal coating properties: Theoretical consideration. *J. Appl. Phys.*, 2009, Vol.106, pp. 0135071–0135078.
- 11 Ivanov E.A., Kotelnikov V.S., Shatalov A.A. et al. *Regulatory document. Rules for personnel certification in the field of non-destructive testing*. Series 28. Issue 3. Team of authors. Moscow, 2010, 58 p.
- 12 *State Standard: R53696-2009. National standard of the Russian Federation. Non-destructive testing. Optical methods. Terms and definitions*. Moscow, Standard inform. 2010, 17 p.
- 13 Tam A. Applications of photoacoustic sensing techniques. *Rev. Mod Phys.* 1986, Vol. 58(2), pp.381.
- 14 Lyamshev L.M. *Laser thermo-optical excitation of sound*. Moscow, 1989, 240 p. [in Russian]
- 15 Ivasev S.S., Girin A.V., Ravodina D.V. *Methods of non-destructive testing*. Krasnoyarsk, 2015, 112p. [in Russian]
- 16 Konstantin A. Flaw detection of welds: characteristics of the main types, rules of execution, advantages and disadvantages. Available at: <https://elsvarkin.ru/tehnologiya/kontrol/defektoskopiya-shvov>.
- 17 Karabutov A.A., Kobeleva L.I., Podymova N.B., et al. Laser optical-acoustic method for local measurement of elastic modules of composite materials strengthened by particles. *Technical acoustics*. 2008, No. 19, pp. 1-15.
- 18 Merzadinova G.T., Sakipov K.E., Sharifov D.M. et al. Laser photoacoustics method for determination of the coefficients of thermal conductivity and thermal diffusivity of materials. *Eurasian Physical Technical Journal*. 2019, Vol. 16, No. 1(31), pp. 94 - 98.

DOI 10.31489/2020No1/98-105

UDC: 62-531.7

STUDY OF DYNAMIC PROCESSES IN BULK MATERIAL DURING ITS BAKING

Nizhegorodov A.I.¹, Gavrilin A.N.², Moyzes B.B.², Kuvshinov K.A.²

¹ Irkutsk National Research Technical University, Irkutsk, Russia, nastromo_irkutsk@mail.ru

² National Research Tomsk Polytechnic University, Tomsk, Russia, mbb@tpu.ru

The article presents the results of research on the dynamics of the base plate of an electric furnace for the heat treatment of bulk materials. The base plate with moving trolley on elastic bonds serves as the base which transports the heat-treated material in the hot part of the heating system with a specified speed and processing time. The experimental total elastic characteristic of the oscillating system is obtained; the amplitude-frequency characteristic is constructed, which characteristic is weak nonlinearity. Experiments have shown that conical springs of different designs do not provide a strong asymmetry in the base plate oscillations and therefore the vibrational transport efficiency is weak in the horizontal position of the prototype furnace. Further experiments were conducted when the furnace was installed at an angle to the horizontal surface. The vibrational transport time of vermiculite was reached 2.7...3.2 s, depending on the excitation frequency settings near the resonance zone. It is shown that the operation of the vibrating base plate may not be stable due to the high sensitivity of the excitation frequency from various factors. Methods for reducing the sensitivity coefficient are considered.

Keywords: bulk materials, electric furnace, vibrating base plate, oscillating system, nonlinear amplitude-frequency characteristic, oscillating system sensitivity to external factors.

Introduction

Electric furnaces with a vibration base platform [1] were developed as an alternative to the fire furnaces for vermiculite backing. First they operated on fuel oil and diesel fuel, and at present natural gas is used as a fuel. But their technical improvement stopped in the early 2000s, with the minimum energy intensity reached about 250...260 mJ/m³. Tests of new modern electric furnaces with a vibratory base platform showed that they more energy efficient and they significantly exceed the outdated fire furnaces: the specific energy intensity of vermiculite backing decreased to 75 ... 82 mJ/m³ [2]. This advantage is due to the fact that the energy of the fire torch is distributed in large working chambers with a volume of 1.2...1.8 m³. With a capacity of 6 m³/hour, the volume of the expanded material in it is 0.0062 m³, which is approximately 0.53% of the volume of the chamber. In electric furnaces of the same capacity, the heating energy is inclosed in a very small production space (0.06...0.08 m³) between the base plate and the thermowell, where backing takes place. Here, the thermal field of electric heaters is incomparably more concentrated.

In addition to the high energy consumption of backing process, the fire furnaces have a number of serious drawbacks: air pollution by combustion products, high fire and explosion hazards, etc. new low energy consumption, furnaces accommodate more the requirements of environmental, industrial and fire safety [3-10]. The article "The development of baking technology for bulk materials based on the use of alternative electric furnace" reviewed the development of the design of an electric furnace prototype and conducted a static study of the parameters of an oscillating system. This research continues to study the dynamics of the developed system and the dynamics of bulk material.

2. Samples and Research Methods

During the dynamic tests, there were calculated the peak values of the vibration displacement (mm) and the root-mean-square vibration velocities (mm/s) and vibration accelerations (m/s^2). The following measuring instruments and equipment were used: National instruments Compact DAQ-9174 chassis with 4 slots for C-series modules, NI 9234 C-series input module and AP-85-100 vibration transducer. Figure 1 shows a mock-up model without a dispenser of heating system and thermal cover (photo), on which the experiments were conducted.

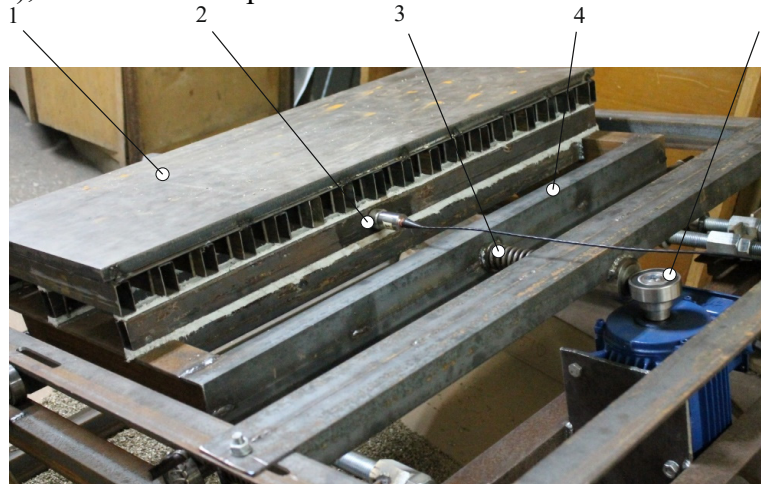


Fig.1. Physical model in the testing process:

1 – base plate, 2 – vibrator converter, 3 – pusher spring, 4 – moving trolley, 5 – eccentric.

Table 1 shows the measurement results. The data from the first and second columns of the table were used to build the amplitude-frequency characteristic – the dependence of peak amplitude values on the excitation frequency f (Hz). Only the amplitude-frequency characteristic area near the resonance was investigated in order to evaluate the nonlinearity of the oscillating system of the experimental furnace at «large oscillations». A vibrodrive was started up (asynchronous engine 5AI 80 V6U2 with nominal frequency $n=930$ rpm and 1.1 kW power), which excited vibrations of the moving trolley with the base plate and provided frequency control f . To control the oscillation frequency, the ACS 150 frequency converter was used.

Figure 2 shows the experimental graphs of the amplitude-frequency characteristic (AFC) of the moving trolley with the base plate on one-sided conical springs. The resonant point corresponds to the excitation frequency of 8.9 Hz, which almost coincides with the calculated value of 8.77 Hz. Graphs analysis shows that behavior of the oscillatory system does not fit into the classical picture characteristic of linear or nonlinear systems. Thus, when increasing the excitation frequency from 6.25 to 11.3 Hz, the moving trolley with the base plate behaves like a nonlinear system with a so-called «soft» characteristic [11, 12]. A specific feature of this effect is a jump-type transition from the pre-resonant mode of small oscillations to the post-resonant mode from point a to point b , where the AFC is breaking [13-17]. However, in the opposite direction, when the excitation frequency decreases, the system goes through resonance at a peak amplitude value of ~ 2.5 mm smoothly, without breaking the AFC, although its downward (left) branch is located almost vertically. The form of the obtained amplitude-frequency characteristic shows a very weak nonlinearity. A harmonic analysis of the oscillation of the moving trolley at resonance $x=f(t)$ detected the presence of a second harmonic with a frequency of $2f$ and an amplitude of 12.4 times less than the amplitude of the main harmonic which corresponds to the excitation frequency. This means the presence of biharmonic oscillations, which can create an asymmetry of the oscillatory motion with a certain combination of harmonic phases and confirms the appearance of a weak nonlinearity of the system. But there was no noticeable asymmetry on the resonant oscillations oscillogram (x).

Table 1. The measurement results of oscillation parameters.

No.	Excitation frequency, [Hz]	Peak value of vibration displacement amplitude, [mm]	Root-mean square value of vibration velocity, [mm/s]	Root-mean square value of vibration acceleration, [m/s]
<i>Excitation frequency increase, f</i>				
1	6.25	0.06	1.7	0.177
2	7.4	0.085	2.8	0.46
3	7.6	0.08	2.6	0.428
4	7.8	0.08	2.8	0.661
5	7.9	0.082	2.9	0.51
6	8.2	0.083	3.1	0.573
7	8.4	0.086	3.2	0.588
8	8.6	0.9	3.54	0.74
9	8.7	0.1	3.87	0.796
10	8.9	0.11	4.32	1.13
11	9.1	1.98	79.8	4.82
12	9.3	1.2	50.3	3.22
13	9.5	0.77	32.3	2.57
14	9.9	0.52	22.9	2.35
15	10.5	0.33	15.4	2.01
16	11.3	0.24	12.2	1.38
<i>Excitation frequency reduction, f</i>				
17	10.9	0.26	12.4	1.39
18	10.1	0.45	20.6	1.57
19	9.5	0.93	39.7	2.86
20	9.1	1.5	62.6	3.67
21	8.9	2.5	100.68	6.3
22	8.9	2.5	104.6	6.3
23	8.9	2.26	90.1	5.2
24	8.7	0.59	23.09	1.75
25	8.6	0.2	7.3	0.806

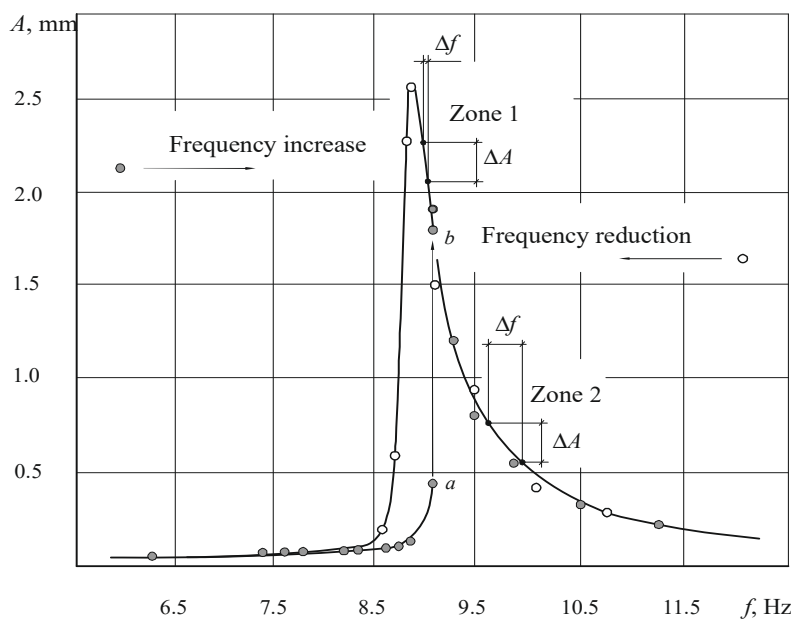


Fig.2. AFC of the oscillatory system.

The exfoliated vermiculite was used when testing the vibrotransport effect in a horizontal position. There was no tendency to unidirectional movement, the chaotic grain movements were observed, which are unacceptable for reasons of wearability and breakage. The tip angle of the base plate is the only factor allows the unidirectional movement of the material on the platform. The increasing an angle to 9° did not give an effect. The transport effect became discernable only at a tilt of 19° and the post-resonant operation mode. The oscillatory system is extremely sensitive to the above-mentioned possible fluctuations due to the high quality factor, expressed in a narrow, elongated resonant peak of the AFC (Fig. 2). The ratio $\varepsilon = \Delta A / \Delta f$ estimates the sensitivity of the ε system to the amplitude deviation during the fluctuation of the excitation frequency. The system is the most sensitive in zone 1 near resonance, since the slightest change in Δf , for example, 0.06 Hz, leads to a change in the amplitude of oscillations by 0.22 mm. The coefficient of sensitivity is approximately equal to $\varepsilon = 3.7$ mm/Hz. Whereas, in zone 2 at $\Delta f \approx 0.31$ Hz and the same $\Delta A \approx 0.22$ mm, the sensitivity coefficient is $\varepsilon = 0.71$ mm/Hz.

So, the sensitivity of the oscillatory system increases by $3.7/0.71 = 5.2$ when passing from zone 2 to zone 1 that is, it increases by more than five times. It is necessary to maintain steady vibration parameters near zone 2 (Figure 2) to ensure the stability of vibrotransporting of the flowing medium in the thermal field of the heating system of the furnace. Here, the feed rate is adjustable, but vibrational acceleration was insufficient ($1.38 \dots 2.35$ m/s², table 1) for particles to overcome friction and start one-way traffic because of the type of conical springs installed on the moving trolley and due to weak non-linearity of the system when levels are horizontal.

The short conical springs with diameters at the top are 16 mm and at the base 64 mm, with length 31 mm were tested to reinforce the nonlinearity of elasticity of the oscillatory system and to achieve the vibro-transport effect. They are designed the way that when fully compressed, the coils of the springs are fitted one into the other and the spring is compressed in length to the thickness of its coil. Figure 3 shows a fragment of the moving trolley with short conical springs and one of such springs.



Fig.3. A fragment of the moving trolley with short conical springs (*a*) and the spring itself (*b*).

The total stiffness of the system decreased and became equal to $c = 210031$ N/m. The natural frequency calculated by the formula (1) in terms of Hz, was 8.3 Hz. During the experiments, the oscillation mode varied, but their frequency changed near the resonant peak of the oscillatory system, where the nonlinearity of the system is very strong. When it was located on the surface of the base plate, the expanded vermiculite (with grain size 2 to 8 mm) tended to move to desired direction at the maximum amplitude (about 2.3 mm) and in close to the resonance, when the furnace prototype was in horizontal position [18-21].

When the oven was installed at an angle of 9° , this tendency intensified, but the time for moving index marks made in the form of paper pellets and placed in a single-layer array of

expanded vermiculite grains ranged from 15 to 20 s with a base plate length of 0.4 m. Obviously, such movement mode could not provide the required performance of the furnace during the vermiculite baking [22, 23]. For this it was necessary to achieve the time of movement of the material on the platform within 2.7...3.2 s. Therefore, the further of experiments were continued on the former conical springs at a tilt angle of 19°.

When measuring, the frame of the furnace prototype was set at an angle of 19 ° (Figure 1). The cold exfoliated vermiculite was used for experiments. The bottom plate was also cold (23...24 ° C). The expanded vermiculite was poured on the base plate. It was leveled to obtain a single-layer array, evenly distributed over the surface without gaps between the grains. The index mark made in the form of paper pellet was put on the surface of the platform to track the movement of expanded vermiculite. The path section that index mark passed ranged from 0.39 to 0.3 m. with the length of the base plate $l_p=0.4$ m. The time was controlled by a stopwatch; and the average speed in each experiment at each relevant path section l_n was calculated using the formula:

$$v = \frac{l_p}{t}.$$

The rotation frequency of the field in the stator of actuator coils of the driving motor f_m was controlled by digital indicator of the frequency converter and was recalculated to the oscillation frequency of the moving trolley f according to the formula:

$$f = \frac{930}{3000} \cdot f_m,$$

where 3000 – AC mains frequency in rpm (50 Hz), 930 – engine revolutions in rpm.

Since in each experiment the path sections were different, the average movement time of vermiculite grains through the full length of the base platform was calculated using the formula:

$$t_m = \frac{l_p}{v_m}.$$

and the average speed in three experiments was determined as an arithmetic average value.

There are the results of one of the experiments in table 2 as an example.

Table 2. The speed and time of vermiculite movement at $f=9.13$ Hz

Path section, l , [m]	Movement time, t , [s]	Speed, v , [m/s]	Average speed, v_m , [m/s]	Average time, t_m , [s]
0.39	2.47	0.158	–	–
0.37	2.46	0.15	–	–
0.37	3.07	0.121	–	–
–	–	–	0.143	2.79

Figure 4 shows the dependence of the average movement time of index marks on the base plate surface on oscillations frequency in a narrow post-resonant range. In the area from 8.9 to 9.1 Hz (at the very beginning of post-resonant zone, at a resonance of 8.9 Hz), the movement time does not change. The amplitude decrease in this range is compensated by an increase in the angular frequency ω from 55.9 to 57.1 rad/s. Therefore, the vibration acceleration determined by the formula (m/s^2):

$$\ddot{x} = A\omega^2,$$

under the condition of harmonic oscillations, also does not change.

However, a further increase in the oscillation frequency leads to an increase in the vibration acceleration and the movement time of vermiculite grains on the base platform and, approximately at a frequency of 9.13 Hz, the time of movement becomes equal to 2.8 s, which corresponds to the average baking time of vermiculite concentrates. For this oscillatory system figure 4 shows the

frequency range (9.12...9.16 Hz) where the baking time is controlled depending on the type and size of the heat-treating material.

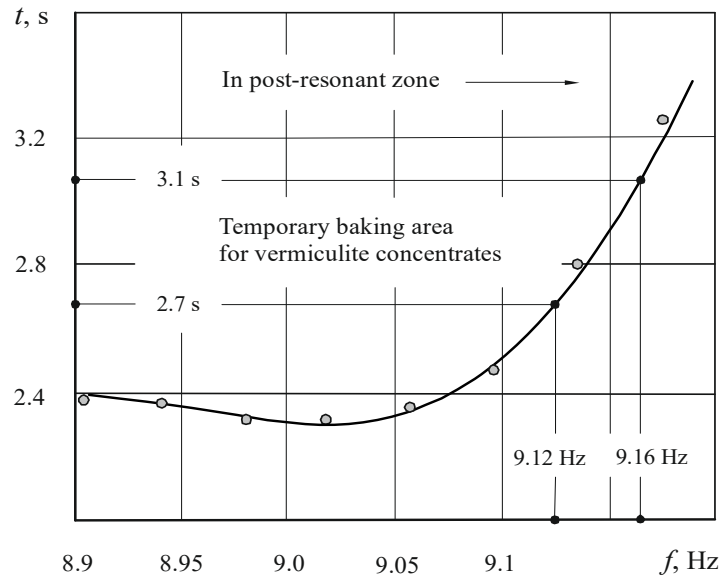


Fig.4. The time change of index mark movement in single-layer array of vermiculite in post-resonant zone.

3. Results and discussion

Thus a prototype furnace with a vibratory base plate was tested and experiments proved that this design can be used for building an industrial three-module furnace for baking vermiculite and other potentially high-temperature-activated bulk materials, for example, sungulite-vermiculite [22-26]. At the same time, its efficiency will be significantly higher than the known modular trigger furnaces by reducing the baking energy intensity from 170...175 to 75...82 mJ/m^3 .

The vibratory base plate on the moving trolley is a vibrating dispenser which provides the flow and time-controlled movement of bulk materials in the thermal field of the electric heating system of the furnace due to the vibrating effect. Experiments have shown that the purpose of research has been achieved. A rational design of the furnace oscillating system has been obtained, the modes of vibratory displacement of bulk materials have been worked out, the frequency range in which heat treatment is carried out for a duration of 2.7...3.1 s has been determined.

Conclusion

Analyzing the obtained results, it is necessary to consider that some shortcomings require further work on the improvement of such furnaces. It has already been noted above that due to the high quality factor, the oscillating system is too sensitive to the above-mentioned possible fluctuations in frequency, rigidity, friction and other factors in high-temperature conditions and the instability of the electrical network. For example, the oscillatory system sensitivity to fluctuations of the excitation frequency in different zones of the frequency response may vary by more than five times, and this will affect the heat treatment time.

Therefore, it is necessary to achieve the possibility of vibro-transporting of bulk medium at horizontal position of the base plate due to non-symmetrical vibrations. It is necessary to create a strong nonlinear elastic behavior of the system, so that its resonance peak would be strongly "bend" to the left [11, 17], and then the sensitivity coefficient of amplitude ε to fluctuations of the excitation frequency can be significantly reduced.

When tilted, the round particles of some bulk materials can simply roll under the gravity, not due to the vibro-transport effect, which will reduce their processing time. There is another important

reason for horizontal installation of the base plate. If there is a slope, an air draft effect occurs, which will cause the movement of external air in the baking space under the thermal cover of the module. It will lead to cooling of the heating system of the furnace unit.

The relative error of the frequencies of the resonant point is only:

$$\Delta = \frac{8.90 - 8.77}{8.90} \cdot 100 \% = 1.46 \%$$

This allows us to conclude about the validity of the results. The research is a continued of the previous authors studies [1-3]. The obtained results allow us to continue work in the development of the electric furnace for the heat treatment of bulk materials. The novelty of the approach used in this study is confirmed by a number of patents for inventions mentioned in the research [1].

Acknowledgements

The research is carried out at Tomsk Polytechnic University within the framework of Tomsk Polytechnic University Competitiveness Enhancement Program grant.

REFERENCES

- 1 Nizhegorodov A.I. Energy efficient electric furnace with moving hearth platform for firing vermiculite. *Refractories and Industrial Ceramics*. 2017, Vol. 58, No. 1, pp. 29 – 34. doi: 10.1007/s11148-017-0049-4.
- 2 Nizhegorodov A.I., Bryanskikh T.B., Gavrilin A.N., Moyzes B.B., Vavilova G.V., Gradoboev A.V., Tlusty J., Tuzikova V. Testing a new alternative electric furnace for vermiculite concentrates heat treatment. *Bulletin of the Tomsk Polytechnic University, Geo Assets Engineering*. 2018, Vol. 329, No 4, pp. 142 – 153.
- 3 Nizhegorodov A.I. The effectiveness of fire and electrical module and trigger kilns vermiculite. *Engineering technology*. 2010, Vol. 1, pp. 32 – 34.
- 4 Lozano-Lunar A. et al. Safe use of electric arc furnace dust as secondary raw material in self-compacting mortars production. *J. of Cleaner Production*. 2019, Vol. 211, pp. 1375 – 1388.
- 5 Santamaria A., Faleschini F., Giacomello G., et al. Dimensional stability of electric arc furnace slag in civil engineering applications. *J. of Cleaner Production*. 2018, Vol. 205, pp. 599 – 609.
- 6 Xu W., Zhang J., Zhang R. Application of multi-model switching predictive functional control on the temperature system of an electric heating furnace. *ISA Transaction*. 2017, Vol. 68, pp. 287 – 292.
- 7 Bryanskikh T.V., Kokourov D.V. Energy efficiency of electric furnaces with movable floor in firing of vermiculite concentrates of different size groups. *Refractories and Industrial Ceramics*. 2017, Vol. 58, pp.368 – 373. doi: 10.1007/s11148-017-0113-0.
- 8 Zvezdin A.V., Bryanskikh T.B. Considering adaptation of electrical ovens with unit-type releasing to peculiarities of thermal energization of mineral raw materials. *IOP Conf. Series: Materials Science and Engineering*. 2017, Vol. 168, No.1, pp. 012003.
- 9 Bryanskikh T.V. A study of the energy efficiency of electric furnaces with vibrating movable platform for heat treatment of mineral ore. *Vest. IrGTU*. 2016, Vol. 12, pp. 12 – 19.
- 10 Tymchak V.M., Gusovskii V.L. *Design of heating and thermal furnaces. Reference*. Moscow, Metallurgiya, 1983, 480 p. [in Russian]
- 11 Blekhman I.I. *Vibrations in engineering: reference book. Oscillations of nonlinear mechanical systems*. Moscow, Mashinostroenie, 1979, 351 p. [in Russian]
- 12 Bauman V.A., Bykhovskij I.I. *Vibration machines and processes in construction*. Moscow, Vysshaya shkola, 1977, 255 p. [in Russian]
- 13 Gvozdkova S.I., Shvartsburg L.E. Analysis of sources and methods for reducing noise by minimizing vibrations of engineering technological processes. *Procedia Engineering*. 2017, Vol. 206, pp.958 – 964.
- 14 Mo J.P.T., Cheung S.C.P., Das R. *Demystifying Numerical Models*. Oxford, 2019, 274 p.
- 15 Sofiyev A.H. Review of research on the vibration and buckling of the FGM conical shells. *Composite Structures*. 2019, Vol. 211, pp. 301 – 317.
- 16 İşçi S. Intercalation of vermiculite in presence of surfactants. *Applied Clay Science*. 2017, Vol. 146, pp. 7 – 13.

- 17 Ritz M., Zdrávková J., Valášková M., Vibrational spectroscopy of acid treated vermiculites. *Vibrational Spectroscopy*. 2014, Vol. 70, pp. 63 – 69.
- 18 Surzhikov A.P., Frangulyan T.S., Ghyngazov S.A. A dilatometric study of the effect of pressing on the kinetics of compression of ultrafine zirconium dioxide powders under thermal annealing. *Russ. Phys. J.* 2012, Vol.55, No.4, pp. 345 – 352. doi: 10.1007/s11182-012-9818-1.
- 19 Surzhikova O. Power supply of remote and almost inaccessible settlements. *IOP Conference Series: Materials Science and Engineering IOP*. 2015, Vol. 81, No.1, pp. 012098. doi 10.1088/1757-899X/81/1/012098
- 20 Bemš, J., Starý, O., Macaš, M., Žegklitz, J., Pošík, P. Innovative default prediction approach. *Expert Systems with Applications*. 2015, Vol. 42, No. 17-18, pp. 6277 – 6285. doi: 10.1016/j.eswa.2015.04.053.
- 21 Surzhikov A.P., Peshev V.V., Pritulov A.M., Gyngazov, S.A. Grain-boundary diffusion of oxygen in polycrystalline ferrites. *Russian Physics Journal*, 1999, Vol.42, No.5, pp. 490 – 495. doi: 10.1007/BF02508222.
- 22 Kremenetskaya I.P., et al. Serpentine minerals amorphization in the technology of magnesia-silicate reagent for immobilization of heavy metals. *Chemistry for Sustainable Development*. 2010, Vol.18, pp. 41 -49.
- 23 Viti C., Hirose T. Thermal decomposition of serpentine during coseismic faulting: Nanostructures and mineral reactions. *J. of Structural Geology*. 2010, Vol. 32, No.10, pp. 1476 – 1484.
- 24 Li J., Hitch M. Mechanical activation of magnesium silicates for mineral carbonation, a review. *Minerals Engineering*. 2018, Vol. 128, pp. 69 – 83.
- 25 Plotnikova I., Redko L., Titova O., Chaykovskaya O. Development of the Production Process Model Based on the Controllable Input Factors. *IOP Conf. Series: Materials Science and Engineering*, 2016, Vol.132, pp. 012023. doi.org/10.1088/1757-899X/132/1/012023.
- 26 Redko V.V., Starikova N.S., Redko L.A., Vavilova G.V. Determination of sensitivity for in-process control of cable product insulation. *IOP Conf. Series: Materials Science and Engineering*. 2015, Vol. 81, No.1, pp. 012083. DOI: 10.1088/1757-899X/81/1/012083.

DOI 10.31489/2020No1/106-112

UDC: 533.682; 533.6.01; 621.548

MODELING AERODYNAMICS OF A WIND TURBINE WITH CYLINDRICAL BLADES IN A TURBULENT AIR FLOW

Sakipova S.E.¹, Tanasheva N.K.², Minkov L.L.³

¹E.A. Buketov Karaganda State University, Karaganda, Kazakhstan, sesaule@mail.ru

²Institute of Applied Mathematics, Karaganda, Kazakhstan, nazgulya_tans@mail.ru

³National Research Tomsk State University, Tomsk, Russia

The article discusses some of the possibilities of computer simulation of aerodynamics flow past a three-bladed wind turbine using the ANSYS FLUENT software package. The peculiarity of the object of study is that the wind wheel consists of three blades rotating around its axis. The system of equations, boundary conditions and made during modeling assumptions are presented. The system of equations in approximating the $k-\epsilon$ model of turbulence is solved by the finite volume method and applying the approach of multiple (nested) coordinate systems using the Ansys-Fluent package. The computational domain was divided into three types of subregions nested within each other. As a result of modeling the velocity field near the wind wheel surface vortex zones were visualized. It is showed that in the vicinity of the wind wheel central disk, the air flow unfolds in the opposite direction to the main flow. The dependences of aerodynamic coefficients on speed are obtained while the cylinders rotation speed varies in the range from 300rpm to 700 rpm.

Keywords: wind turbine, aerodynamics, rotating cylinder, ANSYS FLUENT software packages, drag force, lift force, Reynolds criterion, 3-dimensional modeling.

INTRODUCTION

It is known that to reduce energy security the country needs to deploy a number of renewable energy sources (RES), [1-4]. Statistics show that Central Asian countries rich in fossil fuels, in particular Kazakhstan, are leaders in the renewable energy segment, while countries with low hydrocarbon content have virtually no renewable energy facilities [3]. Despite economic difficulties in Kazakhstan, favorable conditions have been created for the development of renewable energy facilities. As was noted earlier [5-6], wind energy is the most relevant direction for the development of renewable energy sources, since wind power plants are one of the most environmentally friendly methods of energy production. In recent years, a number of domestic and foreign scientists and engineers have developed various original wind power plants, a detailed review of which is presented in [7-10]. An analysis of published works and well-known developments confirms that it is necessary to develop small or medium-sized autonomous wind farms that can efficiently convert wind energy into electrical or thermal energy.

The high level and capabilities of computational technology and 3D computer simulation sometimes allow us to replace complex experimental studies, for example, an aerodynamics of streamlined bodies. This does not exclude experiments in general, but it allows us not to interrupt the study, which is especially important in the absence of real possibilities for conducting practical tests, as at present in the quarantine period of forced self-isolation due to coronavirus. 3D computer modeling allows you to discover new aspects and important results that are very useful in practical implementation. In the present paper some aspects of computer simulation of the aerodynamics of a wind turbine with rotating cylinders using the ANSYS FLUENT software packages are discussed. Despite the fact that a cylindrical body has been used in aero-hydrodynamics for many years, the study and modeling of the aerodynamics of its flow under various conditions are still relevant.

Indeed, the aerodynamics of the flow around a rotating cylinder depends not only on its surface state (smooth, porous, rough) and the shape of its ends (flat, rounded, cone-shaped, etc.), but also on its rotating speed around its axis [7, 11, 12]. For example, in [13] flows were compared over a smooth two-dimensional round cylinder and a finite round cylinder. In particular, the impact due to the textile roughness on the critical transition phenomenon was emphasized.

1. Problem statement and system of equations.

In paper [12] the problem was formulated at stage of solution in an axisymmetric statement, where the dependence on the azimuthal coordinate φ was not taken into account. A computer model of wind turbines with three angled blades is also described and presented in detail. Fluid flow was assumed to be laminar and was described by a system of control equations in dimensional formulation, including: total energy conservation equation; momentum equation; continuity equation with corresponding boundary conditions. An unstructured computational grids of the model was generated in the ANSYS MESH subroutine, computations were performed in the ANSYS CFX and ANSYS FLUENT [14, 15]. Using these software packages a CAD-model of the wind turbine with rotating cylinders having flat disks at its ends has been developed. The results of a 3-D modeling of the dynamics of the aerodynamic drag force of a virtual three-bladed model of a wind turbine with rotating cylindrical blades allowed show in a first approximation, the physical flow pattern in the range of air flow variation from 3 to 10 m/s.

In this case, the following basic assumptions are made to describe the aerodynamics of the flow of air flowing around the rotating cylinders of a wind power plant.

1. The ratio of gas velocity to local sound velocity, $M \ll 0.1$. Due to the low values of the Mach numbers, the air flow can be described by equations valid for an incompressible medium.
2. Given condition 1 and due to insignificant temperature differences in the vicinity of the wind wheel, the flow can be considered isothermal.
3. Due to the high speeds of the incoming air flow, the Reynolds number $Re > 10^4$, at which the ratio of inertial forces to viscosity forces is large enough, the flow can be considered turbulent.

Let consider a system of equations describing the dynamics of the air flow around a wind wheel under given the above conditions.

$$\frac{\partial u_j}{\partial x_j} = 0, \quad (1)$$

$$\frac{\partial \rho u_i}{\partial t} + \frac{\partial \rho u_i u_j}{\partial x_j} + \frac{\partial p}{\partial x_i} = \frac{\partial \tau_{ij}}{\partial x_j}, \quad (2)$$

where $\tau_{ij} = (\mu + \mu_t) \left[\frac{\partial u_j}{\partial x_i} + \frac{\partial u_i}{\partial x_j} \right]$ is the stress tensor.

When using the k- ε turbulence model, the energy equation will be as follows

$$\frac{\partial \rho k}{\partial t} + \frac{\partial \rho k u_j}{\partial x_j} = \frac{\partial}{\partial x_j} \left[\left(\mu + \frac{\mu_t}{\sigma_k} \right) \frac{\partial k}{\partial x_j} \right] + G_k - \rho \varepsilon. \quad (3)$$

The equation of the specific dissipation rate of turbulent energy

$$\frac{\partial \rho \varepsilon}{\partial t} + \frac{\partial \rho \varepsilon u_j}{\partial x_j} = \frac{\partial}{\partial x_j} \left[\left(\mu + \frac{\mu_t}{\sigma_\varepsilon} \right) \frac{\partial \varepsilon}{\partial x_j} \right] + \rho \varepsilon \left(C_1 S - C_2 \frac{\varepsilon}{k + \sqrt{\nu \varepsilon}} \right). \quad (4)$$

The production of turbulent kinetic energy can be described as

$$G_k = \mu_t S^2,$$

where $S = \sqrt{2S_{ij}S_{ij}}$ is a strain rate tensor module.

$$C_1 = \max\left(0.43, \frac{\eta}{\eta + 5}\right), \quad \eta = S \frac{k}{\varepsilon}, \quad C_2 = 1.9 \quad (5)$$

Coefficient of turbulent viscosity

$$\mu_t = \rho C_\mu \frac{k^2}{\varepsilon},$$

where $C_\mu = \frac{1}{A_0 + A_s \frac{kU^*}{\varepsilon}}$, $U^* = \sqrt{S_{ij}S_{ij} + \Omega_{ij}\Omega_{ij}}$, $\Omega_{ij} = \overline{\Omega_{ij}} - \varepsilon_{ijk}\omega_k$.

$\overline{\Omega_{ij}}$ – vorticity tensor in a coordinate system moving with angular velocity.

The following values of constants and parameters are accepted in the calculations:

$$A_0 = 4.04, \quad A_s = 6 \cos(\phi), \quad \phi = \frac{1}{3} \cos^{-1}(\sqrt{6W}), \quad W = \frac{S_{ij}S_{jk}S_{ki}}{\tilde{S}^3}$$

$$\tilde{S} = \sqrt{S_{ij}S_{ij}}, \quad S_{ij} = \frac{1}{2} \left(\frac{\partial u_i}{\partial x_j} + \frac{\partial u_j}{\partial x_i} \right), \quad \Omega_{ij} = \frac{1}{2} \left(\frac{\partial u_i}{\partial x_j} - \frac{\partial u_j}{\partial x_i} \right)$$

Here ε_{ijk} are the components of the Levi-Civitt tensor.

Turbulent Prandtl numbers: $\sigma_k = 1$, $\sigma_\varepsilon = 1.2$.

The boundary conditions for describing the change in the turbulent kinetic energy on the wall are specified as follows

$$\frac{\partial k}{\partial n} = 0. \quad (6)$$

Directly, the value of the dissipation rate of turbulent kinetic energy ε in the near-wall region is calculated from the condition that the kinetic energy production of turbulent pulsations and its dissipation are equal under the assumption of a logarithmic distribution of the average gas velocity.

$$\varepsilon_p = \frac{C_\mu^{0.75} k_p^{1.5}}{\kappa y_p}, \quad (7)$$

where $\kappa=0.42$; y_p is the distance from the center of the wall cell to the wall.

The value of y_p can be determined as follows:

$$y_p = \frac{\mu}{\rho C_\mu^{0.25} k_p^{0.5}} y^*, \quad y^* = 11.225$$

Boundary conditions at the entrance to the computational domain are

$$u_x = 0, \quad u_y = 0, \quad u_z = V \quad (8)$$

$$\varepsilon = C_\mu^{0.75} \frac{k^{1.5}}{0.07 D_h}, \quad k = \frac{3}{2} (V \cdot I)^2 \quad (9)$$

Here D_h is the hydraulic size of the input section of the region, D_h was taken equal to 1 m;

I – is the intensity of turbulent pulsations, $I = 0.1$;

Boundary conditions at the exit from the region: $p = p_H$;

Boundary conditions on the walls of the wind turbine: $u_i = U(t, x, y, z)$,

where $U(t, x, y, z)$ is the speed of the walls, depending on the speed of rotation of the cylindrical blades around its own longitudinal axis and the speed of rotation of the wind wheel around the axis of the wind turbine.

2. The technique of 3-dimensional modeling

The system of equations (1-9) is solved using Ansys-Fluent package using the finite volume method and the approach of multiple (nested) coordinate systems [12, 14]. The entire computational domain is divided into three types of subregions nested into each other, Fig 1. Subregions of the 1st type (cylinders), built around the working wheels of the wind wheel and rotating at the speed of the working cylinders (1); a subregion of the 2nd type (cylinder) built around the wind wheel minus the cylindrical subregions of the 1st type (2); type 3rd subdomain (sphere) surrounding the type 2nd subdomain minus its (3), Fig.1.

The radius of the outer spherical subregion (3) is assumed to be 10 m, the cylindrical subregion (2) has a radius of 2 m and a height of 0.5 m. The cylindrical subregions (1) have a radius of 0.15 m and a height of 1.06 m. A finite-volume mesh constructed in subregions 1 -th type, consists of hexagonal cells, and in subdomains of the 2nd and 3rd type - of tetragonal cells.

The grid view in the $z = 0$ plane is shown in Figure 2. The grid is shown in the XY plane, section of the region $Z = 0$. The total number of cells is 742858.

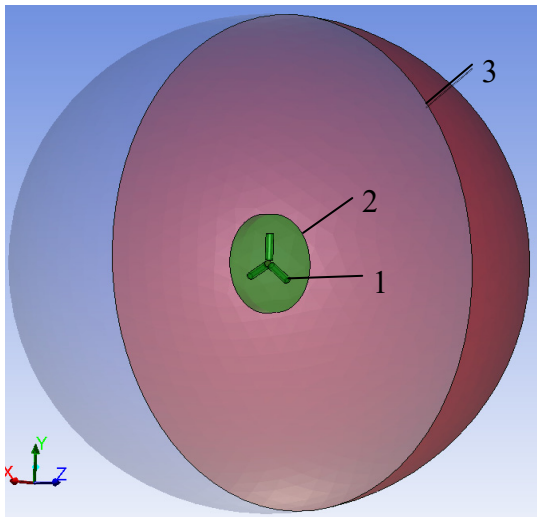


Fig.1. Computing area.

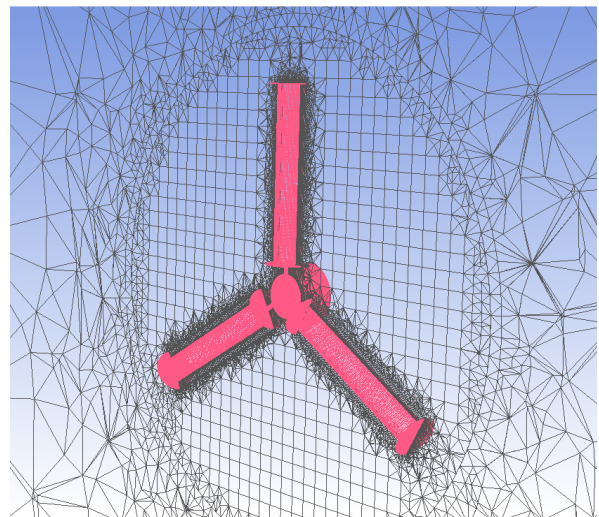


Fig.2. Finite volume mesh

3. Discussion of results

3.1 Modeling the flow field near the wind wheel surface.

The second-order up flow difference scheme in space was used to approximate the convective terms of the system of equations (1-2). The central-difference scheme was used to approximate second-order derivatives. To match the pressure field and the velocity field, the SIMPLE scheme was used [12, 14, 15]. Time derivatives were resolved with a second order of accuracy.

In Fig.3. the longitudinal velocity distributions in the vicinity of a moving wind wheel (plane $z = 0$) are shown for various cylinder speeds at a flow rate $V = 10$ m / s. At low speeds of the

cylinders rotation the flow field is close to symmetrical with respect to three planes of symmetry passing along the axes of the cylinders (Fig.3a), while higher speeds of rotation of the cylinders lead to deformation of the longitudinal velocity field (Fig.3.c). The field is longitudinal speed preserves symmetry when turning 120° relative to the z axis.

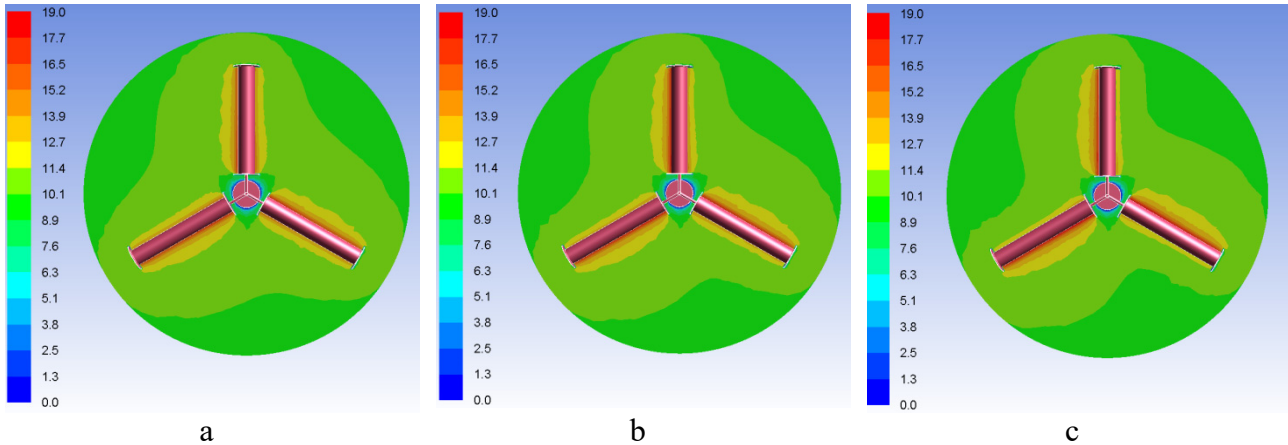


Fig. 3. The distribution of the longitudinal velocity u in the vicinity of a movable wind wheel at different speeds of rotation of a cylindrical blade $n =$: a) 300 rpm; b) 500 rpm; c) 700 rpm. Free airflow velocity $V = 10 \text{ m/s}$.

The deformation of the flow field occurs due to an increase in the velocity of the air flow on one side of the cylinder and a decrease in the flow velocity on the other side, caused by the rotation of the cylinders around their axes in the positive direction (counter clock wise).

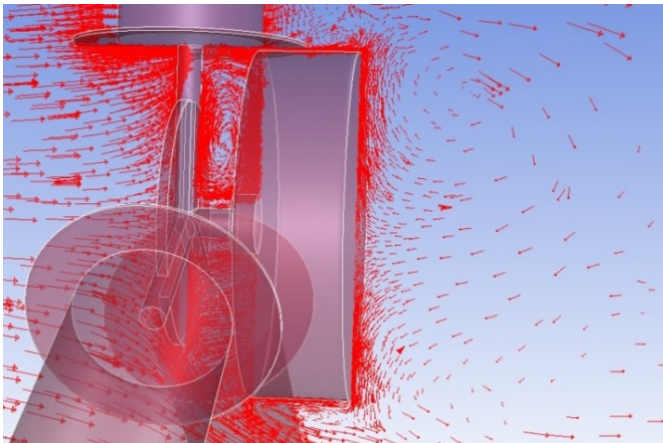


Fig. 4. The velocity field in the plane at the base of the blade, $x = 0$ (plane YZ, cross section $x = 0$).

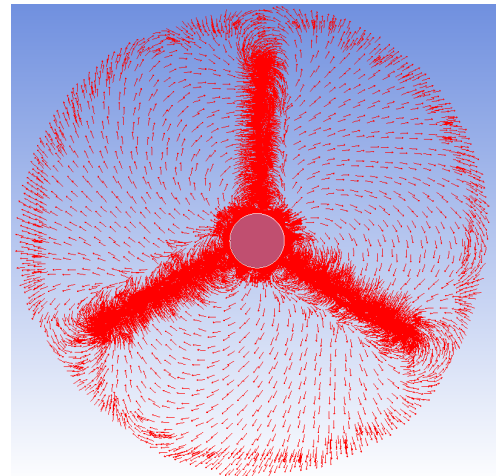


Fig. 5. The flow pattern in the plane $z = 0.15 \text{ m}$.

You can see projections of velocity vectors onto the $x = 0$ plane in the vicinity of the central disk of the wind wheel, Fig.4. It is seen that vortex zones are formed behind the central disk, in which the flow unfolds towards the main flow. The flow pattern in this region is qualitatively the same when the cylinder rotation speed is changing in the range from 300 rpm to 700 rpm.

Figure 5 shows the projections of normalized velocity vectors onto the plane $z = 0.15 \text{ m}$ for a movable wind wheel with cylinders rotating around their axes at a speed of 500 rpm. It can be seen that the air movement has a complex character: in the vicinity of the center of the wind wheel, the flow is swirling clockwise, and on the periphery, the air moves in a direction close to radial, while in the vicinity of the ends of the cylinders the air flows counter clock wise.

3.2 Modeling of aerodynamic characteristics.

This section presents the results of the calculation of the time-averaged values of the drag force and the lifting force acting on one cylinder, and their coefficients, obtained for a movable wind wheel. When solving the system of equations of conservation of mass and conservation of momenta, both viscous and turbulent components were taken into account.

Averaging over time t was carried out according to the formula:

$$\langle f \rangle = \frac{1}{T} \int_0^T f(t) dt.$$

T is the averaging period, the value of the time interval varies from 3 s to 5 s.

This duration is much longer than the period of rotation of the cylinders around its own axis of 0.02 s even at the lowest rotation speed of 300 rpm.

In Fig.6 are shown the results of the aerodynamic characteristics calculating of a wind turbine with rotating cylindrical blades that rotate around axis with speed of 300 rpm, 500 rpm, 700 rpm. An analysis of numerical calculations shows that the drag force coefficient C_x value for the same Reynolds number decreases with increasing speed of rotation of the cylinders around its own axis, as well as the magnitude of the lift force coefficient C_y . To calculate these coefficients, well-known standard formulas were used.

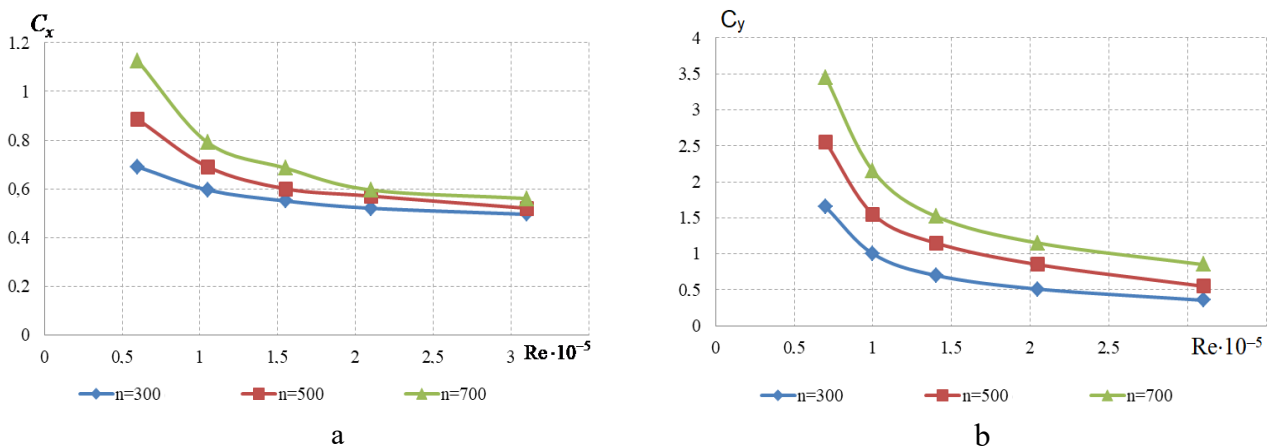


Fig.6. Dependence of the aerodynamical coefficients on the air flow speed at different rotation speeds of the cylindrical blade: a) - drag force coefficient; b) - lifting force coefficient.

But the rotation speed of the cylinders leads to an increase in the drag force of the wind wheel to the incoming flow according to a law close to linear, while with increasing flow velocity, the drag force increases according to the quadratic law. The detected changes in the dynamics of the aerodynamic parameters of a model wind turbine as a function of the speed of the incoming air flow depending on the rotational speed of cylindrical blades confirm the influence of the Magnus effect.

It should be noted that the geometric model of the 3-bladed wind turbine was created in the Gambit package, which has powerful capabilities and provides high accuracy of calculations with an error of less than 1%.

Conclusion

The technique for building a CAD model of a three-bladed wind turbine and simulation of its flow in the ANSYS CFX and ANSYS FLUENT software package had been developed. As a result of three-dimensional modeling, some features have been established in the aerodynamics of the flow around a wind turbine with three rotating cylinders in a turbulent air flow. The results of these studies show that at low flow rates, a rotating cylinder has relatively higher lift ratios, and the effect

increases with increasing turbulence intensity. The obtained simulation results of aerodynamic parameters are in satisfactory agreement with the experimental results. At this stage of the simulation, the action of the Magnus effect on the flow aerodynamics has been detected. So, rotating cylinders can be effectively used as a power element of a wind turbine under choosing the optimal conditions for the flow around.

REFERENCES

- 1 World Renewables 2019. Global Status Report. <https://www.ren21.net/reports/global-statusreport/>
- 2 Karatayev M., Hall S., Kalyuzhnova Y., Clarke M. Renewable Energy Technology Uptake in Kazakhstan: Policy Drivers and Barriers in a Transitional Economy. *Renewable and Sustainable Energy Reviews*. 2016, Vol. 66, pp. 120–136.
- 3 Shadrina, E. *Renewable Energy in Central Asian Economies: Role in Reducing Regional Energy Insecurity*. Tokyo. 2019. Available at: www.adb.org/publications/renewable-energy-central-asianeconomies
- 4 Mukhamediyev I.R., Mustakayev R., et al. Multi-criteria spatial decision making system for renewable energy development support in Kazak-hstan. *IEEE Access*. 2019, Issue 7, pp.122275-122288.
- 5 Martin O. L. Hansen L. *Aerodynamics of Wind Turbines*. London, Sterling, VA, 2008, 208 p.
- 6 Sakipova S.E., Jakovics A., Gendelis S. The Potential of Renewable Energy Sources in Latvia. *Latvian Journal of Physics and Technical Sciences*. Riga, 2016, Vol.53, Issue 1, pp. 3 – 12.
- 7 Kussaiynov K., Sakipova S.E., Tanasheva N.K., Kambayeva Zh.T., et al. Wind turbine based on the Magnus effect. Innovative patent №30462 of 23.09.2015.
- 8 Yershina A.K., Yershina Sh.A., Yershina Ch., Manatbayev R.K. *Wind motor*. Kazakhstan Republic Patent, No.31662. 2016, Bulletin 15, 5 p.
- 9 Yershina A.K., Manatbayev R.K., Sakipova S.E. Some design features of the carousel type wind turbine Bidarrieus. *Eurasian phys. tech. j.* 2019, Vol.16, No. 2(32). – P.63 – 67.
- 10 Kayan V. P., Kochin V. A., Lebid O. G. Studying the Performance of Vertical Axis Wind Turbine Models with Blade Control Mechanism. *Intern. Journal of Fluid Mechanics Research*. 2009, Vol.36, Issue 2, pp. 154 – 165.
- 11 Sakipova S.E., Tanasheva N.K., Kussaiynova A.K. Study of aerodynamics of a two-bladed wind turbine with porous-surfaced cylindrical blades. *Eurasian phys. tech. j.* 2017, Vol.14, No.28, pp.120 – 124.
- 12 Sakipova S.E., Tanasheva N.K. Modeling aerodynamics of the wind turbine with rotating cylinders. *Eurasian phys. tech. j.*, 2019, Vol.16, No. 1(31), pp. 88 – 93.
- 13 Miao J.J., Tsai J.H., Hsu X.Y., et al. On critical transition of flow over a circular cylinder roughened by textile materials. *AIP Conference Proceedings* 2027. 2018, pp. 020004-1 – 020004-10. doi: 10.1063/1.5065082
- 14 ANSYS Fluent software. Available at: <https://www.ansys.com/products/fluids/ansys-fluent>
- 15 Computer modeling of 3D-models of aviation equipment and engineering calculations. Available at: <http://www.ipmce.ru/custom/vsop/themes/3dmodel/>

VARIATION OF SPATIALLY HETEROGENEOUS RADIATION BY COORDINATE-SENSITIVE RECEIVER

Karabekova D.Zh., Khassenov A.K., Kissabekova P.A.,
Satybaldin A.Zh., Tungushbekova M.K.

E.A. Buketov Karaganda State University, Karaganda, Kazakhstan, karabekova71@mail.ru

The developed device is intended to analyze the state of thermal insulation of underground pipelines. The proposed heat flow meter uses current heating of the sensor element in the process of temperature measurement. This will improve the accuracy of temperature measurement and maintain the reference temperature measured previously using current heating. The developed device has several identical plates, each of which can receive radiation. Formulas for determining energy parameters based on calibration of a coordinate-sensitive receiver by a spatially uniform heat flow generated by an electric current are obtained.

Keywords: thermal methods of non-destructive testing, thermal energy, battery-operated thermoelectric sensor, heat flow meter, energy balance

Introduction

Numerous studies show that the most complete technical diagnostics requirements of thermal networks and technological facilities are currently satisfied with non-destructive control methods, which are based on monitoring and automated registration of the temperature state of processes. Currently, the method of thermal non-destructive testing has become one of the most popular in heat engineering, construction and industrial production. The experience of foreign countries shows the effective use of heat flow meters of non-destructive control for the purposes of normative state of objects and building structures [1].

All known thermal methods of non-destructive testing are based on the use of thermal energy of a controlled object, which spreads throughout its surface area. The resulting temperature field becomes a source to inform the operator of the presence or absence of all kinds of defects both on the surface and in the depth of the material from which the controlled product is made by assessing the processes of heat transfer occurring inside the object. Among the numerous types of non-destructive testing, a special place is given to the thermal method of control. Since 65 – 95% of the existing forms of energy in electronic equipment eventually turn into thermal, which confirms the expediency of choice, which characterizes the parameters' qualities, technical states and the generated heat energy [2].

1. Problem statement

Thermal control is based on measuring, monitoring and analyzing the temperature of controlled objects. The main condition for the application of thermal control is the presence of thermal flows in the controlled object. The process of transmission of thermal energy, the release or absorption of heat in the object leads to the fact that its temperature changes relative to the environment. The distribution of temperature on the surface of the object is the main parameter in the thermal method, since it carries information about the peculiarities of the heat transfer process, the mode of operation of the object, its internal structure and the presence of hidden internal defects [3]. In the devices of the thermal method of control, the information about defects is carried by the temperature and thermal flow of the surface of the controlled object, the values of which are determined by the change in the thermal and geometric characteristics of the violations. In this regard, the development and creation of thermal flow devices for heat supply systems are of particular interest.

As the results of numerous studies of thermal insulation of underground thermal networks show, the most effective method of non-destructive testing is based on comparison of calculated and experimental values of temperature distribution on the surface of the ground over heat networks [4]. Thermal methods of non-destructive testing have been widely used for various types of protective coatings, for the analysis of the state of thermal insulation of underground pipelines, construction structures, etc. [5].

The extensive practice of testing underground heat networks has shown that methods based on monitoring of the temperature state of the heat conductors are most fully satisfied with all the requirements of their technical diagnostics. The most effective among them is the method of non-destructive control of the state of thermal insulation of the channel-free heat conductors, based on comparison of calculated and experimental values of the distribution of temperature on the surface of the ground (coating) over the heat networks.

A fault in the thermal insulation causes a change in the temperature on the protective coating surface. It is possible to conclude the state of thermal insulation on the basis of the data on the surface temperature of insulation and the temperature field inside the object under investigation. The temperature field of the insulation surface can be obtained using thermocouples or resistance thermometers by contact method. However, this method of temperature measurement results in significant errors due to the temperature field distortion in the contact area. The accuracy is significantly reduced by measuring the average value of the temperature fields on the entire surface of the thermal probe contact with the product. Thermal flow sensors can be used for this purpose.

Non-contact methods of measurement are the most promising for the study of these sources. Currently used for this purpose, the radiation receivers have a flat sensitive element with pronounced angular sensitivity dependence, and therefore giving sufficiently good results only when measuring the radiation of point sources. Applied spherical and hemispherical nozzles to a flat sensitive element allow only a small decrease in accuracy of measurements and increase their efficiency. At the same time, calibration methods are developed only for cases of radiation pulse duration much more or much less than the constant time of the device [6].

In order to solve these problems, we have developed several modifications of thermal flow sensors, whose readings are independent of changes in the state of the environment. A common element of these devices is a battery thermoelectric sensor of a special design, acting as a thermoelectric converter of thermal flow [7].

2. Experimental part

Developed thermal flow meter, works according to the auxiliary wall method. The thermometric module contains a thermal electric thermal flow converter, which is based on a battery thermoelectric sensor. The thermoelectric sensor is made in the form of a limited cylinder, one base of which represents the working surface, the second base has thermal contact with the body having an ambient temperature. Built-in heaters allow the thermal flow through the thermoelectric sensor in directions perpendicular to its bases. The heat flow generated by the heater is an instrument monitor with which the thermal flows of the objects under investigation are compared. Areas with possible insulation faults result in an increase in the signal output of the thermal flow meter [8, 9].

In the device, the heat flow flows through the protective film to the sensitive element, the hot junctions of the thermal battery have a thermal contact with the protective film, and the cold junctions with the heat stabilizer (figure 1). In this case, the role of a heat stabilizer is performed by a massive body that transmits further heat flow through the bottom of the housing to the radiator. To exclude heat transfer from the side surface, the sensing element is surrounded by a heat insulator, and the entire system is closed by a conical side surface [7]. When a defect occurs in the pipeline, the temperature changes sharply, and a temperature anomaly of a fairly regular shape occurs, which differs by several degrees from the average temperature of the earth's surface.

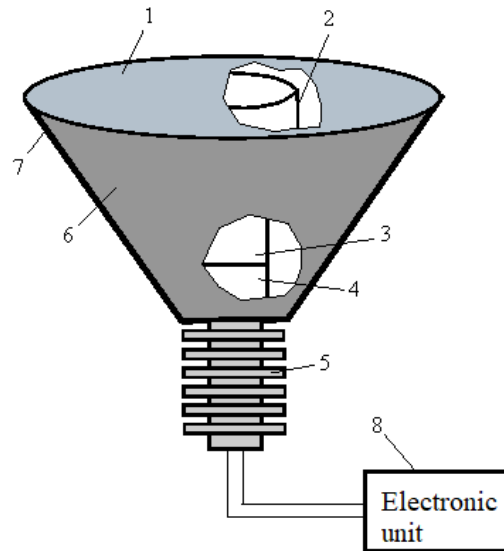


Fig.1. Schematic representation of the heat flow device:
1-protective film; 2-calibration winding, 3-sensing element; 4-heat stabilizer; 5-radiator; 6-heat insulator; 7-side surface, 8-electronic unit

Abnormally high values of energy losses detected in this case indicate sections of the pipeline with completely or partially destroyed thermal insulation or mechanical damage to the pipeline material [8].

3. Results and discussions

Studies were conducted to calibrate the heat flow sensor. Using the standard calibration table of copper-constantan (table 1), from the thermoelectric moving force temperature increments are determined.

Table 1. The calibration table temperature sensor

№	$\Delta t, ^\circ C$	$\Delta \varepsilon, mV$	A	α_{av}
1	0	0	0	0.7824
2	5	4	0.8	
3	7	5.9	0.8428	
4	10	8.1	0.81	
5	15	12	0.8	
6	20	15.4	0.77	
7	25	19.2	0.768	
8	30	22.8	0.76	
9	35	26.2	0.7485	
10	40	29.7	0.7425	

A sensitive element is used as a thermoelectric battery converter. The sensitive element of such a receiver is a solid plate that serves as a heating element at the same time, or on it is a heating element. Let's divide the sensitive element into n equal square sections with side Δx and thickness d (fig. 2). The area of contact of this site with the neighboring one is $\Delta x d$, the area of the irradiated surface is Δx^2 , the number of areas adjacent to the data is m . Maximum value $m=4$.

The energy balance equations for time t for any phase of the sensing element have the following form:

$$W_{st} + W_{rej} = W_u + W_T \tag{1}$$

where $W_{st}=C\vartheta_e$ – the amount of energy stored; C and ϑ_e - heat capacity and average excess temperature of the any section, respectively; $W_{rej}=\alpha_e\Delta x^2\int_0^t\vartheta_e dt$ - the amount of rejected energy as a result of heat exchange with the environment; α_e - heat transfer coefficient; $W_u=\eta\Delta x^2\omega_e$ - absorbed part of the radiation energy; W_e – the surface density of radiation energy; $W_T = \lambda d \sum_{i=1}^m \int_0^t (\vartheta_i - \vartheta_e) dt$ - the amount of energy delivered to the site from the adjacent thermal conductivity; λ - thermal conductivity; ϑ_i - average excess temperature.

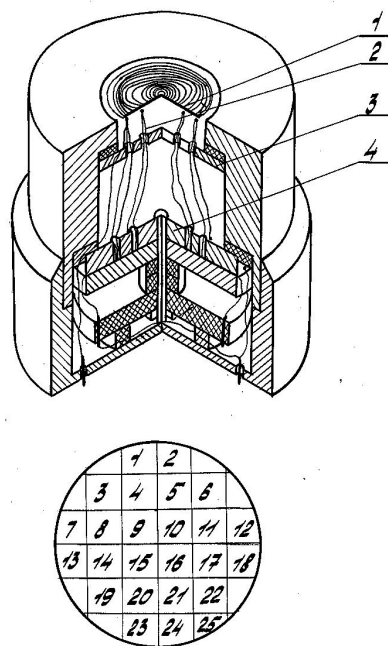


Fig.2. Schematic representation of the receiver and the separation of its sensing element into sections controlled by single thermocouples: 1- spiral; 2- single thermocouple instrument; 3- screen; 4- thermostatic element.

By substituting the value of W_{st} , W_{rej} , W_u , and W_T in the expression and taking into account the relationship between the mean excess site temperature and the response of the controlling temperature, we obtain a formula for determining the surface density of radiation energy in the any site during the time t :

$$\omega_e = \frac{1}{\eta} \left\{ A_{1e} [(1 - A_{2em})] \int_0^t U_e dt - A_{2e} \int_0^t U_e dt - A_{2e} \sum_{i=1}^m \int_0^t U_i dt \right\} \tag{2}$$

where U_e and U_i - reactions of thermocouples that control the regions; A_{1l} , A_{2l} and A_{3l} , coefficients, that equal to:

$$A_{1l} = \frac{\alpha l}{k}; A_{2l} = \frac{\lambda d}{\alpha l \Delta x^2}; A_{3l} = \frac{C}{k \Delta x^2} \tag{3}$$

k - Seebeck coefficient of the thermo element.

The coefficients A_{1l} , A_{2l} and A_{3l} can be determined experimentally. To determine A_{1l} and A_{2l} , let's look at the stationary heating of the sensing element. The energy balance equation for time t for the first section will take the form:

$$W_{rej} = W_u + W_T, \quad (4)$$

$$\text{where } W_{rej} = \alpha_e \Delta x^2 \vartheta_e t; W_u = \eta \Delta x^2 E_l t; W_T = \lambda t d \sum_{i=1}^m (\vartheta_i - \vartheta_e), \quad (5)$$

E_l - irradiation of the first section.

Substituting the values for W_{rej} , W_u and W_T in the expressions and moving from excessive temperatures, we get a formula for determining the irradiation of the any site:

$$E_l = \frac{A_{1l}}{\eta} \left[U_e - A_{2l} \sum_{i=1}^m (U_i - U_e) \right] \quad (6)$$

If the any section is not irradiated when the sensitive element is irradiated, i.e. $E_l = 0$, then we get expressions for the experimental determination of the coefficient A_{2l} :

$$A_{2l} = \frac{U_e}{\sum_{i=1}^m (U_i - U_e)} \quad (7)$$

To determine the coefficient A_{1l} :

$$A_{1l} = \frac{A_q}{U_e - A_{2l} \sum_{i=1}^m (U_i - U_e)} \quad (8)$$

Given the conditions, we obtain a formula for determining the A_{3l} coefficient:

$$A_{3l} = U_l^{-1} \left\{ A_{qt} - A_{1l} \left[(1 - A_{2l} m) \int_0^t U_i dt - A_l \sum_{i=1}^m U_i dt \right] \right\} \quad (9)$$

Thus, the determination of the surface energy density of radiation at the first site can be carried out using a formula (2), where A_{1l} , A_{2l} and A_{3l} are coefficients determined experimentally using formulas (7) – (9). The determination of site irradiation from stationary heating can be done by formula (6). The coefficients A_{1l} , A_{2l} and A_{3l} are individual characteristics of the every plot, since practically Δx , d , λ and k – change from plot to plot. In addition, A_{1l} and A_{2l} depend on the local heat transfer coefficient. We have experimentally determined the coefficients A_{1l} , A_{2l} and A_{3l} at a heat flux density of 1534 W/m^2 . The dispersion of these coefficients, except for the above reasons, is influenced by the inhomogeneity of the spiral along the irradiated surface, since the spiral consists of turns of metal wire and dielectric gaps between them.

Conclusions

The heat flow meter operates in the range from 50 to 1500 W/m^2 , which corresponds to the normative heat losses, which are $\sim 300 \text{ W/m}^2$. The measurement time with secondary equipment is ~ 1 min. The measurement error is 3% of the measured value. The conducted measurements confirm the principal possibility of using the proposed device for implementing the thermal method of non-destructive testing. Formulas are obtained for determining the energy parameters of such radiation, which are based on the calibration of a coordinate-sensitive receiver by a spatially uniform heat flow generated by an electric current.

REFERENCES

- 1 Varganov I.S., Lebedev G.T., Konpov V.V. Current state and main problems of thermal non-destructive testing methods. *Prom. teplotekhnika*, 1983, Vol. 6, №2, pp. 80-93. [in Russian]
- 2 Gerashchenko O.A. *Fundamentals of heat metering system*. Kiev. 1984, 1971p. [in Russian]

3 Gerashchenko O.A., Gerashchenko T.G. Thermometric indicator for diagnostics of the heating system TIDHS-01. Kiev: Chas, 1991, p. 19. [in Russian]

4 Nesteruk D.A., Vavilov V.P. *Teplovoj kontrol' i diagnostika. (Thermal monitoring and diagnostics)*. Tomsk: TPU, 2007, 104 p. [in Russian]

5 Cherepanov V.Ya. *Izmereniya parametrov teploobmena. (Measurement of heat exchange parameters)*. Mir izmerenii, 2005, № 9, pp. 415. [in Russian]

6 Kuritnik I.P., Nussupbekov B.R., Karabekova D.Zh. Device for monitoring underground heating lines. *Bulletin of Karaganda University. Physics Series*, 2014, No. 4(76), pp. 58 – 62. [in Russian]

7 Nussupbekov B.R., Karabekova D.Zh., Khassenov A.K., et al. *Heat flow meter*. Kazakhstan Republic Patent № 1588, 2016, Bulletin 4, 4 p. [in Russian]

8 Nussupbekov B.R., Karabekova D.Zh., Khassenov A.K. Thermal Methods and Non-Destructive Testing Instrumentation. *Measurement Techniques*, 2016, Vol. 59, № 6, pp. 644 – 648.

9 Nussupbekov B.R., Karabekova D.Zh., Khassenov A.K. Heat flow meter for the diagnostics of pipelines. *Proceedings of the Int. Conf. SPIE Photonics Applications in Astronomy, Communications, Industry, and High-Energy Physics Experiments*. Wilga, Poland, 2016, pp. 348 – 354.

Article accepted for publication 25.05.2020

EVALUATION OF THE POTENTIAL ACCURACY OF THE PULSED RADIO SIGNALS SOURCE COORDINATE DETERMINATION BY THE POSITIONING SYSTEM USING A SINGLE UAV-SENSOR

Baldytchev M.T.¹, Laptev I.V.¹, Chebotar I.V.¹, Gaychuk Y.N.¹, Pivkin I.G.¹,
Timoshenko A.V.², Galtseva O.V.³

¹ Cherepovets Higher Military Engineering School of Radio Electronics, Cherepovets, Russia

² OJSC Academician A.L. Mints Radiotechnical Institute, Moscow, Russia

³ National Research Tomsk Polytechnic University, Tomsk, Russia, rabota2013tpu@mail.ru

An approach to determining the coordinates of pulsed radio signals sources by the positioning system in the application of a single unmanned aerial vehicles sensor is shown in this article. The range-difference location method allows to determinate an informative coordinate parameter without retransmission and internal synchronization of receiving points. The result is achieved by improving the well-known scientific and methodological apparatus with considering some features of the operation mode of pulsed radio signals sources. Presenting results of the simulation allow to estimate the influence of main input factors on the potential accuracy of the pulsed radio signal source coordinate determination.

Keywords: coordinate-informative parameter, unmanned aerial vehicles sensor, pulsed radio signals sources, the range-difference location method.

Introduction

Nowadays, pulsed radio signal source coordinate determination by passive means of monitoring is realized by the goniometrical method [1-8] or the range-difference location method. Methods implementation requires two or three receiving points equipped with radio monitoring and communication equipment, which allows have data link. The distance between them must be from one to ten kilometers. Achieving the power availability of pulsed radio signals sources (PRSS), receiving centers are accommodated on unmanned aerial vehicles (UAV). These vehicles have been widely spread nowadays. However, the use of UAVs as a platform for radio monitoring tools for solving the coordinates determination problems of radio emission sources, leads to a number of problems. The main of which are connected with weight and size limitations of the UAV payload, which do not allow to place effective direction finding antenna systems and repeater; instability of UAV spatial orientation, which leads to a sharp increase in errors of direction finding. Along with this, it is known that the smallest error in determining the location (of the existing passive methods of determining the coordinates) provides the range-difference location method (RDLM) [9-15].

The features of the range-difference location method include the simplicity of the antenna-feeder system, as well as the invariance to the deviation of the angles of pitch, roll and yaw of the UAV. However, the implementation of classical range-difference location method requires the use of three or more UAVs equipped with radio monitoring tools and communication channels with high bandwidth, necessary for relaying the implementation of the received signal for correlation processing and measurement of the coordinate-informative parameter (CIP).

These features significantly complicate the structure and cost of used equipment, as well as reduce the stability of the positioning system as a whole. In this regard, an urgent task is the search for opportunities to simplify the requirements for communication lines and the structure of the positioning system based on range-difference location method by reducing the number of receiving

points involved to a single unmanned aerial vehicle equipped with radio monitoring equipment and ground control and processing point (GCPP).

1. Range-difference location method

The purpose of the article is to describe the stages of the approach to determining the coordinates of the pulsed radio signals sources by using a single UAV sensor. Development of a simulation model that allows to identify the main factors affecting the accuracy of pulsed radio signals sources positioning and to estimate its limit values in the framework of the proposed approach. The idea of reducing the number of receiving points in the implementation of range-difference location method to one UAV sensor and GCPP (Fig. 1), based on the use of features of the modes of some pulsed radio signals sources. It is occurs when a pulse signal with a constant pulse repetition period (T) for a certain period of time (Δt) are formed [16]. This feature allows determine the coordinates of these sources without retransmitting the received signal and the organization of a high-precision synchronization system required when using two or more receiving points. The proposed approach includes 10 main stages. They are following below.

Stage 1. Evaluation of initial data.

Stage 2. Search for a pulsed radio signal in a given range of operating frequencies, when a pulsed signal is detected, its parameters are evaluated, namely the pulse repetition period and their duration.

Stage 3. Generates a timestamp grid. The timestamp meshing procedure involves four steps:

– pulse normalization and threshold setting;

– measurement of pulse start time (t_0);

– calculation of the timestamp grid ($t_i = t_0 + T \cdot i$, where i is the sequence number of the signal period);

– setting the interrupt timer based on the quantum frequency standard.

Stage 4. Formation of final samples of signal-noise structures. The formation of the reference sample is realized in the sampling block and consists is to record the common-mode and quadrature realization of the detected pulsed radio signal at the first observation point with coordinates (x, y, z) with a duration equivalent to the pulse repetition period (T). Further sampling is carried out at each observation point with fixing the coordinates of these points during the entire time of observation of the source (Δt).

Stage 5. Estimation of coordinate-informative parameter value. The procedure for estimating the coordinate-informative parameter is to find the time offset of the correlation maximum (t_i), obtained as a result of correlation processing of samples of signal-noise designs (S_i), recorded in the i -th moments of time, with the reference sample (S_0), recorded at the first observation point. To do this, the final samples from the sampling unit are fed to the digital correlator. The correlator calculates the modulus of the joint correlation function (JCF) of the final samples. JCF is calculated by discrete convolution of finite samples according to the Equation:

$$z_i = \left| \sum_{s=0}^{2N-1} S_0(s) \cdot S_i(n-s) \right|, \quad (1)$$

where $(2N-1)$ is the volume of JCF; s is the indexation of the final sample samples; S_0 and S_i are the final samples of signal-noise structures at the first and i -th observation point, respectively.

Time delay values (τ_i) corresponding to JCF maxima exceeding the threshold are calculated by the Equation:

$$\tau_i = \frac{N-j}{f_\delta}, \quad (2)$$

where j is the number of ICF samples exceeding the detection threshold of the PRSS; f_δ is the sample rate.

Stage 6. Limitation of the duration of the measurement cycle of the coordinate-informative parameter. Accumulation of time delay array is produced during the source control period (Δt):

$$T \cdot i \leq \Delta t \quad (3)$$

Stage 7. Transmission of observation point coordinates and CIP values to the GCPP. The generated data vector, including the coordinates of observation points and the corresponding CIP value, is transmitted to the GCPP via a communication channel.

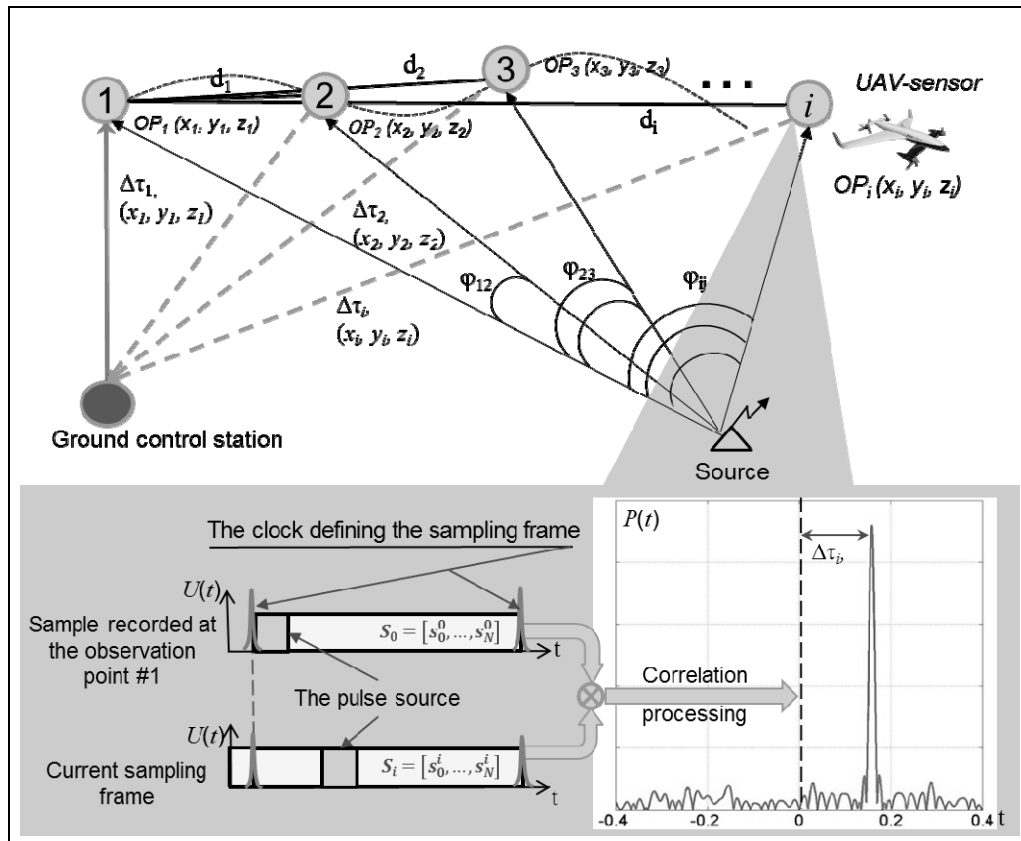


Fig.1. Schematic representation of the implementation of the proposed approach to finding the CIP and determining the coordinates of PRSS

Stage 8. Formation of independent measurements taking into account the geometric factor and the intersection angle.

Stage 9. Calculation of intersection points of position lines and elimination of ambiguity of coordinate estimation. A well-known algorithm is used, with the help of an advanced estimation of the PRSS coordinates on the basis of difference-range measurements [17]. Steps in the disambiguation procedure:

- check for ambiguous solutions;
- calculation of various distances between cross points, selection values and fixations of these points;
- forming points of intersection of two arrays from the common array, according to the condition "which of the fixed points is closer»;
- estimation of the standard deviation of the obtained arrays and selection of the data array with the smallest deviation for further statistical processing.

Stage 10. Statistical processing of intersection points of position lines, estimation of coordinates and their characteristic.

2. Experimental part

In the interests of experimental studies evaluating the potential accuracy of PRSS coordinates determining under the proposed approach, the developed simulation model [18] which allows you to manipulate the dimensions of difference-range location system and the position of the "shiny" points, forming the path of movement of the UAV-sensor, change the energy and time parameters of the source. The received signal has a time delay at the location of the UAV sensor, Doppler frequency shift, additive noise component and several modes formed by a multipath propagation channel:

$$y(t) = Au(t - \tau)\exp(2\pi j[f_c + f_d]t) + \operatorname{Re}\left[\sum_{i=1}^M A(\sigma_i)u(t - \tau_i)\exp(2\pi j[(f_c + f_{d_i})t - f_c\tau_i - \varphi_i])\right] + n(t), \quad (4)$$

where A is the amplitude of the direct signal; $u(t)$ is the envelope signal; $A(\sigma_i)$ is the amplitude of the reflected signal; σ_i is the effective surface scattering of the i -th reflected signal; f_{d_i} is the Doppler shift of the reflected i -th signal; τ_i is the spatial signal delay from i -th "shiny" point; φ_i is a random phase shift; M - the number of reflectors on the road; $n(t)$ is additive Gaussian noise.

The accuracy of coordinates determination is estimated by the example of a radio signal generated by a radar station with the following parameters: radiated pulse power of 1 kW, pulse repetition rate of 100 μ s with a duty cycle of 2%, intra-pulse filling has a carrier frequency of 9.7 GHz with linear frequency modulation (LFM) and frequency deviation of 5 MHz.

2. Results and discussions

The result of signal generation based on the proposed analytical model (Equation (4)) in the time and frequency domains are shown in Fig. 2a and 2b. The direct signal propagates over the shortest distance and has greater energy characteristics than the reflected ones. When calculating the JCF of the reference sample (S_0) and the signal-noise structures (S_i), the increased energy provides a maximum when convolution of direct signals (Fig. 2c), which allows for the filtering of JCF bursts caused by multipath propagation.

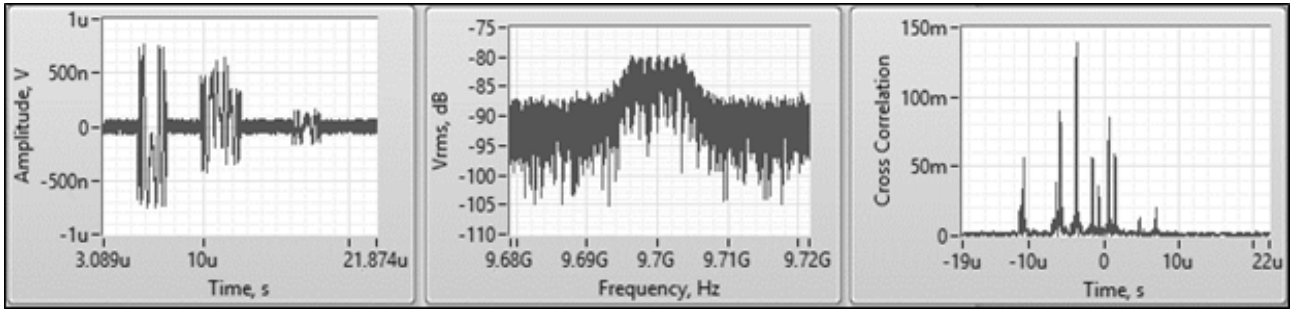
However, there are exceptions to this rule. The direct signal modes formed as a result of reflection from the "shiny" points overcome various distances and are shifted on the time axis when the UAV sensor moves. The interference pattern formed in some cases provides in-phase addition of several modes with a total excess of the direct signal energy.

The described phenomenon leads to significant CIP measurement errors and generates outliers in the resulting sample. CIP measurement outliers are filtered using statistical tools that take into account the possible variation intervals of the measurement result in the current time interval. To calculate the boundaries of the intervals of variation, as well as to plan the experiment, the study of the distribution law of the error in determining the coordinates of the PRSS was performed. Based on the Central limit probability theorem, the hypothesis of the normal distribution of the coordinate determination error is accepted as the null hypothesis H_0 .

Figure 3a shows the dependence of the error variance $R_{\text{MSE}(\text{RS})}$ and its average value on the number of experiments in the series (B) at a fixed value of other input factors. The result of Shapiro-Wilk test with significance level $\alpha = 0.05$ confirmed the validity of the null hypothesis about the normal error distribution law and provided the possibility of reasonable application of the student's t-test to determine the volume of a representative sample.

Figure 3a shows that the variance of the error $R_{\text{MSE}(\text{RS})}$ does not undergo significant changes at 100 or more experiments in the series, the result of the t-test showed that the volume of experiments $B = 100$ is sufficient to obtain an unbiased estimate of the average trend of the random variable $R_{\text{MSE}(\text{RS})}$ with a significance level $\alpha = 0.05$. The result of the radio-signal source coordinate determination depends on several input factors: the geometrical factor of the mutual arrangement of the source and the trajectory of UAV-sensor, the signal-to-noise ratio at the receiving end, the

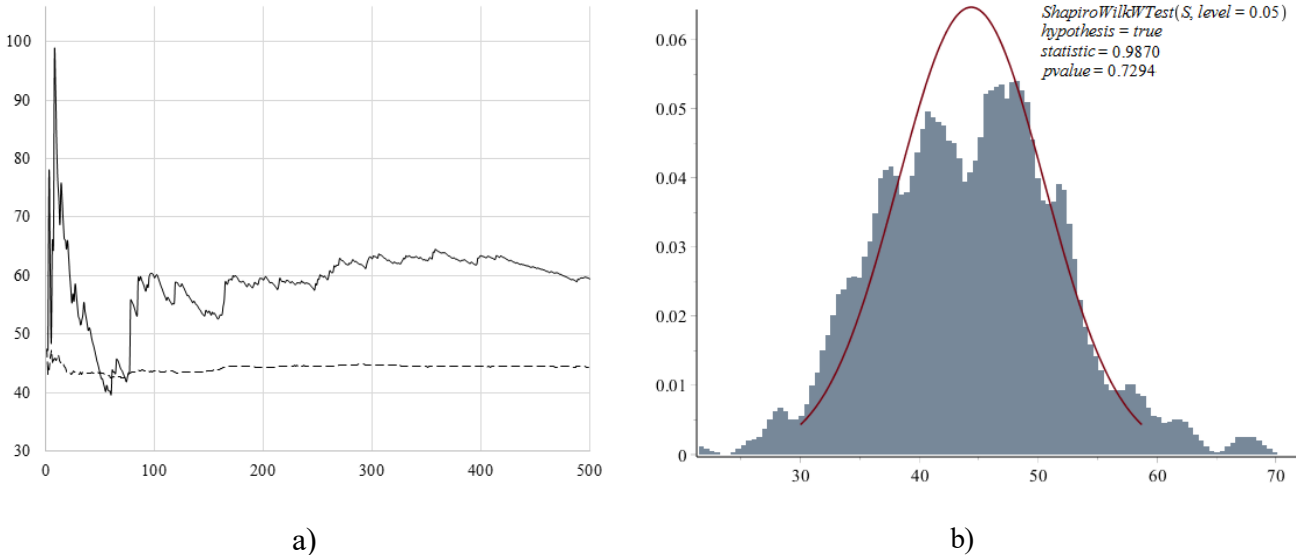
number of measurement points coordinate-informative parameters, the positioning accuracy of UAV-sensor, the operating time of the radiation source, etc.



a) b) c)

Fig.2. Result of simulation of the PRSS signal at the receiving point:

a) signal in time domain; b) the spectrum of the LFM signal; c) result of JCF calculation



a)

b)

Fig. 3. The result of a statistical study of the distribution law of the coordinate determination error:

a) Variation of deviation and mean error of coordinate determination from the number of experiments; b) Frequency histogram of $R_{MSE(RS)}$ error and theoretical probability distribution density

The geometric dilution of precision (GDOP) when using range-difference location method has a significant impact on the value of coordination error $R_{MSE(RS)}$ [17]. CIP measurements are performed by a mobile UAV sensor, which leads to a change in time of both the GDOP and the signal-to-noise ratio. The GDOP value weighted by SNR's parameters is calculated using the Equation:

$$D = \frac{\sqrt{\frac{1}{q_{12} \left(2 \sin \frac{\varphi_{12}}{2}\right)^2} + \frac{1}{q_{23} \left(2 \sin \frac{\varphi_{23}}{2}\right)^2}}}{\sin \gamma} = 2 \sqrt{\left(\frac{l_{12}}{q_{12}} + \frac{l_{23}}{q_{23}}\right) l_{13}}, \quad (5)$$

where

$$l_{12} = \frac{r_2(r_2 + \Delta r_{12})}{d_{12}^2 - \Delta r_{12}^2}, \quad l_{23} = \frac{r_2(r_2 + \Delta r_{23})}{d_{12}^2 - \Delta r_{23}^2}, \quad l_{13} = \frac{(r_2 + \Delta r_{23})(r_2 + \Delta r_{12})}{d_{13}^2 - (\Delta r_{12}^2 + \Delta r_{23}^2)},$$

where q_{12} and q_{23} are power SNR for measuring mutual delay between measurement points OP1 and OP2, OP2 and OP3; φ_{12} , φ_{23} are angles of sight in the measurement of CIP; γ is angle of intersection of position lines; d_{12} , r_1 , ... Δr_{23} are geometric dimensions of system elements at measurement points (Fig. 1).

Changing the value of the GDOP and the signal-to-noise ratio is shown in Fig.4. Analysis of the above dependencies allows us to conclude that the geometric factor and the signal-to-noise ratio should be taken into account in the statistical processing of the results of coordination. So at the measuring points (OP \in [330, 390]), signal-to-noise ratio deviation by the superposition of direct and reflected signals, is in the range SNR \in [7.5 dB, 12.5 dB], which leads to fluctuations of the weighting factor D twice (D \in [10^{-7} , $2 \cdot 10^{-7}$]). Obviously, the use of parameter (D) as a weighting factor in the statistical processing of CIP measurement results will improve the accuracy of determining the coordinates of the PRSS.

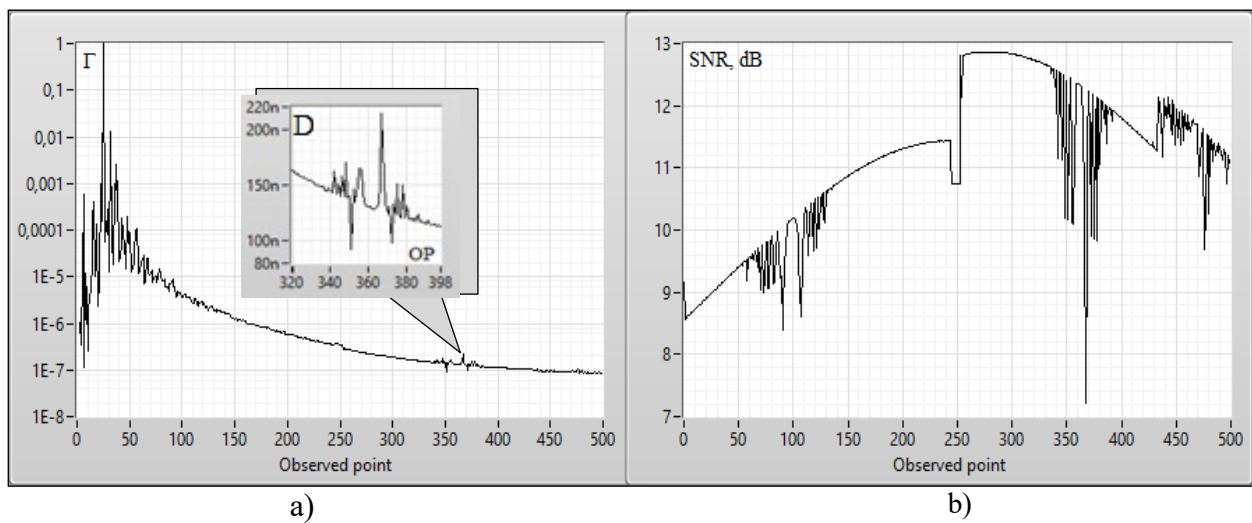


Fig.4. Dynamics of geometric factor and SNR changes during UAV sensor movement

The accuracy of determining the UAV sensor coordinates with other constant values of the input factors also has a significant impact on the error of determining the location of the radio signal source. Statistical estimates of the coordinate measurement error are obtained at the following distance to the source $R_{UAV-RS} = 12000$ m and the signal-to-noise ratio $SNR \geq 15$ dB. The analysis of the obtained estimates allows us to conclude that the use of existing positioning systems GPS/GLONASS with $R_{MSE(UAV)} \leq 10$ m, subject to the application of the proposed approach to coordinate measurement, will ensure the accuracy of determining the coordinates of $R_{MSE(RS)} \leq 40$ m.

Reducing the distance between the source and the UAV sensor (R_{UAV-RS}) leads to reduction both the absolute value of the coordinate measurement error and the relative error expressed as a percentage of the distance to the source. In order to determine the conditions and boundaries of the application of the proposed approach, the dependence of the coordinate measurement error on the number of CIP measurement points on the UAV sensor route at different values of the signal-to-noise ratio at the receiving point is studied (Fig.5).

The analysis of the above dependences allows us to conclude that at the level of the received signal $SNR < 3$ dB there is a sharp increase in the average error of determining the coordinates of the source. To minimize the error ($R_{MSE(RS)}$), you should take a sample of the measurement results of the maximum volume CIP ($N \rightarrow \max$). The peculiarity of the proposed approach to determining the location of PRSS is the ability to achieve the required accuracy of the coordination by controlling the measurement time of CIP.

Figure 6 shows the dynamics of reducing the error $R_{MSE(RS)}$ with increasing flight time UAV sensor Δt for different accuracy of calculating the own coordinates $R_{MSE(UAV)}$.

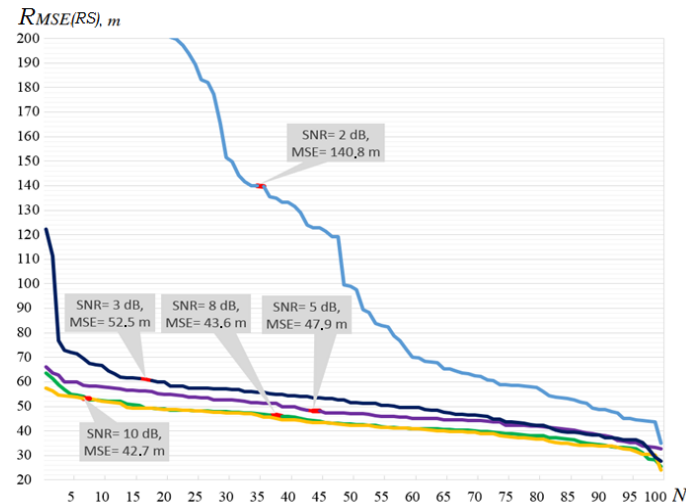


Fig.5. Dependence of the coordinate determination error (MSE) on the number of measurement points on the route at different average signal-to-noise ratio (SNR)

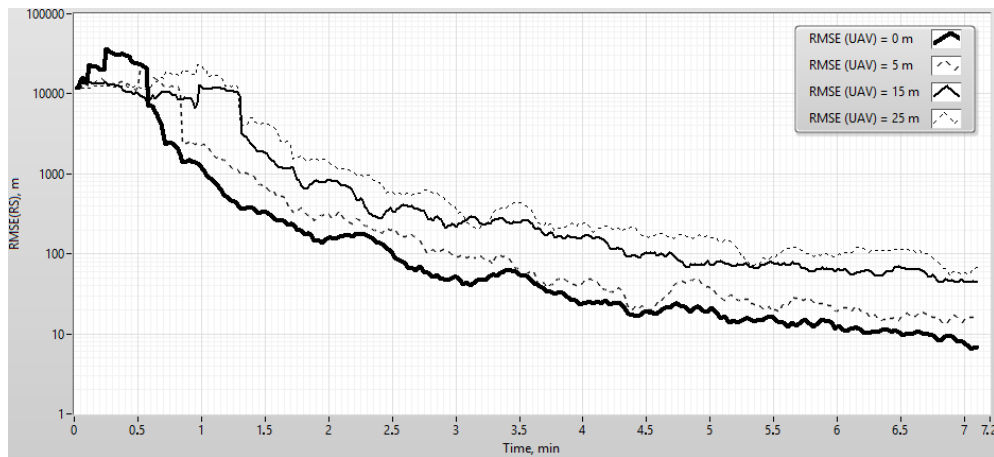


Fig.6. Error in determining the coordinates of $R_{MSE(RS)}$ for different accuracy in calculations the own coordinates of the UAV sensor.

Application of global positioning system GPS / GLONASS with $R_{MSE(UAV)} \leq 10$ m will allow to achieve accuracy of determination of coordinates $R_{MSE(RS)} \leq 110$ m during time of measurement $\Delta t \geq 3$. To achieve the accuracy of determining the coordinates $R_{MSE(RS)} \approx 40$ m the required flight duration of the UAV-sensor to accumulate samples of CIP will be about 5 minutes. These dependences are obtained at a signal-to-noise ratio $SNR \approx 5$ dB at a distance of $R_{UAV-RS} \approx 12$ km in the presence of three "shiny" points with the reflected signal energy at the receiving point of 30-70% of the direct signal power.

Conclusion

An approach to determining the coordinates of pulsed radio signals sources is based on the range-difference location method, which allows to measure CIP without retransmitting the signal using a single UAV sensor unlike the known methods; it significantly reduces the requirements for communication channels and increases the survivability of the system. The result is achieved through the development of scientific and methodological apparatus that allows using the operation mode features of the pulsed radio signals source, namely the formation of a pulsed signal with a constant pulse repetition period for a certain period of time.

The lack of errors associated with universal time system and the difference in the amplitude-frequency characteristics of the receiving paths in systems with several receiving points allows to achieve significantly better results in the accuracy of the coordinate determining. It is advisable to use a weighting factor that allows taking into account the GDOP and the signal-to-noise ratio at each measurement point on the UAV sensor route when statistically processing the results of CIP measurements. The required accuracy of coordinate determination can be achieved by changing the CIP sample accumulation time up to 15 – 20 meters for the modern technological level of the UAV sensor onboard equipment depending on the tasks to be solved.

REFERENCES

- 1 Li C., Weihua Z. Hybrid tdoa/aoa mobile user location for wideband CDMA cellular systems. *IEEE Trans. Wireless Commun.* 2002, Vol. 1, No. 3, pp. 439 – 447.
- 2 Dempster A.G. Dilution of Precision in Angle-of-Arrival Positioning Systems. *Electron. Lett.* 2006, Vol. 42, No.5, pp. 291 - 292.
- 3 Kułakowski P., Vales-Alonso J., Egea-López E., Ludwin W., García-Haro J. Angle-of-arrival localization based on antenna arrays for wireless sensor networks. *COMPUT ELECTR ENG.* 2010, Vol. 36, No. 6, pp. 1181 - 1186.
- 4 Xu J., Ma M., Choi L.L. AOA Cooperative Position Localization. *Proceeding of the IEEE Global Telecommunications Conference. 2008*, pp. 3751- 3755.
- 5 Du H.J., P.Y. Lee. *Technical Memorandum, DRDC Ottawa TM 2004-256*, 2004, 24 p.
- 6 So H.C., Hui S.P. Constrained location algorithm using TDOA measurements. *IEICE T FUND ELECTR.* 2003, Vol. E86-A, No. 12, pp. 3291- 3293.
- 7 So H.C., Ching P.C., Chan Y.T. A new algorithm for explicit adaptation of time delay. *IEEE T SIGNAL PROCES.* 1994, Vol. 42, No.7, pp. 1816 – 1820.
- 8 Featherstone W., Strangeways H. Mobile transmitter AOA estimation under multipath conditions using an MLE based super resolution algorithm and comparison with weighted spectrum methods. *Proceeding of the IEE Colloquium Novel Methods of Location and Tracking of Cellular Mobiles and their System.* 1999, pp. 4 - 4, doi: 10.1049/ic:19990241.
- 9 Pages-Zamora A., Vidal J., Brooks D.H. Closed-form solution for positioning based on angle of arrival measurements. *Proceeding of the 13th IEEE International Symposium on Personal, Indoor and Mobile Radio Communications.* 2002, Vol. 4, pp. 1522 - 1526.
- 10 Ho K., Chan Y. Solution and performance analysis of geolocation by TDOA. *IEEE T AERO ELEC SYS.* 1993, Vol. 29, No. 4, pp. 1311 - 1322.
- 11 Ho K.C., Chan Y.T. Geolocation of a known altitude object from TDOA and FDOA measurements. *IEEE T AERO ELEC SYS.* 1997, Vol. 33, No.3, pp. 770 - 783.
- 12 Hashemi-Sakhtsari A., Dogancay K. Recursive Least Squares Solution to Source Tracking using Time Difference of Arrival. *Proceeding of the IEEE International Conference on Acoustics, Speech and Signal Processing.* 2004, Vol. 2, pp. 385 - 388.
- 13 Lee S.C., Lee W.R., You K.H. TDoA Based UAV Localization Using Dual-EKF Algorithm. In: Ślęzak D., Kim T., Stoica A., Kang B.H. (eds). *Control and Automation.* 2009, Vol. 65, pp. 47 - 54.
- 14 Venkatraman S., Caffery J.J. Hybrid TOA/AOA Techniques for Mobile Location in Non-Line-of-Sight Environments. *Proceeding of the IEEE Conference Wireless Communications and Networking*, 2004, Vol. 1, pp. 274 - 278.
- 15 Cheung K.W., So H.C., Ma W.K., Chan Y.T. A constrained least squares approach to mobile positioning: algorithms and optimality. *EURASIP J ADV SIG PR.* 2006, Vol. 1, pp. 1 - 23.
- 16 Baldychev M.T., Pivkin I.G., Gaychuk Yu.N., Pechurin V.V., Laptev I.V. *A method for determining the location of sources of pulsed radio signals.* Russian Federation Patent No. 2695321, 2019, 10 p.
- 17 Demichev I.V., Yevgeniev D.N., Shaidulin Z.F. Estimation of coordinates of object in view of influence of the geometrical factor. *Journal Science Intensive Technologies.* 2010, No. 9, pp. 44 - 50.
- 18 Pivkin I.G., Pechurin V.V., Baldychev M.T., et al. *Model of a one – position system for determining the location of radio emission sources.* Russian Federation Certificate of State Registration of a Computer Program No.2019613634, 2019, 1 p.

DOI 10.31489/2020No1/127-131

UDC 537.533.2

DEVELOPMENT OF A DEVICE FOR DETERMINING WORK ELECTRON OUTPUT

Makeeva O.V.¹, Oleshko V.S.², Fedorov A.V.², Yurov V.M.³

¹ Moscow State University of Technologies and Management, Moscow, Russia, makeeva-oks@yandex.ru

² Moscow Aviation Institute (National Research University), Moscow, Russia, ovs_mai@mail.ru

³ E.A. Buketov Karaganda State University, Karaganda, Kazakhstan, exciton@list.ru

The surface is the most important component of metal parts and it is necessary to control its condition at all stages of the life cycle of the part - during its production, operation and repair. To carry out reliable non-destructive testing of metal parts, specially developed tools and methods for its use are necessary. The measuring electrode of the sensor of the measuring device of the contact potential difference and the surface of the metal part to be controlled form a capacitor, between the plates of which the contact potential difference occurs. The sensor of the device is a kind of intermediary between the contact potential difference and the measuring circuit. The portable complex for measuring the contact potential difference developed by the authors on the basis of a portable digital oscilloscope allows non-destructive testing of the surface of metal parts during their production, operation or repair to be performed continuously.

Keywords: non-destructive testing, metal part, surface, capacitor, contact potential difference.

Introduction

In modern engineering, multicomponent alloys based on Al, Fe, Ti, Cu, Ni, Cr, and other metals are widely used as materials for machine parts [1]. The surface is the most important component of metal parts and it is necessary to control its condition at all stages of the life cycle of the part - during its production, operation and repair. The surface layer of metal parts can be considered as part of a solid body, which includes its constituent molecules, atoms, protons, neutrons, electrons, vacancies, dislocations, and other components, each of which has energy. Surface conduction electrons are constantly in diffuse motion without leaving the surface in vacuum at a low temperature. However, with increasing temperature, the potential energy can reach such a value that the electron can leave the metal surface. Part of the electrons constantly jumps off the surface of the metal, but then returns back, because its potential energy is insufficient to fly over the potential barrier. It turns out that the metal surface is surrounded by an electronic cloud and electric forces are directed inside the metal surface. To overcome these forces and leave the metal surface, you need to do a job called electron work function (EWF). To determine the EWF you need to measure the potential difference (CPD).

The theory of CPD is directly related to the zone theory of solids. Considering the contact of two metals with different electron work function, we find that the electrons of the upper metal levels with a lower work function (EWF) will be located at low levels of the second metal with a larger work function (REE). As a result of this, the first metal will be charged positively, and the second will be negatively charged. In this case, the energy levels will shift, since the Fermi levels of both metals coincide. Also, the functions of the metals remain constant, and the potential energy of these metals at points outside their surface will differ. These differences lead to the appearance of a potential difference. To assess the state of energy of a metal surface, one needs to measure CPD. When we know the energy state of a metal surface, this is necessary for coating, welding of various metals and more. Knowledge of the energy state of the surface of metal parts is important, for

example, when applying protective coatings, bonding, soldering, welding and other technological operations.

1. Materials and methods

To carry out reliable non-destructive testing of metal parts, specially developed tools and methods for its use are necessary. The measuring electrode (ME) of the sensor of the measuring device of the CPD and the surface of the controlled metal part form a capacitor (DC), between which the CPD occurs. The sensor of the device is, in a way, an intermediary between the CPD and the measuring circuit.

The following functional requirements apply to capacitive sensors:

1. An easy-to-analyze form of dependence between input and output characteristics, preferably linear.
2. Sufficient sensitivity. Our studies have shown that, due to the energy heterogeneity of the surface of metal parts of machines, it is necessary to ensure the sensitivity of the measuring device of the measurement factor of 1 mV.
3. Stability of characteristics, the least influence of environmental parameters (humidity, temperature, atmospheric pressure, electromagnetic fields, radiation, etc.). In order to fulfill this requirement, it is necessary to use shielding of the sensor from spurious interference and to use metal having stable characteristics over time as an ME material. Most often, the developers of measuring devices for CPD use Au, Ni, or Cu [2–7].
4. Short measurement time of the CPD.
5. Ease of installation and operation.
6. Maintainability.
7. Low cost.

The indicated properties must be achieved when creating a measuring device for CPD.

The advantages of the method of DC method of the CPD are:

- the capacitor can be manufactured with high accuracy;
- the capacitor has low losses (the passage of electric current through capacitive resistance is not accompanied by heat loss) and a high efficiency;
- small effect of electric forces on the mechanical parts of the capacitor;
- the shape of the capacitor type sensor can be adapted to various surface shapes of the QS.

The disadvantage of capacitor methods for measuring physical quantities are small capacitance values. Therefore, it is necessary to use power amplifiers of the electric signal, or high-frequency oscillations of the capacitor plates, which does not always ensure the stability of the readings of the measuring device. In addition, the measurement error of the CPD can increase the electromagnetic interference arising in the circuit as a result of the remote location from the ME of the signal amplifier [8]. Therefore, it is advisable to place the preliminary signal amplifier directly in the sensor of the measuring device.

2. Discussion of results

The quality of the capacitor with alternating electric current (which occurs with DC) is best characterized by the time constant (product of capacitance and parallel resistance) Q_V [8]:

$$Q_V = \omega \cdot R \cdot C = \omega \cdot T, \quad (1)$$

where $\omega = 2\pi F$ is the circular frequency of the alternating current, rad/s; F is the frequency of alternating electric current, Hz; R - resistance, Ohm; C is the capacitance of the capacitor, F; T - period, s.

The resistance R at a high circular frequency ω is determined not only by insulation, but also includes other losses, for example, dielectric hysteresis losses, and therefore, according to formula (1), it increases in proportion to the circular frequency ω [8]. The vibrating ME of the sensor that implements the DC principle included in the alternating current circuit has the resistance R the lower, the higher the frequency F of the alternating current according to formula (1) [8]. The capacitance of the capacitor, the plates of which form the controlled part and measuring electrode (ME), depends on their shape (we chose a flat ME), the overlap area, dielectric constant (in our case, this is air) and the distance between its plates [8].

With the formation of ME and controlled by the metal part of the capacitor, the plates of which they are, the charge of the capacitor Q can be determined on the basis of the following formula [9]:

$$Q = C \cdot U = \frac{\epsilon_0 \cdot \epsilon \cdot S \cdot U}{d}$$

where $\epsilon_0 \approx 8.8542 \cdot 10^{-12}$ F/m is the electric constant (dielectric constant of vacuum); ϵ is the relative dielectric constant, for dry air $\epsilon \approx 1,0006$; S is the area of ME, m^2 ; U is the voltage across the capacitor; d is the gap between ME and capacitor plates (CO), m

In the case of a DC, the plates of which are ME vibrating with a frequency ω and the surface of the CO, then the capacitance S_{din} will change according to the law [9]:

$$C_{\text{din}}(t) = \frac{\epsilon_0 \cdot \epsilon \cdot S}{d_0 + d_1 \cdot \sin(\omega t)} = C \cdot \frac{1}{1 + m \cdot \sin(\omega t)}$$

where d_0 is the average distance between the ME and the surface of the controlled metal part; d_1 is the vibration amplitude of the ME; t is the time; $m = d_1/d_0$ is the modulation coefficient of the DC.

In this case, an electric current $I(t)$ will occur in the circuit [9]:

$$I(t) = U \cdot \frac{\partial C}{\partial t} = -\epsilon \cdot \epsilon_0 \cdot S \cdot U \cdot \frac{d_1 \cdot \omega \cdot \cos(\omega t)}{d_0 + d_1 \cdot \sin(\omega t)^2}$$

The sensors of measuring devices for measuring the CPD by the DC method are exposed to various factors that reduce the sensitivity and reliability of this method — intrinsic noises, interference from electromagnetic fields, spurious communication capacitances, etc. [9-12]. This requires careful shielding, the use of other structural design solutions in the construction of instrument sensors.

The method for measuring the CPD developed by us has the following features:

- the contact potential difference is measured by a digital oscilloscope that records the voltage and frequency of the periodically changing CPD between the controlled part and the ME of the device's sensor;

- shielding of sensor elements and wires;

- amplification of registered CPD and filtering of spurious signals;

- preparation of the surfaces of the part and the sensor for measuring the CPD.

We chose a Micsig TO1104 tablet type portable digital oscilloscope with a sensitivity of measuring electric voltage of 0.5 mV as the recorder of CPD. The authors connected the sensor connected to the oscilloscope themselves. The main part of the design of the sensor of the measuring device of the CPD is an electronic circuit that allows the IE of the sensor in contact with the metal part to operate in self-oscillating mode. In addition, the sensor includes a preliminary signal amplifier. The CPD measurement complex developed by the authors is shown in Figure 1.

The circuit diagram of the sensor is shown in Figure 2. The sensor housing (Figure 3) was designed in the Solid Works program and printed on a Picaso3D Designer 3D printer. The sensor housing is designed to provide a gap between ME and CO equal to 0.5 mm at rest of ME. The indicated design features of the sensor make it possible to perform a reliable measurement of the

CPD of metals. The authors continue to improve the design of the sensor for measuring the CPD of metal parts of machines.

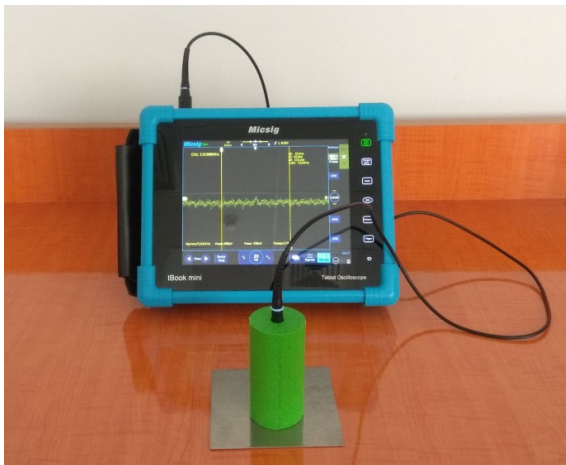


Fig.1. Complex for measuring the contact potential difference of metal parts.

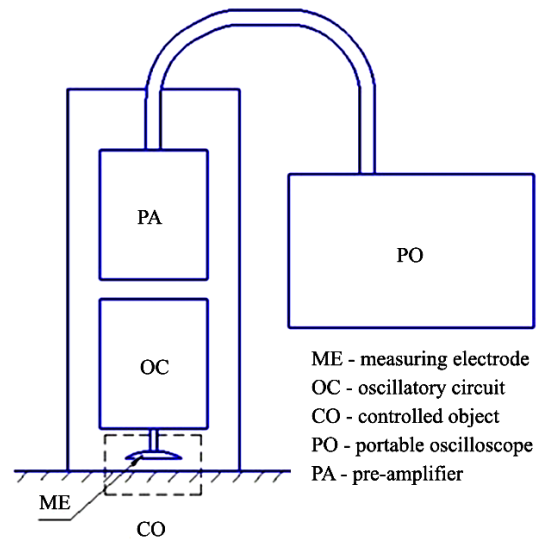


Fig.2. Schematic diagram of the sensor.

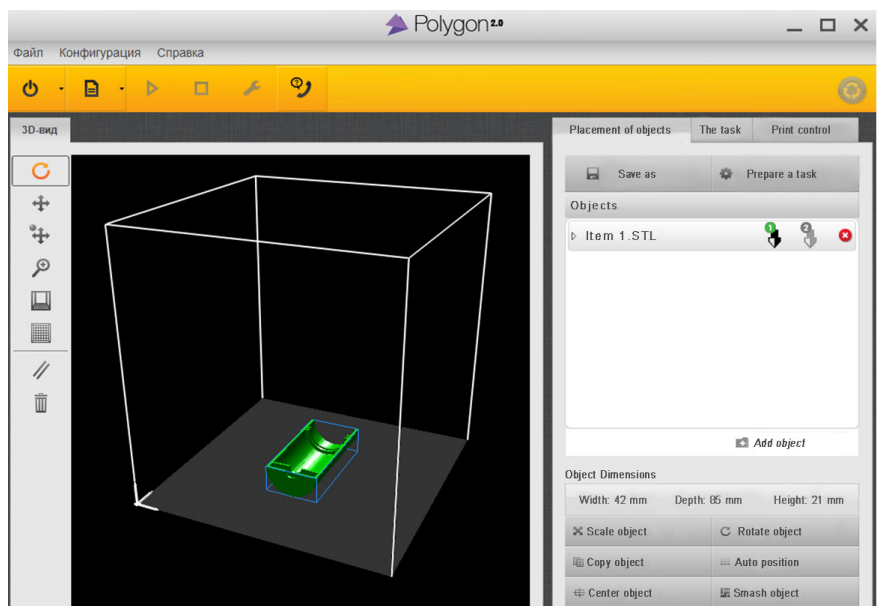


Fig.3. Polygon 2.0: Picaso3D Designer 3D Printer Operator.

Conclusion

Developed by the authors, a portable measurement complex of the CPD based on a portable digital oscilloscope allows non-destructive testing of the surface of metal parts in the process of their production, operation or repair to be carried out continuously. The results of measurements of the contact potential difference of metals were processed by methods of mathematical statistics. The results of experimental studies have shown a direct effect of changes in ambient temperature on the contact potential difference and the electrons work function of metal samples, which has an average

correlation It is found that atmospheric pressure and relative humidity have a weak effect on the contact potential difference and the electrons work function of the metals under study, their influence can be neglected. The effect of equilibrium and non-equilibrium environmental parameters on the contact potential difference and electrons work function of metal samples is studied. The results confirming the reduction of the contact potential difference (increase in the electrons work function) of metals, as well as an increase in the mean square deviation of the measurement results under non-equilibrium environmental conditions are obtained.

Our further work will consist in the development of a technique for measuring the CPD on the surface of machine parts [13–15].

Acknowledgements

The work was performed according to the program of the Ministry of Education and Science of the Republic of Kazakhstan. Grants No. 0118PK000063 and No. Φ .0780.

REFERENCES

- 1 Betsofen S.Ya., Osintsev O.E., Knyazev M.I., Dolgova M.I., et al. Quantitative phase analysis of Al-Cu-Li-Mg alloys. *Bulletin of the Moscow Aviation Institute*. 2016, Vol. 23, No. 4, pp. 181–188.
- 2 Musokhranov M.V. *Technological support for the quality of the surface layer of the guiding elements of mechanical engineering*. Diss. of Techn. Sciences Cand. Moscow, Bauman MSTU, 2006, 138 p.
- 3 Zharin A.L., Gusev O.K., Svistun A.I., Tyavlovsky A.K. Friction surface control by contact potential difference methods // *Izvestiya TulGU. Technical science*. 2011. Issue. 5. Part 2. - P. 286-295.
- 4 Kocharov E.A. *Physical methods in the control of materials and the development of high technology*. Moscow, VVIA named after prof. N.E. Zhukovsky. 2008, 447 p.
- 5 Kryachko V.V., Levin M.N., Tatarintsev A.V., et al. A non-contact method for studying the charge state of a semiconductor – insulator interface. *Journal of Technical Physics*. 2004, Vol. 74, Issue 10, pp. 128 – 133.
- 6 Loskutov S.V. *Regularities of the formation of the energy relief of a metal surface*. News of the Zaporizhzhyan State University. 1999, No. 1, pp. 138 – 142.
- 7 Petrov L.M., Plikhunov V.V. Determination of the energy state of the surface of structural metallic materials after technological influences. *Aviation industry*. 2012, No. 1, pp. 22 – 26.
- 8 Grachev A.V., Churakov P.P. Converter of parameters of non-contact capacitive sensors for conductodiometric measurements // *Bulletin of the Samara Scientific Center of the Russian Academy of Sciences*. 2016. Vol. 18. No. 4 (7). - P. 1363-1368.
- 9 Tyavlovsky A.K., Zharin A.L. Analysis of the method of measuring the surface potential of dielectrics according to the scheme of current compensation. *Instruments and methods of measurements*. 2011, No. 2 (3), pp. 136 – 144.
- 10 Kompaneyets I.V., Komolov V.M., Shkilko A.M. Assessment of the sensitivity of the contact potential difference meter. *Bulletin of NTU "KhPI": Series "New Solutions in Modern Technologies"*. 2010. No. 46, pp. 89 – 94.
- 11 Kolesnikov V.P. *Electrometry. Theoretical foundations of electrometry methods*. - Perm, 2019. - 264 p.
- 12 Panteleev K.V. *Methods and means of measuring the contact potential difference based on the analysis of the compensation dependence of the Kelvin probe*. Abstract. Diss. of Candidate of Technical Sciences. Minsk: Belarusian Nat. tech. Univ. 2016, 26 p.
- 13 Oleshko V.S., Yurov V.M. Fluctuation of the contact potential difference in determining the work function of electrons from structural materials by the ionization method. *Proceeding of the 10th Intern. Conf. "Chaos and structures in nonlinear systems. Theory and experiment"*, Almaty, 2017, pp. 165 – 169.
- 14 Oleshko V.S., Guchenko S.A., Yurov V.M. Determination of the surface energy of solid metals. *Proceeding of the XIV Int. Scientific Conf. "Solid State Physics, Functional Materials, and New Technologies" (FTT-2018)*, Bishkek-Karaganda, 2018, pp. 124-128.
- 15 Yurov V.M., Oleshko V.S. The impact of the environment on the contact potential difference of metal machine parts. *Eurasian Physical Technical Journal*. 2019, Vol. 16, No.1 (31), pp. 99 – 108.

DOI 10.31489/2020No1/132-137

UDC: 538.9:539.8

BIRTH AND FUSION IN A SOL-GEL PROCESS WITH LOW DIFFUSION

Temiraliev A.^{1,2}, Tompakova N.¹, Fedosimova A.^{1,2}, Dmitriyeva E.¹, Lebedev I.¹,
Grushevskaya E.^{1*}, Mukashev B.¹, Serikkanov A.¹

¹ Satbayev University, Institute of Physics and Technology, Almaty, Kazakhstan

² Al-Farabi Kazakh National University, Almaty, Kazakhstan, grushevskaiya@bk.ru

Based on the developed methods of nonlinear dynamics of the mapping of Poincare sections, a numerical simulation of the formation of thin SnO₂ films in sol-gel chemical reactions against the background of weak diffusion where carried out. Numerical calculations were carried out in the framework of dynamically determined chaos in intense opposing processes of merging and decay. For a chemically active medium in the sol-gel process, the differential diffusion equation with an internal source of nonlinearity is used. The simulation results qualitatively confirm the experimental fact of the emergence of Poisson-stable fractal cluster structures. The presence of fractal structures in the experimental results on thin films means the presence of nonlinear collective phenomena. The method of nonlinear self-organization of stable structures in a multi-particle system with competing internal processes is thought to be interesting for new technologies.

Keywords: Chaos, fractal, thin films, sol-gel process.

Introduction

A significant concentration of a huge number of interacting objects leads to the emergence in the dynamic system of new collective properties when any local perturbation, with a sufficient density of particles, affects the entire condensed medium. The nature of collective excitations determines the various properties of the system and leads to the emergence of various nanostructured ensembles. In complex open systems with a huge number of interacting objects, collective phenomena such as self-organization of structures arise. Such a collective action in the formation of structures G. Haken called "synergetics" [1]. Nanoclusters and particles with a large surface area have excess potential energy and high chemical activity. Therefore, no activation energy is required for aggregation processes and reactions with other compounds for the appearance of substances with new properties.

As A. Poincare once pointed out: in some non-integrable mechanical systems, the evolution of which, although determined by the Hamiltonian approach, may lead to unpredictable chaotic behavior. In real systems, irreversible dissipative processes are present, such as diffusion or a chemical reaction, and entropy grows in them. In this case, it is effective to use the methods of the nonlinear theory of dynamical systems, when instead of differential equations the Poincaré maps with bifurcations and other phenomena of the nonlinear theory are used. Knowledge of elementary microscopic processes will allow to identify the collective organization of a macroscopic cluster. The correlated interaction of a large number of elements of an ensemble can lead to the well-known phenomenon of self-organization.

The thin layers of tin dioxide SnO₂ can change the electrical conductivity during gas adsorption and this became the basis for their use in semiconductor sorption sensors along with other applications. Currently, several methods for producing tin dioxide based on the sol-gel technology have been developed [2–4]. For gas-sensitive sensors, films with a controlled porous structure are of particular interest. Essential is the fact of experimental confirmation of the occurrence of fractal-cluster structures of colloidal particles of the dispersed phase.

Models for the formation of fractal structures differ in clusterization mechanisms: models of diffusion-limited aggregation [5], models of cluster-cluster aggregation [6]. The low probability of particles or clusters sticking together leads to deep penetration of the clusters into each other and the formation of small fractal clusters [7-13].

We simulate a sol-gel process with harsh chemical reactions against the background of slow diffusion by a nonlinear parabolic equation. In diffusion processes, the mass flow is due to the motion of particles participating in Brownian thermal chaotic motion with energy kT (T -absolute temperature, Boltzmann k -constant). Mathematical models of diffusion processes are based on the fundamental laws of conservation of matter in the integral or differential form of the Ostrogradsky-Gauss equations. For small differences in the concentration of the substance $u(r, t)$, we apply the law for the diffusion flux: $[D \cdot \text{grad } u(r, t)]$. In case of significant changes in concentration over time, the law of diffusion applies: $\dot{u}_t = D \cdot \ddot{u}_{rr}$

1. Modeling the process of formation of fractal structures in thin films

The concentration of reagents, depending on the scheme and mechanism of the dynamic process, can simultaneously decrease in proportion to the concentration and increase in parallel competing, sequential or reversible chemical reactions. Given that the diffusion process for the concentration of the substance $u(r, t)$ in the approximation of deterministic dynamic chaos is described by the diffusion equation with dynamically determined chaos. So, the differential equation of the diffusion process in a chemically active medium with a dynamically determined randomness associated with the quadratic nonlinearity u^2 can be represented in the form [14]:

$$k_p \cdot \frac{\partial u(x, t)}{\partial t} = \frac{\partial}{\partial x} \left[D(u) \frac{\partial u(x, t)}{\partial x} \right] + k(t) \cdot \varphi(u),$$

with diffusion coefficient $D(u)$, porosity coefficient k_p [11] and evolution parameter $k(t)$ in a quadratically nonlinear function:

$$\varphi(u) = A(\alpha \cdot u - \beta \cdot u^2)$$

with a normalization coefficient A , which will determine the degree of rigidity of the process.

The nonlinear function $\varphi(u)$ is the density of the internal source of the formation of structures in the evolutionary competition of the processes of generation and recombination of the elements of a substance (atoms, ions, molecules, clusters) of a dynamic system with production coefficients α and absorption β . For certain values of the evolution parameter $k(t)$, the so-called dynamically determined chaos arises. The expected characteristics of a thin film of tin dioxide are determined mainly by the fractal dimension of the clusters, which are determined by the evolution parameter $k(t)$ of the deterministic chaotic dynamical system. The evolution parameter may also depend on the influence of thermal effects on the properties of films $[k(t) \rightarrow k(t, T)]$.

We solve the diffusion equation with an internal source with boundary and initial conditions:

$$\begin{cases} \frac{\partial u(x, t)}{\partial t} = \frac{\partial^2 u(x, t)}{\partial x^2} + k(t) \cdot \varphi(u) \\ u(x, 0) = \varphi(x), & 0 \leq x \leq 1 \\ u(0, t) = u(1, t) = 0 \end{cases}$$

After replacing the partial derivatives by their discrete analogues, we obtain a difference scheme:

$$\frac{(u_{i+1,j} - u_{i,j})}{\Delta t} = \frac{\sigma}{(\Delta x)^2} (u_{i+1,j-1} - 2u_{i+1,j} + u_{i+1,j+1}) + \frac{1-\sigma}{(\Delta x)^2} (u_{i,j-1} - 2u_{i,j} + u_{i,j+1})$$

For $\sigma=1/2$, the average of the two central derivatives is obtained (the Crank-Nichols scheme), for $\sigma=0$ the usual explicit scheme and $\sigma=1$ the implicit scheme.

We rewrite the implicit difference scheme ($\sigma = 1$)

$$\frac{(u_{i+1,j} - u_{i,j})}{\Delta t} = \frac{D}{(\Delta x)^2} (u_{i+1,j-1} - 2u_{i+1,j} + u_{i+1,j+1}) + f(u_{i,j})$$

as:

$$A_j u_{i+1,j-1} - B_j u_{i+1,j} + C_j u_{i+1,j+1} = F_j$$

The value from the lower layer, which is known, we have enclosed in the coefficient F_j . The remaining coefficients are expressed in steps of time, space and D . So we got difference equations that are connected by a system of linear algebraic equations.

2. Results and discussions

The results of computer numerical calculations of the differential equation of evolution of the state of a dynamic system in the sol-gel process are shown in Figures 1.

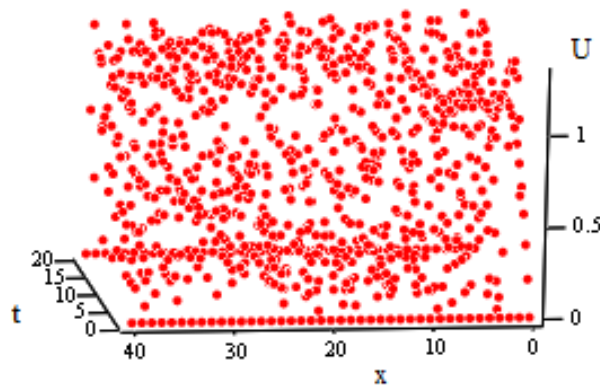


Fig.1. Formation of thin film structure in a sol-gel process at $k=0.97$

The formation of structures depends on the evolution time, which in our model is determined by the parameter $k(t)$ and is shown in Figure 2. Moderation is programmed by setting several pairs of initial conditions for the concentration of reagents. A combined matrix is formed from separate matrices of solutions of the nonlinear differential equation for different initial conditions. The calculations of the evolution of the dynamic system of a chemical reaction with diffusion of this sol-gel formation of thin films are shown in Figures 1 and 2. The constructed trajectories on the phase plane reflect the dynamics of the concentration of intermediate products of the chemical reaction.

Model parameters are initial concentrations. A study is being made of the solution of a nonlinear differential equation depending on various initial conditions. There is a direct proportion to the ripening temperature of thin films and the evolution time in modeling the sol-gel system. More specifically, this is the number of steps in numerically solving a differential equation. The model is constructed in accordance with the idea of the so-called Prigogine brussellator [15] for solving the system of equations of an autocatalytic chemical reaction with diffusion. Moderation is programmed by setting several pairs of initial conditions for the concentration of reagents.

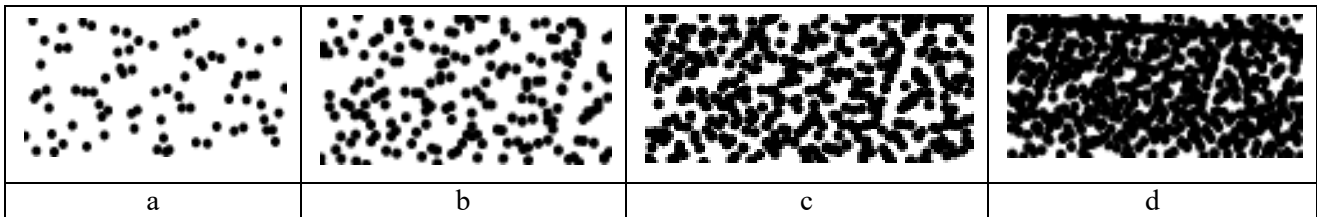


Fig.2. Stages of the formation of U-surface structures of a thin SnO_2 film with parameter:
 a) $k = 0.1$; b) $k = 0.2$; c) $k = 0.5$; d) $k = 0.9$.

A combined matrix is formed from separate matrices of solutions of the nonlinear differential equation for different initial conditions. The calculations of the evolution of the dynamic system of a chemical reaction with diffusion - sol-gel formation of thin films are shown in Figures 3 and 4.

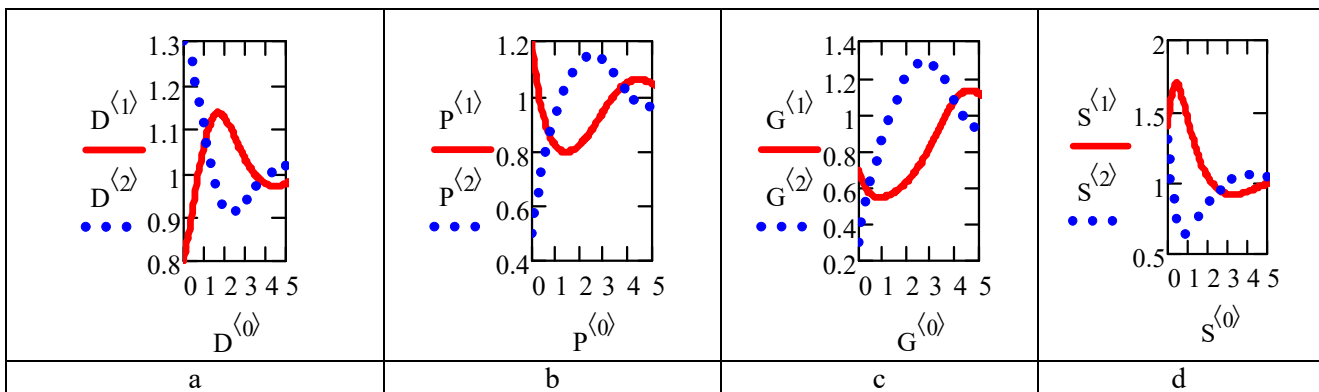


Fig.3. The graph of the time dependence of the solution of the differential equation:

- a) for the distribution function D under initial conditions 0.8 and 1.3; b) function P under initial conditions 0.5 and 1.2; c) function G under initial conditions 0.7 and 0.3; d) function S under initial conditions 1.4 and 1.3.

The constructed trajectories on the phase plane reflect the dynamics of the concentration of intermediate products of a chemical reaction. The parameters of the model are the initial concentration. We present a part of the program code for further calculations presented in Figures 3.

$$\begin{aligned}
 \underline{\underline{F}}(t, y) &:= \begin{bmatrix} -(k+1) \cdot y_0 + (y_0)^1 \cdot y_1 \cdot k + 1 \\ k \cdot y_0 - (y_0)^1 \cdot y_1 \cdot k \end{bmatrix} & \underline{\underline{D}} &:= \text{rkfixed} \left[\begin{bmatrix} 0.8 \\ 1.3 \end{bmatrix}, t_0, t_1, N, F \right] \\
 N &:= 500 \quad t_0 := 0 \quad t_1 := 20 & \underline{\underline{P}} &:= \text{rkfixed} \left[\begin{bmatrix} 1.2 \\ 0.5 \end{bmatrix}, t_0, t_1, N, F \right] \\
 \underline{\underline{G}} &:= \text{rkfixed} \left[\begin{bmatrix} 0.7 \\ 0.3 \end{bmatrix}, t_0, t_1, N, F \right] \\
 \underline{\underline{S}} &:= \text{rkfixed} \left[\begin{bmatrix} 1.4 \\ 1.3 \end{bmatrix}, t_0, t_1, N, F \right]
 \end{aligned}$$

From Figure 4 it can be seen that all the trajectories from the solution of the system of differential equations that come from different starting points converge to the so-called attractor

with coordinates (1.1) from the theory of nonlinear dynamical systems. In this case, this attractor is a “node”. The counteraction of various direct and reverse chemical reactions along with coagulation and peptization in a dispersed medium in sol-gel processes with a stochastic diffusion component leads to the establishment of a certain stationary state with equilibrium concentrations. This will allow obtain optimal parameters.

Conclusion

The presence of fractal structures in the experimental results on thin films means the presence of nonlinear collective phenomena associated with the stochastic process. Fractal dimension is an essential parameter for understanding the properties of film roughness. Algorithms of evolutionary programs were developed and numerical computer calculations were performed for a model representation of the formation of nano-structured clusters of thin films. An interesting review of the fractal analysis of thin films is given in [16]. The formation of structures in dynamically determined chaos [17, 18] provides the key to the development of new nano-structured materials, new quantum technologies.

The method of forming structures within the framework of the introduced nonlinear equation for competing processes of decay and fusion against the background of weak diffusion is new approaches for the mechanism of structure formation. The results of computer modeling indicate the collective effects of self-organization of stable structures. The nonlinear evolution of many-particle sol-gel dynamics with opposing chemical reactions leads to the formation of fractal clusters, which corresponds to the available experimental data on the fractal structure in thin films. The performed numerical calculations within the framework of dynamically determined chaos, like any calculations in deterministic chaos, can be unambiguously reproduced.

Acknowledgments

This work was supported by grant AP05134263 and BR05236404 of Ministry of Education and Science of Kazakhstan Republic.

REFERENCES

- 1 Haken H. Application of the maximum information entropy principle of self organizing systems. *Zeitschrift für Physik B Condensed Matter. Springer*, 1985, Vol.61, pp.335-338.
- 2 Dmitrieva E.A., Mukhamedshina D.M., Beisenkhanov N.B., Mit' K.A. The effect of NH_4F and NH_4OH on the structure and physical properties of thin SnO_2 films synthesized by the sol-gel method. *Glass Physics and Chemistry*. 2014, No. 31, pp.31 -36.
- 3 Mukashev B.N. et al. Influence of structure changes of oxide films on their physical properties. *Materials Science and Engineering B*, 2005, No. 118, pp. 164-169.
- 4 Mukhamedshina D.M., Beisenkhanov N.B., Mit' K.A., Botvin V.A., Valitova I.V., Dmitrieva E.A. Influence of plasma treatments on the properties of SnO_x thin films. *High Temperature Material Processes*, 2006, Vol.10, pp.603-616, DOI:10.1615/HighTempMatProc.v10.i4.110.
- 5 Witten T A. Jr., Sander L M. Diffusion-limited aggregation, a kinetic critical phenomenon. *Phys. Rev. Lett.*, 1981, Vol.47, pp.1400.
- 6 Brinker C.J., Scherer G.W. Sol gel glass: I, gelation and gel structure. *J.: Non-Cryst. Solids*, 1985, Vol.70, pp.301.
- 7 Moshnikov V.A., Alexandrova O. A. New nanomaterial. Synthesis. Diagnostics. Modeling. *SPb.: Publishing house Etu "LETI"*, 2015.
- 8 Pan Tan, Yihao Liang, Qin Xu, Eugene Mamontov, Jinglai Li, Xiangjun Xing, Liang Hong. Gradual crossover from subdiffusion to normal diffusion: a many-body effect in protein surface water. *Phys. Rev. Lett.*, 2018, Vol.120, No.248101.

- 9 Thai M. Hoang, Rui Pan, Jonghoon Ahn, Jaehoon Bang, H. T. Quan, Tongcang Li. Experimental test of the differential fluctuation theorem and a generalized Jarzynski equality for arbitrary initial states. *Phys. Rev. Lett.*, 2018, Vol.120(8), DOI:10.1103/PhysRevLett.120.080602.
- 10 Zhang W. et al. Unexpected stable stoichiometries of sodium chlorides. *Science*, Vol.342, Is.6165, pp. 1502-1505, DOI: 10.1126/science.1244989.
- 11 Martinson L.K., Malov Yu.I., Differential equations of mathematical physics. M.: MSTU, 2002.
- 12 Dmitriyeva E.A., Mukhamedshina D.M., Mit' K.A., Lebedev I.A., Girina I.I., Fedosimova A.I., Grushevskaya E.A. Doping of fluorine of tin dioxide films synthesized by sol-gel method. *News of the National Academy of Sciences of the Republic of Kazakhstan (series of geology and technical sciences)*. 2019, V.433, pp.73–79, DOI: 10.32014/2019.2518-170X.9.
- 13 Korolenko P.V. et al. Innovative methods of analysis of stochastic processes and structures in optics. Fractal and multifractal methods. M.: Moscow state University, SINP, 2004.
- 14 Fedosimova A.I., Dmitrieva E.A., Lebedev I.A., Temiraliev A.T., Temiraliev A.T., Abishev M.E., Baitimbetova B.A., Ryabikin Yu.A., Serikkanov A.S. Modeling the process of formation of fractal structures in thin films. *IOP Conf. Series: Journal of Physics: Conf. Series*, 2018, Vol.1141, No.012004, DOI:10.1088/1742-6596/1141/1/012004.
- 15 Nicolis G., Prigozhin I. *Self-organization in non-equilibrium systems*. M.: Mir, 1979.
- 16 Fredrick M. Mwema, Esther T. Akinlabi, Oluseyi P. Oladijo. Fractal Analysis of Thin Films Surfaces: A Brief Overview. *Advances in Material Sciences and Engineering*, 2019, pp. 251-263.
- 17 Grushevskaya E.A., Ibraimova S.A., Dmitriyeva E.A., Lebedev I.A., Mit' K.A., Mukhamedshina D.M., Fedosimova A.I., Serikkanov A.S., Temiraliev A.T. Sensitivity to ethanol vapour of thin films SnO₂ doped with fluorine. *Eurasian Chemico-Technological Journal*, 2019, Vol.21, pp.13–17, DOI: 10.18321/ectj781.
- 18 Ryaguzov A.P., Kudabayeva M.A., Nemkayeva R.R., Guseinov N.R., Myrzabekova M.M. Study of the structure of amorphous carbon films modified with silicon oxide. *Eurasian Physical Technical Journal*, 2019, Vol.16, No.1(31), pp. 6 – 11.

DOI 10.31489/2020No1/138-144

UDC: 621.386-783.4

CALCULATION OF STRUCTURAL PARAMETERS AND DESIGN OF A PROTECTIVE SHIELD FOR AN X-RAY SYSTEM

Plotnikova I.V.¹, Redko L.A.¹, Baus S.S.², Starý O.³, Kassymov S.S.⁴, Baltabekov A.S.⁴

¹ National Research Tomsk Polytechnic University, Tomsk, Russia, inna@tpu.ru

² Kazan National Research Technical University named after A.N. Tupolev, Kazan, Russia

³ Czech Technical University in Prague, Prague, Czech Republic, oldStar@centrum.cz

⁴ E.A. Buketov Karaganda State University Karaganda, Kazakhstan

The need to calculate the radiation protection of the radiation system is the basis in which diagnostic, design or assembly activities are carried out as part of non-destructive testing. The paper provides an analysis of the design features of x-ray systems and their technical characteristics, operating conditions, diagnostic capabilities of modern tomographic systems. The dependences of the distribution of X-ray radiation and voltage on the thickness of the protective screen are given. The calculation of the thickness of the protective screen is presented, which will allow you to design the body of the protective screen of the x-ray system. The above studies will facilitate the work of specialists in the development of new modifications of x-ray systems.

Keywords: model, control, design, x-ray radiation, characteristic

Introduction

Any corporation needs a system of non-destructive testing to view the penetration of the internal structure of an object without damaging it. This technology is used in the nuclear, gas, shipbuilding, ship repair and other industries [1, 2]. Detection of defects in a controlled product and its internal structure can be carried out by various types of non-destructive testing, one of which is x-ray tomography. This type of tomography fully controls the geometry and nature of the volume distribution of density, and also allows to see the elemental composition of the product without destroying it. This type of tomography allows to control in detail the geometric structure and nature of the volume distribution of density and elemental composition without destroying the product [3]. In addition, this provides fundamentally new opportunities, especially, the ability to reproduce the internal structure of thick, heterogeneous industrial products of complex shape without overlapping shadows of various elements.

Nowadays with the rapid development of x-ray control systems [4] designers solve a problem with design of the x-ray systems' filter for the restriction of the x-ray radiation exit from working area, for the purpose of personnel protection against the radiation. Often before the team of designers there is a dilemma between reduction of mass of a system and the system effectiveness of protection [5, 6]. Safety of the personnel that work at this system depends on the exact calculation of constructional parameters. The matters are resolved due to the calculation of constructional parameters for the purpose of formation of the most effective system parameters [7], to carrying out skilled tests [8, 9]. Modern requirements for x-ray safety when carrying out nondestructive control and the rule demand that any system based on radiations of big power has to have a specially developed system and the certified protection against x-ray radiation [10-12].

When creating a new x-ray tomograph systems the design stage is fundamental [13]. At this stage the key parameters of technical system according to the specification pay off, essentially new technical solutions are developed [14, 15], configuration of system is made [16, 17]. Activities for

the development and design of x-ray systems have a tested character; the choice of the constructional parameters is made by means of theoretical formulas of weakening of x-ray radiation when passing through the material and also the intuitive selection of the accessories which correspond to these parameters [18]. These calculations are very labor-consuming and characterize only a situational (static) condition of x-ray optical system within the specifically chosen values of factors which don't allow to estimate fully behavior of system (change of output parameter) at change of factors values. This fact significantly complicates the work on the development and design of x-ray optical system. In this regard the decision to define and create a method of determination of mathematical dependence which will allow to model the process and to analyze the behavior of the system has been made, will significantly reduce temporary expenses and will increase the quality and also accuracy of the developed systems.

1. Samples and Research Methods

The most wide spread systems for the industrial non-destructive testing (NDT) is x-ray tomographs [19]. X-ray tomographs are divided into several types: by the sizes to the studied sizes, technical characteristics, a scope etc. [20]. Now the most popular direction of development of these systems for the NDT can be considered microtomographs [21]. These systems allow to investigate internal structure of the objects with micron sizes. These systems are characterized by tension on an x-ray tube from 10 to 160 kV, the small size of a focal spot - from 1 to 10 microns [10]. The X-ray optical system which is intended for the NDT consists of the following elements [12, 22]:

- a source of x-ray radiation – an x-ray tube;
- detector of x-ray radiation [12];
- the system of positioning with a working surface;
- the software for processing of shadow images and formation of two or three-dimensional images, depending on a type of the x-ray tomograph [23];
- a control system – a hardware and software system on management of system mechanics [24];
- power supply unit;
- filter.

One of the most difficult and responsible sections of x-ray systems' design for nondestructive control is calculation of radiation protection – the filter. In all cases the main room for holding actions within the nondestructive control is the workshop in which diagnostic, design or assembly actions are carried out and in which the x-ray radiator as a source of ionizing radiation is placed [12]. From here the necessity of carrying out the calculation of system radiation protection, i.e. definition of lead or other equivalent of stationary means of radiation protection follows [25, 26]. Having decided on parameters and the sizes of x-ray optical system and also a source of x-ray radiation, there is a task of calculation of the lead screen of protection against x-ray radiation for safe work on this system according to the international standards [27].

The calculation of the lead screen from x-ray radiation consists of three actions:

- determination of necessary coefficient of x-ray radiation weakening which shows in how many times it is necessary to reduce the dose power to the admissible size;
 - determination of lead protection thickness that is necessary for the deceleration of power of the dose absorbed in the air that is created by a source of x-ray radiation to the admissible size [8];
 - recalculation of the found lead protection thickness on that material from which there are designed the building constructions or other devices;
 - choice of the quality of filter material and its structure.
- The shortcomings of the applied methods of calculation of radiation protection are:
- physically incorrect expression of the key calculated parameter – coefficient of weakening of radiation,

– lack of accounting of orientation of primary bunch of radiation and the movement of the last one during the research (the panoramic tomographs, x-ray computer tomographs that can scan devices),

– the outdated list and working loadings of the x-ray diagnostic devices used in practice, including devices with digital receivers of the image, outdated standards and units of measure of maximum permissible radiation levels.

A special role when calculating the constructional parameters of system is played by such parameters of material as quality and uniformity of material of the filter (availability of foreign particulates, susceptibility to wear), existence of places of deformation [12], sutural and welded connections. The requirements to the systems:

– The system of the x-ray tomograph' filter has to be completely certified according to the ROV standard.

– All systems have to correspond to the local rules and resolutions. For example, in Great Britain it "Rules of the address with sources of ionizing radiation".

– The maximum admissible value of level of the filter radiation leakage shouldn't exceed 5 mSv/h (in the USA), 1 mSv/h (in the other countries).

– After the installation and obtaining the certificate all the x-ray systems undergo the final testing in order to avoid casual radiation of personnel.

The main settlement parameter is a physically correct coefficient of frequency rate of weakening. The coefficient of frequency rate of easing represents the relation of power of the x-ray radiation absorbed dose in this point of air in lack of protection of D_0 to the admissible power of the absorbed dose in air N_D [5]. For the calculation of coefficient of x-ray radiation weakening when determining power of a dose in air in x-rays for an hour use Equation

$$K = \frac{I}{R} \cdot N_D,$$

where I - is the standard anode current of a x-ray tube; R - is the distance from an x-ray tube to the place of protection, m; N_D - is the admissible power (exposition) dose of radiation absorbed in air, P/hour.

Size of N_D is found by means of help tables. Necessary thickness of lead protection depends on the coefficient of easing and tension on an x-ray tube and is found in special help tables, which depends on coefficient of x-ray radiation weakening and also tension on an x-ray tube. As it was already noted, passing through the substance, x-ray radiation is absorbed. Materials with a high density most strongly absorb the x-ray radiation therefore the case of x-ray installation is often manufactured of lead, and in some x-ray generators for additional protection against radiation the copper is used. For a start we will designate the key parameters at design of the filter: tension of an x-ray tube; tube power; angle of distribution of an x-ray bunch; distance of an x-ray tube from filter walls; thickness of lead material; level of an x-ray bunch after passing of the filter; existence of sutural connections.

For obtaining dependence of key parameter of an x-ray tube, i.e. the tension and thickness of the filter for creation of mathematical model the following parameters have been determined:

- power of an x-ray tube should be 10 W.
- the angle of distribution of an x-ray bunch should be 90 degrees.
- distance of an x-ray tube from filter walls should be 0.03 mm.
- range of the considered tension should be from 60 to 160 kV.
- the radiation size when passing the filter shouldn't exceed the size of 1 mSv/h, according to the international standards of safety.

2. Results and discussions

In general, a large number of experiments have been made for increase in accuracy of mathematical model, with a step of the tension of the x-ray radiation of 5 kV. The results of an experiment are presented in the Figure 1. In this figure two lines are presented, the line 1 shows the results of theoretical calculations by means of the formulas given above, and the line 2 shows the results of empirical researches at what thickness of the filter, the system completely conforms to the requirements for x-ray safety.

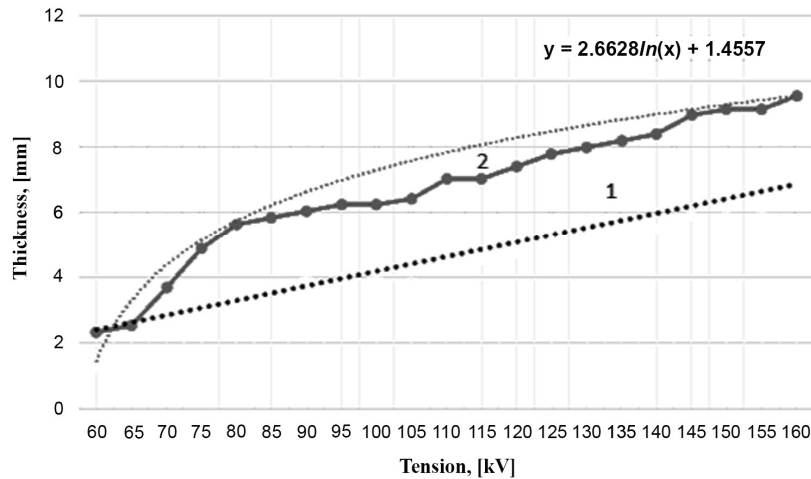


Fig.1. Dependence of tension on filter thickness

On the basis of empirical data, the mathematical model is defined. It submits to the logarithmic law and it is equal to

$$y = 2.66628 \cdot \ln(x) + 1.4557.$$

Proceeding from this schedule it is visible that theoretical calculations don't allow with the required accuracy to count the constructional parameters of the filter and here it is nothing to do without the manual selection. The created mathematical model solves this problem and allows to determine the required parameters of the x-ray system filter with high precision.

For obtaining the dependence of thickness of the filter in a lead equivalent from the angle of distribution of x-ray radiation (parameter of an x-ray tube) for the mathematical model creation the following parameters have been determined:

1. power of an x-ray tube should be 10 W.
2. tension should be 120 kV.
3. distance of an x-ray tube from filter walls should be 0.03 mm.
4. range of an angle of distribution of an x-ray stream should be from 15 to 170 degrees.
5. the radiation size when passing the filter shouldn't exceed the size of 1 mSv/h, according to the international standards of safety.

In general, a number of experiments, with a step of an angle of distribution of an x-ray bunch, that are equal to 5 degrees have been produced. The results of an experiment are presented in the Figure 2. In this figure the empirical results which display the dependence of filter thickness on a radiation bunch angle are presented. At this thickness the system completely conforms to the requirements for x-ray safety. On the basis of empirical data, the mathematical model which submits to the polynomial law of the 3rd degree

$$y = -0.0051 \cdot x^2 + 0.095 \cdot x^2 - 0.73311 \cdot x + 12.133$$

The created mathematical model solves a problem of the automated calculation of constructional parameters within these system parameters and allows to determine the required parameters of the x-ray system filter with high precision, without resorting to the means of manual

selection which is not easy, isn't safe and also is temporarily expensive. Excerpts for various modes and parameters of the protective lead screen for the x-ray system, intended for the designed rooms for constant stay of personnel are presented in the Table 1. For this purpose, we will take R=0.3 m.

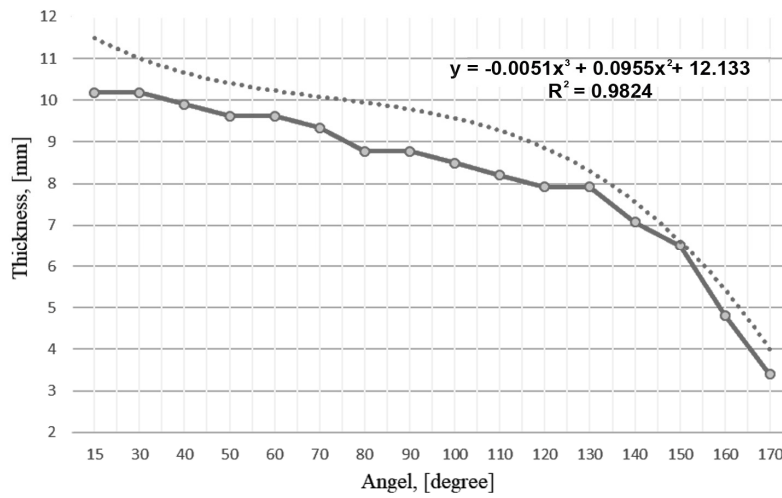


Fig.2. Dependence of an angle of distribution of x-ray radiation and filter thickness

Table 1 presents the empirical model of the dependence of the thickness of the protective screen of an x-ray tomograph on various combinations of parameters of the x-ray optical system. As can be seen from Table 1, when identical parameters are set on the x-ray tube (power, current strength, scattering angle) and, changing only the voltage value, a gradual increase in the thickness of the protective shield is observed, the size of which is achieved at 12.1 mm at a voltage of 140kV. But it is worth noting one behavioral feature of the x-ray protection system. With a progressive increase in the scattering angle and output voltage of the x-ray tube, a progressive increase in the thickness of the protective screen is no longer observed.

Table 1. Calculation of filter thickness

No	Current, [mA]	Angle of dispersion	Tension	Thickness of protection, not less than, [mm]
1	0.1	30	80	8.9
2	0.1	30	120	10.8
4	0.1	45	160	10.7
5	0.1	60	180	11.2

On the contrary, the magnitude of the screen once increases, then decreases in comparison with the previous empirical indication and the entire distribution of the obtained values. This is due to the properties of the intensity value of the output x-ray beam, the propagation model, as well as the value and influence of this or that parameter on the thickness of the protective screen of the x-ray optical system. The most problematic places in the design of the protective shield of an x-ray optical system are places in which different blocks of materials are interconnected. Much attention has to be paid to the sutural and welded connections in case filter layer as the data of the place are the most problem at design of these systems [28]. A big role at design of the filter of x-ray system plays a room type in which it will be applied. During the applying the same values that were in the second series of experiments, it has been found out that in places where the sutural or welded compounds of lead material are observed, holes in the filter are observed where the values of intensity of x-ray radiation exceeds the established norms. The size of excess in many aspects depends on a type and quality of sutural connection, the more professionally this seam is executed, the less the value is. This result is presented in the Figure 3.

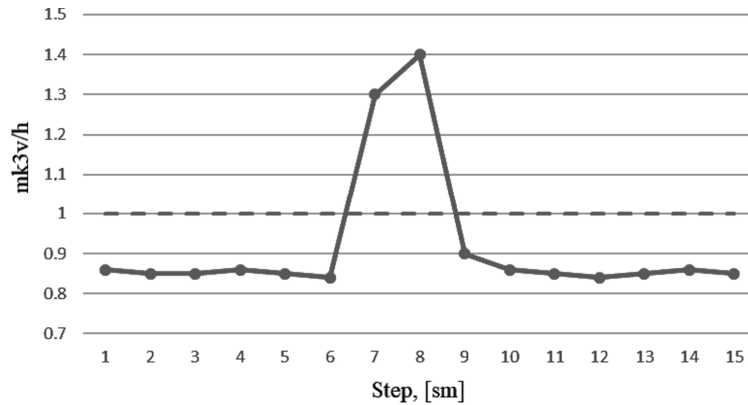


Fig.3. Level of an x-ray radiations

In the situations considered in the Figure 3 it is necessary to accept additional patches over the main material in order to avoid the radiation of personnel. The size of an additional patch is often equal to 1.6 from the main thickness of a leaf.

Conclusion

In the conclusion there is necessary to note that in this article the mathematical models for design of the x-ray systems filter are received, their key characteristics, the main dependences of parameters and also recommendations about design of the x-ray system filter are defined. The unique capabilities of the method of industrial X-ray computed tomography can most effectively be used in the development of technological processes, the development of new products and materials, the control of critical components and mechanisms. Knowing the dependence that was received from the practical data it is possible to calculate precisely constructional parameters of system, and it means that it isn't required it is required additional actions, such as manual selection of material thickness, etc. This fact favorably distinguishes this mathematical dependence on the available theoretical means of calculation. This model has the importance in practice as it allows to design the case of the x-ray system filter that facilitates the work of engineers and constructs on development of new modifications of x-ray systems.

Acknowledgements

The research is carried out at Tomsk Polytechnic University within the framework of Tomsk Polytechnic University Competitiveness Enhancement Program grant.

REFERENCES

- 1 Antropov A.P., Ragutkin A.V., Melnikov P.V., Luchnikov P.A., Zaitsev N.K. Composite material for optical oxygen sensor. *IOP Conference Series: Materials Science and Engineering*. 2018, Vol. 289.
- 2 Seynaeve P.C., Broos J.I. The history of tomography. *Journal Belge de Radiologie*. 1995, Vol. 78, No.5, pp. 284 – 288.
- 3 Kowaluk T., Woźniak A. Influence of measurement parameters settings on the results of the CT measurement. *Advances in Intelligent Systems and Computing*. 2018, Vol. 644, pp. 607-612.
- 4 Stock S.R. *Micro Computed Tomography: Methodology and Applications*. Boca Raton, FLCRC Press, Taylor & Francis Group. 2009, 364 p. doi: 10.1201/9781420058772.
- 5 Körner M., Weber C.H., Wirth S., et al. Advances in digital radiography: Physical principles and system overview. *Radio Graphics*. 2007, Vol. 27, No 3, pp. 675 – 686. doi: 10.1148/rg.273065075.
- 6 Hsieh J. *Computed tomography: principles, design, artifacts, and recent advances*. Bellingham. SPIE Press; Hoboken: Wiley Interscience. 2009, 556 p.
- 7 Dobbins J.T., Godfrey D.J. Digital x-ray tomosynthesis: current state of the art and clinical potential. *Physics in Medicine and Biology*. 2003, Vol. 48, No 19, pp. 65 – 106. doi: 10.1088/0031-9155/48/19/R01.

- 8 Gomi T., Hirano H., Nakajima M., Umeda T. X-ray digital linear tomosynthesis imaging. *Journal of Biomedical Science and Engineering*. 2011, No 4, pp. 443 – 453.
- 9 Blinov A.B., Blinov N.N. Radiation Load in X-Ray Computer Tomography. *Biomedical Engineering*. 2011, Vol. 44, No.5, pp. 180 – 181.
- 10 Baus S.S., Redko L.A., Yanushevskaya M.N. X-ray Tomographic System Behavior Prediction Based on a Mathematical Model. *IOP Conference Series: Materials Science and Engineering*. 2016, Vol. 189, No.1, pp. 1 – 5.
- 11 Dunsmuir J., Bennett S., Fareria L., Mingino A., Sansone M. X-ray microtomographic imaging and analysis for basic research. *Powder Diffraction*. 2006, Vol. 21, No.2, pp.125 – 131.
- 12 Landis E.N., Keane D.T. X-ray microtomography, *Materials Characterization*. 2010, Vol. 61, No.12, pp. 1305 – 1316.
- 13 Gavrilin A., Moyzes B., Kuvshinov K., Vedyashkin M., Surzhikova O. Determination of optimal milling modes by means of shock-vibration load reduction on tool and peak-factor equipment. *Materials Science Forum*. 2019, Vol. 942, pp. 87 – 96.
- 14 Dorr A., Sled J.G., Kabani N. Three-dimensional cerebral vasculature of the CBA mouse brain: A magnetic resonance imaging and micro computed tomography study. *Neuroimage*. 2007, Vol. 35, No 4, pp.1409-423 DOI: [10.1016/j.neuroimage.2006.12.040](https://doi.org/10.1016/j.neuroimage.2006.12.040)
- 15 Kowaluk T., Woźniak A. Influence of measurement parameters settings on the results of the CT measurement, *Advances in Intelligent Systems and Computing*. 2018, Vol. 644, pp. 607 – 612.
- 16 Plotnikova I.V., Chicherina N.V., Bays S.S., Bildanov R.G., Stary O. The selection criteria elements of X-ray optics system, *IOP Conference Series: Materials Science and Engineering*, 2018, Vol. 289, No.1, pp.012029.
- 17 Li. Y. Mathematical models for radiographic exposure and their application. *NDT & E International*. 1999, Vol. 25, No. 4–5, pp. 183–189.
- 18 Dunsmuir J.H., Bennett S., Fareria L., Mingino A., Sansone S. X-ray microtomographic imaging and analysis for basic research. *Powder Diffraction*. 2006, Vol. 21, No. 2, pp.125-131, doi: 10.1154/1.2204956
- 19 Tsai C.-L., Tsai M.-J. Significance of weld undercut in design of fillet welded T-joints, *Welding Research Supplement*. 1984, Vol. 2, pp.64 – 70.
- 20 Faraz A. Effect of Welding Parameters on the Structural Performance of Fusion Welded Extruded and Injection Molded HDPE Joints. *Journal of Space technology*. 2014, Vol. 1, pp. 114 – 119.
- 21 Lai H.S. Effect of defects on the burst failure of butt fusion welded polyethylene pipes. *Journal of Mechanical Science and Technology*. 2016, Vol. 30, pp. 1973–1981.
- 22 Barber P., Atkinson J.R. The use of tensile tests to determine the optimum conditions for butt fusion welding certain grades of polyethylene, polybutene-I and polypropylene pipes. *Journal of materials science*. 1974, Vol. 9, pp. 1456–1466.
- 23 Luchnikov P.A., Vetrova V.V., Zubkov N.P., Surzhikova, O.A. Chernova, N.I. Deformable Polymer Dielectric Films in Phase Light Modulators. *IOP Conference Series: Materials Science and Engineering*. 2017, Vol. 189, pp. 012027.
- 24 Luchnikov P.A. Defect formation in fluoropolymer films at their condensation from a gas phase. *IOP Conference Series: Materials Science and Engineering IOP*. 2018, Vol. 289, pp. 012037.
- 25 Yurov V.M., Goncharenko V.I., Vasiliev S.L., Dmitriev S.A., Yurgenson S.A. Experimental study of changes in the structure of polymer material by computational x-ray tomography. *Eurasian Physical Technical Journal*. 2019, Vol.16, No.2 (32) pp. 26 – 30.
- 26 Yurov V.M., Goncharenko V.I., Vasiliev S.L., Dmitriev S.A., Yurgenson S.A. X-ray computed tomography – based analysis of impact damage propagation in composition materials. *Eurasian Physical Technical Journal*, 2019, Vol.16, No.2 (32) pp. 31 – 35.
- 27 Surzhikova O. Power supply of remote and almost inaccessible settlements. *IOP Conf. Series: Materials Science and Engineering IOP*. 2015, Vol. 81, No. 1, pp. 012098.
- 28 Surzhikov A.P., Pritulov A.M., Lysenko E.N., Sokolovskii A.N., Vlasov V.A., Vasendina E.A. Dependence of lithium-zinc ferrosphal phase composition on the duration of synthesis in an accelerated electron beam. *Journal of Thermal Analysis and Calorimetry*. 2012, Vol. 110, No 2, pp. 733 – 738.

FINITE DIFFERENCE METHOD IMPLEMENTATION FOR NUMERICAL INTEGRATION HYDRODYNAMIC EQUATIONS MELTS

Kazhikenova S.Sh.¹, Belomestny D.², Shaltakov S.N.¹, Shaihova G.S.¹

¹Karaganda State Technical University, Karaganda, Kazakhstan, sauleshka555@mail.ru

²Duisburg-Essen University, Duisburg, Germany

The liquid state theory is not a simple section of the modern theory of metallurgical processes. Any substance in liquid state is a difficult object to establish not only quantitative, but also qualitative patterns, being that liquid state is intermediate between solid and gaseous states. Theoretical hydrodynamics has long attracted attention of various specialties' scientists: comparative simplicity of the basic equations, precise problems formulation and clarity of its experiments inspired hope of getting a dynamic phenomena's complete description occurring in melts. In describing continuous media's dynamic properties the following systems of equations were obtained: for a viscous melt - the Navier – Stokes equations, for an ideal melt - the Euler equations, for a weakly compressible melt - the Oberbeck – Boussinesq equations. In fundamental research and in the field of applied research these mathematical models are generally accepted for modeling melt flow. Theoretical processes descriptions occurring in melts are based on the Stokes – Kirchhoff theory, which, with the frame of classical hydrodynamics, revealed phenomenological connections between the molten systems' kinetic properties. Numerous hydrodynamic paradoxes point to that long and thorny path that has been covered since its inception. First long stage was associated with the study and research of ideal incompressible liquid's potential flows. Mathematical methods of their research using the theory of complex variable functions seemed almost perfect. Imperfection of the ideal liquid theory was indicated by the famous Euler-Dalamber paradox: the total force acting on a body flowing around a potential flow is equal to zero. Then a mathematical model of a viscous incompressible fluid with its basic Navier-Stokes equations was created. Proposed section outlines various methods for solving and studying the Navier – Stokes equations. At the present stage, a great effort is made to find localized hydrodynamics equations solutions.

Keywords: Metal melt, hydrodynamic equations, velocity profile, mathematical modeling, computer simulation, density functional

Introduction

Objective - to obtain the most simple regularization of the original system of hydrodynamic equations containing a physical sense. As known [1, 2], hydrodynamic equations approximation leads to non-linear systems of equations. Therefore, their solution is accompanied by complex problems. These problems create difficulties in solving multidimensional tasks using fairly well-known implicit schemes in time. The task of obtaining original system's the simplest regularization, containing a certain physical meaning, becomes urgent. In order to solve these tasks, in our opinion, most constructive approach is a splitting method. In this connection, we considered various approaches to the splitting schemes construction for the Navier - Stokes equations in the weak approximation sense.

Main task of article is to determine the viscous incompressible melt's motion, if external forces acting on the melt are known, the boundary mode and, for a non-stationary flow, the initial velocity field. Basically, we assume that there is a coordinate system in which the filled with the melt is unchanged. The assumption of the field's constancy is fulfilled in such practically important tasks as the problem of flowing a solid body with an infinite flow; the problem of the liquid motion under

the action of volume forces in a vessel with solid walls moving in a known manner in space and others.

3. Decision problem

We consider a flat flow. Let Ω – area of Euclidean space R^n , and $x = (x_1, x_2)$. We divide whole space $R^n(x, t)$ on elementary cells, the area of which:

$$x_i = k_i h, \quad h > 0, \quad k_i = 0, \pm 1, \pm 2, \dots,$$

where $t = k\Delta t; k = 1, 2, \dots, n; h$ – step.

We form difference ratios by x_i :

$$v_{x_i}(x, t) = \frac{1}{h} [v(x + he^j, t) - v(x, t)], \quad v_{\bar{x}_i}(x, t) = \frac{1}{h} [v(x, t) - v(x - he^j, t)]$$

Shift by x_i is defined as:

$$v^{\pm i}(x, t) = v(x \pm he^j, t)$$

Consider the temperature model of inhomogeneous melt [3, 4] in the area $\Omega \subset R^2$:

$$\rho \left(\frac{\partial v}{\partial t} + (v \cdot \nabla) v \right) = \mu \Delta v - \nabla p + e \theta \rho + \rho f, \quad (1)$$

$$\frac{\partial \rho}{\partial t} + (v \cdot \nabla) \rho = 0$$

$$\operatorname{div} v = 0$$

$$\rho \left(\frac{\partial \theta}{\partial t} + (v \cdot \nabla) \theta \right) = \operatorname{div}(\lambda(\theta) \nabla \theta) + \mu \sigma,$$

$$\sigma = \sum_{i,j=1}^2 \left(\frac{\partial v_i}{\partial x_j} + \frac{\partial v_j}{\partial x_i} \right)^2,$$

with initial boundary conditions:

$$v|_{t=0} = v_0(x), \rho|_{t=0} = \rho_0(x), \theta|_{t=0} = \theta_0(x), v|_S = 0, \frac{\partial \theta}{\partial n}|_S = 0, t \in [0, T],$$

where σ – is energy dissipation, $v(x, t)$ – velocities' vector function, $\theta(x, t)$ – temperature field, $\rho(x, t)$ – density field, $p(x, t)$ – pressure field, $f(x, t)$ – mass force vector, μ – melt viscosity, $\lambda(\theta)$ – thermal conductivity coefficient, n – external normal to the boundary of S , $e = \{0, 1\}$.

In order to demonstrate given method after appropriate transformations, we rewrite equation (1) in form:

$$\frac{\partial v}{\partial t} + \sum_{k=1}^n Z_k(v) - \frac{1}{\varepsilon} \nabla \operatorname{div} v = f, \quad (2)$$

where:

$$Z_k(w) = -\gamma \frac{\partial^2 w}{\partial x_k^2} + v_k \frac{\partial w}{\partial x_k} + \frac{1}{2} \frac{\partial v_k}{\partial x_k} w$$

There are various approximations of difference operator Z_k . We take this operator in the form proposed in [4-9]:

$$Z_k^m(w) = -\gamma w_{x_k \bar{x}_k} + \frac{1+k}{2} v_k^{m-\frac{k}{2}} w_{x_k} + \frac{1}{2} v_k^{m-\frac{k}{2}} w_{\bar{x}_k} + \frac{1}{2} v_{kx_k}^{m-\frac{k}{2}} w_{x_k}$$

Then equation (2) can be represented by following difference scheme:

$$\frac{1}{\Delta t} \left(v_1^{m-\frac{1}{2}} - v_1^{m-1} \right) + \tau_2^m \left(v_1^{m-\frac{1}{2}} \right) = \frac{1}{2} f_1^{m-\frac{1}{2}}, \quad (3)$$

$$\frac{1}{\Delta t} \left(v_1^{m-\frac{1}{2}} - v_1^{m-1} \right) + \tau_2^m \left(v_1^{m-\frac{1}{2}} \right) = \frac{1}{2} f_1^{m-\frac{1}{2}}, \quad (3)$$

$$\frac{1}{\Delta t} \left(v_1^m - v_1^{m-\frac{1}{2}} \right) + \tau_1^m \left(v_1^m \right) - \frac{1}{\varepsilon} \left(v_{1x_1}^m + v_{2x_2}^{m-\frac{1}{2}} \right)_{\bar{x}_1} = \frac{1}{2} f_1^m, \quad (4)$$

$$\frac{1}{\Delta t} \left(v_2^{m-\frac{1}{2}} - v_2^m \right) + \tau_2^m \left(v_2^{m-\frac{1}{2}} \right) - \frac{1}{\varepsilon} \left(v_{1x_1}^{m-1} + v_{2x_2}^{m-\frac{1}{2}} \right)_{\bar{x}_2} = \frac{1}{2} f_2^{m-\frac{1}{2}}, \quad (5)$$

$$\frac{1}{\Delta t} \left(v_2^m - v_2^{m-\frac{1}{2}} \right) + \tau_1^m \left(v_2^m \right) = \frac{1}{2} f_2^m, \quad (6)$$

where $m = 1, 2, \dots, N$.

To complete construction of the difference scheme, initial and boundary conditions should be added to these equations. Without deriving formulas for boundary conditions, we write:

$$\left\| v_1^{m-\frac{1}{2}} \right\|^2 - \left\| v_1^{m-1} \right\|^2 + \left\| v_1^{m-\frac{1}{2}} - v_1^{m-1} \right\|^2 + 2\gamma \Delta t \left\| v_{1x_2}^{m-\frac{1}{2}} \right\|^2 = \Delta t \left(f_1^{m-\frac{1}{2}}, v_1^{m-\frac{1}{2}} \right),$$

$$\left\| v_1^m \right\|^2 - \left\| v_1^{m-\frac{1}{2}} \right\|^2 + \left\| v_1^m - v_1^{m-\frac{1}{2}} \right\|^2 + 2\gamma \Delta t \left\| v_{1x_1}^m \right\|^2 +$$

$$+ \frac{2\Delta t}{\varepsilon} \left[\left\| v_{1x_1}^m \right\|^2 + \left(v_{1x_1}^m, v_{2x_2}^{m-\frac{1}{2}} \right) \right] = \Delta t \left(f_1^m, v_1^m \right),$$

$$\left\| v_2^{m-\frac{1}{2}} \right\|^2 - \left\| v_2^{m-1} \right\|^2 + \left\| v_2^{m-\frac{1}{2}} - v_2^{m-1} \right\|^2 + 2\gamma \Delta t \left\| v_{2x_2}^{m-\frac{1}{2}} \right\|^2 +$$

$$+ \frac{2\Delta t}{\varepsilon} \left[\left\| v_{2x_2}^{m-\frac{1}{2}} \right\|^2 + \left(v_{1x_1}^{m-1}, v_{2x_2}^{m-\frac{1}{2}} \right) \right] = \Delta t \left(f_2^{m-\frac{1}{2}}, v_2^{m-\frac{1}{2}} \right),$$

$$\left\| v_2^m \right\|^2 - \left\| v_2^{m-\frac{1}{2}} \right\|^2 + \left\| v_2^m - v_2^{m-\frac{1}{2}} \right\|^2 + 2\gamma \Delta t \left\| v_{2x_1}^m \right\|^2 = \Delta t \left(f_2^m, v_2^m \right)$$

Thus, we obtain equations (3) – (6), which are solved separately. This allows you to write machine programs for the numerical finite-difference methods implementation. We consider application of proposed method on Dirichlet problem example for the Poisson equation given in [6-15]. Integration is performed in a rectangular lattice in accordance with fig. 1. Asterisk indicates internal nodes, boundary nodes are denoted by «*».

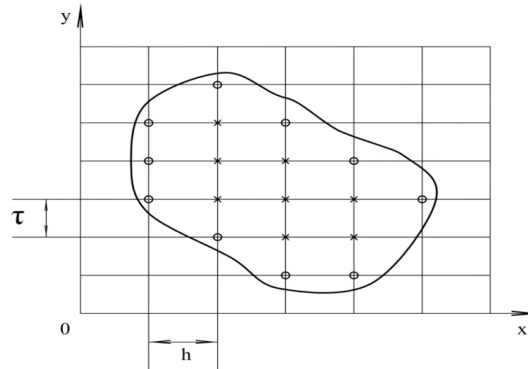


Fig.1. Integration area

4. Results and discussions

According to the reference data, solution of the Poisson equation is given in table 1. For the control example in Table 2 we give the Dirichlet problem’s solution already with different boundary conditions from same reference sources. Comparing first and second Dirichlet boundary value problems’ solutions from reference sources presented in tables 1 and 2 with program results for solving boundary value problems presented in tables 3 and 4, we see a satisfactory coincidence of solutions for a given accuracy $\varepsilon = 10^{-1}$.

Table 1. First Dirichlet boundary value problem’s solution for the Poisson equation from reference sources

Y	X					
	0.00	0.40	0.80	1.20	1.60	2.00
0.00	0.00	0.00	0.00	0.00	0.00	0.00
0.20	0.08	0.32	0.51	0.72	0.99	0.84
0.40	0.32	0.72	1.07	1.41	1.78	1.76
0.60	0.72	1.23	1.68	2.12	2.56	2.76
0.80	1.28	1.82	2.65	3.22	3.82	3.84
1.00	2.00	2.44	2.96	3.56	4.24	5.00

Table 2. Second Dirichlet boundary value problem’s solution for Poisson equation from reference sources

Y	X					
	0.00	0.40	0.80	1.20	1.60	2.00
0.00	1.00	1.40	1.80	2.20	2.60	3.00
0.20	2.00	1.05	0.95	1.08	1.44	2.96
0.40	2.00	1.02	0.60	0.59	0.93	2.84
0.60	4.00	1.36	0.78	0.63	0.93	2.64
0.80	5.00	2.78	2.12	1.81	1.64	2.36
1.00	6.00	5.84	5.36	4.56	3.44	2.00

Table 3 - First Dirichlet boundary value problem's solution for the Poisson equation with a given accuracy $\varepsilon = 10^{-1}$

Y	X										
	0.000	0.200	0.400	0.600	0.800	1.000	1.200	1.400	1.600	1.800	2.000
0.0	0.000	0.000	0.000	0.000	0.000	0.000	0.000	0.000	0.000	0.000	0.000
0.2	0.080	0.241	0.262	0.264	0.266	0.269	0.272	0.276	0.280	0.330	0.840
0.4	0.320	0.303	0.301	0.303	0.305	0.308	0.311	0.315	0.320	0.447	1.760
0.6	0.720	0.356	0.305	0.306	0.308	0.310	0.314	0.318	0.323	0.538	2.760
0.8	1.280	0.429	0.310	0.308	0.310	0.313	0.316	0.320	0.325	0.636	3.840
1.0	2.000	0.523	0.315	0.311	0.313	0.315	0.319	0.323	0.329	0.741	5.000
1.2	2.880	0.639	0.322	0.314	0.316	0.319	0.322	0.326	0.332	0.854	6.240
1.4	3.920	0.776	0.330	0.318	0.320	0.323	0.326	0.330	0.337	0.974	7.560
1.6	5.120	0.935	0.341	0.323	0.326	0.329	0.332	0.336	0.343	1.105	8.960
1.8	6.480	1.248	0.581	0.613	0.674	0.744	0.821	0.906	1.002	1.946	10.44
2.0	2.000	2.440	2.960	3.560	4.240	5.000	5.840	6.760	7.760	8.840	10.00

Table 4 - Second Dirichlet boundary value problem's solution for the Poisson equation with a given accuracy $\varepsilon = 10^{-1}$

Y	X										
	0.000	0.200	0.400	0.600	0.800	1.000	1.200	1.400	1.600	1.800	2.000
0.0	1.000	1.200	1.400	1.600	1.800	2.000	2.200	2.400	2.600	2.800	3.000
0.2	2.000	1.109	1.011	1.012	1.016	1.019	1.023	1.026	1.029	1.138	2.960
0.4	3.000	1.215	1.004	0.997	0.996	0.994	0.992	0.990	0.988	1.087	2.840
0.6	4.000	1.325	1.007	0.997	0.995	0.993	0.991	0.988	0.985	1.074	2.640
0.8	5.000	1.436	1.009	0.996	0.994	0.992	0.989	0.986	0.983	1.057	2.360
1.0	6.000	1.546	1.012	0.995	0.993	0.990	0.987	0.984	0.981	1.035	2.000
1.2	7.000	1.656	1.015	0.994	0.992	0.989	0.986	0.983	0.979	1.008	1.560
1.4	8.000	1.767	1.017	0.994	0.991	0.988	0.984	0.981	0.977	0.977	1.040
1.6	9.000	1.877	1.020	0.993	0.990	0.986	0.983	0.979	0.975	0.942	0.440
1.8	10.00	2.018	1.059	1.027	1.022	1.016	1.009	1.000	0.992	0.917	-0.24
2.0	6.000	5.960	5.840	5.640	5.360	5.000	4.560	4.040	3.440	2.760	2.000

Table 5 - First Dirichlet boundary value problem's solution for the Poisson equation with a given accuracy $\varepsilon = 10^{-4}$

Y	X					
	0.000	0.400	0.800	1.200	1.600	2.000
0.00	0.000	0.000	0.000	0.000	0.000	0.000
0.20	0.080	0.301	0.508	0.750	1.001	0.800
0.40	0.320	0.730	1.055	1.430	1.851	1.710
0.60	0.720	1.221	1.666	2.101	2.590	2.732
0.80	1.280	1.790	2.599	3.202	3.798	3.884
1.00	2.000	2.490	2.981	3.549	4.290	5.001

It should be noted that the increase in accuracy leads to an increase in the cost of machine time, which is 45 minutes. In general, a large number of experiments have been made for increase in accuracy of mathematical model, with a step of the tension of the x-ray radiation of 5 kV.

Conclusion

Obtained results show compiled program's correctness, as well as correctness of the stated boundary value problems for hydrodynamic equations considered by us above. In this article, we establish one of the important moments of the Navier – Stokes equations' theory: the unique stationary problems' solvability in the case of their linearization. This is most easily done in a Hilbert space with a well-defined extension of the solution concept, which will be described below. Here are specific algorithms for computer programming.

REFERENCES

- 1 Conca Carlos. On the application of the homogenization theory to a class of problems arising in fluid mechanics. *J. Math. Poursat Appl.* 1985, Vol.64, No.1, pp. 31 – 35.
- 2 Malik M.R., Zang T.A., Hussaini M.Y. A spectral collocation method for the Navier-Stokes equations. *J. Comput. Phys.* 1985, Vol. 61, No.1, pp. 64 – 68.
- 3 Gresho P.M. Incompressible fluid dynamics: some fundamental formulation issues. *Annu. Rev. Fluid Mech.*, 1991, Vol.23, pp. 413 – 453. [in Russian]
- 4 Issagulov A.Z., Belomestny D., Shaikhova G.S., et al. Functions of atoms radial distribution and pair potential of some semiconductors melts. *The Bulletin the National Academy of Sciences of the Republic of Kazakhstan.* 2019, No. 4, pp. 6 – 14. DOI: [10.32014/2019.2518-1467.86](https://doi.org/10.32014/2019.2518-1467.86)
- 5 Kazhikenova S.Sh., Belomestny D. Fundamental Characteristics of Reliability in Technological Processes in Ferrous Metal Industry. *The Bulletin the National Academy of Sciences of the Republic of Kazakhstan.* 2019, No. 2, pp. 120 – 127. DOI: [10.32014/2019.2518-1467.50](https://doi.org/10.32014/2019.2518-1467.50)
- 6 Ladyzhenskaya O.A. *Mathematical problems of the dynamics of a viscous incompressible fluid.* M. Nauka, 1970, 288p. [in Russian]
- 7 Kazhikenova S.Sh. On the difference method of the ocean model. *Bulletin of KazNU. Ser. mat., fur., inf.* 2002, No. 3 (31), pp. 99 – 101. [in Russian]
- 8 Abramov A., Yukhno L.F. Solving some problems for systems of linear ordinary differential equations with redundant conditions. *Zh. Vychisl. Mat. Mat. Fiz.*, 2017, No. 57:8, pp. 1285 – 1293, <https://doi.org/10.7868/S0044466917080026>
- 9 Kato Yasumasa, Tanahashi Takahico. Finite-element method for three-dimensional incompressible viscous flow using simultaneous relaxation of velocity and Bernoulli function. 1st report flow in a lid-driven cubic cavity at Re=5000. *Trans. Jap. Soc. Mech. Eng.* 1991, Vol. 57, No.540, pp. 2640 – 2647.
- 10 Honda Itsuro, Ohba Hideki, Tanigawa Yuji, Nakiama Tetsuji. Numerical analysis of a flow in a three-dimensional cubic cavity. *Trans. Jap. Soc. Mech. Eng.* 1991, Vol. 57, No. 540, pp. 2627-2631.
- 11 Yan X. Wei L, Lei Yao, Xin Xue, et al. Numerical Simulation of Meso-Micro Structure in Ni-Based Superalloy During Liquid Metal Cooling. *Proceedings of the 4th World Congress on Integrated Computational Materials Engineering. The Minerals, Metals & Materials Series.* 2017, pp. 249 – 259.
- 12 Barannyk, T.A., Barannyk A.F., Yuryk I.I. Exact Solutions of the Nonlinear Equation. *Ukrains'kyi Matematychnyi Zhurnal*, 2017, Vol. 69, No. 9, pp. 1180-1186
- 13 Tleugabulov S., Ryzhonkov D., Aytbayev N., Koishina G., Sultamurat G. The reduction smelting of metal-containing industrial wastes. *News of the National Academy of Sciences of the Republic of Kazakhstan, Series of Geology and Technical Sciences*, 2019, Vol 1, No. 433, pp. 32 – 37. <https://doi.org/10.32014/2019.2518-170X.3>
- 14 Skorokhodov S.L., Kuzmina N.P. Analytical-numerical method for solving an Orr–Sommerfeld-type problem for analysis of instability of ocean currents. *Zh. Vychisl. Mat.& Mat. Fiz.*, 2018, No. 8:6, pp. 1022–1039; <https://doi.org/10.7868/S0044466918060133>
- 15 Iskakova, N.B., Assanova A.T., Bakirova E.A. Numerical Method for the Solution of linear boundary-Value Problem for Integro-differential Equations Based on spline approximations. *Ukrains'kyi Matematychnyi Zhurnal*, 2019, Vol. 71, No. 9, pp. 1176 – 1191. <http://umj.imath.kiev.ua/index.php/umj/article/view/1508>.

DOI 10.31489/2020No1/151-156

UDC: 621.38.049.77

DESIGN AND RESEARCH OF THE BEHAVIORAL MODEL FOR THE MODULAR REDUCTION DEVICE

Aitkhozhayeva Y.Zh.¹, Tynymbayev S.², Adilbekkyzy S.³, Skabylov A.^{4*}, Ibraimov M.⁴¹ K.I. Satbayev Kazakh National Research Technical University, Almaty, Kazakhstan² Almaty University of Power Engineering and Telecommunications, Almaty, Kazakhstan³ L.N. Gumilyov Eurasian National University, Nur-Sultan, Kazakhstan⁴ al-Farabi Kazakh National University, Almaty, Kazakhstan, skabylov212@gmail.com

A behavioral model of the modular reduction device with optimal hardware costs was designed in CAD Quartus Prime Lite Edition. An algorithm of operation is implemented in the Verilog HDL language. A method is used where, at each step of the calculation, the value of either tripled, doubled, or single value of the module is subtracted from the most significant bits shifted to the left by two. Functional and timing modeling of the behavioral model algorithm using examples was carried out and the correctness of the algorithm was confirmed. The device circuit at the register transfer level (RTL) for the low-budget FPGA Cyclone VE 5CEBA4F23C7 from Altera is obtained. A timing analysis was performed using a time analyzer to determine the maximum clock frequency for the principal and behavioral models in various working conditions.

Keywords: asymmetric crypto-algorithms, hardware encryption, modular reduction, behavioral model, design.

Introduction

New information and communication technologies, which are the technological drivers of the Fourth Industrial Revolution, bring with them not only new opportunities, but also new challenges of ensuring information security. The relevance of these problems is evident against the backdrop of a global trend towards an increase in the number of cyber-attacks, leading to significant financial, material and human losses. Systems based on new technologies, such as Blockchain, Cloud Computing, Internet of Things (IOT), Cyber-Physical Systems (CPS), are systems with an unlimited number of network interaction participants. High-speed symmetric encryption, requiring the transfer of an individual secret key to each participant, is not applicable to protect information in such systems. Besides, the use of asymmetric encryption, in which public keys are distributed to participants of network interaction, is associated with the issue of low speed of asymmetric cryptographic algorithms. Complex and cumbersome procedures for modular exponentiation very large integers during encryption and decryption in asymmetric cryptographic algorithms are time consuming. The transition from software to hardware implementation of asymmetric encryption can improve the characteristics of encryption in terms of performance. However, the hardware implementation does not improve the performance of asymmetric cryptographic algorithms so much as to approach the speed of symmetric cryptographic algorithms.

The international research community pays great attention to solving the problem of improving the performance of asymmetric cryptosystems. The emphasis is on the hardware implementation of asymmetric cryptographic algorithms. The most complex basic operation of modular exponentiation large numbers with asymmetric encryption is the modular reduction. Moreover, in many research papers, acceleration of asymmetric encryption is proposed by accelerating the operation of modular reduction of integers by developing new and adapting (modifying) existing algorithms and circuit solutions of modular reduction devices [1-12].

1. Purpose and objectives

There are an increase in speed is achieved by increasing the hardware costs, which are directly proportional to the capacity of the given numbers in most solutions. Therefore, their use in reducing multi-bit numbers is justified if there are no requirements for optimizing hardware costs. It should be borne in mind that increasing hardware costs leads to increased power consumption and lower reliability. The actual issue is the accelerated determination of the remainder modulo an arbitrary number (modular reduction) with optimization of hardware costs and low cost.

The functional block diagram of a device for modular reduction of binary integers with optimization of hardware costs and low cost is developed and presented by the authors in [13]. The purpose of this work is to design and study the behavioral model of this modular reduction device, to determine its advantages and disadvantages compared to the principal model. In previous studies, the design of the circuit diagrams of the device blocks and the principal model of the entire device as a whole was performed [14, 15]. For the design and debugging of the principal model CAD Quartus Prime Lite Edition Version 16.0 (Altera) was used. The implementation of the device is focused on the low-budget board DE0-CV with an integrated circuit FPGA of the Cyclone VE base family, manufactured by Altera (the parent organization of Intel) - 5CEBA4F23C7.

The objectives of this study are to develop a behavioral in Verilog HDL language, to study it and to perform a comparative analysis of the principal model and behavioral model of a device using a textual description of circuits of a device for quickly reducing binary integers modulo from the point of view of hardware and time costs when implementing a device on a low-budget FPGA family Cyclone VE base – 5CEBA4F23C7. Cyclone series low-cost boards are designed for use in a variety of applications where low power consumption and low cost are key parameters. Therefore, the Cyclone family is the optimal solution for mass, cost-critical applications.

2. Designing a behavioral model of the high-speed device for modular reduction

The structure of the considered device of fast reduction of numbers modulo consists of a controlling block, a block of shift register, a block of former of the multipliers of the module P , and a block of former of the partial remainders r_i (Figure-1). In this device, to accelerate the calculation of the remainder twice when dividing the $2n$ -bit number A by the n -bit module P , we used the method where, at each step of the calculation, the value P of either tripled ($3P$), or doubled ($2P$), or a single (P) value of the module P is subtracted from the high-order bits of the previous remainder ($4r_{i-1}$) shifted by two bits to the left.

The controlling block receives the signals *Reset*, *Start*, clock pulses (CP), $K = n/2$ (n - the capacity of the module P , $n/2$ - determines the number of clock pulses required to perform the operation of reduction modulo). In the block of former of the multipliers of the module P the binary representation and ones' complement (for further subtraction operations) of the doubled and tripled module ($2P$ and $3P$) are pre-calculated. The Block of shift register is used initially to store the reducible number A , then the partial remainders, and to shift them to the left by two bits with the subsequent supply of the most significant bits ($4r_{i-1}$) to the partial remainder shaper.

An analysis of the performance of the principal and behavioral models of the module for fast reduction of numbers was performed using the Quartus Prime Time Quest Timing Analyzer. The time relationships that must be respected for the proper operation of the project were determined, and the signal transit time was compared with the time required for the stable operation of the project (Figure-1 and Figure-2). Comprehensive static timing analysis includes analysis of all signal paths. The Time Quest Timing Analyzer shows data required times, data arrival times, and clock arrival times. With its help, you can check the circuit performance and detect possible timing violations.

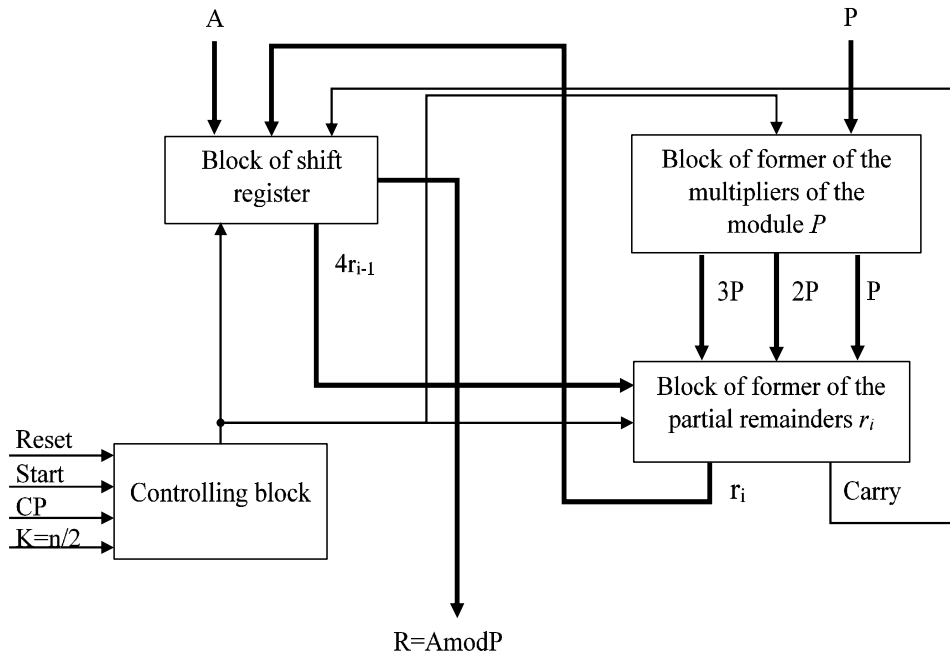


Fig.1. Structural diagram of a device for fast reduction of numbers module [14].

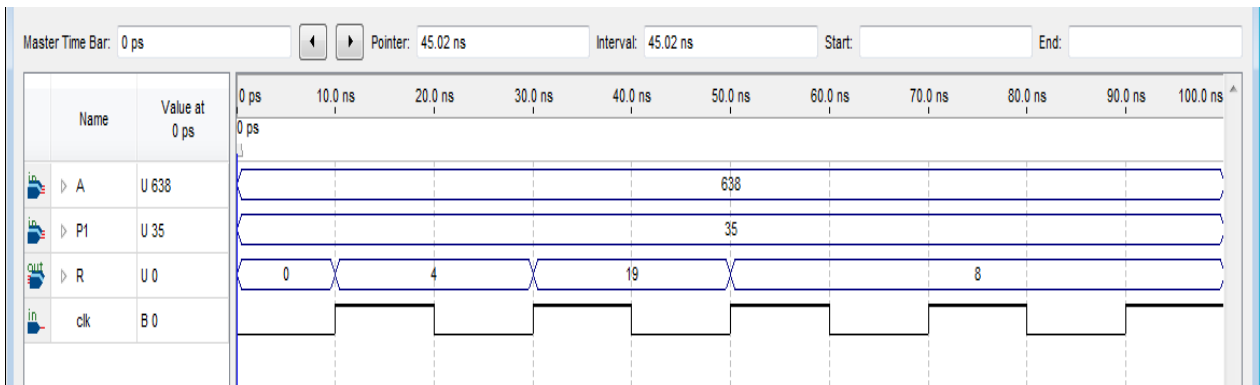


Fig.2. Timing diagrams with the value of the reducible number $A = 638$ and the module $P1 = 35$.

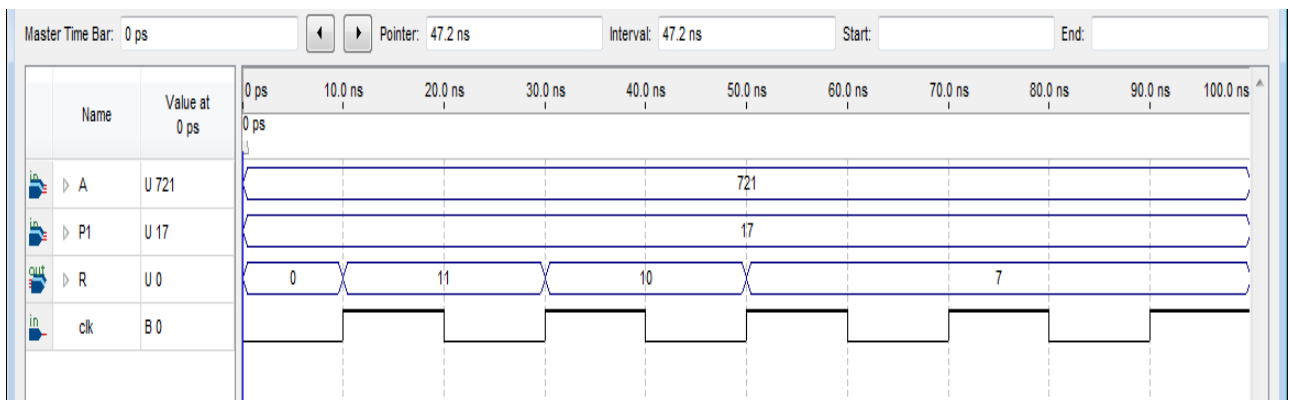


Fig.3. Timing diagrams, with the value of the reducible number $A = 721$ and the module $P1 = 17$.

3. Results and Discussions

The analysis of delays (Time Analysis) in the logic circuit is performed to determine the conditions under which the circuit operates reliably. These conditions include the maximum clock frequency (F_{MAX}) at which the circuit will produce the correct result. Time reports were created for all critical paths in the project. Multilateral analysis made it possible to verify the design (the principal and behavioral models) under various operating conditions, changing the voltage, speed, and temperature when performing a static timing analysis of the design (Fig. 4).

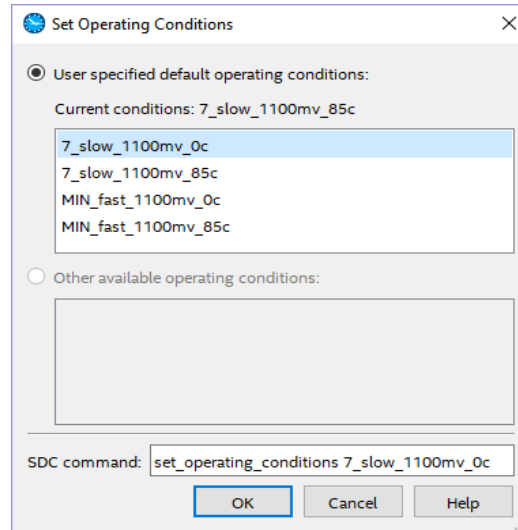


Fig.4. Selection of an operating condition for multilateral analysis.

The maximum delay in the circuit corresponds to the critical path, which determines the longest period and, accordingly, the maximum frequency of the device (F_{MAX}). Fig. 5 represent fragment of the analysis result for determining the maximum clock frequency of the principal model under various operating conditions.

Slow 1100mV 85C Model				
	Fmax	Restricted Fmax	Clock Name	Note
1	27.43 MHz	27.43 MHz	Start	
2	30.8 MHz	30.8 MHz	Reset	
3	33.25 MHz	33.25 MHz	Clk	

Slow 1100mV 0C Model				
	Fmax	Restricted Fmax	Clock Name	Note
1	27.6 MHz	27.6 MHz	Start	
2	30.83 MHz	30.83 MHz	Reset	
3	32.91 MHz	32.91 MHz	Clk	

Fast 1100mV 85C Model				
	Fmax	Restricted Fmax	Clock Name	Note
1	52.21 MHz	52.21 MHz	Start	
2	63.0 MHz	63.0 MHz	Clk	
3	66.54 MHz	66.54 MHz	Reset	

Fast 1100mV 0C Model				
	Fmax	Restricted Fmax	Clock Name	Note
1	56.54 MHz	56.54 MHz	Start	
2	68.77 MHz	68.77 MHz	Clk	
3	72.53 MHz	72.53 MHz	Reset	

Fig.5. Determination of the maximum clock frequency under various operating conditions of the device for fast reduction of numbers modulo for the principal model.

Slow 1100mV 85C Model				
	Fmax	Restricted Fmax	Clock Name	Note
1	117.3 MHz	117.3 MHz	clk	

Slow 1100mV 0C Model				
	Fmax	Restricted Fmax	Clock Name	Note
1	115.18 MHz	115.18 MHz	clk	

Fast 1100mV 85C Model				
	Fmax	Restricted Fmax	Clock Name	Note
1	248.57 MHz	248.57 MHz	clk	

Fast 1100mV 0C Model				
	Fmax	Restricted Fmax	Clock Name	Note
1	267.52 MHz	267.52 MHz	clk	

Fig.6. Determination of the maximum clock frequency under various operating conditions of the device for fast reduction of numbers modulo for the behavior model.

Figure 6 represent fragment of the analysis result for determining the maximum clock frequency of the behavioral model under various operating conditions. The compiler report contains detailed information about the results of project processing and its components. Of the summary reports that contain complete information about the hardware costs of compiled projects, the main characteristics obtained are presented in table 1.

Table 1. Resources used FPGA.

Resource Name	Principal model	Behavioral model	Total FPGA Resources
Adaptive Logic Module (ALM)	72	74	18480
Registers	22	65	73920
I/O Pins	48	29	224
Logic Array Block (LAB)	12	11	1848

Table 1 shows how many total resources (ALM, Registers, I/O Pins, LAB) are available in Altera FPGA - 5CEBA4F23C7 and how many resources are required to implement a *12-bit* binary number reduction using a *6-bit* binary module. The table does not show data for the Combinational Adaptive Look-Up Table (ALUT), since ALUTs are logical constructs from ALM hardware and are not an independent FPGA resource.

Information on ALUT in the compiler report: for the principle model - *116*, for the behavioral model - *122*. The compiler report also contains information on the average fan-out coefficient for the output: for the principle model - *2.55*, for the behavioral model - *2.56*. Analysis of timing characteristics shows that the behavioral model is faster than the principal model, regardless of the operating conditions of the device. The threshold maximum frequency during operation of the device in the worst conditions (voltage *1100 mV* and temperature *85*) for both the principal model and the behavioral model is almost two times lower than the threshold maximum clock frequency of the device under normal conditions. Moreover under normal operating conditions, the maximum clock frequency for the principal model is $F_{MAX} = 68.77 \text{ MHz}$, for the behavioral model $F_{MAX} = 267.52 \text{ MHz}$, which is higher than the clock frequency of existing special RSA processors (from *5 MHz* to *30 MHz*), which are implemented on very-large-scale integration (VLSI) devices [16].

An analysis of the resources used and available shows that to implement the proposed high-speed modular reduction device for $n = 6$, both in principle model and in behavior model, no more than *0.6%* of the available resources of the low-budget FPGA Cyclone VE 5CEBA4F23C7 were used. A comparative analysis shows that the hardware of high-speed modular reduction device in the graphical description of the schematic diagram (principle model) will be *10.5%* less, since the device developer himself chooses the necessary resources at the design stage. While using textual methods for describing circuits, CAD independently distributes resources according to a given logic, which leads to non-optimal resource consumption.

Conclusion

The development of a modular reduction device using a behavioral model makes it possible to obtain a faster device compared to using a principle model, but with high hardware costs. The obtained results confirm the possibility of using the low-budget FPGA Cyclone VE 5CEBA4F23C7 to implement a high-speed modulator for binary numbers with high bit grid ($n \leq 1000$).

The FPGAs of the Cyclone VE family also include multipliers, DSP blocks, and internal RAM. The results obtained with the implementation of the modular reduction device in Cyclone VE 5CEBA4F23C7, on the use of hardware resources and the maximum clock frequency provide grounds for a real discussion and solution of issues of implementing a crypto processor on one

FPGA board of the Cyclone VE family. The device can be used both in crypto-processors and in digital computing devices to accelerate the division operation. Low cost Cyclone family FPGAs allow them to be used in mass solutions where it is necessary to provide low power consumption and low cost.

Acknowledgements

The presented results were obtained during research in the framework of the state order for the implementation of the scientific program for the budget program of the Republic of Kazakhstan "Development of science", the subprogram "Program-targeted financing of subjects of scientific and/or scientific and technical activity" of the scientific and technical program: BR053236757 "Development of software and hardware and software for cryptographic protection of information during its transmission and storage in info-communication systems and general purpose networks"

REFERENCES

- 1 Hars L., Joye M., Quisquater J. Long Modular Multiplication for Cryptographic Applications. Cryptographic Hardware and Embedded Systems. *CHES 2004, Lecture Notes in Computer Science*, 2004, Issue 3156, pp. 45 – 61.
- 2 Petrenko V.I., Sidorchuk A.V., Kuz'minov J.V. *Device for generating remainder with arbitrary modulus*: pat. 2368942 C2 Russian Federation. No. 2007124282/09; Publ. 27.09.2009, Bull. No. 27, 9 p.
- 3 Pankratova I.A. *Number-theoretical methods of cryptography*. Tomsk, Tomsk State University, 2009, 120 p.
- 4 Zakharov V.M., Stolov E.L., Shalagin S.V. *Apparatus for generating remainder for given modulo*: pat 2421781 C1 Russian Federation.No. 2009138613/08; Publ. 20.06.2011, Bull. No. 17, 9 p.
- 5 Kopytov V.V., Petrenko V.I., Sidorchuk A.V. *Device for generating remainder from arbitrary modulus of numbe*. Pat.2445730 C2 Russian Federation. No.2010106685/08; Publ. 20.03.2012, Bull. No.8, 8p.
- 6 Skryabin I., Sahin Y.H. *Support operations for encryption algorithms with public key and their implementation in the microprocessor Elbrus*. 2013. Available at: www.myshared.ru/slide/213088
- 7 Eran Pisek, Plano, T.X., Th.M. Henige, Dallas, T.X. *Method and apparatus for efficient modulo multiplication*: pat. No. 8417756 B2 United States. No.12/216,896; Publ. 09.04.2013, 12 p.
- 8 Aitkhozhayeva Y. Zh., Tynymbayev S.T. Aspects of hardware reduction modulo in asymmetric cryptography. *Bulletin of National Academy of Sciences of the Kazakhstan*. 2014, No. 5(375), pp. 88 – 93.
- 9 Markus Bockes, Munich (DE); Jurgen Pulkus, Munich (DE) *Method for arbitrary-precision division or modular reduction*: pat. 9042543 B2 United States. No. 13/885, 878; Publ. 26.05.2015, 12p.
- 10 Yu H., Bai G., Hao J., Wang C. Yap Efficient Modular Reduction Algorithm Without Correction Phase. *Frontiers in Algorithmics. Lecture Notes in Computer Science*, 2015, Vol. 9130, pp. 304 – 313.
- 11 Tynymbayev S.T., Aitkhozhayeva Y.Zh. The remainder generator by an arbitrary modulus of the number: pat. 30983 The Republic of Kazakhstan. No. 014/1450.1; Published 15.03.2016, 5 p.
- 12 Kovtun M., Kovtun V. *Review and classification of algorithms for dividing and modulating large integers for cryptographic applications*. 2017. Available at: <http://docplayer.ru/30671408-Obzor-i-klassifikaciya-algoritmov-deleniya>
- 13 Tynymbayev S.T., Aitkhozhayeva Y.Zh, Adilbekkyzy S. High speed device for modular reduction. *Bulletin of National Academy of Sciences of the Republic of Kazakhstan*. 2018, No. 6 (376), pp. 147 – 152.
- 14 Adilbekkyzy S. Aitkhozhayeva Y.Zh., Tynymbayev S.T. Modeling of the partial reminder former of the modular reduction device. *Eurasian Union of Scientists*. 2019, Vol. 6 (63), pp. 47 – 51.
- 15 Tynymbayev S.T., Aitkhozhayeva Y.Zh, Adilbekkyzy S., et al. Development and modeling of schematic diagram for the modular reduction device. *Problems of Informatics*, 2019, No. 4, pp.42 – 52.
- 16 Kramarov S.O., Mityasova O.Yu., Sokolov S.V., Tishchenko E.N., Shevchuk P.S. *Cryptographic information security*. Moscow: RIOR Publishing Center, 2018, 322 p.

MODELING OF FLOOD INUNDATION FOR ZHABAY RIVER BASIN IN CENTRAL KAZAKHSTAN REGION

Baktybekov K.S., Aimbetov A., Rakhimzhanov B.K.* , Murat A.

JSC "National Company "Kazakhstan Gharysh Sapary", Nur-Sultan, Kazakhstan,
rahimzhanovberik@gmail.com

Frequency analysis is the estimation of how often a specified event will happen. This is the most important statistical technique in understanding the nature and magnitude of high discharge in a river. In this paper, the flood frequency of the Zhabay River Basin in the Central Kazakhstan Region is analyzed. The frequency analysis has been carried out using Gumbel's distribution on based the eight-year flood data in the Zhabay River Basin which was provided by the hydrometeorological service "Kazhydromet". The expected floods for various return periods (T) is obtained. Additionally, the digital terrain model for the Zhabay River Basin is presented. This model was provided by the first Kazakhstan Earth remote sensing satellite KazEOSat-1. The results of the research would be useful in forecasting floods in the Central Kazakhstan region.

Keywords: modeling, floods, Zhabay River Basin, frequency analysis, Gumbel's distribution, KazEOSat -1.

Introduction

Flood is a natural hazard that may cause great damages to human civilization. It is studied worldwide using hydrologic as well as hydraulic models [1, 2]. Flood frequency analysis (FFA) is the estimation of how often a specified event will occur. In order to obtain the probability distribution of flood analyzing before the estimation can be done the stream flows data are important. FFA is the universal method used for the estimation of the recurrent interval of any hydrological event that is pivotally essential for the management of flood with respect to planning, design, and operations through the use of fundamental knowledge of flood characteristics [3-5]. Much research has been done to analyze flood by methods such as GIS [6-8], Gumbel's distribution [9], L-moments [10], Powel distribution [11], Log-Normal, and the Log Pearson Type III distributions [12].

During spring floods, some territory of Kazakhstan suffers from flooding. For example, the city of Atbasar in the Akmola region has been regularly flooded for the past few years. In Atbasar the major floods were in 2014 and 2017. The threat came from the Zhabay River, where the water level rose sharply due to intense snowmelt. In 2014 and 2017, Atbasar has been declared a state of emergency (ES) of a natural nature. The damage in Atbasar was impressive. For example, in 2014, 330 houses were damaged, and in 2017 more than 650 objects were flooded, as well as livestock, agricultural land. Many residents lost all their property and were left without housing [13, 14]. Thus, a study of the flood inundation of the Zhabay River is a relevance area.

The aim of this research is to analyze the flood frequency for the Zhabay River Basin in the Central Kazakhstan region by applying Gumbel's distribution. Such distribution is used to represent the distribution of the maximum level of a river in a particular year if there was a list of maximum values for the past several years. It is also useful in predicting the chance that an extreme earthquake, flood, or other natural disasters will occur.

In work, we use peak flow discharges data that were provided by hydrometeorological service RSE "Kazhydromet" of the Ministry of Ecology, Geology and Natural Resources of the Republic of Kazakhstan [15]. By Gumbel's distribution, the research of flood inundation of the Zhabay River

has not been studied before. We obtain a new result of the expected flood for different return periods for the Zhabay River. In addition, the digital terrain model for the Zhabay River Basin is presented. The results of research can be applied to predict future flood inundation in the city Atbasar.

1. Materials and Methods

1.1 Study Area

The study area is Zhabay River Basin that locates in Akmola region, Central Kazakhstan. The river locates between Latitude and Longitude as $52^{\circ}19'0.16''\text{N}$ – $68^{\circ}10'44.95''\text{E}$, $52^{\circ}15'35.81''$ – $69^{\circ}0'34.68''\text{E}$, $51^{\circ}47'56.54''\text{N}$ – $68^{\circ}13'30.54''\text{E}$, $51^{\circ}48'55.84''\text{N}$ – $^{\circ}0'52.58''\text{E}$. The Zhabay River is one of the large tributaries of the Esil (Ishim) River, flowing mainly in the Akmola Region, and is included in the Ishim River Basin. According to the latest data, the length of the river is 196 km. The catchment area is 8800 km². The river flows through the territories of the following settlements-Pokrovka, Borisovka, Atbasar (Atbasar district), Sandyktau, Balkashino (Sandyktau district) and also has 14 tributaries, such as Zhylandy, Aydabol, Sarymsakty.

In Fig.1 we present digital terrain model for the Zhabay River Basin. The figure was produced with satellite KazEOSat-1 data of the JSC "National Company "Kazakhstan Gharysh Sapary". KazEOSat-1 is the first Kazakhstan Earth remote sensing satellite. The technological feature of KazEOSat-1 is the ability to shoot in stereo, which allows us to get digital terrain models. Digital terrain models are key components of flood modeling systems.

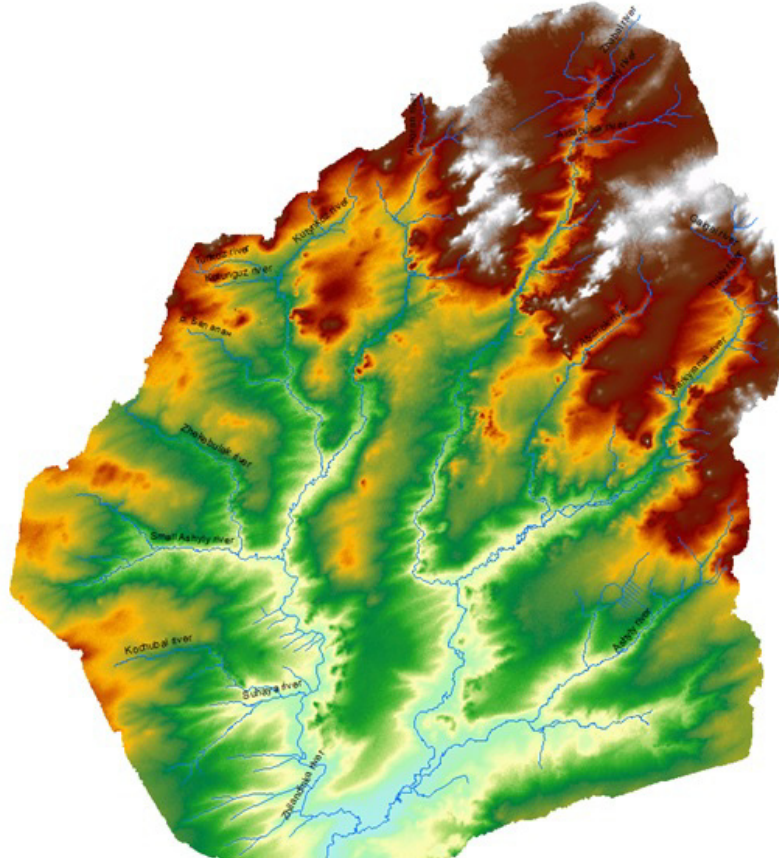


Fig. 1. Digital terrain model for the Zhabay River Basin that was produced with KazEOSat-1 data

1.2 Data Used

For this research, the annual peak flood series data for 8 years varying over the period, 2011 to 2018 for the Zhabay River Basin were presented by hydrometeorological service RSE “Kazhydromet” [15]. In Table 1 we present the used peak flow discharges data in our research.

Table 1. Observed floods in corresponding years based on data [15]

	Year	Peak flood in m ³ /s
1	2011	202
2	2012	246
3	2013	194
4	2014	1750
5	2015	80,9
6	2016	623
7	2017	3290
8	2018	154

1.3 Gumbel's distribution

In 1941 E. J. Gumbel began developing the method of an extreme-value probability distribution to analyze the magnitude frequency relation of annual peak discharges. Until now his method still enjoys great favor among hydrologist-statisticians. The Gumbel's distribution method is used to analyze the extreme value of different return period of 10 years, 20 years, 50 years and 100 years using observed discharged data. In research, we apply Gumbel's distribution to carry out the flood frequency analysis of the Zhabay River Basin using 8 years annually peak flow data (2011-2018). In this method, the variate x (flood peak discharge) with recurrence interval T is given by

$$x_T = \bar{x} + K s_{n-1}, \quad (1)$$

where x_T is flood peak discharge, \bar{x} –average value x , s_{n-1} - standart deviation that defined by

$$s_{n-1} = \sqrt{\frac{\sum(x-\bar{x})^2}{N-1}}, \quad (2)$$

here K – is the frequency factor expressed as

$$K = \frac{y_T - \bar{y}_n}{\sigma_n}, \quad (3)$$

here y_T - is the reduced variate that is given by

$$y_T = -\ln [\ln [\frac{T}{T-1}]], \quad (4)$$

where \bar{y}_n - Gumbel's reduce mean variable, which defined from Gumbel's Table 2; σ_n -reduce standard deviation, a function of sample size n that defined from Gumbel's Table 2.

The data in Table 2 were obtained by Gumbel [16] and we apply these data to obtain frequency factor K by equation (3). Because our period of study is 8 year we use case $n = 8$. It is mean that from Table 2 we apply reduced mean variable $\bar{y}_n = 0.4843$ and reduce standard deviation $\sigma_n = 0.9043$.

Table 2. Gumbel's reduced mean variable and standard deviation based on data number [16]

n	\bar{y}_n	σ_n	n	\bar{y}_n	σ_n	n	\bar{y}_n	σ_n
8	0.4843	0.9043	16	0.5157	1.0316	24	0.5296	1.0864
9	0.4902	0.9288	17	0.5181	1.0411	25	0.5309	1.0915
10	0.4952	0.9497	18	0.5202	1.0493	26	0.5320	1.0961
11	0.4996	0.9676	19	0.5220	1.0566	27	0.5332	1.1004
12	0.5035	0.9833	20	0.5236	1.0628	28	0.5343	1.1047
13	0.5070	0.9972	21	0.5252	1.0698	29	0.5353	1.1086
14	0.5100	1.0095	22	0.5268	1.0754	30	0.5362	1.1124
15	0.5128	1.0206	23	0.5283	1.0811	31	0.5371	1.1159

2. Results and discussions

Gumbel's distribution is applied to carry out the flood frequency analysis of the Zhabay River using 8 years annually peak flow data (2011-2018). The maximum flood of 3290 m³/s was recorded in 2017 whereas the lowest flood of 154 m³/s occurred in 2018. The mean flood is 817.45 m³/s. Based on the Gumbel's distribution described in section 1.3, the important parameters as return period, probability, reduced variate were computed in Table 3 while Table 4 shows the various discharges expected alongside their return periods.

Table 3. Computation results by Gumbel's distribution

N	Water year, x	Flood peak	Oder (m)	Return Period	Probability	Reduced Variate
1	2011	202	1	9	0.11	2.14
2	2012	246	2	4.5	0.22	1.38
3	2013	194	3	3	0.33	0.90
4	2014	1750	4	2.25	0.44	0.53
5	2015	80.9	5	1.8	0.56	0.21
6	2016	623	6	1.5	0.67	-0.09
7	2017	3290	7	1.29	0.78	-0.41
8	2018	154	8	1.13	0.89	-0.79

Table 4. Computation of expected flood for the Zhabay River

Return Period, T (in years)	Reduced Variate, y_T	Frequency Factor, K	Expected Flood, x_T
2	0.37	-0.13	669.0
5	1.50	1.12	2097.88
10	2.25	1.95	3043.92
25	3.20	3.00	4239.26
50	3.90	3.78	5126.02
100	4.60	4.55	6006.24
200	5.30	5.32	6883.24
250	5.52	5.57	7165.19
500	6.21	6.34	8040.28
1000	6.91	7.10	8914.75

In Table 4, the frequency factor K is calculated based on equation (3). Moreover, Gumbel's reduced mean variable \overline{y}_n and standard deviation $\overline{\sigma}_n$ can be selected using Table 2 in case $n = 8$. The reduced variate y_T and expected flood x_T are calculated by equations (4) and (1). Analyze the results in Table 4 we see that in case $T = 2$ expected flood in Zhabay River is $669 \text{ m}^3/\text{s}$. It is almost the same amount as in the 2016 year. However, our result shows that in the case of return period $T \geq 5$ we can assume the next flood inundation of the Zhabay river because the expected flood is $2097.88 \text{ m}^3/\text{s}$ and more. This amount of water is bigger than observed in the 2014 year and 2017 year when in city Atbasar was declared a state of emergency of a natural nature because of flood inundation in the Zhabay River.

Conclusion

In this paper, flood frequency analysis had been carried out for the Zhabay River Basin in Central Kazakhstan region using peak flow data. The observed data (Table 2) were provided by hydrometeorological service RSE "Kazhydromet" of the Ministry of Ecology, Geology and Natural Resources of the Republic of Kazakhstan. According to the 8 years history of the Zhabay River, the maximum outcome in 2017 the amount of flood discharge is $3290 \text{ m}^3/\text{s}$. And the second maximum flood discharge happens in 2014 with the amount of flood discharge $1750 \text{ m}^3/\text{s}$.

In work, we used Gumbel's distribution that is a statistical method often used for predicting extreme hydrological events such as floods. What is different from other methods is that the value of frequency factor K depends upon the number of years of record. In this research, the estimation of frequency factor K using $n=8$.

We performed a flood frequency analysis of the Zhabay River using annual peak flow or maximum discharge data obtained in the river for the years 2011–2018 (Table 2). The results in Table 4 show the expected floods in the river reach for return periods of 2yrs, 5yrs, 10yrs, 25yrs, 50yrs, 100yrs, 200yrs, 250yrs, 500yrs, and 1000yrs. By analyzing the result in Table 4 we predict that the next higher flood inundation will be in return period $T=5$ with the amount $2097.88 \text{ m}^3/\text{s}$. We assume that the reason floods are the global impacts of climate change and the effects of transboundary waters (water comes to us).

In addition in Fig.1, we present the digital terrain model for the Zhabay River Basin. This model was produced with Kazakhstan Earth remote sensing satellite KazEOSat-1 of the JSC "National Company "Kazakhstan Gharysh Sapary".

Acknowledgements

The research was supported by the Ministry of Education and Science of the Republic of Kazakhstan, Grant number: AP05133188

REFERENCES

- 1 Duisenbai N., Baktybekov K., Aimbetov A., Tuleukulova D., Rakhimzhanov B. Development and implementation of scientific based methodology of predicting and modeling of flood and inundation using kazeosat-1, 2 space craft remote sensing datas. *Proceedings of the Intern. Multidisciplinary Scient. Geo Conf. "Surveying Geology and Mining Ecology Management SGEM"*, 2018, Vol. 18, pp. 253 – 258.
- 2 Manfreda S., Nardi F., Samela C., Grimaldi S., et al. Investigation on the Use of Geomorphic Approaches for the Delineation of Flood Prone Areas. *Journal of Hydrology*, 2014, Vol. 517, pp. 863–876.
- 3 Ling Kang L., Jiang Sh., Hu X., Li, Ch. Evaluation of Return Period and Risk in Bivariate Non-Stationary Flood Frequency Analysis. *Water*, 2019, Vol.11, pp.79-83.
- 4 Odunuga Sh., Raji SA. Flood Frequency Analysis and Inundation Mapping of Lower Ogun River Basin. *Journal of Water Resource and Hydraulic Engineering*, 2014, Vol.3, pp. 48–59.
- 5 Plekhanov P.A., Medeu N.N. Extreme hydrological phenomena in the Essil river basin: genesis, general patterns of manifestation. *Journal of ecological Engineering*, 2019, Vol.20, No, 7 , pp. 187–195.

- 6 Domeneghetti A., Schumann G.J, Tarpanelli, A. Preface: Remote Sensing for Flood Mapping and Monitoring of Flood Dynamics. *Remote Sens.*, 2019, Vol.11, No. 8, pp. 943-948.
- 7 Feloni E.G., Mousadis I., Baltas E. Flood vulnerability assessment using a GIS-based multi-criteria approach. The case of Attica region. *Journal of Flood Risk Management*, 2019, Vol.13, pp. 1–15.
- 8 Houessou-Dossou E.A., Gathenya J.M., Njuguna M., Gariy Z.A. Flood frequency analysis using participatory GIS and Rainfall data for stations in Narok Town, Kenya. *Hydrology*, 2019, Vol.6, pp.90-94.
- 9 Bharali B. A Study on Frequency Analysis for Puthimari Catchment by Gumbel Distribution Method. *Journal of Civil Engineering and Environmental Technology*, 2015, Vol.2, pp. 19 – 22.
- 10 Noto L. V, La Loggia G. Use of L-Moments Approach for Regional Flood Frequency Analysis in Sicily, Italy. *Water Resour. Manag.*, 2009, Vol.23, pp. 2207-2211.
- 11 Rakhimzhanov B.K., Murat A., Shaikhova G.N. Flood estimation for Zhabay River Basin in Akmola Region. *Journal of Physics: Conference Series* 2019, Vol.1391, pp. 012168 (1-5).
- 12 Izinyon O. C., Ihimekpen N., Igbinoba G. E. Flood Frequency Analysis of Ikpoba River Catchment at Benin City Using Log Pearson Type III Distribution. *Journal of Emerging Trends in Engineering and Applied Sciences*, 2011, Vol. 2, No. 1, pp. 50–55.
- 13 Fakhrudanova I.B., Petrova L.E. Floods on the Zhabai river in Atbasar town: Consequences, causes, recommendations for reducing the risk of flood *Materials of International practical science conference "Shoqan Oqulary - 22"*, 2018,. Vol. 6, pp. 234-239, [in Russian]
- 14 Website: An unprecedented flood overwhelmed Atbasar: the dam was destroyed. Available at: <https://ru.sputniknews.kz/regions/20170417/2031784/nebyvaloe-polovode-zahlestnulo-atbasar-razrushena-plotina.html> [in Russian]
- 15 Data from the hydrometeorological service RSE “Kazhydromet” of the Ministry of Ecology, Geology and Natural Resources of the Republic of Kazakhstan. Available at: <https://www.kazhydromet.kz/>, 2019.
- 16 Onen F, Bagatur T. Prediction of Flood Frequency Factor for Gumbel Distribution Using Regression and GEP Model. *Arab J. Sci. Eng.*, 2017, Vol.42, pp. 3895–3906.

THE HIGH-RESOLUTION ELECTROSTATIC ENERGY ANALYZER FOR SPACE RESEARCH

Saulebekov A.O.¹, Vénos D.², Kambarova Zh.T.³

¹Lomonosov Moscow State University, Kazakhstan branch, Nur-Sultan, Kazakhstan

²Nuclear Physics Institute, Czech Academy of Sciences, Řež, Czech Republic

³E.A. Buketov Karaganda State University, Karaganda, Kazakhstan, kambarova@bk.ru

The energy analyzer of charged particle beams for space research is proposed. The developed electron-optical scheme of the energy analyzer of the charged particle beam is built on the basis of the electrostatic decapole-cylindrical field. The design of the energy analyzer is described. Equipotential portraits of the electrostatic decapole-cylindrical field are constructed. The trajectories of charged particles are calculated. A study of the parameters of the energy analyzer was carried out. The proposed energy analyzer has a high resolution and can be used in the development of spectrometers for space exploration.

Keywords: energy analyzer, electrostatic field, decapole-cylindrical mirror, electron-optical scheme, focusing order.

Introduction

Studying the dynamics of particle beams is of great interest for various problems that arise when constructing a theory of devices for studying the energy spectra of charged particles, the formation and transportation of charged particle beams in plasma and vacuum, and the injection of particle beams into plasma in laboratory conditions and in space.

The solution of problems related to highly sensitive analysis (substances in microelectronics, ecology, archeology, biology; geophysics, particle flows in interplanetary space in cosmic physics, etc.) was made possible thanks to the development and application of physical analysis methods. Moreover, today, the most widely used physical methods are spectroscopic methods, from which a group of actively developing corpuscular spectroscopy methods, including methods of electron spectroscopy, should be distinguished. However, there is a wide range of unresolved problems in this area, which determines the need for detailed theoretical and practical research. For example, the problems of modern spectral analysis are being actualized, which must be solved under conditions of a sharp increase in the requirements for resolution and sensitivity of the equipment, the complexity of the experiment geometry, the need to simultaneously investigation several parameters, speed up the research process, etc.

Space investigation is impossible to imagine without modern technology and equipment. Every year, for study extraterrestrial space, hundreds of satellites are launched into orbit, which are equipped with advanced equipment that allows to remotely study physical processes, their impact on the Earth, and record various space objects. Spectrometers, as the main tool for space investigation, began to be used more than half a century ago. In general, the modeling of spectrometers for research in space is an actual problem of science.

Cylindrical mirror type energy analyzers are widely used in the study of resonance phenomena in gases, in spectroscopy for chemical analysis, for obtaining spectra of secondary electrons, photoelectrons, autoelectrons, Auger electrons, as well as in space research, in studying the interaction of atomic particles with a solid surface and plasma diagnostics.

1. Axially-symmetrical multipoles

For a potential multipole with plane symmetry N in the cylindrical system coordinates, we can write the following [1]:

$$U(r, \alpha, z) = \sum_{n=0}^{\infty} A_{n,N}(r, z) r^{nN} \cos nN\alpha. \quad (1)$$

The corresponding term $n = 0$ describes the axially-symmetrical component of the field. Corresponding potentials for other members can be written as follows:

for $n = 1$, this equation describes the distribution of the potential of an infinitely plane capacitor $U(x,y)=A_1x$; for $n = 2$, this equation $U(x,y)=A_2(x^2-y^2)$ is this distribution of potentials is explained by the quadrupole, then are potentials of four alternating identical infinite hyperbolic surfaces. Accordingly, $n = 3$ corresponds to a hexapole, $n = 4$ to an octupole, $n = 5$ to a decapole.

A mathematical method for constructing a new class of multipole-cylindrical fields formed by the superposition of a cylindrical field and circular multipoles was proposed in [2-3]. Based on the multipole approach, a wide range of various potential fields has been developed that are of practical interest for studying the mirror effect of these fields on a charged particles beam.

A wide variety of synthesized multipole-cylindrical fields opens up the prospect for the development of new effective energy analysis systems. For example, decapole-cylindrical fields, the potential properties of which have not yet been fully disclosed, may be of practical interest. It is necessary to continue theoretical studies that would allow to determine and expand the functionality of the practical application of multipole-cylindrical fields.

The electron-optical scheme of an electrostatic decapole-cylindrical mirror energy analyzer was firstly proposed in [4], in which the proportion of the cylindrical field and decapole are equal to $\mu=1$ and $\gamma=-1/100$ respectively. The trajectories of charged particles beam with the angular divergence in the axial plane were calculated. The electron-optical parameters of the proposed energy analyzer with the second-order angular focusing were calculated, and the optimal electron-optical scheme of device was determined.

The numerical modeling of the electron-optical scheme of the electrostatic decapole-cylindrical mirror energy analyzer at $\mu=1$ and $\gamma=-1/100$ was carried out in work [5]. The second-order angular focusing regimes of the “ring-ring” and “axis-ring” types were found. The focusing properties of the decapole-cylindrical energy analyzer were calculated.

The scheme of the energy analyzer based on the decapole-cylindrical field with the contributions of a cylindrical field $\mu=3/2$ and a circular decapole $\gamma=-1/100$ was proposed in [6]. Trajectory analysis of the motion of charged particles beams was performed. The design features of the scheme of the proposed energy analyzer were described. Numerical models of energy analyzer schemes based for two angular focusing regimes are obtained.

In this work, the high-resolution energy analyzer based on the decapole-cylindrical field for space research was proposed.

2. Scheme of decapole-cylindrical mirror energy analyzer

The potential of the deflecting field is a superposition of a cylindrical field and a circular decapole

$$U(\rho, z) = \mu \ln(1 + \rho) + \gamma U_d(\rho, z) \quad (2)$$

Where $\ln(1+\rho)$ is cylindrical field, μ is coefficient specifying the weight contribution of the cylindrical field, $U_d(\rho, z) = U_0 \rho \left(z^4 - 2\rho^2 z^2 + \frac{1}{5} \rho^4 \right)$ is circular decapole, γ is weight contribution of circular decapole.

The algorithm for determining equipotential lines in a decapole-cylindrical field is presented below.

$$U_d(r, Z) = U_0 \left[\rho \left(\xi^4 - 2\rho^2 \xi^2 + \frac{1}{5} \rho^4 \right) \right] = U_0 f_d,$$

$$U = U_0 [\mu \ln r + f_d],$$

$$\frac{U}{U_0} = \mu \ln r + f_d,$$

$$-\frac{U}{U_0} + \mu \ln(1+\rho) + \rho \left(\xi^4 - 2\rho^2 \xi^2 + \frac{1}{5} \rho^4 \right) = 0,$$

$$1) \frac{U}{U_0} = 0; 0.1; 0.2; \dots 1.$$

2) We set the values of ρ from 0 1;

3) We obtain the values of ξ for $R(\xi) = 0$;

$$R(\xi) = \frac{-U}{U_0} + \mu \ln(1+\rho) + \rho \left(\xi^4 - 2\rho^2 \xi^2 + \frac{\rho^4}{5} \right)$$

Given

$$R(\xi) = 0$$

Find $(\xi) \rightarrow$

3. Results

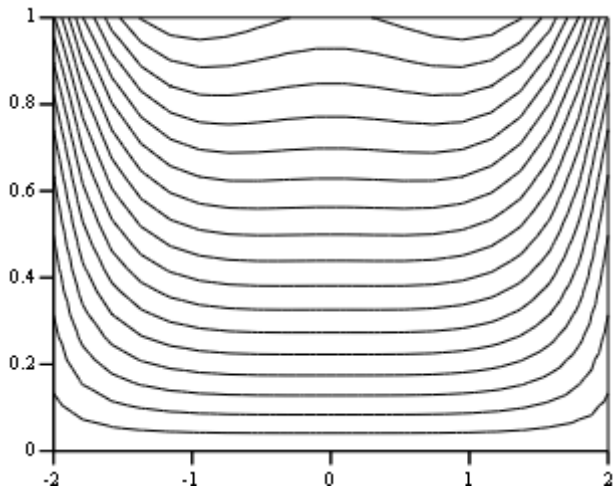
The fig.1 (a-g) presents families of equipotential portraits of an electrostatic decapole-cylindrical field with various contributions of a cylindrical field μ and a circular decapole γ . The analyzer field can be constructed in the form of a superposition of the base field and a set of circular multipoles, which coaxially with the base field.

Due to the small component of the circular field, the distribution of equipotentials of the decapole-cylindrical field, which have a slight deviation from straight lines, is close to the distribution of equipotentials of the cylindrical field.

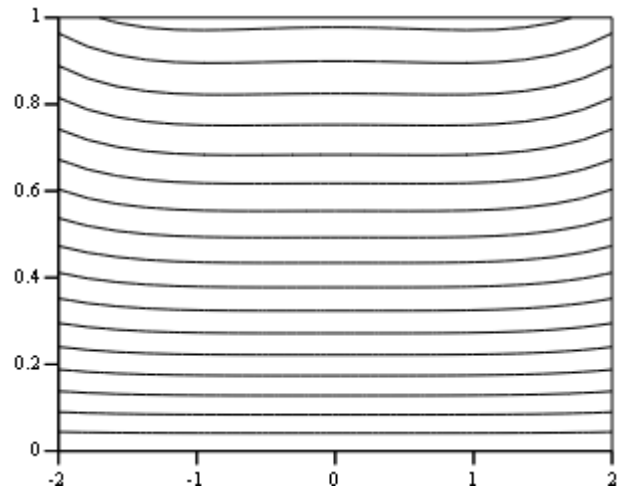
The energy analyzer consists of an inner cylindrical electrode which is at zero potential, and axially symmetrical outer deflecting electrode, which under potential and the generatrix of which coincides with one of the equipotentials of the decapole-cylindrical field.

The scheme of the energy analyzer with a decapole-cylindrical field (2), in which the contributions of the cylindrical field and circular decapole are equal to $\mu=1$ and $\gamma=-\frac{1}{100}$ respectively, is shown in Fig. 2. According to the scheme, a beam of charged particles emerging from the ring source **A** is reflected by the mirror field and focused into the ring image **B**.

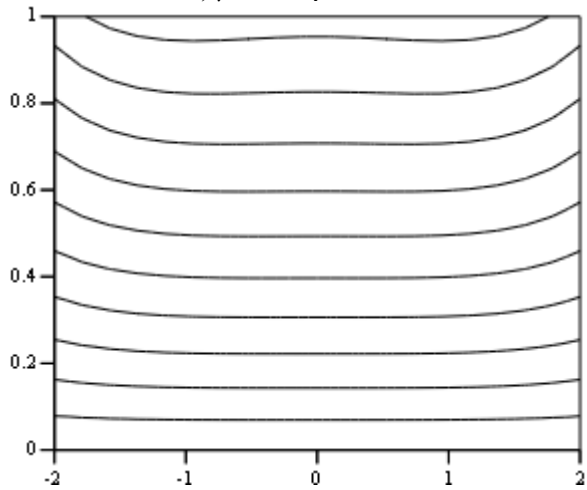
The trajectories of charged particles motion were calculated by using the approximate - analytical method for calculation the trajectories of charged particles in multipole-cylindrical fields. Results of calculation the axial trajectory in a decapole-cylindrical field are presented in table 1.



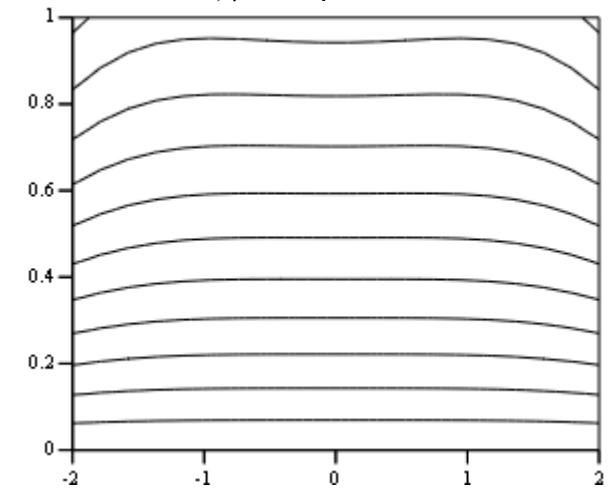
CreateMesh (R, -2, 2, 0, 1)
a) $\mu=2.5, \gamma=-0.1$



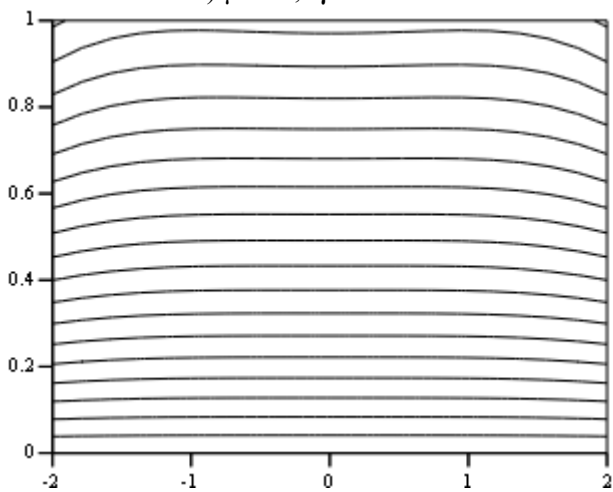
CreateMesh (R, -2, 2, 0, 1)
b) $\mu=2.5, \gamma=-0.01$



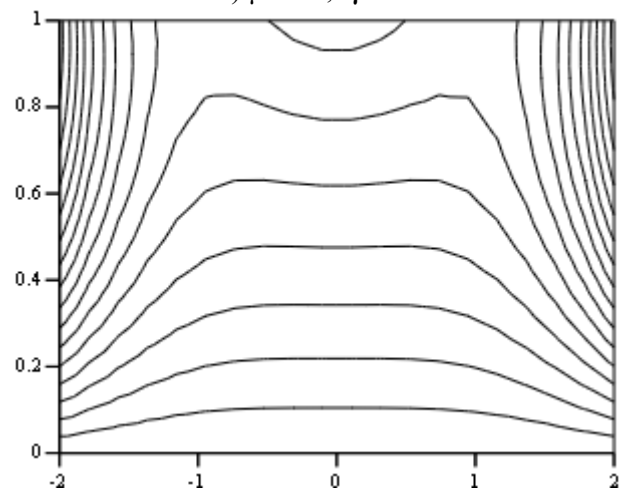
CreateMesh (R, -2, 2, 0, 1)
c) $\mu=1.5, \gamma=-0.01$



CreateMesh (R, -2, 2, 0, 1)
d) $\mu=1.5, \gamma=0.01$

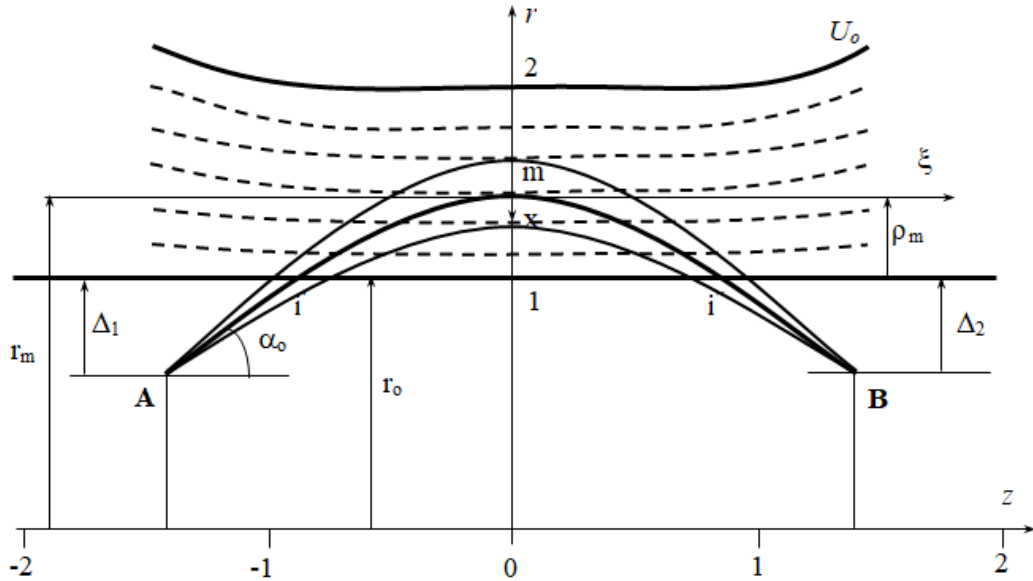


CreateMesh (R, -2, 2, 0, 1)
f) $\mu=2, \gamma=0.01$



CreateMesh (R, -2, 2, 0, 1)
g) $\mu=1, \gamma=0.1$

Fig. 1. Families of equipotential portraits of the electrostatic decapole-cylindrical field with various contributions of a cylindrical field and a circular decapole



A is the source of charged particles, i' is entrance ring slit, i'' is exit ring slit, B is the detector
Fig. 2. The scheme of the energy analyzer based on the decapole-cylindrical field, in which the shares of the cylindrical field and decapole are equal to $\mu = 1$ and $\gamma = -1/100$ respectively.

Table 1 –Results of calculation the axial trajectory in a decapole-cylindrical field

P	α_0 , (degree)	$R=1+\rho_m$	ξ_m	Δ	l	D	A_{III}
0.5500	36.8346	1.3543	0.9896	0.3968	3.0386	2.3834	-8.438

where α_0 is the entrance angle of the trajectory; $\Delta = \Delta_1 = \Delta_2$ is the amount of removal of the source and its image from the surface of the inner cylindrical electrode; ξ_m is the half projection of the trajectory onto the symmetry axis in the field of a decapole-cylindrical mirror, $R = 1 + \rho_m$ is the coordinate of the turning point of the trajectory, l is the focal length equal to the full projection of the trajectory onto the symmetry axis of the mirror from the source to its image, satisfying the focusing conditions, $D = \frac{\partial l}{\partial \epsilon}$ is the relative linear dispersion in energy, $A_{III} = \frac{1}{3!} \frac{d^3 l}{d \alpha^3}$ is coefficient of cubic angular aberration. All longitudinal parameters are expressed in units of the radius r_0 of the inner cylindrical electrode.

Using numerical calculation by the R-Kutta method, the following data for the lateral branches of trajectory are obtained (table 2). The initial angular spread is 12° , $\Delta\alpha = \alpha - \alpha_0 = \pm 6$.

Table 2 –Results of calculation the lateral branches of trajectory

$l(0)$	$l(-6)$	$l(+6)$	$\Delta l(\pm 6)$	$\delta = \frac{D}{\Delta l}$
3.0478	3.0526	3.0506	0.0076	313.6

Thus, the specific energy dispersion, which characterizes the resolution of the decapole-cylindrical field, calculated for particles with an initial angular spread of 12° , is twice the specific dispersion of the cylindrical mirror analyzer $\Delta L (\pm 6) = 0.036$ [7].

Fig.3 shows the dependences of the particle arrival point on the entrance angle α_0 for the angular focusing regime of the “ring-ring” type for various values of the energy of the charged particles. The curve (for a particle with energy $E/V = 1$) corresponds to the second-order angular focusing. It can be seen from Fig. 3 that the optimal range of entrance angles of particles to analyzer field is the range of angles from 30° - 42° , providing a maximum luminosity $\Omega = 12\%$ and the best focusing of the particle beam.

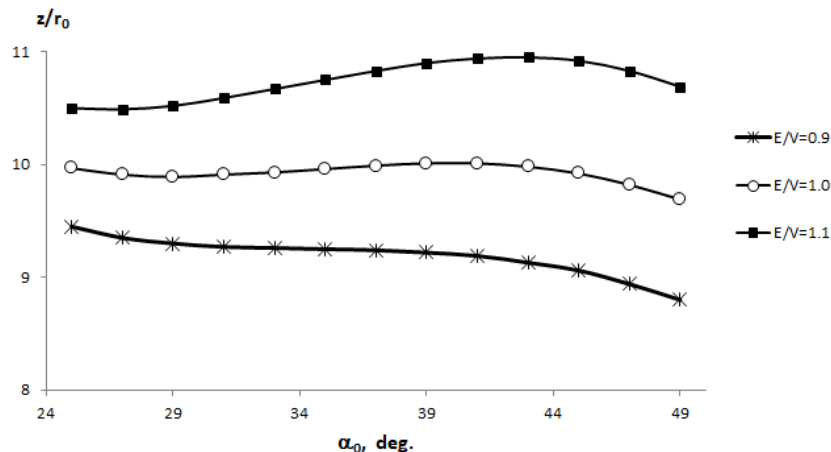


Fig. 3. The dependence of the particle arrival point on the entrance angle α_0 .

Conclusion

The model of the device will make it possible to register flows of elementary particles from cosmic space, to obtain various spectra with high resolution. The device is compact and lightweight, and can be installed in a spacecraft. The proposed device can be used in various intermediate stages of matching particle beams, for example, for studying ion fluxes in cosmic space, for studying the elemental composition of celestial bodies in space research.

REFERENCES

- 1 Silad'i M. *Electron and ion optics*. Moscow: Mir, 1990, - 639 p.
- 2 Zashkvara V.V., Tyndyk N.N. Axial-symmetrical multipoles, their application. *Zh.Tech.Phys.*, 1991, Vol.61, No.4. pp.148-157.
- 3 Zashkvara V.V., Tyndyk N.N. Potential fields based on circular multipole series. *Nuclear Instrum. and Meth.*, 1996, Vol. A370, pp.452-460.
- 4 Ashimbayeva B.U., Chokin K.Sh., Saulebekov A.O., Kambarova Zh.T. Decapole-cylindrical mirror energy analyzer. *Bulletin of Karaganda University*, 2012, No. 4 (68), - pp. 86-92.
- 5 Kambarova Z.T., Trubitsyn A.A., Saulebekov A.O. Axially symmetric energy analyzer based on the electrostatic decapole-cylindrical field. *Technical Physics*, 2018, Vol.63(11), pp.1667–1671. doi.org/10.1134/S1063784218110142
- 6 Kambarova Z.T., Saulebekov A.O., Saulebekova D.A. Modeling of electrostatic decapole-cylindrical mirror analyzer. *IOP Conference Series: Materials Science and Engineering* 12, 2017. pp. 012078. DOI:10.1088/1757-899X/168/1/012078
- 7 Zashkvara V.V., Korsunskiy M.I., Kosmachev O.S. Focusing properties of an electrostatic mirror with a cylindrical field. *Zh.Tech.Phys.*, 1966, Vol.36, No.1, pp. 132-138.

TRAVELING WAVE SOLUTIONS OF TWO-DIMENSIONAL NONLINEAR SCHRÖDINGER EQUATION VIA SINE-COSINE METHOD

Shaikhova G.N., Kutum B.B.

L.N. Gumilyov Eurasian National University, Nur-Sultan, Kazakhstan, kuttykadam@mail.ru

In this work, an analytical study of the two-dimensional nonlinear Schrödinger equation is presented, namely, the applicability of the sine-cosine method to search for the exact solution as a traveling wave. The widely known nonlinear Schrödinger equation plays an important role in the study of the theory of nonlinear waves in various fields of physics and has a huge number of exact solutions. This equation describes the evolution of the changing amplitude of nonlinear waves in various systems, such as weakly nonlinear and highly dispersive. One of the methods for obtaining exact solutions is the sine-cosine method. The advantage of this method is its simplicity and reliability in obtaining solutions to nonlinear problems. According to the method, the nonlinear evolution equation is reduced to the associated ordinary differential equations by wave transformation and then solved by sine or cosine functions. As a result of the applicability of the sine-cosine method, the traveling wave solutions are obtained for a two-dimensional nonlinear Schrödinger equation. 2D-graphs and 3D-graphs of the obtained solutions are shown.

Keywords: two-dimensional, nonlinear Schrödinger equation, sine-cosine method, traveling wave, solution.

Introduction

Nonlinear equations with dissipation and dispersion effects that arise in scientific applications have been under the huge size of investigations. They have various applications in various fields of science, such as mathematical and chemical physics, solid state physics. Many vigorous methods, such as Hirota method [1-3], the extended tanh method [4-6], the sine-cosine method [6-8], Darboux transformation [9-13], Kudryashov method [14] and others were successfully applied to study these types of equations. One striking example of this type of equation is the nonlinear Schrödinger equation, which plays an important role in the theory of nonlinear waves.

The two-dimensional nonlinear Schrödinger equation

$$iq_t + q_{xy} - vq = 0, \quad (1)$$

$$v_x + 2(|q|^2)_y = 0 \quad (2)$$

is a typical soliton equation with rich physical and mathematical applications [15-19]. This equation was proposed in [15] and was later deduced in [16], [17]. The conservation laws of equation (1)-(2) is studied in [18], rogue wave solutions are obtained by Hirota method in [19].

In this work we study the system of equations (1)-(2) by the sine-cosine method that have been extensively studied and widely applied for a wide variety of nonlinear problems [6-8].

1. The scheme of sine-cosine method

In this section, we describe the sine-cosine method [6]. According to the sine-cosine method by using a wave variable

$$u(x, t) = u(x - ct) \quad (3)$$

the partial differential equation

$$E_1(u_t, u_x, u_{xx}, u_{xxx}, \dots) = 0, \quad (4)$$

can be converted to ordinary differential equation

$$E_2(u, u', u'', u''', \dots) = 0. \quad (5)$$

Then the equation (5) is integrated as long as all terms contain derivatives where integration constants are considered zeros. The solutions of ordinary differential equation (5) can be expressed in the form

$$u(x, t) = \lambda \cos^\beta(\mu\xi), \quad |\xi| \leq \frac{\pi}{2\mu}, \quad (6)$$

or

$$u(x, t) = \lambda \sin^\beta(\mu\xi), \quad |\xi| \leq \frac{\pi}{\mu}, \quad (7)$$

where the parameters λ , μ and β will be determined, and μ is wave number and c is wave speed respectively [6]. The derivatives of (6) become

$$(u^n)' = -n\beta\mu\lambda^n \cos^{n\beta-1}(\mu\xi) \sin(\mu\xi), \quad (8)$$

$$(u^n)'' = -n^2\mu^2\beta^2\lambda^n \cos^{n\beta}(\mu\xi) + n\mu^2\lambda^n\beta(n\beta-1)\cos^{n\beta-2}(\mu\xi), \quad (9)$$

And the derivatives of (7) have next forms

$$(u^n)' = -n\beta\mu\lambda^n \sin^{n\beta-1}(\mu\xi) \cos(\mu\xi), \quad (10)$$

$$(u^n)'' = -n^2\mu^2\beta^2\lambda^n \sin^{n\beta}(\mu\xi) + n\mu^2\lambda^n\beta(n\beta-1)\sin^{n\beta-2}(\mu\xi), \quad (11)$$

and so on for the other derivatives. Applying (6)-(11) into the reduced ordinary differential equation (5) we obtain a trigonometric equation of $\cos^\beta(\mu\xi)$ or $\sin^\beta(\mu\xi)$ terms. Then, we determine the parameters by first balancing the exponents of each pair of cosine or sine to determine β . Next, we collect all coefficients of the same power in $\cos^k(\mu\xi)$ or $\sin^k(\mu\xi)$, where these coefficients have to vanish. The system of algebraic equations among the unknown β , λ , and μ will be given and from that, we can determine coefficients.

2. Using the sine-cosine method

We consider the two-dimensional nonlinear Schrodinger equation (1)-(2). By transformation

$$q(x, y, t) = e^{i(ax+by+dt)}Q(x, y, t), \quad (12)$$

the equation (1)-(2) can be converted to

$$i(tdQ + Q_t) + (-baQ + tbQ_x + taQ_y + Q_{xy}) - vQ = 0, \quad (13)$$

$$v_x + 2((Q^2)_y = 0. \quad (14)$$

We separate real and imaginary part in the equation (13)-(14) and obtain

$$-dQ - baQ + Q_{xy} - vQ = 0, \quad (15)$$

$$tQ_t + bQ_x + aQ_y = 0, \quad (16)$$

$$v_x + 2(Q^2)_y = 0 \quad (17)$$

Substituting the wave transformation

$$Q(x, y, t) = Q(\xi) = Q(x + y - ct), \quad (18)$$

$$v(x, y, t) = V(\xi) = Q(x + y - ct), \quad (19)$$

into system of equation (15)-(17) we obtain that

$$Q(-d - ba) + Q'' - vQ = 0, \quad (20)$$

$$Q'(-c + b + a) = 0, \quad (21)$$

$$V' + 2(Q^2)' = 0. \quad (22)$$

From equation (21) we obtain that $c = b + a$. Then we integrate equation (22) and obtain

$$V = -2Q^2. \quad (23)$$

Substituting (23) into (20) we get

$$Q(-d - ba) + Q'' + 2Q^3 = 0. \quad (24)$$

We solve the equation (24) by the sine-cosine method. According to method the solution of the (24) can be found by transformation

$$Q = \lambda \cos^\beta(\mu\xi), \quad (25)$$

and

$$Q = \lambda \sin^\beta(\mu\xi). \quad (26)$$

To find cosine solution we use (25) and its derivative

$$Q'' = -\mu^2 \beta^2 \lambda \cos^\beta(\mu\xi) + \mu^2 \lambda \beta(\beta - 1) \cos^{\beta-2}(\mu\xi). \quad (27)$$

Substitute (25) and (27) into (24) we get

$$\lambda(-d - ba) \cos^\beta(\mu\xi) - \mu^2 \beta^2 \lambda \cos^\beta(\mu\xi) + \mu^2 \lambda \beta(\beta - 1) \cos^{\beta-2}(\mu\xi) + 2\lambda^3 \cos^{3\beta}(\mu\xi) = 0. \quad (28)$$

From (28) we find β :

$$\beta - 2 = 3\beta \text{ then } \beta = -1. \quad (29)$$

Substitute (29) in (28) we obtain next equation

$$\lambda(-d - ba) \cos^{-1}(\mu\xi) - \mu^2 \lambda \cos^{-1}(\mu\xi) + 2\mu^2 \lambda \cos^{-3}(\mu\xi) + 2\lambda^3 \cos^{-3}(\mu\xi) = 0. \quad (30)$$

From the equation (30) we have the next sytem

$$\cos^{-1}(\mu\xi): \lambda(-d - ba) - \mu^2 \lambda = 0, \quad (31)$$

$$\cos^{-3}(\mu\xi): 2\mu^2 \lambda + 2\lambda^3 = 0. \quad (32)$$

From (31) we obtain

$$\mu = \sqrt{d + ba}, \quad (33)$$

and from (32) we get

$$\lambda = \sqrt{d + ba}. \quad (34)$$

Substituting (33)-(34) into (25) and then obtained expression into (12) and (19) we have cosine solution

$$q_1(x, y, t) = e^{t(ax+by+dt)} \sqrt{d + ba} \times \cos^{-1} \left(t\sqrt{d + ba} \times (x + y - ct) \right), \quad (35)$$

$$v_1(x, y, t) = -2(d + ba) \times \cos^{-2} \left(t\sqrt{d + ba} \times (x + y - ct) \right), \quad (36)$$

where $c = b + a$.

By same way we can find sine solution

$$q_2(x, y, t) = e^{t(ax+by+dt)} \sqrt{d + ba} \times \sin^{-1} \left(t\sqrt{d + ba} \times (x + y - ct) \right), \quad (37)$$

$$v_2(x, y, t) = -2(d + ba) \times \sin^{-2} \left(t\sqrt{d + ba} \times (x + y - ct) \right), \quad (38)$$

where $c = b + a$.

2D-graphs and 3D-graphs forms of the obtained solutions are presented in next Fig.1-6.

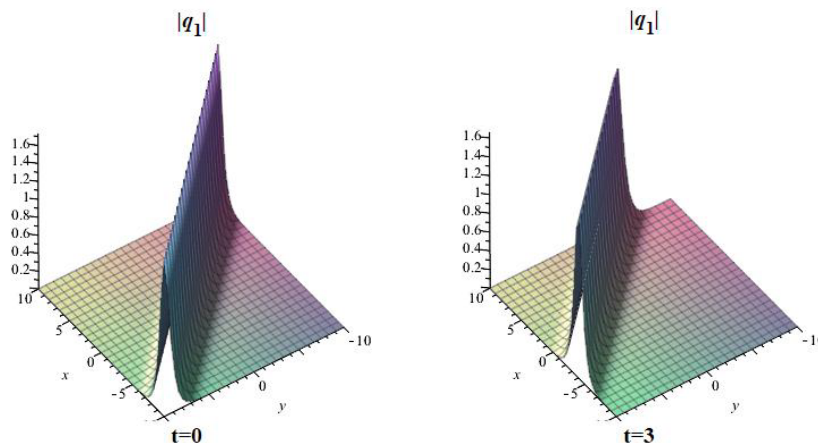


Fig.1. The 3D-graphs of the solution q_1 when $a = 1$, $b = 1$, $d = 2$

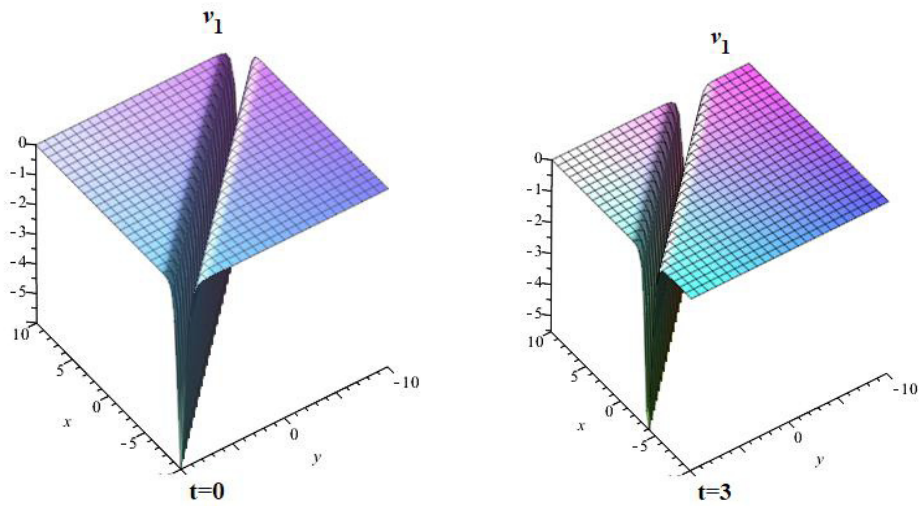


Fig. 2. The 3D-graphs of the solution v_1 when $\alpha = 1, b = 1, d = 2$

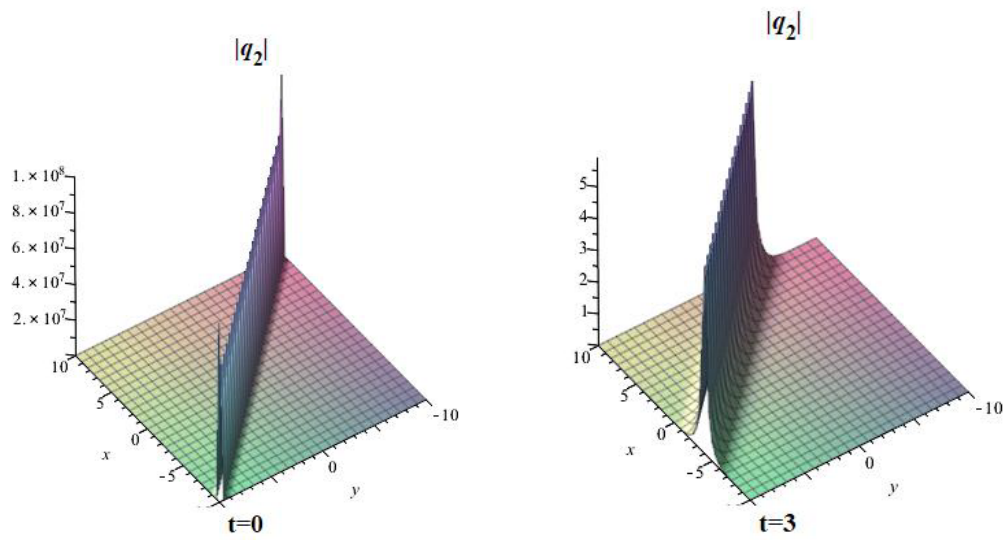


Fig.3. The 3D-graphs of the solution q_2 when $\alpha = 1, b = 1, d = 2$

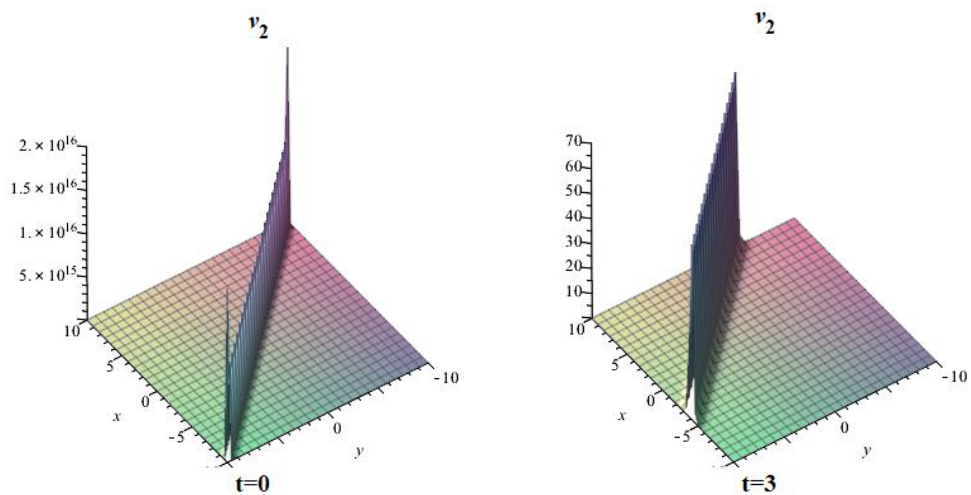


Fig. 4. The 3D-graphs of the solution v_2 when $\alpha = 1, b = 1, d = 2$

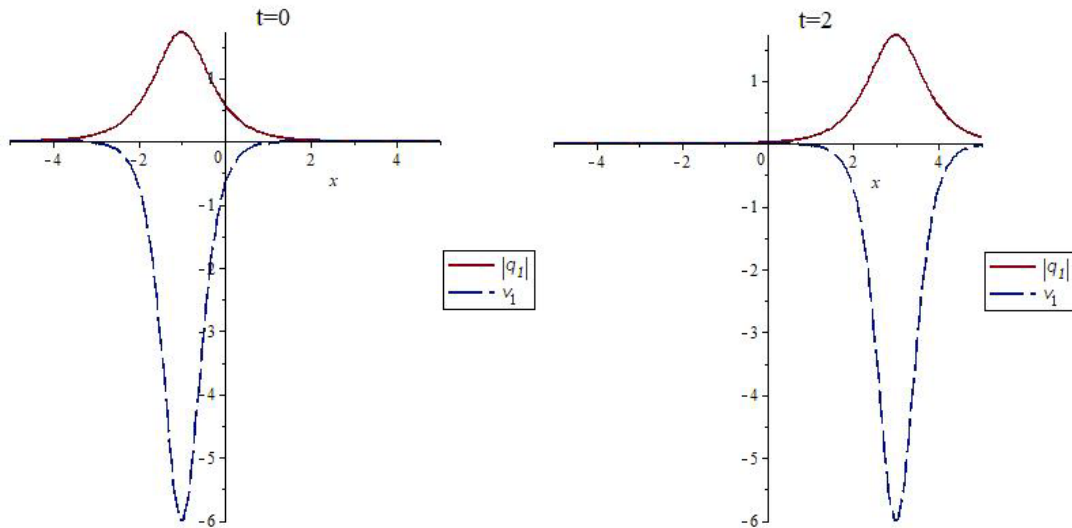


Fig. 5. The 2D-graphs of the solutions q_1 (solid line), v_1 (longdash line) with the parameters $a = 1, b = 1, d = 2$

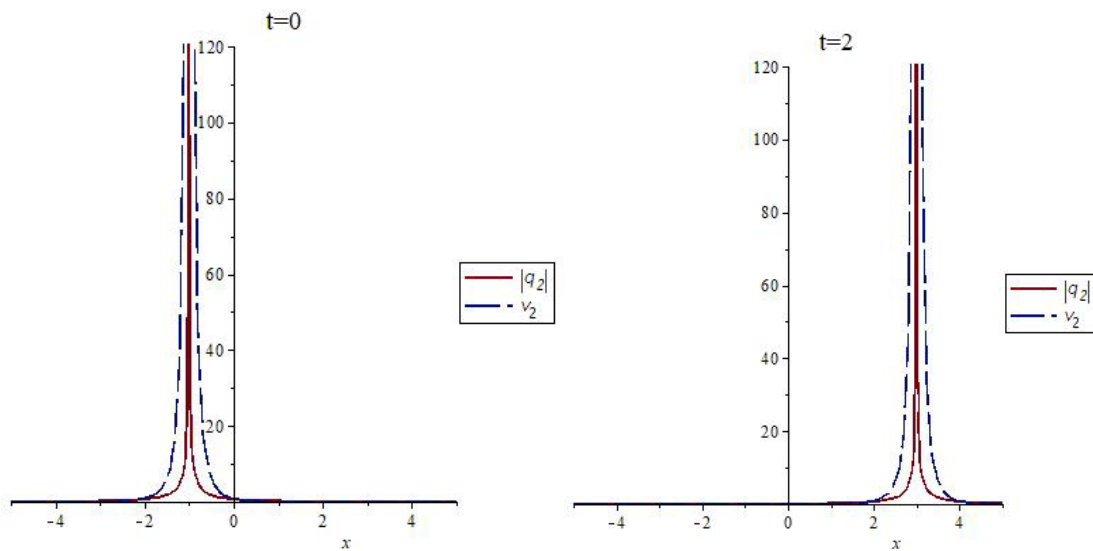


Fig. 6. The 2D-graphs of the solutions q_2 (solid line), v_2 (longdash line) with the parameters $a = 1, b = 1, d = 2$

In Fig.1 - 4 we present 3D plots of the travelling wave solutions (35)-(38). It can be seen that the waves keep their directions, widths, and amplitudes invariant during the propagation on the $x - y$ plane.

Fig.5 displays the dynamics of the traveling wave in 2D plot. As we see the amplitude of solution v_1 (long dash line) bigger than the amplitude of solution q_1 (solid line).In Fig.6, we show the 2D-graphs for the solutions q_2 (solid line) and v_2 (long dash line) with the parameters $t=0$ and $t=2$. As we notice solutions (37)-(38) are traveling to the right by saving shape.

Conclusion

In this work, we investigated the two-dimensional nonlinear Schrodinger equation by applying the sine-cosine method. The nonlinear Schrodinger equation has many applications in different areas of physics. We constructed various exact traveling wave solutions for this equation. The dynamics of the obtained traveling waves are shown in 2D-graphs and 3D-graphs forms. In figures,

the traveling waves keep their directions, widths, and amplitudes invariant during the propagation. The sine-cosine method is a good mathematical tool for obtaining exact solutions for nonlinear wave equations in mathematical physics and other fields.

Acknowledgements

The article is performed as part of the financial support of the scientific and technical program (F. 0811, No. 0118RK00935) of the MES of the Republic of Kazakhstan.

REFERENCES

1. Mukhanmedina K.T., Syzdykova A.M., Shaikhova G.N. Soliton solutions of two-component Hirota equation. *Bulletin of the Karaganda university. Mathematics series*, 2015, No.4(80), pp. 103-107.
2. Kutum B.B., Shaikhova G.N. q-soliton solution for two-dimensional q-Toda lattice. *Bulletin of the Karaganda University. Physics series*, 2019, No.2(95), pp. 22–26.
3. Kutum B.B., Yesmakhanova K.R., Shaikhova G.N. The differential-q-difference 2D Toda equation: bilinear form and soliton solutions. *Journal of Physics: Conference Series*, 2019, Vol. 1391, 012122.
4. Yesmakhanova K., Bekova G., Shaikhova G. Travelling wave solutions for the two-dimensional Hirota system of equations. *AIP Conf. Proc.*, 2018, Vol.1997, pp. 020039. doi:10.1063/1.5049033
5. Serikbayev N.S., Shaikhova G.N., Yesmakhanova K.R., Myrzakulov R. Traveling wave solutions for the (3+1)-dimensional Davey-Stewartson equations. *Journal of Physics: Conference Series*, 2019, Vol. 1391, pp. 012166.
6. Wazwaz A. *Partial differential equations and solitary waves theory*. 2009, Springer, 746 p.
7. Wazwaz A.M. A sine-cosine method for handling nonlinear wave equations. *Mathematical and Computer Modeling*, 2004, No 40(5), pp. 499–508.
8. Shaikhova G.N., Kutum B.B., Altaybaeva A.B., Rakhimzhanov B.K. Exact solutions for the (3+1)-dimensional Kudryashov-Sinelshchikov equation. *Journal of Physics: Conference Series*, 2019, Vol.1416, pp. 012030.
9. Bekova G., Yesmakhanova K., Ozat N., Shaikhova G. Dark and bright solitons for the two-dimensional complex modified Korteweg-de Vries and Maxwell-Bloch system with time-dependent coefficient. *Journal of Physics: Conference Series*, 2018, Vol. 965, pp.012035.
10. Yesmakhanova K., Shaikhova G., Bekova G., Myrzakulov R. Exact solutions for the (2+1)-dimensional Hirota-Maxwell-Bloch system. *AIP Conf. Proc.*, 2017, Vol. 1880, pp. 060022.
11. Yesmakhanova K., Bekova G., Myrzakulov R., Shaikhova G. Lax representation and soliton solutions for the (2+1)-dimensional two-component complex modified Korteweg-de Vries equations. *Journal of Physics: Conference Series*, 2017, Vol. 804, pp.012004.
12. Bekova G., Yesmakhanova K., Myrzakulov R., Shaikhova G. Darboux transformation and soliton solution for the (2+1)-dimensional complex modified Korteweg-de Vries equations. *Journal of Physics: Conference Series*, 2017, Vol. 936, pp. 012045.
13. Bekova G., Shaikhova G., Yesmakhanova K., et al. Darboux transformation and soliton solution for generalized Konno-Ohno equation. *Journal of Physics: Conference Series*, 2019, Vol. 1416, pp. 012003.
14. Shaikhova G. Traveling wave solutions for the two-dimensional Zakharov-Kuznetsov-Burgers equation. *Bulletin of the Karaganda University. Mathematics series*, 2018, No.4(92), pp. 94–98.
15. Zakharov V.E. Solitons. *Topics in Current Physics*, 1980, Berlin, Springer, 389 p.
16. Strachan I.A.B. A new family of integrable models in (2+1) dimensions associated with Hermitian symmetric spaces. *J. Math. Phys.*, 1992, Vol. 33(7), pp. 2477–2482.
17. Strachan I.A.B. Some integrable hierarchies in (2 + 1) dimensions and their twistor description. *J. Math. Phys.*, 1993, Vol. 34(1), pp. 243–259.
18. Bekova G.T., Shaikhova G.N., Yesmakhanova K.R., Myrzakulov R. Conservation laws for two dimensional nonlinear Schrödinger equation. *AIP Conference Proceedings*, 2019, Vol. 2159, pp. 030003.
19. Rao J., Wang L., Liu W., He J. Rogue-wave solutions of the Zakharov equation. *Theoretical and Mathematical Physics*, 2017, Vol. 193(3), pp. 1783–1800.

SUMMARIES	ТҮСІНІКТЕМЕЛЕР	АННОТАЦИИ
<p>Николаев Е. В., Астафьев А.Л., Николаева С.А., Лысенко Е.Н., Зейниденов А.К. LI-TI-ZN ФЕРРИТ КЕРАМИКАСЫНЫҢ ЭЛЕКТРЛІК ҚАСИЕТТЕРІНІҢ БІРТЕКТІЛІГІН ЗЕРТТЕУ. Бұл мақалада литий феррит керамикасының электр өткізгіштігінің біртектілігінің таралуы зерттелген. Электр өткізгіштікті зерттеу цирконий диоксиді қосылған литий алмастырған феррит үлгілерінде жүргізілді (0%; 0,2%; 0,3%; 0,5 мас.%). Эксперименттік үлгілер стандартты керамикалық технологияны қолданылуымен 2 сағат бойы 1010°C температурада пісірілді. Электр өткізгіштіктің температуралық тәуелділіктері екі зондты әдіспен (ағу кедергісі) алынған. Жүргізілген талдауға сәйкес беттік қабаттарда электр өткізгіштіктің таралуы химиялық құрамына байланысты өзгеретіні және бұл таралу біртекті сипатқа ие екендігі анықталды. Сондай-ақ белсендіру энергиясы мен өлшеу қателігі есептелген.</p> <p>Николаев Е.В., Астафьев А.Л., Николаева С.А., Лысенко Е.Н., Зейниденов А.К. ИССЛЕДОВАНИЕ ОДНОРОДНОСТИ ЭЛЕКТРИЧЕСКИХ СВОЙСТВ Li-Ti-Zn ФЕРРИТОВОЙ КЕРАМИКИ. В данной статье было исследовано распределение однородности электропроводности литиевой ферритовой керамики. Исследования электропроводности проводились на образцах литий замещенного феррита с добавлением диоксида циркония (0%; 0,2%; 0,3%; 0,5 мас.%). Экспериментальные образцы были спечены при температуре 1010 °С в течение 2 часов с использованием стандартной керамической технологии. Температурные зависимости электропроводности получены двухзондовым методом (сопротивление растекания). Согласно проведенному анализу было установлено, что распределение электропроводности в поверхностных слоях изменяется в зависимости от химического состава, и это распределение имеет неоднородный характер. Также были рассчитаны энергия активации и погрешность измерения.</p>		
<p>Еремин Е.Н., Гученко С.А., Юров В.М. CrNiTiZrCu ЖОҒАРЫ ЭНТРОПИЯЛЫ ҚАПТАМАЛАРДЫҢ ТОЗУҒА ТӨЗІМДІЛІГІ ЖӘНЕ ТРИБОЛОГИЯЛЫҚ ҚАСИЕТТЕРІ. Жұмыста алғашқы рет механикалық легирлеу әдісімен жоғары энтропиялы қорытпа синтезделіп, белгілі бір шарттарда вакуумда термиялық өңдеуден өткізілді. CrNiTiZrCu қаптамасының микроқаттылығы жоғары энтропиялы эквивалентті қорытпалардың қаттылығынан жоғары. CrNiTiZrCu қаптамасының тозуға төзімділігі $3 \cdot 10^{-4}$ г/мин құрайды, ал бұл өз кезекте тозуға төзімділігі бойынша арнайы болаттарға сәйкес келеді. Жоғары энтропиялы қаптама қабатты кристалдардың үйкеліс деңгейінде төмен үйкеліс коэффициентіне (0.04) ие, бұл оларды жоғары энтропиялы қорытпалардан (шамамен 0.4-0.6) бір реттілікке ерекшеленеді. Олар антифрикциялы, бұл энергия ресурстардың үнемдеуін қамтамасыз етеді. Бұл қаптама Қарағанды қ. турбомеханикалық зауытында 20X13 болаттан жасалған турбиналық қалақтарды өндіруде қолданылады.</p> <p>Еремин Е.Н., Юров В.М., Гученко С.А. ИЗНОСОСТОЙКОСТЬ И ТРИБОЛОГИЧЕСКИЕ СВОЙСТВА ВЫСОКО-ЭНТРОПИЙНЫХ ПОКРЫТИЙ CrNiTiZrCu. В работе впервые синтезирован высокоэнтропийный сплав методом механического легирования с последующей термической обработкой в вакууме при определенных условиях. Микротвердость покрытия CrNiTiZrCu не уступает и в большинстве случаев превосходит твердость высокоэнтропийных эквивалентных сплавов. Износостойкость покрытия CrNiTiZrCu составляет $3 \cdot 10^{-4}$ г/мин, что также отвечает специальным сталям по износостойкости. Высокоэнтропийное покрытие обладает низким коэффициентом трения (0.04) на уровне трения слоистых кристаллов, что отличает их от высокоэнтропийных сплавов (около 0.4-0.6) на порядок. Оно оказываются антифрикционными, что со всей очевидностью приводят к экономии энергоресурсов. Покрытие уже используется при изготовлении турбинных лопаток из стали 20X13 на турбомеханическом заводе г. Караганды.</p>		
<p>Сенють В.Т. БОР НИТРИДІНІҢ НЕГІЗІНДЕ МАТЕРИАЛ ҚҰРЫЛЫМЫНА ЖОҒАРЫ ҚЫСЫМ МЕН ТЕМПЕРАТУРА ЖАҒДАЙЛАРЫНДА МЕХАНИКАЛЫҚ БЕЛСЕНДІРУДІҢ СИНЕРГЕТИКАЛЫҚ ӘСЕРІН ЗЕРТТЕУ. Мақалада жоғары қысымда және температураларда гексагональды бор нитридінің механикалық белсендіруден және пісіруден кейінгі бор нитридінің негізіндегі материалды зерттеу нәтижелері қарастырылған. Алынған материалдың құрылымы мен фазалық құрамы материалды алу технологиясына және синтездеу шарттарынан күшті тәуелділікте екендігі көрсетілген. Механикалық белсендіруден кейін бор нитридінің ұнтағын химиялық тазартуы бордың гексагональды нитридінің температура фазасының төмендеуіне әкеледі. Пісіру процесіндегі жоғары қысым кристаллит өлшемі 50 нм-ге жуық бордың куб нитридінің негізінде материалдың қалыптасуына ықпал етеді. Бор нитридінің алюминиймен қосымша модификациясы және екінші механикалық белсендірумен бірге пісіру қысымын 7.7-ден 5.5 ГПа-ға дейін</p>		

төмендетеді. Сонымен бірге бұл рекристаллизация процесінің салдарынан бордың куб нитридінің түйіршіктерінің өсуіне әкеледі.

Сенють В.Т.

ИЗУЧЕНИЕ СИНЕРГЕТИЧЕСКОГО ЭФФЕКТА МЕХАНИЧЕСКОЙ АКТИВАЦИИ И СПЕКАНИЯ В УСЛОВИЯХ ВЫСОКИХ ДАВЛЕНИЙ И ТЕМПЕРАТУР НА СТРУКТУРУ МАТЕРИАЛА НА ОСНОВЕ НИТРИДА БОРА.

В статье рассмотрены результаты исследования материала на основе нитрида бора после механической активации и спекания при высоких давлениях и температурах гексагонального нитрида бора. Показано, что структура и фазовый состав получаемого материала сильно зависят от технологии получения и условий синтеза материала. Последующая химическая очистка порошка нитрида бора после механической активации приводит к снижению содержания фазы температурах гексагонального нитрида бора. Высокое давление в процессе спекания способствует формированию материала преимущественно на основе кубического нитрида бора с размером кристаллитов порядка 50 нм. Дополнительное модифицирование нитрида бора алюминием в сочетании со второй механической активации снижают давление спекания с 7,7 до 5,5 ГПа. В то же время это приводит к росту зерна кубического нитрида бора вследствие процесса рекристаллизации.

Суржиков А.П., Лысенко Е.Н., Малышев А.В., Петрова А., Гынгазов С.А., Аймуханов А.К. ФЕРРИТТЕРДЕГІ РАДИАЦИЯЛЫҚ ТЕРМИЯЛЫҚ КҮЙДІРУ КЕЗІНДЕГІ ФАЗАЛЫҚ ТҮРЛЕНДІРУЛЕР.

Литий-титан ферритті ұнтақтардың және радиациялық-термиялық және термиялық эффекттер жағдайында ыдыратылған керамикалық үлгілердің фазалық құрамының, морфологиясының және ақаусыз құрылымының электронды микроскопиялық зерттеу жүргізілді. Феррит үлгілерін радиациялық-термиялық түрлендіру сынамаларды электронды үдеткіш көмегімен (1,5-2,0) МэВ энергиясы бар импульсті электронды шокпен сәулелендіру арқылы жүзеге асырылды. Импульстегі сәулелік ток (0,5-0,9) А, сәулелену импульсінің ұзақтығы 500 мкс, пульстің қайталану жиілігі (5-50) Гц, сынаманы қыздыру жылдамдығы -1000 С/мин дейін іске асырылды. Үлгілер қалыңдығы 15 мм болатын шам отты жеңіл қорапта сәулелендірілді. Микроқұрылымды зерттеу электронды микроскоптың көмегімен жарықтың дифракциялық электронды микроскопиясымен жүргізілді. Ферриттердің қалыптасу процесінің радиациялық қарқындылығының ең ықтималды моделі ферриттің аралық фазаларының дәндерінде суброгендік шекаралардың ыдырауы кезінде пайда болған қыздыру кезіндегі дислокациялардың радиациялық тежелу механизмі бола алатындығы көрсетілген.

Суржиков А.П., Лысенко Е.Н., Малышев А.В., Петрова А., Гынгазов С.А., Аймуханов А.К. ФАЗОВЫЕ ПРЕОБРАЗОВАНИЯ В ФЕРРИТАХ ПРИ РАДИАЦИОННО-ТЕРМИЧЕСКОМ СПЕКАНИИ.

Проведены электронно-микроскопические исследования фазового состава, морфологии и дефектной структуры литий-титановых ферритовых порошков и керамических образцов, спеченных в условиях радиационно-термического и теплового воздействий. Радиационно-термическое спекание образцов ферритов осуществляли путем облучения заготовки импульсным электронным пучком с энергией (1,5-2,0) МэВ с использованием электронного ускорителя. Ток пучка в импульсе составлял (0,5-0,9) А, длительность импульса облучения-500 мкс, частота следования импульсов - (5-50) Гц, скорость нагрева заготовки -1000 °С/мин. Образцы облучали в коробке из легкого шамотного материала с толщиной дна 15 мм. Исследования микроструктуры проводили методами электронно-дифракционной микроскопии на свету с использованием электронного микроскопа. Показано, что наиболее вероятной моделью радиационной интенсификации процесса спекания ферритов может служить механизм радиационного торможения дислокаций при нагреве, образующихся во время распада субзеренных границ в зернах промежуточных фаз феррита.

Оспанәлі Ә.Т., Кенжегулов А.К., Жумадилов Б.Е., Суюндықова Г.С., Медянова Б., Партизан Г., Алиев Б.А.

ЭЛЕКТРОСПИННИНГ ӘДІСІМЕН ПОЛИАКРИЛОНИТРИЛ НЕГІЗІНДЕ КӨМІРТЕКТІ НАНОТАЛШЫҚТЫ АЛУ.

Көміртекті наноталшықтар жоғары меншікті беті бар үздіксіз армирулеуге ие болғандықтан, оларды төмен бағада және көп мөлшерде алуға болады, олар дәстүрлі көміртекті нанотүтіктермен салыстырғанда тиімді. Осы жұмыстың негізгі мақсаты полимерлік ерітінді арқылы электроспиннинг әдісімен алынған полиакрилонитрилді (ПАН) негізін құрушы ретінде пайдалана отырып, көміртекті ПАН талшықты өңдеу болып табылады. Мақалада электроспиннинг әдісімен ПАН-талшықтары алынғаны және олардың сипаттамасы, ПАН-наноталшықтарын орау арқылы көміртекті нанотүтіктерді одан әрі дамыту туралы хабарланады. Көміртекті нанотүтіктердің негізін құрушы ретінде алынған диаметрі 100-500 нм диапазонында болатын ПАН-наноталшықтары ПАН/ДМФ ерітіндісінде электроспиннинг әдісімен алынды. Түзуленген наноталшықтар 250°C температурада 1 сағат бойы ауада тұрақтандырылды. Сондай-ақ аргон газының атмосферасында 600-ден 900°C-қа дейінгі диапазонда карбонизацияның соңғы температурасын өзгерту арқылы көміртектендірудің бірнеше процедуралары зерттелді, және көміртекті наноталшықтар 700°C

температурада және 1 сағатта сәтті алынды. Тұрақтандырылған және көміртектендірілген ПАН-наноталшықтарының морфологиясы сканерлеуші электронды микроскопия (СЭМ) әдісімен зерттелді. СЭМ көмегімен алынған нәтижелер тұрақтандырылған және көміртектендірілген ПАН-наноталшықтарының орташа диаметрі айтарлықтай азайғанын көрсетті.

Оспанали А.Т., Кенжегулов А.К., Жумадилов Б.Е., Суюндыкова Г.С., Медянова Б., Партизан Г., Алиев Б.А.

ПОЛУЧЕНИЕ УГЛЕРОДНЫХ НАНОВОЛОКОН НА ОСНОВЕ ПОЛИАКРИЛОНИТРИЛА МЕТОДОМ ЭЛЕКТРОСПИННИНГА.

Поскольку углеродные нановолокна содержат непрерывное армирование с высокой удельной поверхностью, связанной с тем, что их можно получить при низкой стоимости и в большом количестве, по сравнению с традиционными углеродными нанотрубками они оказались экономически выгоднее. Основной целью данной работы является переработка углеродных нановолокон с использованием в качестве предшественника полиакрилонитрила (ПАН), полученного методом электроспиннинга через полимерный раствор, с последующим использованием в качестве армирования в полимерных композитах. В статье сообщается о получении и характеристике ПАН-нановолокон методом электроспиннинга и дальнейшем развитии скручивания ПАН-нановолокон в углеродные нановолокна. ПАН-нановолокна в качестве предшественника углеродных нановолокон с диаметрами в диапазоне 100-500 нм были получены методом электроспиннинга в растворе ПАН/ДМФ. Выровненные нановолокна сначала стабилизировались на воздухе при температуре 250°C в течение 1 часа. Мы также исследовали несколько процедур карбонизации путем изменения конечной температуры карбонизации в диапазоне от 600 до 900°C в атмосфере аргона, и углеродные нановолокна были успешно получены при температуре 700°C и 1 час. Морфология ПАН, стабилизированных и карбонизированных нановолокон была исследована методом сканирующей электронной микроскопии (СЭМ). Результаты, полученные с помощью СЭМ, показали, что средний диаметр стабилизированных и карбонизированных ПАН-нановолокон значительно уменьшился.

Назаров Қ.М., Кичанов С.Е., Ел АбдА., Таман М., Козленко Д.П.

ЦЕМЕНТ ЕРІТІНДІЛЕРІНЕ СУДЫҢ ЕНУІН НАҚТЫ УАҚЫТ РЕЖИМІНДЕ ЖЫЛУЛЫҚ НЕЙТРОНДЫҚ РАДИОГРАФИЯ КӨМЕГІМЕН ЗЕРТТЕУ.

Цемент ерітінділерінің беріктігі мен тұрақтылығын бағалау үшін судың цементке қатынасы әр түрлі болған жағдайларда цемент ерітінділерге судың жұтылуы нейтрондық радиография көмегімен зерттелді. Үлгілердің суды жұтуы кезінде, жұтылу уақытының өтуіне байланысты нейтрондық радиографиялық суреттер үнемі алынып отырды. Су фронтының уақыт бойынша эволюциясы немесе ену тереңдігі мен судың ағым бағыты бойынша таралуы цемент ерітінділерінің әр түрлі компоненттерімен және жұтылған судың нейтрондармен өзара әрекеттесуіндегі айырмашылықтары негізінде анықталды. Алынған нәтижелер цемент ерітінділеріндегі судың таралуының сипаттамалық параметрлерін алу үшін капиллярлар теориясы аясында талқыланды. Кеуекті ортадағы ылғалдың тасымалын зерттеу үшін нейтронды радиографияның қуатты әдіс екендігі көрсетілді.

Назаров К.М., Кичанов С.Е., Ел АбдА., Таман М., Козленко Д.П.

ИССЛЕДОВАНИЕ ПРОНИКНОВЕНИЕ ВОДЫ В ЦЕМЕНТНЫЕ РАСТВОРЫ С ИСПОЛЬЗОВАНИЕМ РАДИОГРАФИИ НА ТЕПЛОВЫХ НЕЙТРОНАХ В РЕЖИМЕ РЕАЛЬНОГО ВРЕМЕНИ.

С помощью нейтронной радиографии, было изучено поглощение воды в цементный раствор с различным отношением воды к цементу, чтобы оценить долговечность и стабильность этих растворов. Во время поглощения воды образцами, регулярно были получены нейтрон-радиографические изображения по истечении времени поглощения. Временная эволюция положения фронта воды или глубина проникновения и распределение содержания воды вдоль направления потока были определены на основе различий во взаимодействиях нейтронов с различными компонентами цементных растворов и поглощенной воды. Полученные результаты обсуждались в рамках теории капилляров для получения характерных параметров распространения воды в цементных растворах. Было показано, что нейтронная радиография является мощным методом исследования переноса влаги в пористых средах.

Кадыржанов К.К., Тынышбаева К., Углов В.В.

АУЫР ХЕ²²⁺ ИОНДАРЫМЕН СӘУЛЕЛЕНУДІҢ КАРБИДТІ КЕРАМИКАНЫҢ МЕХАНИКАЛЫҚ ҚАСИЕТТЕРІНЕ ӘСЕРІН ЗЕРТТЕУ.

Жұмыста кремний карбиді (SiC) негізіндегі керамиканың қасиеттеріне энергиясы 440 кэВ болатын ауыр Хе²²⁺ иондарының және 10¹⁴, 5x10¹⁴, 10¹⁵ ион/см² сәулелену ағындарының сәулелену әсерін зерттеу нәтижелері келтірілген. Сәулелендіру түрін таңдау және дозалық жүктеме ақаулы аймақтарды жабу әсерінің нәтижесінде қалыңдығы 200 нм болатын қабаттың радиациялық зақымдануларын модельдеу мүмкіндігімен негізделген. Алынған нәтижелердің ғылыми жаңалығы - карбидті керамиканың беткі қабатының радиациялық зақымға механикалық және беріктік қасиеттерінің тұрақтылығын жүйелі түрде зерттеу. Зерттеу барысында сәулелендірілген керамика жағдайында зақымдану тереңдігі сәулеленудің әсеріне байланысты иондық

жолдың 20-30%-дан асатындығы анықталды. Радиациялық зақымданудың негізгі механизмі - ақаулардың дислокациялық тығыздығының жоғарылауы және үлкен дозалар кезінде бұзылған аймақтардың қалыптасуы. Жеделдетілген қартаю процестерін модельдеудің нәтижесінде сәулелендірілген сынамалар үшін жарылуға төзімділіктің төмендеуі 10% -дан аспайтыны анықталды. Жүргізілген зерттеулер кремний карбидінің керамикасының беткі қабаттың радиациялық зақымдануына тұрақтылығының жоғары мәндерін көрсетті.

Кадыржанов К.К., Тынышбаева К., Углов В.В.

ИССЛЕДОВАНИЕ ВЛИЯНИЯ ОБЛУЧЕНИЯ ТЯЖЕЛЫМИ ИОНАМИ Xe^{22+} НА МЕХАНИЧЕСКИЕ СВОЙСТВА КАРБИДНЫХ КЕРАМИК.

В работе представлены результаты исследования влияния облучения тяжелыми ионами Xe^{22+} с энергией 440 кэВ и флюенсами облучения 10^{14} , 5×10^{14} , 10^{15} ион/см² на свойства керамик на основе карбида кремния (SiC). Выбор типа облучения и дозовой нагрузке обусловлен возможностью моделирования радиационных повреждений приповерхностного слоя толщиной 200 нм в результате эффекта перекрывания дефектных областей. Научная новизна полученных результатов заключается в систематических исследованиях устойчивости механических и прочностных свойств приповерхностного слоя карбидных керамик к радиационному повреждению. В ходе проведенных исследований установлено, что в случае облученных керамик глубина повреждений превышает расчетную длину пробега ионов на 20-30% в зависимости от флюенса облучения. Основным механизмом радиационных повреждений является увеличение дислокационной плотности дефектов и образованием областей разпорядочения в случае больших доз. В результате моделирования процессов ускоренного старения установлено, что для облученных образцов снижение величины трещиностойкости не превышает 10%. Проведенные исследования показывают высокие значения устойчивости керамик карбида кремния к радиационным повреждениям приповерхностного слоя.

Диханбаев К.К., Бондарев А.И., Икрамова С.Б., Шабдан Е.

АММИАКТЫҢ ГАЗДЫҚ АДСОРБЦИЯ ШАРТЫНДАҒЫ КРЕМНИЙ НАНОЖІПТЕРІНІҢ ЭЛЕКТРЛІК ҚАСИЕТТЕРІ.

Қоршаған орта мониторингі кезінде әр түрлі заттардың газдық фаза құрамын және концентрациясын өлшеудің маңызы зор. Мұндай мәселені шешу үшін резистивті типтегі шалаөткізгіш сенсорлар айтарлықтай қызығушылықты тудырады. Кремнийлік наножіп негізіндегі ұсынылып отырған сенсорлар жоғары сезгіштік және бөлме температурасында жұмыс жасау секілді бірнеше артықшылықтарға ие. Бұл өз кезегінде құрылымды жеңілдетіп, берілгіштердің құнын төмендетеді. Мұның бәрі зерттелініп отырған газ сенсорларының маңыздылығын көрсетеді.

Диханбаев К.К., Бондарев А.И., Икрамова С.Б., Шабдан Е.

ЭЛЕКТРИЧЕСКИЕ СВОЙСТВА КРЕМНИЕВЫХ НАНОНИТЕЙ В УСЛОВИЯХ ГАЗОВОЙ АДСОРБЦИИ АММИАКА.

При мониторинге окружающей среды большое значение имеют измерения концентрации и состава газовой фазы различных веществ. Для решения таких задач интерес представляют полупроводниковые сенсоры резистивного типа. Предлагаемые сенсоры на основе кремниевых нанонитей обладает рядом преимуществ высокая чувствительность и работать при комнатной температуре. Это в свою очередь упрощает конструкции и снижает себестоимость датчиков. Все это указывает на актуальность исследуемого газового сенсора.

Рахадиллов Б.К., Буйткенов Д.Б., Wieleba W., Кылышканов М.К., Ерболатулы Д.

ДЕТОНАЦИЯЛЫҚ ГАЗДЫ ТОЗАҢДАТУ РЕЖИМІНІҢ Ti-Si-C ЖАБЫНДАРЫНЫҢ ФАЗАЛЫҚ ҚҰРАМЫНА ЖӘНЕ АДГЕЗИЯЛЫҚ БЕРІКТІГІНЕ ӘСЕРІ.

Жұмыста детонациялық оқпанды жарылғыш ацетилен-оттегі қоспасымен толтыру көлемінің әр түрлі мәндерінде алынған Ti-C-Si негізіндегі детонациялық жабындардың фазалық құрамы мен беріктік сипаттамаларын зерттеу нәтижелері қарастырылады. Детонациялық оқпанды жарылғыш қоспамен 70% - ға дейін толтыру көлемін ұлғайтқан кезде негізінен TiC фазаларынан тұратынын көрсетті. Өйткені жоғары жылдамдықты соққы әсерінің нәтижесінде жоғары температураға дейін қыздырылған Ti_2SiC_2 ұнтағы TiC-ке ішінара ыдырайды. Рентгендік талдаудың нәтижелері 50% және 60% - ға жарылыс қоспасымен толтырылған кезде Ti_3SiC_2 төмен ыдырау дәрежесіне қол жеткізуге болады, жабындар негізінен Ti_3SiC_2 аз мөлшерде TiC фазаларынан тұрады. Детонациялық оқпанды жарылғыш ацетилен-оттегі қоспасымен толтыру дәрежесі ұлғайған кезде тозаңданатын ұнтақтарының қызу температурасы артады. Жабындар құрамындағы TiC фазасының көлемдік құрамының өсуі Ti-C-Si жабындысының қаттылығының азаюына әкеледі. Жабындардың адгезиялық беріктігін зерттеу нәтижелері детонациялық оқпанды жару қоспасымен толтыру көлемінің адгезиялық беріктікке әсері шамалы екенін көрсетті. Сонымен қатар, детонациялық әдіспен алынған Ti-C-Si негізіндегі барлық жабындар жақсы адгезиялық беріктікті көрсетті.

Рахадиллов Б.К., Буйткенов Д.Б., Wieleba W., Кылышканов М.К., Ерболатулы Д.

ВЛИЯНИЕ РЕЖИМА ДЕТОНАЦИОННОГО ГАЗОВОГО НАПЫЛЕНИЯ НА ФАЗОВЫЙ СОСТАВ И АДГЕЗИОННУЮ ПРОЧНОСТЬ ПОКРЫТИЙ Ti-Si-C.

В работе рассматриваются результаты исследований фазового состава и прочностных характеристик детонационных покрытий на основе Ti-C-Si, полученных при разных значениях объема заполнения детонационного ствола взрывчатой ацетилен-кислородной смесью. Определено, что при увеличении объема заполнения детонационного ствола взрывчатой смесью до 70 % покрытия состоят в основном из фаз TiC. Так как, в результате высокоскоростного ударного взаимодействия нагретый до высоких температур порошок Ti_3SiC_2 частично разлагается на TiC. Результаты рентгенофазового анализа показали, что при заполнении ствола взрывчатой смесью на 50 % и 60 % можно достичь низкой степени разложения Ti_3SiC_2 , покрытия в основном состоят из фаз Ti_3SiC_2 с небольшим содержанием TiC. Это связано с тем, что при увеличении степени заполнения детонационного ствола взрывчатой ацетилен-кислородной смесью увеличивается температура нагрева напыляемого порошка. Определено, что рост объемного содержания фазы TiC в составе покрытий приводит к уменьшению твердости покрытия Ti-C-Si. Результаты исследования адгезионной прочности покрытий показали, что влияние объема заполнения детонационного ствола взрывчатой смесью на адгезионную прочность незначительно. При этом, все покрытия на основе Ti-C-Si, полученные детонационным методом, показали хорошую адгезионную прочность.

Шаринов М.З., Хайитов Д.Э., Раупова И.Б., Садикова М.И.

ГЕКСАГОНАЛДЫ СИММЕТРИЯ КЕРНЕУЛЕРІНІҢ $FeVO_3$ МОНОКРИСТАЛДЫ ДОМЕН ҚҰРЫЛЫМЫНА ЖӘНЕ МАГНИТТЕЛУ ПРОЦЕСІНЕ ӘСЕРІ.

Гексагоналды (C_3 -симметрия) механикалық кернеулердің көмегімен $FeVO_3$ монокристалының базистік жазықтығындағы қосымша магниттік анизотропия индукцияланды. Магнитооптикалық әдіспен анизотропияның әлсіз жеңіл жазықтықты ферромагнетиктің магниттелу процесіне әсері зерттелді. Зерттелген кристалда қосымша магниттік анизотропияның пайда болуы оның 180° –ты домен құрылымын домендік шекаралар кристалдың базистік жазықтығында өзара $\sim 120^\circ$ бұрыштарын құрайтын құрылымға түрлендіруге алып келеді, бірақ әдеттегі 120° – домен құрылымымен салыстырғанда пайда болатын домендердегі спонтанды магниттік векторының азимуты домендік шекаралардың ұзындығын бойлай өзгереді. $FeVO_3$ кристалының домендік құрылымын қайта құрылуы кернеуден туындаған магнитті гистерезис пішінін және коэрцитивті күштің шамасын өзгертіп, техникалық магниттелу процесіне елеулі әсер етеді.

Шаринов М.З., Хайитов Д.Э., Раупова И.Б., Садикова М.И.

ВЛИЯНИЕ НАПРЯЖЕНИЙ ГЕКСАГОНАЛЬНОЙ СИММЕТРИИ НА ДОМЕННУЮ СТРУКТУРУ И ПРОЦЕСС НАМАГНИЧИВАНИЯ МОНОКРИСТАЛЛА $FeVO_3$.

С помощью гексагональных (C_3 – симметрии) механических напряжений индуцирована дополнительная магнитная анизотропия в базисной плоскости монокристалла $FeVO_3$. Магнитооптическим методом исследовано влияние наведенной напряжением анизотропии на процесс намагничивания этого слабого легкоплоскостного ферромагнетика. Показано, что возникновение в исследованном кристалле дополнительной магнитной анизотропии приводит к преобразованию его доменной структуры из 180° – ной в структуру, в которой доменные границы образуют в базисной плоскости кристалла между собой углы $\sim 120^\circ$, однако в отличие от обычной 120° – ной доменной структуры азимут вектора спонтанной намагниченности в возникающих доменах изменяется вдоль длины доменных границ. Установлено, что вызванная напряжением перестройка доменной структуры кристалла $FeVO_3$ оказывает заметное влияние на процесс технического намагничивания, изменяя форму магнитного гистерезиса и величину коэрцитивной силы.

Карипбаев Ж., Алтысова Г., Мусаханов Д., Лисицын В., Кукенова А., Тулегенова А.

ЭЛЕКТРОНДЫ СӘУЛЕНІҢ КӨМЕГІМЕН СИНТЕЗДЕЛГЕН YAG:Ce КЕРАМИКАНЫҢ N_2 ЛАЗЕРІМЕН ҚОЗДЫРЫЛҒАН УАҚЫТҚА ТӘУЕЛДІ ЛЮМИНЕСЦЕНЦИЯСЫ.

Бұл жұмыста қуатты қатаң радиацияның ағындарын пайдаланып, люминофорды синтездеуге әрекет жасалды. Ақ жарықты шығаратын диодтар (жарық диодтары) энергияны үнемдеу және ұзақ қызмет көрсету сияқты керемет қасиеттеріне байланысты жақсы жарық беретін құрылғылар болып саналады. Синтезделген керамика YAG: Ce және YAGG: Ce люминофорларына тән қасиеттерге ие. Зерттеу үшін люминофорлардың 10 түрі таңдалды. Люминофорлар Se_2O_3 және модификатор ретінде қосылған гадолиний иондарының қатысуымен ерекшеленді. Жұмыс Қазақстан Республикасы Білім және ғылым министрлігінің AP08052050 гранты аясында жүзеге асырылды. Бұл зерттеуді Томск политехникалық университетінің бағдарламасы қолдады.

Карипбаев Ж., Алтысова Г., Мусаханов Д., Лисицын В., Кукенова А., Тулегенова А.

РАЗРЕШЕННАЯ ВО ВРЕМЕНИ ЛЮМИНЕСЦЕНЦИЯ ОБРАЗОВАННОЙ ЭЛЕКТРОННО-ЛУЧЕВЫМ СИНТЕЗОМ YAG: Ce-КЕРАМИКИ, ВОЗБУЖДАЕМАЯ N_2 -ЛАЗЕРОМ.

В настоящей работе предпринята попытка синтеза люминофора, с использованием мощных потоков жесткой радиации. Белые светодиоды (LED) считаются хорошими осветительными приборами благодаря своим непревзойденным качествам, таким как энергосбережение и длительный срок службы. Синтезированная

керамика обладает характерными свойствами люминофоров YAG:Ce, YAGG:Ce. Всего для исследования было выбрано 10 видов люминофоров. Люминофоры различались наличием в них ионов Ce_2O_3 и гадолиния, включенных в качестве модификатора. Работа выполнена в рамках гранта AP08052050 Министерства образования и науки Республики Казахстан. Работа выполнена при поддержке Программы Томского политехнического университета.

Обухов С.Г., Плотников И.А., Масолов В.Г.

ЖЕЛ ЭНЕРГЕТИКАСЫНЫҢ ЕСЕПТЕРІН ШЕШУ ҮШІН ЖЕЛ ЖЫЛДАМДЫҒЫНЫҢ ДИНАМИКАЛЫҚ МОДЕЛІ.

Берілген жұмыс жел энергетикасының есептерін шешуге арналған жел жылдамдығының динамикалық моделін әзірлеуге арналған. Желдің уақытша моделі тұрақты және турбулентті болып табылатын екі құраушы түрінде ұсынылған. МЭК 61400-1: 2005 ұсынған Каймальдің спектрлік моделі жел жылдамдығының турбуленттік құраушысын сипаттау үшін пайдаланылды. Турбуленттіліктің параметрлерін есептеу үшін бастапқы деректер жел энергетикалық қондырғының класы болып табылады, ол өз кезекте орналасуымен, жел дөңгелегінің айналу өісінің биіктігімен және модельдеудің берілген уақыт аралығындағы орта жылдамдықпен анықталады. Жел моделін компьютерлік іске асыру шығу дабылдары қосылатын қалыптастырушы сүзгіштерге әсер ететін ақ шудың статистикалық тәуелсіз көздері негізінде жүзеге асырылады. Алынған нәтижелерді талдауы сүзгіштерді қалыптастыру әдісінің негізінде жүзеге асырылған жел ағынының моделі жел жылдамдығының бойлық құраушысын адекватты үлгілеуді қамтамасыз етеді және жел энергетикасының есептерін шешу үшін пайдаланылуы мүмкін.

Обухов С.Г., Плотников И.А., Масолов В.Г.

ДИНАМИЧЕСКАЯ МОДЕЛЬ СКОРОСТИ ВЕТРА ДЛЯ РЕШЕНИЯ ЗАДАЧ ВЕТРОЭНЕРГЕТИКИ.

Данная работа посвящена разработке динамической модели скорости ветра, предназначенной для решения задач ветроэнергетики. Временная модель ветра представлена в виде двух составляющих - постоянной и турбулентной. Спектральная модель Каймаля, рекомендованная МЭК 61400-1: 2005, используется для описания турбулентного компонента скорости ветра. Исходными данными для расчета параметров турбулентности являются класс ветроэнергетической установки, который определяется ее расположением, высотой оси вращения ветроколеса и средней скоростью ветра за указанный интервал времени моделирования. Компьютерная реализация модели ветра осуществляется на основе статистически независимых источников белого шума, действующих на формирующие фильтры, выходные сигналы которых суммируются. Анализ полученных результатов показывает, что модель ветрового потока, реализованная на основе метода формирования фильтров, обеспечивает адекватное моделирование продольной составляющей скорости ветра и может быть использована для решения задач ветроэнергетики.

Төлеуов Ғ.Қ., Исатаев М.С., Сейдулла Ж.Қ., Зулбухарова Э.М., Масина М.Н.

ЖАЗЫҚ АҒЫНШАНЫҢ ДИНАМИКАСЫНА БҮЙІРЛІК ПЛАСТИНАЛАРДЫҢ ҮЙКЕЛІС КЕДЕРГІСІНІҢ ӘСЕРІН ЕСЕПТЕУ.

Бұл мақала бүйірлік пластиналардың үйкеліс кедергісінің жазық ағыншаның аэродинамикасына әсерін есептеу бойынша ғылыми зерттеулердің жалғасы болып табылады. Алдыңғы жұмыстарда кедергісі турбулентті шекара қабаты үшін есептелді. Бұл мақалада жазық еркін ағыстың даму заңдылықтарына бүйірлік пластиналардың үйкеліс кедергісінің әсерін есептеу нәтижелері келтірілген. Бүйірлік пластиналардың арасындағы ағынша ағысының сызбасы тұрғызылды. Ламинарлық шекаралық қабат үшін кедергіні есептеу жүргізілді. Бірінші жуықтауда ағыншаның максималды жылдамдығының өзгерісін сипаттайтын есептік формула алынды. Теориялық есептерді эксперименттік деректермен салыстырғанда жақсы үйлесімділікті көрсетті.

Төлеуов Ғ.Қ., Исатаев М.С., Сейдулла Ж.Қ., Зулбухарова Э.М., Масина М.Н.

РАСЧЕТ ВЛИЯНИЯ СОПРОТИВЛЕНИЯ ТРЕНИЯ ТОРЦОВЫХ ПЛАСТИН НА ДИНАМИКУ ПЛОСКОЙ СТРУИ.

Данная статья является продолжением научных исследований по расчету влияния сопротивления трения концевых пластин на аэродинамику плоской струи. В предыдущих работах сопротивление рассчитывалось для турбулентного пограничного слоя. В данной статье приведены результаты расчета влияния сопротивления трения торцовых пластин на закономерности развития плоской свободной струи. Построена схема потока струи между торцевыми поверхностями. Проведен расчет сопротивления для ламинарного пограничного слоя. Получена формула для расчета изменения максимальной скорости струи в первом приближении. Сравнение теоретических расчетов с экспериментальными данными показало хорошее согласие.

Шарифов Д.М., Сақыпов К.Е., Мерзадинова Г.Т., Қалиева Ж.Е., Усербаев М.Т.

ЖЫЛУЭНЕРГЕТИКАЛЫҚ НЫСАНДАРДЫ ТЕХНИКАЛЫҚ ДИАГНОСТИКАЛАУДЫҢ ЛАЗЕРЛІК ОПТИКО-АКУСТИКАЛЫҚ ӘДІСІНІҢ КЕЙБІР ЕРЕКШЕЛІКТЕРІН ЗЕРТТЕУ.

Мақалада жылу энергетикалық объектілерді техникалық диагностикалау кезінде лазерлік оптикалық-акустикалық (ЛОА) әдісті қолдану ерекшеліктерін зерттеу нәтижелері келтірілген. Диагностикалаудың бірқатар технологиялық маңызды есептерін шешуде қолданылатын әдістің ерекшеліктері көрсетілген, атап айтқанда: құбырлардың дәнекерленген жіктерінің сапасын бақылау, қалдық кернеуді, материалдардың құрылымдық, механикалық, серпімді қасиеттерін анықтау. Ультрадыбыстық толқындарды қозудың лазерлік оптоакустикалық әдісінің физикалық негіздері теориялық зерттелді. Бұл әдіс бақылау объектісінде кең жолақты ультрадыбыстық сигналдардың лазерлік термооптикалық қозуына негізделеді. Зерттелетін нысанның жұқа беткі қабатына жұтылып, лазерлік импульс кең жолақты ультрадыбыстық импульсті қоздырады. Объектіде тарала отырып, қозғалатын ультрадыбыстық импульс (жоғары уақытша ажыратумен өткен немесе шашыраған ультрадыбыстық дабыл тіркеледі) зерттелетін объект туралы ақпарат алады.

Шарифов Д.М., Сакипов К.Е., Мерзадинова Г.Т., Қалиева Ж.Е., Усербаев М.Т.

ИССЛЕДОВАНИЕ НЕКОТОРЫХ ОСОБЕННОСТЕЙ ЛАЗЕРНОГО ОПТИКО-АКУСТИЧЕСКОГО МЕТОДА ТЕХНИЧЕСКОЙ ДИАГНОСТИКИ ТЕПЛО-ЭНЕРГЕТИЧЕСКИХ ОБЪЕКТОВ.

В статье приводятся результаты исследования особенностей применения лазерного оптического-акустического (ЛОА) метода при технической диагностике теплоэнергетических объектов. Показаны отличительные особенности применяемого метода при решении ряда технологически важных задач диагностирования, в частности: контроль качества сварных швов труб, определения остаточного напряжения, структурных, механических, упругих свойств материалов. Теоретически исследованы физические основы лазерного оптоакустического метода возбуждения ультразвуковых волн. Показано, что данный метод основывается на лазерном термооптическом возбуждении широкополосных ультразвуковых сигналов в объекте контроля. Поглощаясь в тонком поверхностном слое исследуемого объекта, лазерный импульс возбуждает широкополосный ультразвуковой импульс. Распространяясь в объекте, возбуждаемый ультразвуковой импульс (регистрируется либо прошедший, либо рассеянный ультразвуковой сигнал с высоким временным разрешением) несёт информацию об исследуемом объекте.

Нижнегородов А.И., Гаврилин А.Н., Мойзес Б.Б., Кувишинов К.А.

КҮЙДІРУ КЕЗІНДЕГІ СУСЫМАЛЫ МАТЕРИАЛДАҒЫ ДИНАМИКАЛЫҚ ПРОЦЕСТЕРДІ ЗЕРТТЕУ.

Мақалада сусымалы материалдарды термоөндеуге арналған электр пешінің тірек плитасының динамикасын зерттеу нәтижелері келтірілген. Серпімді байланыстардағы жылжымалы арбалы тірек плитасы термоөңделген материалды берілген жылдамдықпен және өңдеу уақытымен күйдіру жүйесінің ыстық бөлігіне тасымалдайтын негіз болып табылады. Тербелмелі жүйенің эксперименттік жиынтық серпімді сипаттамасы алынды, әлсіз сызықты еместікті сипаттайтын амплитудалық-жиілік сипаттамасы құрылды. Эксперименттер әртүрлі конструкциялардың конустық серіппелер тірек плитасының тербелісінің күшті асимметриясын қамтамасыз етпейтінін көрсетті, сондықтан тәжірибелі пештің көлденең жағдайдағы әлсіз тербелістің тиімділігін қамтамасыз ете алмайды. Одан әрі эксперименттер пешті көлденең бетке бұрышпен орнату кезінде жүргізілді. Вермикулитті тасымалдаудың тербелмелі уақыты резонанстық аймаққа жақын қозу жиілігінің күйге келтіруіне байланысты 2,7...3,2 с-қа жетті. Дірілдейтін тірек плитасының жұмысы әртүрлі факторлардан қозу жиілігінің жоғары сезгіштікке байланысты тұрақты болмайтыны көрсетілген. Сезгіштік коэффициентін төмендету әдістері қарастырылды.

Нижнегородов А.И., Гаврилин А.Н., Мойзес Б.Б., Кувишинов К.А.

ИССЛЕДОВАНИЕ ДИНАМИЧЕСКИХ ПРОЦЕССОВ В СЫПУЧЕМ МАТЕРИАЛЕ ПРИ ЕГО ОБЖИГЕ.

В статье представлены результаты исследований динамики опорной плиты электропечи для термообработки сыпучих материалов. Опорная плита с подвижной тележкой на упругих связях служит основанием, которое транспортирует термообработанный материал в горячую часть системы обжига с заданной скоростью и временем обработки. Получена экспериментальная суммарная упругая характеристика колебательной системы, построена амплитудно-частотная характеристика, характеризующая слабую нелинейность. Эксперименты показали, что конические пружины различных конструкций не обеспечивают сильной асимметрии колебаний опорной плиты, и поэтому эффективность вибрационного переноса слаба в горизонтальном положении опытной печи. Дальнейшие эксперименты проводились при установке печи под углом к горизонтальной поверхности. Колебательное время переноса вермикулита достигло 2,7...3,2 с, в зависимости от настроек частоты возбуждения вблизи резонансной зоны. Показано, что работа вибрирующей опорной плиты не может быть стабильной из-за высокой чувствительности частоты возбуждения от различных факторов. Рассмотрены методы снижения коэффициента чувствительности.

Сакипова С.Е., Танашева Н.К., Миньков Л.Л.

АЙНАЛМАЛЫ ЦИЛИНДРЛІК ҚАЛАҚШАЛЫ ЖЕЛ ТУРБИНАСЫНЫҢ ТУРБУЛЕНТТІК АҒЫНЫМЕН ОРАП ӨТУ АЭРОДИНАМИКАСЫН МОДЕЛЬДЕУ.

Мақалада ANSYS FLUENT бағдарлама пакетін пайдалана отырып, үш қалақшалы жел турбинасының аэродинамикалық орап өтудің компьютерлік модельдеудің кейбір мүмкіндіктері қарастырылды. Зерттеу объектісінің ерекшелігі—жел дөңгелегі өз өсінің айналасында айналатын үш цилиндрлік қалақшадан тұрады.

Турбуленттілік моделінің $k-\varepsilon$ жақындаудағы теңдеулер жүйесі Ansys-Fluent пакетінде алуан (тіркемеленген) координаттар жүйесінің жақындауды қолдануымен ақырғы көлем әдісімен шешіледі. Есептеу аймағы бір-біріне кіріктірілген үш түрлі субаймаққа бөлінген. Модельдеу нәтижесінде құйынды дөңгелек бетінің маңында жылдамдықтар өрісі визуализацияланған. Жел дөңгелегінің орталық дискісінің маңында ауа ағыны негіз ағынға қарама-қарсы бағытта ашылады. 300-ден 700 айн / мин аралықта цилиндрлердің айналу жылдамдығы өзгерген кезде аэродинамикалық коэффициенттердің жылдамдыққа тәуелділіктері алынды.

Сакипова С.Е., Танашева Н.К., Миньков Л.Л.

МОДЕЛИРОВАНИЕ АЭРОДИНАМИКИ ОБТЕКАНИЯ ТУРБУЛЕНТНЫМ ПОТОКОМ ВЕТРОТУРБИНЫ С ВРАЩАЮЩИМИСЯ ЦИЛИНДРИЧЕСКИМИ ЛОПАСТЯМИ.

В статье рассматриваются некоторые возможности компьютерного моделирования аэродинамического обтекания трехлопастной ветротурбины с использованием пакета программ ANSYS FLUENT. Особенностью объекта исследования является то, что ветроколесо состоит из трех цилиндрических лопастей, вращающихся вокруг своей оси. Система уравнений в приближении $k-\varepsilon$ модели турбулентности решается в пакете Ansys-Fluent методом конечных объемов с применением подхода множественных (вложенных) систем координат. Вычислительная область была разделена на три типа субрегионов, вложенных друг в друга. В результате моделирования визуализировано поле скоростей вблизи поверхности вихревого колеса. Показано, что вблизи центрального диска ветряного колеса воздушный поток разворачивается в направлении, противоположном основному. Получены зависимости аэродинамических коэффициентов от скорости при изменении скорости вращения цилиндров в диапазоне от 300 до 700 об / мин.

Қарабекова Д.Ж., Хасенов А.К., Қисабекова П.Ә., Сатыбалдин А.Ж., Тунгушбекова М.К.

КООРДИНАТАЛЫҚ – СЕЗГІШ ҚАБЫЛДАҒЫШПЕН КЕҢІСТІКТІК БІРТЕКТІ ЕМЕС СӘУЛЕЛЕНУІНІҢ ӨЗГЕРУІ.

Дайындалған аспап жер асты құбырларының жылу оқшаулауының жай-күйін талдауға арналған. Ұсынылған жылу ағынын өлшеуіш температураны өлшеу процесінде сезгіш элементтің тоқ жылуын пайдаланады. Бұл температураны өлшеу дәлдігін арттырады және алдын-ала өлшенген реперлік температураны тоқпен қыздыру арқылы ұстап тұруға мүмкіндік береді. Өзірленген аспап бірнеше бірдей пластиналардан құрылады, олардың әрқайсысы сәуле қабылдай алады. Электр тоғымен жасалатын кеңістіктік біртекті жылу ағынымен координаталық-сезгіш қабылдағышты калибрлеу негізіндегі энергетикалық параметрлерді анықтау үшін формулалар алынды.

Қарабекова Д.Ж., Хасенов А.К., Қисабекова П.А., Сатыбалдин А.Ж., Тунгушбекова М.К.

ИЗМЕНЕНИЕ ПРОСТРАНСТВЕННО НЕОДНОРОДНОГО ИЗЛУЧЕНИЯ КООРДИНАТНО – ЧУВСТВИТЕЛЬНЫМ ПРИЕМНИКОМ.

Разработанный прибор предназначен для анализа состояния тепловой изоляции подземных трубопроводов. Предлагаемый измеритель теплового потока использует токовый нагрев чувствительного элемента в процессе измерения температуры. Это позволит повысить точность измерения температуры и поддерживать с помощью токового нагрева реперную температуру, измеренную предварительно. Разработанный прибор имеет несколько идентичных пластин, каждая из которых может принимать излучения. Получены формулы для определения энергетических параметров, в основе которых лежит калибровка координатно-чувствительного приемника пространственно однородным тепловым потоком, создаваемым электрическим током.

Балдычев М.Т., Лаптев И.В., Чеботарь И.В., Гайчук Ю.Н., Пивкин И.Г., Тимошенко А.В., Гальцева О.В.

ҰШҚЫШСЫЗ ҰШУ АППАРАТЫНЫҢ БІР СЕНСОрын ҚОЛДАНУЫМЕН ЖАЙҒАСТЫРУ ЖҮЙЕСІМЕН ИМПУЛЬСТІК РАДИОДАБЫЛДАР КӨЗІНІҢ КООРДИНАТТАРЫН АНЫҚТАУДЫҢ ПОТЕНЦИАЛДЫ ДӘЛДІГІН БАҒАЛАУ

Мақалада ұшқышсыз ұшу аппаратының бір сенсорын қолдануымен жайғастыру жүйесімен импульстік радиодабылдар көздерінің координаттарын анықтау әдісі ұсынылған. Орналасу орнын анықтаудың айырғыш-қашықтықты өлшеу әдісі қабылдау нүктелерін ретрансляциясыз және ішкі синхрондаусыз ақпараттық-координаттық параметрді алуға мүмкіндік береді. Импульстік радиодабылдар көздерінің жұмыс режимінің кейбір ерекшеліктерін ескере отырып, белгілі ғылыми-әдістемелік аппаратты жетілдіру есебінен нәтижеге қол жеткізіледі. Модельдеудің берілген нәтижелері негізгі кіріс факторларының импульстік радиодабылдар көзінің координаттарын анықтаудың потенциалды дәлдігіне әсерін бағалауға мүмкіндік береді.

Балдычев М.Т., Лаптев И.В., Чеботарь И.В., Гайчук Ю.Н., Пивкин И.Г., Тимошенко А.В., Гальцева О.В.

ОЦЕНКА ПОТЕНЦИАЛЬНОЙ ТОЧНОСТИ ОПРЕДЕЛЕНИЯ КООРДИНАТ ИСТОЧНИКА ИМПУЛЬСНЫХ РАДИОСИГНАЛОВ СИСТЕМОЙ ПОЗИЦИОНИРОВАНИЯ С ИСПОЛЬЗОВАНИЕМ ОДНОГО ДАТЧИКА БЕСПИЛОТНОГО ЛЕТАТЕЛЬНОГО АППАРАТА.

В статье представлен метод определения координат источников импульсных радиосигналов системой

позиционирования при применении одного датчика беспилотного летательного аппарата. Разностно-дальномерный метод определения местоположения позволяет получить информативно-координатный параметр без ретрансляции и внутренней синхронизации точек приема. Результат достигается за счет совершенствования известного научно-методического аппарата с учетом некоторых особенностей режима работы источников импульсных радиосигналов. Представленные результаты моделирования позволяют оценить влияние основных входных факторов на потенциальную точность определения координат источника импульсного радиосигнала.

Макеева О.В., Олешко В.С., Федоров А.В., Юров В.М.

ЭЛЕКТРОНДАРДЫҢ ШЫҒУ ЖҰМЫСЫН АНЫҚТАЙТЫН ҚҰРЫЛҒЫ ӨЗІРЛЕУ.

Бет металл бөлшектердің маңызды құрамдас бөлігі болып табылады және оны өндіру, пайдалану және жөндеу кезінде детальдің өмір циклінің барлық кезеңдерінде оның жағдайын бақылау қажет. Металл бөлшектерді бұзбайтын сенімді бақылауын жүргізу үшін осы үшін арнайы әзірленген құралдар мен оны қолдану әдістемесі қажет. Потенциалдардың контактілі айырымын өлшеу аспабының берілгішінің өлшеу электроды және бақыланатын металл бөлшектің беті конденсаторды құрайды, оның астарлары арасында потенциалдардың контактілі айырымы пайда болады. Аспаптың берілгіші потенциалдар мен өлшеуішсұлбасы арасындағы дәнекер болып табылады. Авторлармен әзірленген портативті цифрлық осциллограф негізінде потенциалдардың контактілік айырымын өлшеудің жылжымалы кешені металл бөлшектерінің бетін өндіру, пайдалану немесе жөндеу процесінде бұзбайтын бақылауды үздіксіз режимде орындауға мүмкіндік береді.

Макеева О.В., Олешко В.С., Федоров А.В., Юров В.М.

РАЗРАБОТКА УСТРОЙСТВА ОПРЕДЕЛЕНИЯ РАБОТЫ ВЫХОДА ЭЛЕКТРОНОВ.

Поверхность является важнейшей составляющей металлических деталей и необходим контроль ее состояния на всех этапах жизненного цикла детали — при ее производстве, эксплуатации и ремонте. Для проведения достоверного неразрушающего контроля металлических деталей необходимы специально разработанные для этого средства и методика его применения. Измерительный электрод датчика прибора измерения контактной разности потенциалов и поверхность контролируемой металлической детали образуют конденсатор, между обкладками которого и возникает контактная разность потенциалов. Датчик прибора является, своего рода, посредником между контактной разностью потенциалов и измерительной схемой. Разработанный авторами переносной комплекс измерения контактной разности потенциалов на основе портативного цифрового осциллографа позволяет выполнять в непрерывном режиме неразрушающий контроль поверхности металлических деталей в процессе их производства, эксплуатации или ремонта.

Теміралиев А., Томпакова Н., Грушевская Е., Федосимова А., Дмитриева Е., Лебедев И., Мукашев Б., Серикканов А.

ТӨМЕН ДИФФУЗИЯЛЫҚ ҮДЕРІСТЕРДЕЗОЛЬ-ГЕЛЬДІҢ ПАЙДА БОЛУЫ ЖӘНЕ БІРІГУІ

Пуанкаре қималарын бейнелеудің сызықсыз динамикасының әзірленген әдістерінің негізінде әлсіз диффузия фонында химиялық реакцияларда SnO_2 жұқа қабықшаларының пайда болу процесін сандық модельдеу жүргізілді. Сандық есептеулер қарқынды қарама-қарсы бірігу және ыдырау процестерінде динамикалық детерминирленген хаос шеңберінде жүргізілді. Золь-гель процестерінде химиялық белсенді орта үшін ішкі сызықты емес көзі бар диффузияның дифференциалды теңдеуі қолданылады. Модельдеу нәтижелері Пуассон-тұрақты фракталдық кластерлік құрылымдардың пайда болуының эксперименттік нәтижесін сапалы түрде растайды. Жұқа қабықшаларда тәжірибелік нәтижелерде фракталдық құрылымдардың болуы сызықты емес, тек ұжымдық құбылыстардың болуын білдіреді. Көп бөлшекті жүйеде бәсекелес ішкі процестермен тұрақты құрылымдарды желілік емес өзін-өзі ұйымдастыру әдісі жаңа технологиялар үшін қызықты болып табылады.

Теміралиев А., Томпакова Н., Федосимова А., Дмитриева Е., Лебедев И., Грушевская Е., Мукашев Б., Серикканов А.

ОБРАЗОВАНИЕ И СЛИЯНИЕ В ЗОЛЬ-ГЕЛЬ ПРОЦЕССАХ С НИЗКОЙ ДИФФУЗИЕЙ

На основе разработанных методов нелинейной динамики отображения сечений Пуанкаре проведено численное моделирование процесса образования тонких пленок SnO_2 в золь-гель химических реакциях на фоне слабой диффузии. Численные расчеты проводились в рамках динамически детерминированного хаоса в интенсивных противоположных процессах слияния и распада. Для химически активной среды в золь-гель-процессах используется дифференциальное уравнение диффузии с внутренним источником нелинейности. Результаты моделирования качественно подтверждают экспериментальный факт возникновения Пуассон-устойчивых фрактальных кластерных структур. Наличие фрактальных структур в экспериментальных результатах на тонких пленках означает наличие нелинейных коллективных явлений. Метод нелинейной самоорганизации устойчивых структур в многочастичной системе с конкурирующими внутренними процессами представляется интересным для новых технологий.

Плотникова И.В., Редько Л.А., Баус С.С., Стары О., Касымов С.С., Балтабеков А.С.

РЕНТГЕНДІК ЖҮЙЕ ҮШІН ҚҰРЫЛЫМДЫҚ ПАРАМЕТРЛЕРДІ ЕСЕПТЕУ ЖӘНЕ ҚОРҒАҒЫШ ЭКРАНЫҢ КОНСТРУКЦИЯСЫ

Сәулелену жүйесінің радиациялық қорғанысын есептеуді жүргізу қажеттілігі бұзбайтын бақылау аясында диагностикалық, жобалау немесе құрастырушы іс-шаралары жүзеге асырылатын негіз болып табылады. Мақалада пайдалану жағдайына байланысты рентгендік жүйелердің конструктивтік ерекшеліктері мен олардың техникалық сипаттамаларына талдау жасалған. Рентгендік сәулеленудің таралуы мен кернеудің қорғағыш экранының қалыңдығынан тәуелділігі келтірілген. Рентген жүйесінің қорғағыш экран корпусын жобалауға мүмкіндік беретін қорғаныш экранының қалыңдығын есептеуі ұсынылған. Келтірілген зерттеулер рентген жүйелерінің жаңа модификацияларын әзірлеу бойынша мамандардың жұмысын жеңілдетеді.

Плотникова И.В., Редько Л.А., Баус С.С., Стары О., Касымов С.С., Балтабеков А.С.

РАСЧЕТ СТРУКТУРНЫХ ПАРАМЕТРОВ И КОНСТРУКЦИЯ ЗАЩИТНОГО ЭКРАНА ДЛЯ РЕНТГЕНОВОЙ СИСТЕМЫ

Необходимость проведения расчета радиационной защиты системы излучения есть основа, в котором осуществляются диагностические, проектировочные или сборочные мероприятия в рамках неразрушающего контроля. В статье дан анализ конструктивных особенностей рентгеновских систем и их технических характеристик в зависимости от условий эксплуатации. Приведены зависимости распределения рентгеновского излучения и напряжения от толщины защитного экрана. Представлен расчет толщины защитного экрана, который позволит проектировать корпус защитного экрана рентгеновской системы. Приведенные исследования облегчат работу специалистов по разработке новых модификаций рентгеновских систем.

Кажыкенова С.Ш., Беломестный Д., Шалтаков С.Н., Шайхова Г.С.

МЕТАЛЛ БАЛҚЫТПАЛАРДЫҢ ГИДРОДИНАМИКА ТЕНДЕУЛЕРІН САНДЫҚ ИНТЕГРАЛДАУ АЛГОРИТМІ.

Сұйық күй теориясы қазіргі металлургиялық процестер теориясының қарапайым бөлімі емес. Сұйық күйдегі кез-келген зат сұйық күйдің қатты және газ тәрізді күйлер арасындағы аралық болып табылатындығымен сандық қана емес, сонымен бірге сапалық заңдылықты да анықтау қиын объект болып табылады. Теориялық гидродинамика бұрыннан бері әртүрлі мамандық ғалымдарының назарын аударды: негізгі тендеулердің салыстырмалы қарапайымдылығы, есептердің дәл тұжырымдалуы және эксперименттердің нақтылығы ерітінділерде болатын динамикалық құбылыстардың толық сипаттамасын алуға мүмкіндік берді. Үздіксіз медианың динамикалық қасиеттерін сипаттауда келесі тендеулер жүйесі алынды: тұтқыр балқымалар үшін - Навье - Стокс тендеулері, идеалбалқыма үшін - Эйлер тендеулері, әлсіз сығылатын балқымалар үшін - Обербек - Буссинеск тендеулері. Іргелі зерттеулерде және қолданбалы зерттеулер саласында бұл математикалық модельдер әдетте балқыманың ағымын модельдеу үшін қабылданады. Балқытуда пайда болатын теориялық процестердің сипаттамалары Стокс - Кирхгоф теориясына негізделген, ол классикалық гидродинамика аясында балқытылған жүйелердің кинетикалық қасиеттері арасындағы феноменологиялық байланыстарды ашты. Көптеген гидродинамикалық парадокстар ол пайда болғаннан бері өткен ұзақ және тікенді жолды көрсетеді. Бірінші ұзақ кезең идеал сығылмайтын сұйықтықтың ықтимал ағындарын зерттеумен байланысты болды. Күрделі ауыспалы функциялар теориясын қолдана отырып, ерттеудің математикалық әдістері өте жақсы көрінді. Идеал сұйық теориясының жетілмегендігін әйгілі Эйлер-Даламбер парадоксы көрсетті: потенциалды ағынның айналасында ағып жатқан денеге әсер ететін жалпы күш нөлге тең. Оның негізгі Навье-Стокс тендеулері бар тұтқыр сығылмайтын сұйықтықтың математикалық моделі жасалды. Ұсынылған жұмыста Навье - Стокс тендеулерін шешудің және зерттеудің әртүрлі әдістері сипатталған. Қазіргі кезеңде гидродинамика тендеулерінің локализацияланған шешімдерін табуға көп күш жұмсалады.

Кажыкенова С.Ш., Беломестный Д., Шалтаков С.Н., Шайхова Г.С.

КОНЕЧНО-РАЗНОСТНЫЙ МЕТОД ДЛЯ РЕАЛИЗАЦИИ ЧИСЛЕННОГО ИНТЕГРИРОВАНИЯ УРАВНЕНИЙ ГИДРОДИНАМИКИ РАСПЛАВОВ.

Теория жидкого состояния не является простым разделом современной теории металлургических процессов. Любое вещество в жидком состоянии является сложным объектом для установления не только количественных, но и качественных закономерностей, поскольку жидкое состояние является промежуточным между твердым и газообразным состояниями. Теоретическая гидродинамика издавна привлекала внимание ученых разных специальностей: сравнительная простота основных уравнений, точная постановка задач и ясность их экспериментов внушали надежду получить полное описание динамических явлений, происходящих в расплавах. При описании динамических свойств сплошных сред были получены следующие системы уравнений: для вязкого расплава - уравнения Навье - Стокса, для идеального расплава - уравнения Эйлера, для слабо сжимаемого расплава - уравнения Обербека - Буссинеска. В фундаментальных исследованиях и в области прикладных исследований эти математические модели являются общепринятыми для моделирования течения расплава. Теоретические описания процессов, происходящих в расплавах, основаны на теории Стокса-Кирхгофа, которая в рамках классической гидродинамики выявила

феноменологические связи между кинетическими свойствами расплавленных систем. Многочисленные гидродинамические парадоксы указывают на тот длинный и тернистый путь, который был пройден с момента его создания. Первый длительный этап был связан с изучением и исследованием потенциальных течений идеальной несжимаемой жидкости. Математические методы их исследования с использованием теории сложных переменных функций казались почти идеальными. На несовершенство теории идеальной жидкости указал знаменитый парадокс Эйлера-Даламбера: полная сила, действующая на тело, обтекающее потенциальный поток, равна нулю. Затем была создана математическая модель вязкой несжимаемой жидкости с ее основными уравнениями Навье-Стокса. Предлагаемая работа описывает различные методы решения и изучения уравнений Навье - Стокса. На современном этапе прилагаются большие усилия для поиска решений уравнений локализованной гидродинамики.

Айтқожаева Ж., Тынымбаев С., Адилбекқызы С., Скабылов А., Ибраимов М.

МОДУЛЬ БОЙЫНША БӨЛУ ҚҰРЫЛҒЫСЫНЫҢ ӘРЕКЕТТІК МОДЕЛІН ЖОБАЛАУ ЖӘНЕ ЗЕРТТЕУ.

CAD Quartus Prime Lite Edition бағдарламасында құрылғының оңтайлы шығындармен модуль бойынша бөлу құрылғысының әрекеттік моделі әзірленді. Жұмыс алгоритмі Verilog HDL тілінде жүзеге асырылған. Әрбір есептеу қадамында модульдің үш еселік, екі еселік немесе жалғыз мәнінің екі таңбаға жылжыған жоғарғы белгілік биттерден шегеріледі. Мысалдарды пайдалана отырып, әрекет моделінің алгоритмін функциялық және уақыт бойынша модельдеу орындалды және алгоритмнің дұрыстығы дәлелденді. Altera FPGA Cyclone VE 5CEBA4F23C7 арналған регистрларды жіберу деңгейдегі (RTL) құрылғы диаграммасы алынды. Уақыт талдауы әртүрлі жұмыс жағдайындағы принциптік және әрекеттік модельдері үшін максималды тактілік жиілігін анықтау үшін уақыт талдағышының көмегімен жүргізілді.

Айтқожаева Ж., Тынымбаев С., Адилбекқызы С., Скабылов А., Ибраимов М.

ПРОЕКТИРОВАНИЕ И ИССЛЕДОВАНИЕ ПОВЕДЕНЧЕСКОЙ МОДЕЛИ УСТРОЙСТВА ДЕЛЕНИЯ ПО МОДУЛЮ.

В CAD Quartus Prime Lite Edition была разработана поведенческая модель устройства приведения по модулю с оптимальными ресурсными затратами на оборудование. Алгоритм работы реализован на языке Verilog HDL. Используется метод, где на каждом шаге вычисления значения трехкратного, удвоенного или единственного значения модуля вычитается из старших битов, сдвинутых влево на два. Выполнено функциональное и временное моделирование алгоритма поведенческой модели с использованием примеров и подтверждена правильность алгоритма. Получена схема устройства на уровне передачи регистров (RTL) для FPGA Cyclone VE 5CEBA4F23C7 от Altera. Анализ времени был выполнен с использованием анализатора времени, чтобы определить максимальную тактовую частоту для принципиальной и поведенческой моделей в различных условиях работы.

Бактыбеков К.С., Аимбетов А., Рахимжанов Б.К., Мурат А.

ОРТАЛЫҚ ҚАЗАҚСТАН АЙМАҒЫНДАҒЫ ЖАБАЙ ӨЗЕНІНІҢ БАССЕЙНІНДЕ СУ ТАСҚЫНЫН МОДЕЛЬДЕУ

Жиілікті талдау - бұл белгілі бір оқиғаның қаншалықты жиі болатынын бағалау. Бұл су тасқынының жиілігін талдау кезінде өзендегі судың максималды ағымының сипаты мен көлемін түсінудің маңызды статистикалық әдісі. Бұл жұмыста су тасқынының жиілігін талдау үшін Орталық Қазақстан аймағының Жабай өзенінің бассейнін зерттеу нәтижелері келтірілген. Гумбел таралуы моделі көмегімен су тасқыны туралы ең жоғары деректерге жиіліктік талдау жасалды. Бұл әдіс әр түрлі қайталау кезеңінде күтілетін тасқын суды болжау үшін тиімді. Нәтижелер сегіз жылдардағы Жабай өзенінің су тасқынының әртүрлі деректерін пайдалана отырып алынды. Су тасқыны туралы мәліметтер Казгидромет гидрометеорологиялық қызметі ұсынған. Гумбел таралуы моделі арқылы әр түрлі кезеңдерде (Т) күтілетін су тасқыны болу мүмкіндігі болжайды. Сонымен қатар, Жабай өзенінің бассейні үшін сандық жер бедерінің моделін ұсынамыз. Бұл модель бірінші қазақстандық жердегі қашықтықтан зондтаудың KazEOSat-1 жер серігі арқылы алынған. Зерттеу нәтижелері Орталық Қазақстан аймағында су тасқынын болжауда пайдалы болады.

Бактыбеков К.С., Аимбетов А., Рахимжанов Б.К., Мурат А.

МОДЕЛИРОВАНИЕ НАВОДНЕНИЯ ДЛЯ БАССЕЙНА РЕКИ ЖАБАЙ В ЦЕНТРАЛЬНО-КАЗАХСТАНСКОЙ ОБЛАСТИ

Частотный анализ - это оценка того, как часто будет происходить указанное событие. Это наиболее важный статистический метод для понимания характера и величины максимального расхода воды в реке при анализе частоты наводнений. В данной работе с целью анализа частоты наводнений представлены результаты исследования бассейна реки Жабай Центрально-Казахстанской области. Частотный анализ имеющихся данных о пиковых паводках был выполнен с использованием распределения Гумбеля. Этот метод эффективен для прогнозирования ожидаемого паводка для разных периодов возврата. Результаты получены с применением различных данных о паводках за 2011-2018 гг. бассейна реки Жабай, данные о паводках предоставлены гидрометеорологической службой «Казгидромет» (Казахстан). Распределением Гумбеля получены ожидаемые паводки для различных периодов возврата (Т). Кроме того, проанализированы

метеорологические наземные данные реки Жабай и представлена цифровая модель местности для бассейна реки Жабай. Результаты исследования будут полезны при прогнозировании наводнений в Центрально-Казахстанской области.

Саулебеков А.О., Венос Д., Камбарова Ж.Т.

ҒАРЫШТЫҚ ЗЕРТТЕУЛЕРГЕ АРНАЛҒАН ЖОҒАРЫ АЖЫРАТУҒА ИЕ ЭЛЕКТРСТАТИКАЛЫҚ ЭНЕРГИЯ ТАЛДАҒЫШЫ.

Ғарыштық зерттеулер үшін зарядталған бөлшектер ағындарының энергия талдағышы ұсынылған. Зарядталған бөлшектер ағындарының энергия талдағышының әзірленген электронды-оптикалық сұлбасы электрстатикалық декаполь-цилиндрлік өріс негізінде құрастырылған. Энергия талдағыштың конструкциясы сипатталған. Электрстатикалық декаполь-цилиндрлік өрістің эквипотенциалдық суреттері тұрғызылған. Зарядталған бөлшектердің траекториясы есептелген. Энергия талдағыштың параметрлеріне зерттеу жүргізілді. Ұсынылған энергия талдағыш жоғары ажыратуға ие және ғарышты зерттеу үшін спектрометрлерді әзірлеуде пайдаланылуы мүмкін.

Саулебеков А.О., Венос Д., Камбарова Ж.Т.

ЭЛЕКТРОСТАТИЧЕСКИЙ ЭНЕРГОАНАЛИЗАТОР С ВЫСОКИМ РАЗРЕШЕНИЕМ ДЛЯ КОСМИЧЕСКИХ ИССЛЕДОВАНИЙ.

Предложен энергоанализатор пучков заряженных частиц для космических исследований. Разработанная электроно-оптическая схема энергоанализатора пучка заряженных частиц построена на основе электростатического декаполь-цилиндрического поля. Описана конструкция энергоанализатора. Построены эквипотенциальные портреты электростатического декаполь-цилиндрического поля. Рассчитаны траектории заряженных частиц. Проведено исследование параметров энергоанализатора. Предлагаемый энергоанализатор имеет высокое разрешение и может быть использован при разработке спектрометров для исследования космоса.

Шайхова Г.Н., Кутум Б.Б.

СИНУС ЖӘНЕ КОСИНУС ӘДІСІМЕН ЕКІ ӨЛШЕМДІ СЫЗЫҚТЫ ЕМЕС ШРЕДИНГЕР ТЕҢДЕУІНІҢ ҚУМА ТОЛҚЫНДЫҚ ШЕШІМІ .

Бұл жұмыста екі өлшемді сызықты емес Шредингер теңдеуін, атап айтқанда қума толқын түрінде нақты шешімді іздеу үшін синус және косинус әдісінің қолданылуын аналитикалық зерттеу ұсынылған. Кең танымал сызықты емес Шредингер теңдеуі физиканың әртүрлі салаларында сызықты емес толқындар теориясын зерттеуде маңызды рөл атқарады және көптеген нақты шешімдерге ие. Бұл теңдеу әлсіз сызықты емес және жоғары дисперсті сияқты әртүрлі жүйелерде сызықты емес толқындардың өзгеретін амплитудасының эволюциясын сипаттайды. Дәл шешімдерді алу әдістерінің бірі – синус және косинус әдісі. Бұл әдістің артықшылығы - сызықты емес есептерді шешу кезінде оның қарапайымдылығы мен сенімділігі. Бұл әдіске сәйкес, сызықты емес эволюциялық теңдеу толқындық түрлендіру арқылы ассоциацияланған қарапайым дифференциалдық теңдеулерге әкеледі, содан кейін синус немесе косинус функциялары арқылы шешіледі. Синус-косинус әдісі арқылы екі өлшемді сызықты емес Шредингер теңдеуі үшін қума толқынның шешімдері алынды. Алынған шешімдердің 2D-кестелері мен 3D-кестелері ұсынылған.

Шайхова Г.Н., Кутум Б.Б.

БЕГУЩЕЕ ВОЛНОВОЕ РЕШЕНИЕ ДВУМЕРНОГО НЕЛИНЕЙНОГО УРАВНЕНИЯ ШРЕДИНГЕРА МЕТОДОМ СИНУСА И КОСИНУСА.

В данной работе представлено аналитическое исследование двумерного нелинейного уравнения Шредингера, а именно применимость метода синуса и косинуса для поиска точного решения в виде бегущей волны. Широко известное нелинейное уравнение Шредингера играет важную роль в изучении теории нелинейных волн в различных областях физики и имеет огромное количество точных решений. Это уравнение описывает эволюцию изменяющейся амплитуды нелинейных волн в различных системах, таких как слабо нелинейные и высокодисперсные. Одним из методов получения точных решений является метод синуса и косинуса. Преимущество этого метода заключается в его простоте и надежности при получении решения нелинейных задач. Согласно этому методу, нелинейное эволюционное уравнение сводится к ассоциированным обыкновенным дифференциальным уравнениям с помощью волнового преобразования, а затем решается с помощью функций синуса или косинуса. С помощью метода синус-косинуса получены решения бегущей волны для двумерного нелинейного уравнения Шредингера. Представлены 2D-графики и 3D-графики полученных решений.

**INFORMATION
ABOUT AUTHORS**
**АВТОРЛАР ТУРАЛЫ
МӘЛІМЕТТЕР****СВЕДЕНИЯ
ОБ АВТОРАХ**

- Adilbekkyzy, S.** – Master, L.N. Gumilyov Eurasian National University, Nur-Sultan, Kazakhstan.
- Aimbetov, A.** – Vice-chairman, JSC National Company «Kazakhstan Gharysh Sapary», Nur-Sultan, Kazakhstan.
- Aimukhanov, A.K.** – PhD, Professor, Physical-Technical Faculty, E.A. Buketov Karaganda State University, Karaganda, Kazakhstan.
- Aitkhozhayeva, Y.Zh.** – Candidate of techn.sciences, Associate Professor, K.I.Satbayev Kazakh National Research Technical University, Almaty, Kazakhstan.
- Aliev, B.A.** – Doctor of phys.-math.sciences, Professor, al-Farabi Kazakh National University, Almaty, Kazakhstan.
- Alpyssova, G.** - PhD student, Department of technical physics, L.N. Gumilyov Eurasian National University, Nur-Sultan, Kazakhstan.
- Astafyev, A.L.** – Candidate of techn.sciences, Researcher of Scientific-research laboratory of electronics, non-conductors and semiconductors, National Research Tomsk Polytechnic University, Tomsk, Russia.
- Baktybekov, K.S.** - Doctor of phys.-math. sciences, Professor, Head of methodology and Scientific Research Department Geoinformation Data and Services Center, JSC National Company «Kazakhstan Gharysh Sapary», Nur-Sultan, Kazakhstan.
- Baldytchev, M.T.** - Candidate of techn.sciences, Researcher, Cherepovets Higher Military Engineering School of Radio Electronics, Cherepovets, Russia.
- Baltabekov, A.S.** - Candidate of phys.-math.sciences, Associate Professor, E.A. Buketov Karaganda State University, Karaganda, Kazakhstan.
- Baus, S.S.** - Graduate student, Kazan National Research Technical University named after A.N. Tupolev, Kazan, Tatarstan, Russia.
- Belomestny, D.** – PhD, Duisburg-Essen University, Duisburg, Germany.
- Bondarev, A.I.** - Master, Senior Lecturer, al-Farabi Kazakh National University, NNLOT, Almaty, Kazakhstan.
- Buitkenov, D.** - Master, Junior Researcher, National Research laboratory of collective use, S.Amanzholov East Kazakhstan State University, Ust-Kamenogorsk, Kazakhstan.
- Chebotar, I.V.** - Candidate of techn.sciences, Head of Scientific Research Department, Cherepovets Higher Military Engineering School of Radio Electronics, Cherepovets, Russia
- Dikhanbaev, K.K.** - Candidate of phys.-math.sciences, Senior Lecturer, Leading Researcher, al-Farabi Kazakh National University, NNLOT, Almaty, Kazakhstan.
- Dmitriyeva, E.** - Candidate of phys.-math.sciences, Leading researcher, LLP Institute of Physics and technology, Almaty, Kazakhstan.
- El, Abd A.** – PhD, Professor, Head of neutron activation analysis group, Reactor Physics Department, Nuclear Research Center, Atomic Energy Authority Cairo, Egypt.
- Eremin, E.N.** - Doctor of Technical Sciences, Professor, Omsk State Technical University, Head of Department, Omsk, Russia.
- Fedorov, A.V.** – student, Moscow Aviation Institute (National Research University), Moscow, Russia.
- Fedosimova, A.** - Master, Research associate, LLP Institute of Physics and technology, Almaty, Kazakhstan.
- Galtseva, O.V.** - Candidate of techn.sciences, Associate Professor, School of Non-Destructive Testing, National Research Tomsk Polytechnic University, Tomsk, Russia.
- Gavrilin, A.N.** - Candidate of techn.sciences, Associate Professor, National Research Tomsk Polytechnic University, Tomsk, Russia.
- Gaychuk, Y.N.** - Candidate of techn.sciences, Researcher, Scientific Department, Cherepovets Higher Military Engineering School of Radio Electronics, Cherepovets, Russia.
- Ghyngazov, S.A.** - Doctor of techn.sciences, Leading Researcher, Research Laboratory for Electronics, Dielectrics and Semiconductors, Research School of High-Energy Physics, Tomsk Polytechnic University, Tomsk, Russia.
- Grushevskaya, E.** - Master of physics, Junior researcher, LLP Institute of Physics and technology, Almaty, Kazakhstan.
- Guchenko, S.A.** - PhD candidate, Researcher, E.A. Buketov Karaganda State University, Karaganda, Kazakhstan.
- Hayitov, D.E.** - Senior Lecturer, Department of Physics, Bukhara Engineering - Technological Institute, Bukhara, Uzbekistan.
- Ibraimov, M.K.** – PhD, Associate Professor, al-Farabi Kazakh National University, Almaty, Kazakhstan.

- Ikramova, S.B.** – PhD student, Junior researcher, al-Farabi Kazakh National University, NNLOT, Almaty, Kazakhstan.
- Isataev, M.S.** – Candidate of phys.-math.science, Associate Professor, al-Farabi Kazakh National University, Almaty, Kazakhstan.
- Kadyrzhanov, K.K.** – Doctor of phys.-math.science, Professor, L.N. Gumilyov Eurasian National University, Nur-Sultan, Kazakhstan.
- Kalieva, Zh.E.** - Candidate of techn.science, Associate Professor, Institute of Scientific, Technical and Economic Research LLP, L.N. Gumilyov Eurasian National University, Nur-Sultan, Kazakhstan.
- Kambarova, Zh.T.** - PhD, Associate Professor, Physical-Technical Faculty, E.A. Buketov Karaganda State University, Karaganda, Kazakhstan.
- Karabekova, D.Zh.** - PhD, Associate Professor, Physical-Technical Faculty, E.A. Buketov Karaganda State University, Karaganda, Kazakhstan.
- Karipbayev, Zh.** - PhD, Faculty of Physics and Technology, L.N. Gumilyov Eurasian National University, Nur-Sultan, Kazakhstan.
- Kassymov, S.S.** - Candidate of phys.-math.science, Associate Professor, Head of Innovation techniques center, E.A. Buketov Karaganda State University, Karaganda, Kazakhstan.
- Kazhikenova, S.Sh.** - Doctor of techn.science, Professor, Head of the Department of Higher Mathematics, Karaganda State Technical University, Karaganda, Kazakhstan.
- Kenzhegulov, A.K.** – PhD doctor, Senior Lecturer, al-Farabi Kazakh National University, Almaty, Kazakhstan.
- Khasenov, A.** – PhD, Associate Professor, Physical-Technical Faculty, E.A. Buketov Karaganda State University, Karaganda, Kazakhstan.
- Kichanov, S.E.** – PhD, Senior Researcher, Joint Institute for Nuclear Research, Dubna, Russia.
- Kissabekova, P.** – PhD student, Physical-Technical Faculty, E.A. Buketov Karaganda State University, Karaganda, Kazakhstan.
- Kozlenko, D.P.** – Doctor of phys.-math.science, Professor, Head of Department, Joint Institute for Nuclear Research, Dubna, Russia.
- Kukenova, A.** - Master student, Faculty of Physics and Technology, L.N. Gumilyov Eurasian National University, Nur-Sultan, Kazakhstan.
- Kutum, B.B.** - PhD student, L.N. Gumilyov Eurasian National University, Nur-Sultan, Kazakhstan.
- Kuvshinov, K.A.** – Master of engineering and technology, Senior Lecturer, National Research Tomsk Polytechnic University, Tomsk, Russia.
- Kylyshkanov, M.** - Doctor of phys.-math.science, Professor, Senior Researcher, National Research laboratory of collective use, S.Amanzholov East Kazakhstan State University, Ust-Kamenogorsk, Kazakhstan.
- Laptev, I.V.** - Candidate of techn.science, Researcher, Cherepovets Higher Military Engineering School of Radio Electronics, Cherepovets, Russia.
- Lebedev, I.** - Doctor of phys.-math.science, Head of the Laboratory, LLP Institute of Physics and technology, Almaty, Kazakhstan.
- Lisitsyn, V.M.** - Doctor of phys.-math.science, Professor, School of Advanced Manufacturing Technologies, National Research Tomsk Polytechnic University, Tomsk, Russia.
- Lysenko, E.N.** - Doctor of techn.science, Head of the Research Laboratory for Electronics, Dielectrics and Semiconductors, Research School of High-Energy Physics, Tomsk Polytechnic University, Tomsk, Russia.
- Lysenko, E.N.** - Doctor of techn.science, Head of the Research Laboratory for Electronics, Dielectrics and Semiconductors, Research School of High-Energy Physics, National Research Tomsk Polytechnic University, Tomsk, Russia.
- Makeeva, O.V.** – Candidate of techn.science, Associate Professor, Department «Information systems and technologies», Moscow State University of Technologies and Management, Moscow, Russia.
- Malyshev, A.V.** – Candidate of phys.-math.science, Senior Researcher, Control and Diagnostics Department, Engineering School of Non-Destructive Testing and Safety, National Research Tomsk Polytechnic University, Tomsk, Russia.
- Masina, M.N.** – Master, Lecturer, al-Farabi Kazakh National University, Almaty, Kazakhstan.
- Masolov, V.G.** - Candidate of techn.science, General director «VDM-tehnika» LLC, Moscow, Russia.
- Medyanova, B.S.** – Doctoral student, Senior Lecturer, al-Farabi Kazakh National University, Almaty, Kazakhstan.
- Merzadinova, G.T.** - Doctor of techn.science, Professor, Vice-Rector of Research Work, L.N. Gumilyov Eurasian National University, Nur-Sultan, Kazakhstan.

- Minkov, L.L.** - Doctor of of phys.-math.sciences, Professor, Physics and Engineering Faculty, Tomsk State University, Tomsk, Russia.
- Moyzes, B.B.** - Candidate of techn.sciences, Associate Professor, National Research Tomsk Polytechnic University, Tomsk, Russia.
- Mukashev, B.** - Doctor of of phys.-math.sciences, Professor, Academician of the national Academy of Sciences of Kazakhstan, Chief research officer, LLP Institute of Physics and technology, Almaty, Kazakhstan.
- Murat, A.** - Engineer, JSC National Company «Kazakhstan Gharysh Sapary», Nur-Sultan, Kazakhstan.
- Mussakhanov, D.** - Graduate student, School of Advanced Manufacturing Technologies, National Research Tomsk Polytechnic University, Tomsk, Russia.
- Nazarov, K.M.** – Master, Engineer, Frank Laboratory of Neutron Physics, Joint Institute for Nuclear Research, Dubna, Russia; PhD-student, L.N. Gumilyov Eurasian National University Nur-Sultan, Kazakhstan.
- Nikolaev, E.V.** – Candidate of techn.sciences, Researcher of Scientific-research laboratory of electronics, non-conductors and semiconductors, National Research Tomsk Polytechnic University, Tomsk, Russia.
- Nikolaeva, S.A.** – Research-assistant of Scientific-research laboratory of electronics, non-conductors and semiconductors, National Research Tomsk Polytechnic University, Tomsk, Russia.
- Nizhegorodov, A.I.** – Doctor of techn.sciences, Professor, Irkutsk National Research Technical University, Irkutsk, Russia.
- Obukhov, S.G.** - Doctor of techn.sciences, Professor, School of Energy & Power Engineering, National Research Tomsk Polytechnic University, Tomsk, Russia.
- Oleshko, V.S.** – Candidate of techn.sciences, Associate Professor, Department of «Aircraft», Moscow Aviation Institute (National Research University), Moscow, Russia.
- Ospanali, A.T.** – Postgraduate student, al-Farabi Kazakh National University, Almaty, Kazakhstan.
- Partizan, G.** – PhD doctor, Acting Assistant Professor, al-Farabi Kazakh National University, Almaty, Kazakhstan.
- Petrova, A.** – Master, Junior Researcher, Engineering School of Non-Destructive Testing and Safety, National Research Tomsk Polytechnic University, Tomsk, Russia.
- Pivkin, I.G.** - Researcher, Department of Information Technology, Cherepovets Higher Military Engineering School of Radio Electronics, Cherepovets, Russia.
- Plotnikov, I.A.** – Candidate of techn.sciences, Associate Professor, School of Energy & Power Engineering, National Research Tomsk Polytechnic University, Tomsk, Russia.
- Plotnikova, I.V.** - Candidate of techn.sciences, Associate Professor, School of Non-Destructive Testing, National Research Tomsk Polytechnic University, Tomsk, Russia.
- Rakhadilov, B.K.** - PhD, Senior Researcher, Research center "Surface engineering and Tribology», S.Amanzholov East Kazakhstan State University, Ust-Kamenogorsk, Kazakhstan.
- Rakhimzhanov, B.K.** - PhD, Head of Image Processing Department, JSC National Company «Kazakhstan Gharysh Sapary», Nur-Sultan, Kazakhstan.
- Raupova, I.B.** - Master, Lecturer, Department of Physics, Bukhara Engineering - Technological Institute, Bukhara, Uzbekistan.
- Redko, L.A.** - Candidate of techn.sciences, Associate Professor, School of Non-Destructive Testing, National Research Tomsk Polytechnic University, Tomsk, Russia.
- Sadikova, M.I.** - Master, Assistant, Department of Chemistry, Bukhara Engineering - Technological Institute, Uzbekistan.
- Sakipov, K.E.** - Candidate of techn.sciences, Associate Professor, Head of the Heat Power Engineering Department, L.N. Gumilyov Eurasian National University, Nur-Sultan, Kazakhstan.
- Sakipova, S.E.** – Candidate of phys.-math.sciences, Professor, Physical-Technical Faculty, E.A. Buketov Karaganda State University, Karaganda, Kazakhstan.
- Satybaldin, A.Zh.** – Candidate of chem. sciences, Associate Professor, Physical-Technical faculty, E.A. Buketov Karaganda State University, Karaganda, Kazakhstan.
- Saulebekov, A.O.** – Doctor of phys.-math.sciences, Professor, M.V. Lomonosov Moscow State University, Kazakhstan branch, Nur-Sultan, Kazakhstan.
- Senyut, V.T.** - Candidate of techn.sciences, Leading Researcher, Joint Institute of Mechanical Engineering of NAS of Belarus, Minsk, Belarus.
- Serikkanov, A.** - Candidate of phys.-math.sciences, Director, LLP Institute of Physics and technology, Almaty, Kazakhstan.
- Seydulla, Zh.K.** – PhD student, Senior lecturer, al-Farabi Kazakh National University, Almaty, Kazakhstan.
- Shabdan, E.** - PhD, Senior Researcher, al-Farabi Kazakh National University, NNLOT, Almaty, Kazakhstan.

Shaihova, G.S. - Candidate of techn.sciences, Senior Lecturer, Karaganda State Technical University, Karaganda, Kazakhstan.

Shaikhova, G.N. - PhD, Associate Professor, L.N. Gumilyov Eurasian National University, Nur-Sultan, Kazakhstan.

Shaltakov, S.N. - Master, Senior Lecturer, Karaganda State Technical University, Karaganda, Kazakhstan.

Sharifov, D.M. - Candidate of phys.-math.sciences, Associate Professor, Transport and Energy Faculty, L.N. Gumilyov Eurasian National University, Nur-Sultan, Kazakhstan.

Sharipov, M.Z. Doctor of phys.-math.sciences, Head of Physics Department, Bukhara Engineering-Technological Institute, Bukhara, Uzbekistan.

Skabylov, A.A. – PhD student, al-Farabi Kazakh National University, Almaty, Kazakhstan.

Starý, O. - PhD, Associate Professor, Czech Technical University in Prague, Prague, Czech Republic.

Surzhikov, A.P. - Doctor of phys.-math.sciences, Professor, Head of Control and Diagnostics Department, Engineering School of Non-Destructive Testing and Safety, National Research Tomsk Polytechnic University, Tomsk, Russia.

Suyundykova, G.S. – Doctoral student, Senior Lecturer, al-Farabi Kazakh National University, Almaty, Kazakhstan

Taman, M. – PhD, Associate Professor, Department of Structural Engineering, Faculty of Engineering, Tanta University, Tanta, Egypt.

Tanasheva, N.K. – PhD, Senior Researcher, Institute of Applied Mathematics, Ministry of Education and Science of Republic Kazakhstan, Karaganda, Kazakhstan.

Temiraliyev, A. - Candidate of phys.-math.sciences, Senior Lecturer, LLP Institute of Physics and technology, Almaty, Kazakhstan.

Timoshenko, A.V. - Doctor of techn.sciences, Deputy of General Designer, OJSC Academician A.L. Mints Radiotechnical Institute, Moscow, Russia.

Tinishbaeva, K. – PhD student, specialty Nuclear Physics, L.N. Gumilyov Eurasian National University, Nur-Sultan, Kazakhstan.

Toleuov, G.K. – Candidate of phys.-math.sciences, Associate Professor, al-Farabi Kazakh National University, Almaty, Kazakhstan.

Tompakova, N. - Master of physics, Junior researcher LLP Institute of Physics and technology, Almaty, Kazakhstan.

Tulegenova, A. - Candidate of techn.sciences, al-Farabi Kazakh National University, Almaty, Kazakhstan.

Tungushbekova, M. - Master, Physical-Technical Faculty, E.A. Buketov Karaganda State University, Karaganda, Kazakhstan.

Tynymbayev, S. – Candidate of techn.sciences, Professor, Almaty University of Power Engineering and Telecommunications, Almaty, Kazakhstan.

Uglov, V.V. – Doctor of phys.-math.sciences, Professor, Belarusian State University, Minsk, Belarus.

Userbayev, M. T. - Candidate of techn.sciences, Associate Professor, S.Seifullin Kazakh AgroTechnical University, Nur-Sultan, Kazakhstan.

Venos, D. - An employee of the Institute of Nuclear Physics of Academy of Sciences of the Czech Republic, Prague, Czech Republic.

Wieleba, W. - Doctor of Sciences, Professor, Faculty of Mechanical Engineering, Wroclaw University of Science and Technology, Wroclaw, Poland.

Yerbolatuly, D. - Candidate of technical Sciences, Associate Professor, S.Amanzholov East Kazakhstan State University, Ust-Kamenogorsk, Kazakhstan.

Yurov, V.M. - Candidate of phys.-math.sciences, Professor, Director of the Scientific Research Center, E.A. Buketov Karaganda State University, Karaganda, Kazakhstan.

Zeinidenov, A.K. – PhD, Associate Professor, Dean of the Physical-Technical Faculty, E.A. Buketov Karaganda State University, Karaganda, Kazakhstan.

Zhumadilov, B.E. – Postgraduate student, al-Farabi Kazakh National University, Almaty, Kazakhstan.

Zulbukharova, E.M. – Master, Senior lecturer, al-Farabi Kazakh National University, Almaty, Kazakhstan.

About «Eurasian Physical Technical Journal»

ISSN 1811-1165 Key title: Eurasian physical technical journal (Print)
Abbreviated key title: Eurasian phys. tech. j. (Print)

ISSN 2413-2179 Key title: Eurasian physical technical journal (Online)
Abbreviated key title: Eurasian phys. tech. j. (Online)

Eurasian Physical Technical Journal (Eurasian phys. tech. j.) is a peer-reviewed open access international scientific journal publishing original research results on actual problems of Technical Physics and other related fields. Since 2004 Eurasian phys. tech. j. is published in English with periodicity 2 issues per year. Our E.A. Buketov Karaganda University is the main organizer and financial sponsor of Eurasian phys. tech. j. The international editorial board consists of leading physicists from 12 countries.

Since 2008 EAPhTJ is included in the list of publications recommended by the Ministry of Science Education and Science of the Republic of Kazakhstan for publication of the master's and PhD doctoral dissertations main results on Physical and Mathematical sciences.

May 8, 2019 according decision of the international Content Selection & Advisory Board (CSAB) the Eurasian phys. tech. j. had been included into Scopus data base on four scientific areas: Energy, Engineering, Materials Science, Physics and Astronomy.

June 10, 2020 after updating the SCOPUS database the Eurasian Physical Technical Journal received a citation index of 0.2 (with the highest percentile 16% in the Energy).

Publication Ethics and Malpractice Statement

Submission of an article to the Eurasian phys. tech. j. implies that the paper described has not been published previously, that it is not under consideration for publication elsewhere, that its publication is approved by all authors and tacitly or explicitly by the responsible authorities where the paper was carried out, and that, if accepted, it will not be published elsewhere in the same form, in English or in any other language, including electronically without the written consent of the copyright holder. In particular, translations into English of papers already published in another language are not accepted.

For information on Ethics in publishing and Ethical guidelines for journal publication see <http://www.elsevier.com/publishingethics> and <http://www.elsevier.com/journal-authors/ethics>.

The Eurasian phys. tech. j. follows the Code of Conduct of the Committee on Publication Ethics (COPE), and follows the COPE Flowcharts for Resolving Cases of Suspected Misconduct (http://publicationethics.org/files/u2/New_Code.pdf).

To verify originality, your article may be checked by the originality detection service Cross Check <http://www.elsevier.com/editors/plagdetect>.

Authors are responsible for the content of their publications. No other forms of scientific misconduct are allowed, such as plagiarism, falsification, fraudulently data, incorrect interpretation of other works, incorrect citations, etc. Authors are obliged to participate in peer review process and be ready to provide corrections, clarifications, retractions and apologies when needed. All authors of a paper should have significantly contributed to the research.

Reviewers should provide objective judgments and should point out relevant published works which are not yet cited. Reviewed articles should be treated confidentially. The reviewers will be chosen in such a way that there is no conflict of interests with respect to the research, the authors and/or the research funders.

Editors have complete responsibility and authority to reject or accept a paper, and they will only accept a paper when reasonably certain. They will preserve anonymity of reviewers and promote publication of corrections, clarifications, retractions and apologies when needed.

The acceptance of a paper automatically implies the copyright transfer to the Eurasian phys. tech. j.

All submitted papers will be sent for reviewing to leading experts in the given area.

The Editorial Board of the Eurasian phys. tech. j. will monitor and safeguard publishing ethics. The editors reserve the right to accept or reject manuscripts.

GUIDELINES FOR AUTHORS

Research articles, survey papers and short notes are accepted for exclusive publication in the **Eurasian phys. tech. j.** in English. The manuscripts and short notes must contain original results of investigation in the following scientific areas of Physics:

ENERGY.

ENGINEERING.

- **Devices and methods of experiment.**
- **Modeling of the nonlinear physical - technical processes.**

MATERIALS SCIENCE.

PHYSICS AND ASTRONOMY

All publishing manuscripts and short notes must have been recommended by a member of the editor board or by the organization (University), where the work was performed. The author who submitted an article for publication will be considered as a corresponding author.

The paper, short note or review paper shall include an abstract of the contents, not exceeding 200 words and keywords (no more than 10). The abstract must not coincide with the introduction or conclusive part of the work and must not contain references, abbreviations and other unknown words.

All articles should have list of keywords or terms (3 to 10) for indexing purposes.

The text of a paper must not exceed 8-12 pages including tables, figures (no more than 6) and references. A short note must not exceed 4-5 pages including no more than 2 figures. A review paper must not be more than 20 pages (including no more than 10 figures).

The text should be divided on structural parts: **Introduction, Theoretical part, Experimental technique, Results and Discussion, Conclusion**, etc.

Printed copies shall be on good quality paper of International size A4. All texts must be printed in Microsoft Word. It is preferable to use the Times fonts. The text must be printed in 12 point letters, 1.5 intervals. There shall be a margin of 30 mm at the left-hand edge, of 15 mm at the fore edge, of 30 mm at the head of the page and of 30 mm at the tail. All pages must be numbered.

Acknowledgments may be shown at the end of the article text, before **REFERENCES**.

All references must be numbered in the text (for example, [1], [2-4]) and listed in numerical order.

Equations in your paper have to be written using the Microsoft Equation Editor or the MathType (<http://www.mathtype.com>) for (Insert | Object | Create New | Microsoft Equation or MathType Equation).

Tables must be inserted into the text.

Figures should be prepared in a digital form suitable for direct reproduction. Figures shall be submitted on the separate sheets and not included into the text.

The following files must be submitted via e-mail:

- Article text (*.doc);
- Figures (fig1.jpg, fig2.pcx);
- Figure captions (*.txt, *.doc).

